Topics in the gauge/gravity correspondence.

Schofield, Daniel James

Swansea University
Prifysgol Abertawe

Topics in the Gauge/Gravity Correspondence

Daniel James Schofield

Department of Physics

Submitted to Swansea University in fulfilment
of the requirements for the degree of Doctor of Philosophy

2014

Abstract

In this thesis we study two classes of backgrounds in Type IIB supergravity which admit interpretation in terms of dual $\mathcal{N} = 1$ Supersymmetric Field Theories. The first is obtained by wrapping D5 branes on a two-cycle inside the conifold; the second is the class containing the dual to the baryonic branch of Klebanov-Strassler. These backgrounds are related via a 'solution generating procedure' (or *rotation*) and have a number of interesting properties.

First, we study non-Supersymmetric deformations of the baryonic branch by making use of the *rotation* procedure. We interpret these deformations as soft-breaking through the addition of gaugino masses, and calculate various observables which support this picture. We then explore the two-dimensional solution space of supergravity solutions associated with these deformations, finding a number of interesting limiting cases. We see that much of the structure of the Supersymmetric baryonic branch survives, even for large values of the deformation.

Second, we study probe-D7 branes which wrap an internal three-dimensional manifold and lie at the equator of the transverse two-sphere, in the class of wrapped D5 brane backgrounds. We employ this method to model Chiral-symmetry breaking and present a simple diagnostic tool for determining the classical stability of such embeddings. In particular cases we find that a new type of phase transition appears, putting limits on the region of parameter space which can be used to study physics of the dual field theory.

Finally, we study the relationship between confinement in a Quantum Field Theory and the presence of a first-order phase transition in its Entanglement Entropy. We determine the sufficient conditions for such a phase transition and compare to the conditions on a Rectangular Wilson Loop to probe confinement. In certain backgrounds with non-local high energy behaviour, we show that new configurations (associated with the introduction of a UV cutoff) are required in order to recover the otherwise absent phase transition. We also show that a local UV-completion, obtained using the *rotation* procedure, to the non-local theories has a similar effect to the cutoff.

This thesis is based on papers [1–5].

Declaration

This work has not previously been accepted in substance for any degree and is not being concurrently submitted for any degree.

Signed:  (candidate)

Date: 02/10/2014

Statement 1

This thesis is the result of my own investigations, except where otherwise stated. Where correction services have been used, the extent and nature of the correction is clearly marked in a footnote(s). Other sources are acknowledged by footnotes giving explicit references. A bibliography is appended.

Signed:  (candidate)

Date: 02/10/2014

Statement 2

I hereby give consent for my thesis, if accepted, to be available for photocopying and for inter-library loan, and for the title and summary to be made available to outside organisations.

Signed:  (candidate)

Date: 02/10/2014

Contents

Acknowledgements

First and foremost, I would like to thank Maurizio Piai, who has acted as my Ph.D. supervisor during my time at Swansea and further, Carlos Núñez, both of whom I collaborated with on a number of interesting and fruitful projects. Next, I would like to thank all the other individuals who were involved in collaborations over the last three and a half years. I am indebted to you all for teaching me many things about Physics, and putting up with my (often quite simple) questions. I also give thanks to the STFC for funding my Ph.D.

Throughout my studies I have also been supported by the individuals around me. Special thanks go to Benedict Fraser, Niall Macpherson, Wynne Evans and Alessandro Amato, who have been with me since the beginning of my Ph.D. May I wish you all the best of luck in your future endeavours. I also extend thanks to the many other Ph.D. students who have helped me, both inside and outside of Physics, along the way.

Last, but by no means least, I thank my parents and my brother, for their support. I would not be where I am today without you.

List of Figures

LIST OF FIGURES

Chapter 1

Introduction

In the sixteen years since its advent, the Gauge/Gravity Correspondence [6–8], although still only conjectural, has provided us with one of the most effective tools for studying the non-perturbative dynamics of a variety of Quantum Field Theories. It furnishes an equivalence between a field theory at strong coupling and a weakly coupled gravity dual (under suitable conditions). The original correspondence described strongly-coupled $\mathcal{N} = 4$ Super Yang-Mills in four dimensions from the dual point of view of Type IIB string theory propagating on $AdS_5 \times S^5$, but has since been generalised to apply to settings with broken conformal symmetry and reduced Supersymmetry. In this Ph.D. thesis, we shall look at some of these more phenomenologically relevant models, where applying the ideas of the Gauge/Gravity Correspondence allows us to learn more about dual strongly-coupled field theories with realistic features.

Many interesting duals to field theories with low amounts of Supersymmetry are based on the conifold and its variations [9]. There exist various well studied supergravity solutions within this framework [10–14]. These are solutions to Type IIB supergravity which fall within the Papadopolous-Tseytlin (PT) ansatz [15], which is a subtruncation of a more general Supersymmetric consistent truncation of $T^{1,1}$ (the base of the conifold) [16, 17].

Two such solutions, whose dual theories have behaviour similar to that of $\mathcal{N} = 1$ Super Yang-Mills in the IR, and which are globally regular, are the deformed conifold background of Klebanov and Strassler [12] and the Chamseddine-Volkov/Maldacena-Núñez (CVMN) solution [13, 18]. The Klebanov-Strassler background consists of n D3 branes and M fractional D5 branes living at the tip of the deformed conifold, and is dual to a $\mathcal{N} = 1$ cascading $SU(M+n) \times SU(n)$ quiver gauge theory with bifundamental matter fields. In the IR, the theory confines and is essentially $\mathcal{N} = 1$ SU(M) Super Yang-Mills theory. On the other hand, the CVMN solution is a

twisted compactification of D5 branes on a two-cycle of the resolved conifold, preserving $\mathcal{N} = 1$ Supersymmetry. This model also exhibits confinement in the IR, and is dual to $\mathcal{N} = 1$ Super Yang-Mills, plus a tower of 'Kaluza-Klein' massive chiral and vector multiplets.

Both theories exist as points on the baryonic branch of Klebanov-Strassler [14], a one-parameter family of solutions of IIB supergravity, corresponding to different expectation values for a baryonic operator. We shall discuss the relationship between these backgrounds in more detail in Chapter. 2 through a certain 'solution generating procedure' (i.e. a U-duality [19]). Further, these solutions were studied in [20], in the presence of a Vacuum Expectation Value (VEV) for a dimension-six operator. This generated a model with multi-scale dynamics on the baryonic branch with many interesting features.

The presence of residual Supersymmetry has played an important role in the discovery and success of many of these setups, both in guaranteeing the stability of, and in simplifying the search for such solutions, but despite this we are not restricted to examples of this sort. Indeed, there has been considerable headway made in finding solutions where Supersymmetry is completely absent. One such area is in duals of Gauge Theories at finite temperature [21], which are solutions in which a black hole is present in the background, examples of which can be found in [22–25].

Another avenue is to construct dual backgrounds to field theories where supersymmetry has been softly broken through the addition of deformations via relevant operators inserted in the Lagrangian. Then using Supersymmetric theories where the Correspondence is well understood as a reference point, it is then possible to find dual gravity solutions which are the corresponding non-Supersymmetric deformations of these theories, as was achieved for example in [26–31].

These systems should preserve some of the dynamics of the original Supersymmetric case but have completely broken Supersymmetry. As such, we expect the low energy dynamics to be a non-linear combination of the Supersymmetric and non-Supersymmetric effects, and the deformed background will recover the original one asymptotically. It is the fact that the deformed backgrounds share many of the features, such as symmetries, of the Supersymmetric solutions which means that it is viable to make progress on this problem.

We discuss this idea in Chapter. 3, where we find the non-Supersymmetric deformations of the backgrounds discussed in Chapter. 2, compute a number of observables and then exhaustively study the space of solutions generated by such a deformation, finding a number of non-Supersymmetric generalisations of known Supersymmetric backgrounds.

Another aspect of the Correspondence is the study of non-local operators in the dual field theory, by considering the dynamics of probes with end-points on the UV boundary which explore the bulk of the gravity solution. It is thus possible to study Chiral-symmetry breaking, using a stack of N_f Dp branes which introduce dynamical flavors and probe the geometry, as in [32].

If we look for U-shaped embeddings of the probe branes, extending from the boundary to some finite value of the radial coordinate, the theory living on the stack has a $U(N_f)$-symmetry, but the U-shape is a double covering of the radial direction, and effectively we find a $U(N_f)_L \times U(N_f)_R$-symmetry. Due to the merging of the two branches, at a point in the space, this symmetry is broken, and the result is a strongly-coupled model in which the breaking $U(N_f)_L \times U(N_f)_R \to U(N_f)_D$ occurs. The minimum of the U-shape sets the scale of the Chiral-symmetry breaking. This idea was proposed and applied in [33] to the background of [21], using D8 branes to extend in the Minkowski directions and wrap an internal S^4, with the U-shape profile exisiting in the radial coordinate and an internal S^1. These results were generalised to a number of different contexts in [34–36].

Another example was developed by introducing non-Supersymmetric probe-D7 branes * on the backgrounds related to the conifold [37, 38]. This new embedding ansatz was then applied [39] to the multi-scale model discovered in [40]. The interest in this setup arises from the possibility that multi-scale dynamics, as developed from the perspective of the Gauge/Gravity Correspondence, may help in the resolution of a number of problems (such as the size of the S parameter) of models of Electroweak symmetry breaking.

In Chapter. 4, we study probe-D7 branes on the large class of backgrounds defined in Section. 2.2, giving first a general formalism, and then developing an elegant way of analysing the perturbative stability of these probes, without having to perform the heavy duty task of explicitly computing the spectrum of fluctuations. Because of the various complexities of the backgrounds, we find curious phenomena (including a new phase transition associated with an imposed UV cutoff in the background) appearing when introducing the probe branes. We also discuss which of these backgrounds (in the presence of the probe branes) is suitable as a model of Chiral-symmetry breaking (or further, Electroweak symmetry breaking).

The Correspondence also allows for the calculation of certain interesting field theory observables from a holographic perspective. One example we shall discuss is the Entanglement

*Here we shall describe the setup with an abuse of language as "probe-D7 branes" but each time we are actually referring to a stack of D7 branes and a stack of anti-D7 branes in line with the ideas of [37, 38].

Entropy. This is a quantity which was originally defined in quantum mechanical systems, describing the amount of quantum correlations, and has found a wide range of applications in different branches of physics. Reviews of these applications and formalisms can be found in [41–45].

The holographic description was first proposed in [46], in the context of a $d+1$ dimensional Conformal Field Theory, which is dual to an AdS_{d+2} background. The holographic Entanglement Entropy is then given by minimising the d dimensional area in the dual background, whose boundary coincides with the boundary of the entangling region. They then generalised this to duals where the dilaton runs and the volume of the internal space can vary [47]. The authors of [48] applied this generalised prescription to non-conformal theories and found that certain backgrounds, which are dual to confining systems (at zero temperature), exhibit a first-order phase transition in the Entanglement Entropy as a function of the width of the entangling region.

Another well understood observable is that of the Rectangular Wilson Loop [49], which from a holographic perspective also involves minimising an area, and has also been used as a probe of confinement. Due to the similarities in setup, there would seem to be a strong possibility of relating behaviours of these two observables.

More recently, there has been progress in studying the behaviour of the Entanglement Entropy in Field Theories which exhibit non-locality, see for example [50–54]. In a local theory, the degrees of freedom with correlations across the boundary of the entangling region, must live near the boundary, and this leads to an Area-Law for the Entanglement Entropy. * In non-local theories, the behaviour of the Entanglement Entropy deviates from this, and it has been shown to give a Volume-Law behaviour.

In Chapter. 5 we will calculate the Entanglement Entropy in various models of confinement, and compare the equivalent results for the Rectangular Wilson Loop, showing that the calculations fall into the general formalism presented in Section. 4.1. We go on to study a number of examples (including the solutions in Section. 2.2 and generalisations including sources) where the expected phase transition in the Entanglement Entropy is often missing, discuss how this is related to potential non-localities present in the UV of these models, and look at possible way of recovering it.

*Strictly, the Area-Law corresponds to the leading order divergence in the calculation of the Entanglement Entropy.

Chapter 2

A Family of Wrapped D5 Brane Solutions

2.1 Overview

Initially, we present two Supersymmetric field theories, which are connected via 'Higgsing' (see discussion in [19, 20]), although they appear quite different on the surface. The first of the two theories is that found when wrapping N_c D5 branes on a two-cycle inside the resolved conifold, and we shall refer to this as "Theory A". The second is that of the baryonic branch of the Klebanov-Strassler Quantum Field Theory which we shall call "Theory B".

Theory A is generated by starting from a six-dimensional $SU(N_c)$ Supersymmetric Yang-Mills Theory with 16 supercharges, and then performing a special twisted compactification over a two-manifold (which in this case is a two-sphere), preserving 4 of the supercharges. This was studied in [13, 55, 56]. The field content (in the four-dimensional language) is that of a massless vector multiplet, and also a "Kaluza-Klein" (KK) tower of massive chiral and vector multiplets. The form of the Lagrangian, as well as the weakly coupled mass spectrum and degeneracies of the theory can be found in [55, 56]. This theory has an $SU(N_c)$ gauge symmetry, and its global symmetries are

$$SU(2)_L \times SU(2)_R \times U(1)_R. \tag{2.1.1}$$

In the low energy theory (that of four-dimensional $\mathcal{N} = 1$ $SU(N_c)$ Super Yang-Mills), the massless vector multiplet contains a gauge field A_μ and a Majorana spinor λ, both transforming in the adjoint of the gauge group. Strictly, in the UV this theory is related to a Little String Theory, and is only like $\mathcal{N} = 1$ Super Yang-Mills in the IR (and thus it exhibits confinement).

This four-dimensional theory can be thought to be valid at energies lower than the inverse volume of the two-sphere (which is related to the coupling as we discuss around Eq. 2.2.13), but as we move to higher energies (those comparable with the inverse volume of the two-sphere) the KK tower of massive chiral and vector multiplets enter the spectrum again. *

The R-symmetry of the theory is anomalous, breaking $U(1)_R \to \mathbb{Z}_{2N_c}$. Further, in the IR due to the formation of a gluino condensate, there is spontaneous breaking $\mathbb{Z}_{2N_c} \to \mathbb{Z}_2$. The gauge theory has N_c inequivalent vacua as a consequence of this condensation (discussed for instance in [57]), and there exists domain wall configurations interpolating amongst the different vacua, whose tension is related to the different choices of VEV for the condensate (which we shall discuss further in Section. 3.3.5).

Theory B is a quiver, with gauge group $SU(M+n) \times SU(n)$, † and bifundamental matter multiplets A_i, B_α (with $i, \alpha = 1, 2$). The global symmetries in this theory are given by

$$SU(2)_L \times SU(2)_R \times U(1)_B \times U(1)_R. \tag{2.1.2}$$

where the "baryon number" $U(1)_B$ takes $A_i \to e^{i\gamma} A_i$ and $B_\alpha \to e^{-i\gamma} B_\alpha$. Further, the $U(1)_R$ R-symmetry is anomalous, breaking to $\mathbb{Z}_{2M}$. The bifundamentals transform under the local and global symmetries as

$$A_i = \left(M+n,\ \bar{n},\ 2,\ 1,\ 1,\ \frac{1}{2}\right), \qquad B_\alpha = \left(\bar{M}+\bar{n},\ n,\ 1,\ 2,\ -1,\ \frac{1}{2}\right). \tag{2.1.3}$$

There is also a superpotential of the form $W = \frac{1}{\mu}\epsilon_{ij}\epsilon_{\alpha\beta}\,\mathrm{Tr}[A_i B_\alpha A_j B_\beta]$ and this field theory is known to be dual to the Klebanov-Strassler background [12].

The exact beta functions in this theory are given by [12]

$$\beta_{\frac{8\pi^2}{g_1^2}} \sim 3(n+M) - 2n(1-\gamma), \qquad \beta_{\frac{8\pi^2}{g_2^2}} \sim 3n - 2(n+M)(1-\gamma). \tag{2.1.4}$$

where γ is the anomalous dimension of operators $\mathrm{Tr}(A_i B_\alpha)$. Taking $M = 0$, it must be the case that to have agreement with the conformal invariance of the Klebanov-Witten $SU(n) \times SU(n)$ theory [10], and in addition the symmetry of the field theory under $M \to -M$, the anomalous dimension is of the form $\gamma = -\frac{1}{2} + \mathcal{O}\left(\left[\frac{M}{n}\right]^2\right)$. Further discussion of the gauge couplings

*In [27] the authors point out that since these theories are at large $g^2_{YM} N_c$, then the massive modes coming from the presence of the two-sphere are never fully decoupled, and thus these gauge theories are not the pure four-dimensional theories that one would hope for.

†Here, as mentioned already, we have a situation where we have n D3 branes and M fractional $D5$ branes on the conifold. Later on it will often be the case that we relabel M by N_c.

and beta functions can be found in Section. 3.3.2 where we analyse the non-Supersymmetric deformations effect.

As we flow toward the IR, the theory above undergoes Seiberg duality transformations [58] (under which we send $n \to n - M$, decreasing the rank of the gauge groups) every time the gauge coupling (g_1, g_2) of one of the gauge groups moves towards strong coupling, and then diverges (the gauge couplings flow in different directions). This transformation allows us to move to a Seiberg dual description of the theory which is more suitable, and is weakly coupled. These transformations are repeated as we move further towards the IR, until the gauge group is reduced to $SU(M+p) \times SU(p)$, with $0 \leq p < M$. This is what is known as a "duality cascade" [59]. Further discussion of Seiberg duality can be found in Section. 3.3.3 and in Appendix. A.4 where we discuss the effect of the non-Supersymmetric deformation.

When $p = 0$, at the base of the cascade, we are basically left with an $\mathcal{N} = 1$ $SU(M)$ gauge theory. It has many interesting properties (discussed for instance in [12, 59]) including confinement and a discrete spectrum with a mass gap. The theory also includes Chiral-Symmetry Breaking, further (spontaneously) breaking the remaining $\mathbb{Z}_{2M} \to \mathbb{Z}_2$. This is due to the formation of a $\langle\lambda\lambda\rangle$ condensate, and as a consequence the theory has M identical isolated degenerate vacua, and further there are domain walls which separate one vacuum from the next (see further discussion in Section. 3.3.5).

At the "last step" of the cascade, the gauge group is $SU(2M) \times SU(M)$, and here we find that there are both mesons $\hat{\mathcal{M}} \sim AB$, and baryonic operators

$$\begin{aligned}
\mathcal{B} &\sim \epsilon_{\alpha_1\alpha_2\ldots\alpha_{2M}} (A_1)_1^{\alpha_1} (A_1)_2^{\alpha_2} \ldots (A_1)_M^{\alpha_M} (A_2)_1^{\alpha_{M+1}} (A_2)_2^{\alpha_{M+2}} \ldots (A_2)_M^{\alpha_{2M}}, \\
\tilde{\mathcal{B}} &\sim \epsilon^{\alpha_1\alpha_2\ldots\alpha_{2M}} (B_1)_{\alpha_1}^1 (B_1)_{\alpha_2}^2 \ldots (B_1)_{\alpha_M}^M (B_2)_{\alpha_{M+1}}^1 (B_2)_{\alpha_{M+2}}^2 \ldots (B_2)_{\alpha_{2M}}^M .
\end{aligned} \tag{2.1.5}$$

The baryonic operators are both invariant under $SU(2)_L \times SU(2)_R$ global symmetry which rotates A_i, B_α. The moduli space for this theory has two branches [60], a *baryonic*, and a *mesonic*. We shall be interested in the first, that of the baryonic branch [14] * where the mesons $\hat{\mathcal{M}}$ are zero. The baryons on the other hand take

$$\mathcal{B} = i\zeta\Lambda^{2M}, \qquad \tilde{\mathcal{B}} = \frac{i}{\zeta}\Lambda^{2M}, \tag{2.1.6}$$

where the branch has complex dimension one parametrised by ζ, and Λ^{2M} is the strong coupling scale of the gauge group $SU(2M)$. Here the $U(1)_B$ global symmetry is broken spontaneously,

*It turns out that the $SU(2M) \times SU(M)$ is the simplest gauge theory picture of the baryonic branch but it exists for any $n = qM$, where q is an integer.

and the associated massless pseudo-scalar Goldstone mode corresponds to the phase of ζ. This lives in a $\mathcal{N} = 1$ Chiral multiplet (by Supersymmetry), and has a scalar partner (a saxion) corresponding to changing the modulus of ζ [61].

The VEV of the operator whose $\theta\sigma^{\mu}\bar{\theta}$ component is the $U(1)_B$ current, through different values of ζ, gives our position on the baryonic branch [60], and is given by

$$\mathcal{U} \sim \mathrm{Tr}(A^{\dagger}A - B^{\dagger}B). \tag{2.1.7}$$

This will play an important role in our discussions of the gravity dual to the baryonic branch throughout. Finally, note that the Klebanov-Strassler corresponds to having $\zeta = 1$, and corresponds to a particular choice of vacuum with $|\mathcal{B}| = |\tilde{\mathcal{B}}| = \Lambda^{2M}$, and is a particular $\mathbb{Z}_2$ symmetric point on the branch. At any point other than this on the branch, the $\mathbb{Z}_2$ symmetry is broken, and we shall see this in the dual gravity solutions.

It is possible to connect Theory A and Theory B via the 'Higgsing' mentioned earlier. Giving a particular (classical) baryonic VEV to the fields (A_i, B_α) and expanding around it, one can reproduce the degeneracies and field content of [55, 56]. * This connection between weakly coupled field theories can also be realised in the Type IIB solutions dual to the respective field theories, and is manifest as a U-duality [19] or *rotation* (which was studied further in [20, 62–65]). It is to these dual solutions we now turn our attention.

We start with a background which is dual to Theory A, which is the geometry produced by taking the strong-coupling limit of the gauge theory, on a stack of N_c D5 branes wrapping an S^2 inside $T^{1,1}$, extending in the Minkowski directions x^j (with $j = 0, 1, 2, 3$), and located at the tip of the conifold (given by a cone over $T^{1,1}$). This is described by a truncation of Type IIB supergravity which includes only gravity, a dilaton Φ, and a Ramond-Ramond (RR) three-form F_3. A configuration of this kind can be written compactly using the vielbeins

$$\begin{aligned}
&E^{x^j} = e^{\frac{\Phi}{4}}dx^j, \qquad E^{\rho} = e^{\frac{\Phi}{4}+k}d\rho, \qquad E^{\theta} = e^{\frac{\Phi}{4}+h}d\theta, \qquad E^{\varphi} = e^{\frac{\Phi}{4}+h}\sin\theta d\varphi,\\
&E^1 = \frac{1}{2}e^{\frac{\Phi}{4}+g}(\tilde{\omega}_1 + a d\theta), \quad E^2 = \frac{1}{2}e^{\frac{\Phi}{4}+g}(\tilde{\omega}_2 - a\sin\theta d\varphi),\\
&E^3 = \frac{1}{2}e^{\frac{\Phi}{4}+k}(\tilde{\omega}_3 + \cos\theta d\varphi).
\end{aligned} \tag{2.1.8}$$

*Further, in [20], the authors propose the possibility of a *planar equivalence* between the two theories, and discuss the key results which highlight why this could be the case.

where we have used the following $SU(2)$ left-invariant one-forms

$$\tilde{\omega}_1 = \cos\psi\, d\tilde{\theta} + \sin\psi \sin\tilde{\theta}\, d\tilde{\varphi}, \qquad \tilde{\omega}_2 = -\sin\psi\, d\tilde{\theta} + \cos\psi \sin\tilde{\theta}\, d\tilde{\varphi},$$
$$\tilde{\omega}_3 = d\psi + \cos\tilde{\theta}\, d\tilde{\varphi}. \tag{2.1.9}$$

In terms of these, the background and the RR three-form (in Einstein Frame) read

$$ds_E^2 = \sum_i (E^i)^2,$$
$$F_3 = e^{-\frac{3}{4}\Phi}\Big[f_1 E^{123} + f_2 E^{\theta\varphi 3} + f_3(E^{\theta 23} + E^{\varphi 13}) + f_4(E^{\rho 1\theta} + E^{\rho\varphi 2})\Big], \tag{2.1.10}$$

where the range of the five angles spanning the internal space is $0 \leq \theta\,,\, \tilde{\theta} < \pi\,,\, 0 \leq \varphi\,,\, \tilde{\varphi} < 2\pi\,,\, 0 \leq \psi < 4\pi$, and we have used the definitions

$$E^{ijk\ldots l} = E^i \wedge E^j \wedge E^k \wedge \cdots \wedge E^l,$$
$$f_1 = -2N_c e^{-k-2g}, \qquad f_2 = \frac{N_c}{2} e^{-k-2h}(a^2 - 2ab + 1),$$
$$f_3 = N_c e^{-k-h-g}(a-b), \qquad f_4 = \frac{N_c}{2} e^{-k-h-g} b'. \tag{2.1.11}$$

In this setup, we have set $\alpha' g_s = 1$, and the dilaton is a function of the radial coordinate only $\Phi(\rho)$. The full background is then determined by solving the equations of motion for the six functions $\{g, h, k, \Phi, a, b\}$ which also all depend only on the radial coordinate. Further, it is possible to derive and solve a set of BPS equations from the above ansatz, which we shall discuss in more detail shortly.

We shall present a family of solutions in Section. 2.2 which corresponds to the dual Field Theory A coupled to gravity, due to a deformation by a dimension-eight operator inserted into the Lagrangian. Thus the UV of the field theory requires completion, and this is achieved through the aforementioned U-duality/*rotation*. It can be thought of as a solution generating procedure which can be summarised in the following steps [19]:

- Start from the system of Type IIB supergravity solutions describing the backreaction of wrapped D5 branes, with additional RR three-form flux F_3, as described above. *
- Compactify the three spatial Minkowski directions spanned by the original D5 branes on a torus, perform T-dualities along these three directions, leaving us with a Type IIA solution involving D2 branes wrapped on the original S^2, and F_4 (dual to the F_6) flux.

*From the ansatz of the related system of wrapped NS5 branes, perform an S-duality.

- Perform a lift to M-theory (introducing a new direction $x^\sharp$), and then introduce a boost (with rapidity $\hat{\beta}$) to the configuration in the $t - x^\sharp$ plane,

$$t \to \cosh\hat{\beta}t - \sinh\hat{\beta}x^\sharp, \qquad x^\sharp \to -\sinh\hat{\beta}t + \cosh\hat{\beta}x^\sharp. \tag{2.1.12}$$

  meaning we have a configuration with M2 branes, generating (via the boost) KK momentum charges (with an A_1 potential), and a G_4 in 11-dimensions.

- Reduce this configuration back to a Type IIA background which now contains D0 and D2 branes. The background is ingrained with an $\tilde{F}_4 = dA_3 + A_1 \wedge H_3$, an H_3 from the dimensional reduction of G_4, and further an $F_2 = dA_1$.

- Finally, perform T-dualities back along the three spatial Minkowski directions. We are then left with a Type IIB solution with D3 and D5 brane charge, an F_3, an H_3 and a self-dual F_5 flux.

More details on the steps of the procedure are given in [65] . Performing these steps yields the *rotated* background, in which the vielbeins are given by

$$\begin{aligned}
&e^{x^j} = e^{\frac{\Phi}{4}}\hat{h}^{-\frac{1}{4}}\,dx^j, \qquad e^{\rho} = e^{\frac{\Phi}{4}+k}\hat{h}^{\frac{1}{4}}\,d\rho, \qquad e^{\theta} = e^{\frac{\Phi}{4}+h}\hat{h}^{\frac{1}{4}}\,d\theta, \qquad e^{\varphi} = e^{\frac{\Phi}{4}+h}\hat{h}^{\frac{1}{4}}\sin\theta\,d\varphi,\\
&e^1 = \frac{1}{2}e^{\frac{\Phi}{4}+g}\hat{h}^{\frac{1}{4}}(\tilde{\omega}_1 + a\,d\theta), \qquad e^2 = \frac{1}{2}e^{\frac{\Phi}{4}+g}\hat{h}^{\frac{1}{4}}(\tilde{\omega}_2 - a\sin\theta\,d\varphi),\\
&e^3 = \frac{1}{2}e^{\frac{\Phi}{4}+k}\hat{h}^{\frac{1}{4}}(\tilde{\omega}_3 + \cos\theta\,d\varphi).
\end{aligned} \tag{2.1.13}$$

The *rotation* leaves the RR three-form invariant [*], and turns on extra fluxes as described above. The new metric, RR and NS fields are

$$\begin{aligned}
ds_E^2 &= \sum_i (e^i)^2,\\
F_3 &= \frac{e^{-\frac{3}{4}\Phi}}{\hat{h}^{\frac{3}{4}}}\Big[f_1 e^{123} + f_2 e^{\theta\varphi 3} + f_3(e^{\theta 23} + e^{\varphi 13}) + f_4(e^{\rho 1\theta} + e^{\rho\varphi 2})\Big],\\
H_3 &= -\kappa\frac{e^{\frac{5}{4}\Phi}}{\hat{h}^{\frac{3}{4}}}\Big[-f_1 e^{\theta\varphi\rho} - f_2 e^{\rho 12} - f_3(e^{\theta 2\rho} + e^{\varphi 1\rho}) + f_4(e^{1\theta 3} + e^{\varphi 23})\Big],\\
C_4 &= -\kappa\frac{e^{2\Phi}}{\hat{h}}\,dt\wedge dx_1\wedge dx_2\wedge dx_3,\\
F_5 &= \kappa e^{-\frac{5}{4}\Phi - k}\hat{h}^{\frac{3}{4}}\partial_\rho\left(\frac{e^{2\Phi}}{\hat{h}}\right)\left[e^{\theta\varphi 123} - e^{tx_1x_2x_3\rho}\right].
\end{aligned} \tag{2.1.14}$$

[*] The factor of $\hat{h}$ is only present due to the change in definition of the vielbeins.

The form of the NS B_2 potential in this case is given in Eq. A.3.1, with $H_3 = dB_2$. Here we have a new warp factor defined by *

$$\hat{h} = 1 - \kappa^2 e^{2\Phi}. \tag{2.1.15}$$

The constant κ is carefully chosen such that the eight-dimensional irrelevant operator is removed and as such the dual Quantum Field Theory is decoupled from gravity. The correct choice for this to occur is such that $\kappa = e^{-\Phi_\infty}$, where Φ_∞ is the asymptotic value of the dilaton in the UV. A more in-depth discussion of this choice is given in [20, 65].

2.2 A Class of Supersymmetric Solutions

It is possible to derive a system of non-linear, coupled, first-order BPS equations for the background described in Eq. 2.1.10 (details are presented in the Appendix of reference [66]). These can be conveniently repackaged using a particular change of basis functions $\{P, Q, Y, \tau, \sigma, \Phi\}$ in which the equations decouple (explained extensively in [67–69]). This allows us to rewrite the background functions $\{g, h, k, \Phi, a, b\}$ in terms of this new set of basis functions as follows

$$\begin{aligned} 4e^{2h} &= \frac{P^2 - Q^2}{P\cosh\tau - Q}, & e^{2g} &= P\cosh\tau - Q, & e^{2k} &= 4Y, \\ e^{4\Phi} &= \frac{e^{4\phi_0}\cosh^2 2\rho_\Lambda}{Y(P^2 - Q^2)\sinh^2\tau}, & a &= \frac{\sinh\tau}{P\cosh\tau - Q}, & N_c b &= \sigma \end{aligned} \quad . \tag{2.2.1}$$

From here, most of the BPS equations reduce to algebraic relations, and we are left with a single decoupled second-order equation for the function P (which is referred to as the "Master Equation") given by

$$P'' + P'\left(\frac{P' + Q'}{P - Q} + \frac{P' - Q'}{P + Q} - 4\coth(2\rho - 2\rho_\Lambda)\right) = 0. \tag{2.2.2}$$

where

$$Q = (Q_o + N_c)\coth(2\rho - 2\rho_\Lambda) + N_c\left[2\rho\coth(2\rho - 2\rho_\Lambda) - 1\right], \tag{2.2.3}$$

and Q_o and ρ_Λ are two constants of integration. The Master Equation describes a large class of solutions that shall interest us. We are required to fine-tune $Q_o = -N_c$, to avoid a nasty singularity in the IR. Further, we will always take the IR end-of-space to be $\rho_\Lambda = 0$, which

*One must send the rapidity $\hat{\beta} \to \infty$, plus an appropriate rescaling of the Minkowski directions, to gain this form of the background, fluxes and warp factor.

amounts to setting the dynamical scale in terms of which all other dimensional parameters are measured, to one. Note, a solution to the above Master Equation in Eq. 2.2.2 will be a solution to two different backgrounds, which are the backgrounds related by the *rotation* described above.

We can break up the Supersymmetric solutions to the Master Equation by using a rough approximation for P of the form

$$P(\rho) \simeq P_a \equiv \sup\left\{c_0, 2N_c\rho, c_+ e^{4\rho/3}\right\}, \tag{2.2.4}$$

where $c_+ \geq 0$ and $c_0 \geq 0$ are two integration constants. Although this approximation is not a smooth function, the solutions to P, which it approximates, are and thus it will provide us with an illustrative tool in classifying the various solutions of interest. Essentially, P_a is constructed such that P and P' be monotonically increasing, and that for any $\rho \geq 0$ we have $P > Q$. All the regular solutions for P, are either of this form, or can be obtained using a limiting procedure on P_a.

The most notable solution, and the only one which can be written in closed form, is that of the CVMN solution [13, 18], given by $\hat{P} = 2N_c\rho$. This can be thought of as a limiting case (such that $c_+ \to 0$), as all other solutions have $P > 2N_c\rho$, for any $\rho > 0$. This solution has the exact form

$$\begin{aligned} \frac{e^{2g}}{N_c} &= \frac{e^{2k}}{N_c} = 1, & \frac{e^{2h}}{N_c} &= \rho\coth 2\rho - \frac{\rho^2}{\sinh^2 2\rho} - \frac{1}{4}, \\ a &= b = \frac{2\rho}{\sinh 2\rho}, & e^{4\Phi-4\phi_0} &= \frac{N_c}{4} e^{-2h}\sinh^2 2\rho. \end{aligned} \tag{2.2.5}$$

In this solution the dilaton Φ grows indefinitely in the UV. As it will be useful for comparison later we also present here the IR and UV expansions for the CVMN background. The IR expansion (for $\rho \to 0$) takes the form

$$\frac{e^{2h}}{N_c} = \rho^2 - \frac{4}{9}\rho^4 + \mathcal{O}(\rho^6), \quad a = 1 - \frac{2}{3}\rho^2 + \mathcal{O}(\rho^4), \quad e^{4\Phi-4\phi_0} = 1 + \frac{16}{9}\rho^2 + \mathcal{O}(\rho^4), \tag{2.2.6}$$

and in the UV we have an expansion (for $\rho \to \infty$) of the form

$$\frac{e^{2h}}{N_c} = \rho - \frac{1}{4} + \mathcal{O}\left(e^{-4\rho}\right), \qquad a = 4\rho e^{-2\rho} + \mathcal{O}\left(e^{-6\rho}\right), \qquad \Phi = \rho + \mathcal{O}(\log\rho). \tag{2.2.7}$$

The rest of the solutions we shall present are only known in a semi-analytic form, as IR and UV expansions, and a smooth numerical interpolation between them. A second interesting case

occurs when $c_0 = 0$ and $c_+ > 0$, in which case P is always dominated by exponential growth for large ρ. In this case P_a is not a good approximation near to the IR end-of-space where the expansion for P actually takes the form [66]

$$P_\ell = h_1\rho + \frac{4h_1}{15}\left(1 - \frac{4N_c^2}{h_1^2}\right)\rho^3 + \frac{16h_1}{525}\left(1 - \frac{4N_c^2}{3h_1^2} - \frac{32N_c^4}{3h_1^4}\right)\rho^5 + \mathcal{O}(\rho^7), \tag{2.2.8}$$

where the constant $h_1 \geq 2N_c$. In terms of the background functions, we find the expansion in this case to be

$$\begin{aligned}
e^{2g} &= \frac{h_1}{2} + \frac{4h_1}{15}\left(3 - \frac{5N_c}{h_1} - \frac{2N_c^2}{h_1^2}\right)\rho^2 + \mathcal{O}(\rho^4),\\
e^{2h} &= \frac{h_1}{2}\rho^2 - \frac{4h_1}{45}\left(6 - \frac{15N_c}{h_1} + \frac{16N_c^2}{h_1^2}\right)\rho^4 + \mathcal{O}(\rho^6),\\
e^{2k} &= \frac{h_1}{2} + \frac{2h_1}{5}\left(1 - \frac{4N_c^2}{h_1^2}\right)\rho^2 + \mathcal{O}(\rho^4),\\
e^{\Phi-\phi_0} &= 1 + \frac{16N_c^2}{9h_1^2}\rho^2 + \mathcal{O}(\rho^4),\\
a &= 1 - \left(2 - \frac{8N_c}{3h_1}\right)\rho^2 + \mathcal{O}(\rho^4), \qquad b = \frac{2\rho}{\sinh 2\rho}.
\end{aligned} \tag{2.2.9}$$

where ϕ_0 is the ability to shift the dilaton. These IR expansions hold for all solutions in which $c_0 = 0$, and although it is not known in closed form, the relationship between h_1 and c_+ is known numerically

$$c_+ \simeq \frac{3^{1/3}h_1}{4}, \tag{2.2.10}$$

for large values of h_1 and c_+ [62].

If instead we have $c_0 \neq 0$, then we can write the IR expansion for P as [40]

$$P_c = c_0 + \hat{k}_2 c_0\rho^3 + \frac{4}{5}\hat{k}_2 c_0\rho^5 - \hat{k}_2^2 c_0\rho^6 + \frac{16(2c_0^2\hat{k}_2 - 5\hat{k}_2 N_c^2)}{105c_0}\rho^7 + \mathcal{O}(\rho^8), \tag{2.2.11}$$

where now c_0 and $\hat{k}_2$ are the free parameters. The IR expansions of the background functions in this case are given by

$$\begin{aligned}
e^{2g} &= \frac{c_0}{2}\frac{1}{\rho} + \frac{2c_0}{3}\rho + \frac{1}{6}\left(3c_0\hat{k}_2 - 8N_c\right)\rho^4 + \mathcal{O}(\rho^5),\\
e^{2h} &= \frac{c_0}{2}\rho - \frac{2c_0}{3}\rho^3 + \frac{1}{6}\left(3c_0\hat{k}_2 + 8N_c\right)\rho^4 + \mathcal{O}(\rho^5),\\
e^{2k} &= \frac{3c_0\hat{k}_2}{2}\rho^2 + 2c_0\hat{k}_2\rho^4 - 3c_0\hat{k}_2^2\rho^5 + \mathcal{O}(\rho^6),\\
e^{4\Phi-4\phi_0} &= 1 + \frac{32N_c^2}{9c_0^2}\rho^4 - \frac{256N_c^2}{135c_0^2}\rho^6 + \mathcal{O}(\rho^7),
\end{aligned}$$

$$a = 1 - 2\rho^2 + \frac{8N_c}{3c_0}\rho^3 + \frac{10}{3}\rho^4 + \mathcal{O}(\rho^5),$$
$$b = \frac{2\rho}{\sinh 2\rho} = 1 - \frac{2}{3}\rho^2 + \frac{14}{45}\rho^4 + O(\rho^6), \tag{2.2.12}$$

Again, ϕ_0 is the ability to shift the dilaton and the relationship between $\hat{k}_2$ and c_+ is not known analytically. With having two free parameters, we can think of solutions in this class as more general, but this parametrisation should be treated with care. As mentioned above, the CVMN solution is the limiting case, and it is possible using this expansion for P_c to choose small enough values of $\hat{k}_2$, such that at some value of ρ the corresponding solution will be smaller than the CVMN case, and this yields a bad singularity. Thus one must be aware that there is a minimal value of $\hat{k}_2$ depending on the value of c_0 chosen.

All solutions with a non-zero c_0 will be referred to here as 'walking'. This nomenclature refers to the fact that in these solutions, there is a region over which a suitably defined gauge coupling (before *rotation*), is running anomalously slow. By considering a fivebrane (in the probe approximation) wrapping $\Sigma_2 = [\theta = \tilde{\theta}, \varphi = 2\pi - \tilde{\varphi}, \psi = \pi]$, we can define a four dimensional gauge coupling g_4 (essentially defined by the inverse size of the S^2) [40]

$$\frac{g_4^2 N_c}{8\pi^2} = \frac{N_c \coth\rho}{P}. \tag{2.2.13}$$

An example of this is plotted, with the corresponding P, in Fig. 2.1 for a number of solutions with CVMN UV asymptotics. Strictly, as we can rescale the radial coordinate (which is equivalent to regularisation-scheme dependence), this plot does not give us a good idea of how 'long' the walking region is.

Let us now turn our attention to the other possibility for the UV (differing from that of the CVMN solution with linearly growing dilaton). In this case P behaves exponentially for large values of the radial coordinate

$$P_u = c_+ e^{4\rho/3} + \frac{4N_c^2}{c_+}\left(\frac{13}{16} - \rho + \rho^2\right)e^{-4\rho/3} + \left(c_- - \frac{8c_+}{3}\rho\right)e^{-8\rho/3}$$
$$+ \frac{N_c^4}{c_+^3}\left(\frac{18567}{512} - \frac{2781}{32}\rho + \frac{27}{4}\rho^2 - 36\rho^3\right)e^{-16\rho/3} + \mathcal{O}\left(e^{-20\rho/3}\right) \tag{2.2.14}$$

which shows the two free parameters (or integration constants) labelled by $\{c_+, c_-\}$. The

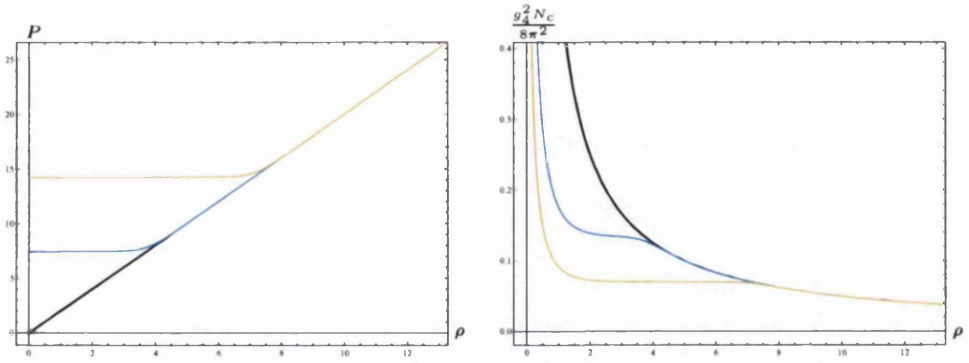

Figure 2.1: Plots of the function $P(\rho)$ on the left, and $\frac{g_4^2 N_c}{8\pi^2}$ on the right, in the CVMN system of D5 branes wrapped on a two-cycle and related walking solutions. The solid black line represents the CVMN solution, while the blue and yellow lines are the related walking solutions with $\rho_* \simeq 4$ and $\rho_* \simeq 7$ respectively. In the case of the yellow walking solution, this coupling varies slowly over the region $2 \lesssim \rho \lesssim \rho_*$, and we call this walking.

background functions have equivalent UV expansions of the form

$$
\begin{aligned}
e^{2g} &= c_+ e^{\frac{4}{3}\rho} + N_c(1-2\rho) + \frac{N_c^2}{c_+}\left(\frac{13}{4} - 4\rho + 4\rho^2\right) e^{-\frac{4}{3}\rho} + \mathcal{O}\left(e^{-\frac{8}{3}\rho}\right), \\
e^{2h} &= \frac{c_+}{4} e^{\frac{4}{3}\rho} - \frac{N_c}{4}(1-2\rho) + \frac{N_c^2}{c_+}\left(\frac{13}{16} - \rho + \rho^2\right) e^{-\frac{4}{3}\rho} + \mathcal{O}\left(e^{-\frac{8}{3}\rho}\right), \\
e^{2k} &= \frac{2c_+}{3} e^{\frac{4}{3}\rho} - \frac{N_c^2}{3c_+}\left(\frac{25}{2} - 20\rho - 8\rho^2\right) e^{-\frac{4}{3}\rho} + \mathcal{O}\left(e^{-\frac{8}{3}\rho}\right), \\
e^{4(\Phi-\Phi_\infty)} &= 1 + \frac{3N_c^2}{4c_+^2}(1-8\rho)\, e^{-\frac{8}{3}\rho} + \mathcal{O}\left(e^{-\frac{16}{3}\rho}\right), \\
a &= 2e^{-2\rho} - \frac{2N_c}{c_+}(1-8\rho)e^{-\frac{10}{3}\rho} + \mathcal{O}\left(e^{-\frac{14}{3}\rho}\right), \qquad b = \frac{2\rho}{\sinh 2\rho},
\end{aligned}
\tag{2.2.15}
$$

The constant c_- is related to c_0, but again the relation is not known in closed form. If one chooses arbitrary values for c_+ and c_-, the solution found will be mildly singular, with only a divergent Kretschmann scalar in the IR [20] (but the other curvature invariants are finite), and would have an IR given by P_c with non-zero c_0. One must carefully tune the value of c_- for a fixed c_+ to recover a globally regular solution with an IR given by P_ℓ. * Thus one may associate the globally regular solutions with $P \to 0$ at the IR end-of-space.

Solutions with UV asymptotics like that of P_u, have a dilaton that approaches a constant Φ_∞ in the UV, and are the solutions to which one may apply the *rotation* procedure. In these

*Again it is possible to choose the value of c_- too small for a particular choice of c_+ such that we find a bad singularity in the IR.

rotated solutions, exploring the baryonic branch (these solutions have a regular IR given by Eq. 2.2.8) amounts to changing the value of h_1, or c_+. In the limit h_1, $c_+ \to \infty$, it is possible to recover the Klebanov-Strassler background [12], which has a constant dilaton. Note that this can be thought of as the opposite end of the baryonic branch to the CVMN solution (with $h_1 \to 2N_c$ or $c_+ \to 0$), but the point is somewhat subtle. Strictly one cannot directly *rotate* the CVMN solution, as $\Phi_\infty \to \infty$ in this case, but instead one may *rotate* a generic baryonic branch solution, and then take corresponding limit. In this case it has been argued that one finds a theory which is well described by fivebranes wrapped on a fuzzy two-sphere [19] which becomes less and less fuzzy as one moves towards the CVMN limit.

It is also of interest to discuss how these dual gravity solutions correspond to particular modifications of the conifold [19]: the *deformed* conifold with a finite three-sphere and a collapsing two-sphere in the IR, and the *resolved* conifold with a finite two-sphere and a collapsing three-sphere in the IR. The geometry produced by placing D5 branes on the two-sphere in the resolved conifold and taking into account the backreaction, leaves us with a geometry with fluxes corresponding to a large bayonic VEV in the dual field theory, and this is close to the CVMN solution (which we would only recover if we were to have an infinite baryonic VEV). In the other extreme, if we are at the other end of the baryonic branch where we can think of the dual field theory having a small Baryonic VEV, and we have a solution which looks like the deformed conifold, with a large three-sphere (and thus close to the Klebanov-Strassler solution). The deformed and resolved conifolds would usually be distinct branches of moduli space, but due to the presence of the fluxes, we have a smooth interpolation between them (a "geomteric transition"). At the end of the next Section, we shall comment on the relation between the scales in the above solutions, and the deformation/resolution of the conifold.

2.3 Further Details of the Supersymmetric Solutions

By looking at the asymptotic behaviour of fields (and combinations of them) it is possible to think of these solutions (and the associated constants) in terms of the operators which are deforming a fixed point (specifically Klebanov-Witten fixed points that are associated with geometry $AdS_5 \times T^{1,1}$ and its dual conformal theory). We may do this as it is understood that a generic field $\mathcal{M} \sim u^{-\Delta}$ as $u \to \infty$ behaves in the following manner: If $\Delta > 0$ (or $\Delta = 0$) it is either an indication of a relevant (or marginal) operator in the Lagrangian, or the VEV for an operator of dimension Δ. If instead, $\Delta < 0$, then it indicates the insertion of an irrelevant

operator of dimension $(4-\Delta)$ into the Lagrangian. We can then link this to our usual length scale via the relation $u = e^{2\rho/3}$. Here we present the analysis, based on expanding in the UV of our Supersymmetric solutions (after *rotation*) near the Klebanov-Witten fixed points, in terms of the five dimensional fields present in the PT ansatz, the corresponding field theory operators in terms of the two gauge groups, and the particular scaling dimensions chosen by the BPS equations [14, 20]

$$\begin{aligned}
&a \to \mathrm{Tr}(W_1^2 - W_2^2), \quad \Delta = 3; && \tilde{g} \to \mathrm{Tr}(A\bar{A} - B\bar{B}), \quad \Delta = 2;\\
&\Phi \to \mathrm{Tr}(F_1^2 + F_2^2), \quad \Delta = 0, 4; && h_1 \to \mathrm{Tr}(F_1^2 - F_2^2), \quad \Delta = 0, 4;\\
&x, p \to \mathrm{Tr} W^2 \bar{W}^2, \quad \Delta = -4, 6; && b, h_2 \to \mathrm{Tr}(A\bar{A} + B\bar{B}) W^2, \quad \Delta = 3, -3\,.
\end{aligned} \tag{2.3.1}$$

Here our background functions $\{a, b, \Phi, g, h, k\}$ are related to those of the PT ansatz $\{a, b, \Phi, x, \tilde{g}, p, \Xi, \chi, h_1, h_2\}$ through the relations

$$\begin{aligned}
&a \to a, \quad b \to b, \quad \Phi \to \Phi, \quad e^{2x} = \frac{\hat{h}}{4} e^{2h+2g+\Phi}, \quad e^{2\tilde{g}} = 4e^{2h-2g}, \quad e^{-6p} = \frac{\hat{h}}{8} e^{2k+h+g+\Phi},\\
&\Xi = -\frac{\kappa}{4} e^{2\Phi+2h+2g} \Phi', \quad h_2 = -\frac{\kappa}{4} f_4 e^{2\Phi+h+g+k}, \quad h_2' = -\kappa e^{2\Phi} \left(\frac{f_3}{2} e^{k+h+g} - \frac{f_2}{4} a e^{k+2g} \right),\\
&h_1' + \chi' = -\kappa e^{2\Phi} \left(f_1 e^{k+2h} + f_3 a e^{k+g+h} - \frac{f_2}{4} a^2 e^{k+2g} \right), \quad h_1' - \chi' = \frac{\kappa}{4} e^{k+2g+2\Phi}.
\end{aligned} \tag{2.3.2}$$

These are written in terms of the background functions after applying the *rotation*. It is also possible to study the system before *rotation* as a truncation of the full PT system. This truncation is achieved by setting $\hat{h} = 1$, $\kappa = 0$ in the above. We can then see this amounts to having $h_1 = 0 = h_2 = \chi = \Xi$, leaving a system of six functions $\{a, b, \Phi, x, p, \tilde{g}\}$ with the following one-to-one mapping between the two notations

$$\begin{aligned}
&a \to a, \qquad b \to b, \qquad \Phi \to \Phi, \qquad e^{2x} = \frac{1}{4} e^{2h+2g+\Phi},\\
&e^{2\tilde{g}} = 4e^{2h-2g}, \qquad e^{-6p} = \frac{1}{8} e^{2k+h+g+\Phi}.
\end{aligned} \tag{2.3.3}$$

We shall return to this operator analysis in the next Chapter when we analyse particular non-Supersymmetric deformation of the given Supersymmetric solutions.

We conclude this Chapter by giving a summary of the relevant scales that exist in the class of solutions described above. We outline them here, following the discussions in [20], *

*These are not necessarily all independent, and changing one may have a non-trivial effect on the others.

- ρ_Λ corresponds to a VEV for a dimension-three operator (the gaugino condensate) related to the background function $a(\rho)$ (also $b(\rho)$) and is invariant under the *rotation* procedure. This is usually associated with the deformation of the conifold, and it sets the scale by which all other quantities are measured. Setting $\rho_\Lambda = 0$ means that the coupling defined in Eq. 2.2.13 diverges below $\rho \simeq 1$.

- ϕ_0 (and also Φ_∞) corresponds to the normalisation of the dilaton and to a marginal coupling. The dilaton Φ is invariant under the *rotation* procedure.

- c_+ (or h_1) is related to the dimension-eight operator (adiabatically switched off via the *rotation* procedure), and is associated with the scale $\bar{\rho}$ above which P is exponentially growing.

- c_- (or c_0) is related to the VEV for a dimension-six operator, and is associated with the scale ρ_* below which P is approximately constant. A related quantity is $M_2 = e^{2h+2g-4k}$ which is invariant under the *rotation*.

- The combination of background functions $M_1 = 4e^{2h-2g} + a^2 - 1$ is related to a VEV for a dimension-two operator and is associated with the resolution of the conifold. It is invariant under the *rotation* procedure and setting it to zero recovers the $\mathbb{Z}_2$ symmetry characteristic of the Klebanov-Strassler background.

Written in terms of these scales, a generic solution for P will be constant (walking) in the IR (for $\rho < \rho_*$), followed by a region where P is linear (CVMN), eventually growing exponentially toward the UV (for $\rho > \bar{\rho}$). It is possible that one or more of these regions may not be present depending on the values of c_0 and c_+ chosen (or equivalently h_1 and c_-).

Chapter 3

Non-Supersymmetric Deformations

In this Chapter we study Non-Supersymmetric deformations of Theory B, that of the baryonic branch of Klebanov-Strassler, which are introduced by the insertion of relevant operators into its Lagrangian. To do this, we shall no longer be able to use the Master Equation described in Eq. 2.2.2, but instead must solve the full equations of motion for the supergravity system dual to Theory A (see Eq. 2.1.8), consisting of six coupled second-order differential equations (that of the Einstein, dilaton and RR-form presented in Appendix. A.1). We further impose that irrelevant operators are absent from the dynamics and that the backgrounds are globally regular. We can then apply the *rotation* procedure described in Section. 2.1, to these non-Supersymmetric background solutions, and thus we find the non-Supersymmetric background dual to Theory B. *

In the first half (mainly based on the work of [1]), we shall concentrate on the case where the breaking can be thought of as 'soft', in which case the Supersymmetry breaking parameters are kept small with respect to the other scale in the problem (that of the strong coupling scale Λ). We shall present the series expansions for the IR and UV of the background in the presence of this Supersymmetry-breaking deformation, which we then use to find a smooth numerical interpolation between them along the whole radial coordinate. We shall then study various field theory quantities, all of which support an interpretation of the dual theory being deformed by the insertion of a relevant operator, that of masses for the gauginos, which break Supersymmetry

*It has been checked that solutions to the equations of motion of the background dual to Theory A (presented in Appendix. A.1) automatically satisfy the equations of motion of the system after the *rotation* procedure.

(and further may influence the other VEVs). To conclude, we make some comments with regard to the stability of these backgrounds, under such a soft breaking.

In the second half (mainly based on the work of [2]), we look to establish a more complete understanding of the space of solutions generated by such a deformation, exploiting the fact that the non-Supersymmetric solutions experience much of the same structure as their Supersymmetric counterparts. This prompts us to explore a two-dimensional solution space which contains a number of previously studied cases. Contained within this solution space is the background dual to the baryonic branch of Klebanov-Strassler (and its interpolation between the CVMN solution, and the Klebanov-Strassler solution), the solutions of [25] and [70] as limiting cases, and we use understanding gained from these to describe generic non-Supersymmetric solutions in terms of particular regions where the Supersymmetric or non-Supersymmetric effects dominate. Further to this, we find another natural non-Supersymmetric generalisation of the Klebanov-Strassler background which preserves the $\mathbb{Z}_2$-symmetry between the two-spheres in the internal space, and finally in the limit where the deformation takes its largest value, we find a solution in which the UV no longer matches the Supersymmetric case asymptotically.

3.1 A Supersymmetry-Breaking Deformation

Let us now introduce the relevant expansions we use to set up our Supersymmetry-breaking deformations. In the IR, our ansatz is such that the solution is regular, and that the two-sphere shrinks to zero at the IR end-of-space, as in Eq. 2.2.9. This gives us expansions of the form

$$\begin{aligned} e^{2g} &= \sum_{n=0}^{\infty} g_n \rho^n, & e^{2h} &= \sum_{n=2}^{\infty} h_n \rho^n, & e^{2k} &= \sum_{n=0}^{\infty} k_n \rho^n, \\ e^{4\Phi} &= \sum_{n=0}^{\infty} f_n \rho^n, & a &= \sum_{n=0}^{\infty} w_n \rho^n, & b &= \sum_{n=0}^{\infty} v_n \rho^n. \end{aligned} \tag{3.1.1}$$

We then proceed by substituting these into the equations of motion (presented in full in Appendix. A.1), finding five independent parameters, taken to be $\{k_0, f_0, k_2, v_2, w_2\}$. To make connection with the Supersymmetric case, we set $k_0 = \frac{h_1}{2}$ and $f_0 = e^{4\phi_0}$, so that we can recover Eq. 2.2.9 by taking

$$k_2 = \frac{2h_1}{5} - \frac{8N_c^2}{h_1}, \qquad v_2 = -\frac{2}{3}, \qquad w_2 = \frac{8N_c}{3h_1} - 2. \tag{3.1.2}$$

Thus we are left with five independent parameters

$$h_1, \qquad \phi_0, \qquad k_2, \qquad v_2, \qquad w_2, \tag{3.1.3}$$

and IR expansions *

$$\begin{aligned}
e^{2g} &= \frac{h_1}{2} + \frac{h_1}{2}\left(1 - \frac{k_2}{h_1} - \frac{4N_c^2}{h_1^2} - \frac{N_c^2 v_2^2}{h_1^2} + \frac{w_2^2}{4}\right)\rho^2 + \mathcal{O}(\rho^4), \\
e^{2h} &= \frac{h_1}{2}\rho^2 - \frac{h_1}{6}\left(1 - \frac{2k_2}{h_1} - \frac{4N_c^2}{3h_1^2} + \frac{3N_c^2 v_2^2}{h_1^2} + \frac{3w_2^2}{4}\right)\rho^4 + \mathcal{O}(\rho^6), \\
e^{2k} &= \frac{h_1}{2} + k_2\rho^2 + \mathcal{O}(\rho^4), \qquad e^{\Phi-\phi_0} = 1 + \frac{N_c^2}{h_1^2}\left(\frac{4}{3} + v_2^2\right)\rho^2 + \mathcal{O}(\rho^4), \\
a &= 1 + w_2\rho^2 + \mathcal{O}(\rho^4), \qquad b = 1 + v_2\rho^2 + \mathcal{O}(\rho^4).
\end{aligned} \tag{3.1.4}$$

In the UV, we use the following ansatz as our generalisation of the Supersymmetric case in Eq. 2.2.15,

$$\begin{aligned}
e^{2g} &= \sum_{m=0}^{\infty}\sum_{n=0}^{m} G_{mn}\rho^n e^{4(1-m)\rho/3}, & e^{2h} &= \sum_{m=0}^{\infty}\sum_{n=0}^{m} H_{mn}\rho^n e^{4(1-m)\rho/3}, \\
e^{2k} &= \sum_{m=0}^{\infty}\sum_{n=0}^{m} K_{mn}\rho^n e^{4(1-m)\rho/3}, & e^{4\Phi} &= \sum_{m=1}^{\infty}\sum_{n=0}^{m} \Phi_{mn}\rho^n e^{4(1-m)\rho/3}, \\
a &= \sum_{m=1}^{\infty}\sum_{n=0}^{m} W_{mn}\rho^n e^{2(1-m)\rho/3}, & b &= \sum_{m=1}^{\infty}\sum_{n=0}^{m} V_{mn}\rho^n e^{2(1-m)\rho/3}.
\end{aligned} \tag{3.1.5}$$

It will turn out that this ansatz will not cover all the cases we will study but we shall discuss these individually as they arise. As in the IR, we substitute this ansatz in to the equations of motion, and in this case we find instead nine independent parameters, which are given by

$$K_{00}, \quad K_{30}, \quad H_{10}, \quad H_{11}, \quad \Phi_{10}, \quad \Phi_{30}, \quad W_{20}, \quad W_{40}, \quad V_{40}, \tag{3.1.6}$$

which again to make contact with the Supersymmetric case we relabel as

$$K_{00} = \frac{2c_+}{3}, \quad H_{10} = \frac{Q_o}{4}, \quad \Phi_{10} = e^{4\Phi_\infty}, \quad K_{30} = \frac{c_- - 64e^{4\rho_\Lambda}c_+^3}{48c_+^2}, \quad W_{40} = 2e^{\rho_\Lambda}. \tag{3.1.7}$$

Then we have nine independent parameters labelled by

$$c_+, \quad c_-, \quad \Phi_\infty, \quad Q_o, \quad \rho_\Lambda, \quad H_{11}, \quad W_{20}, \quad \Phi_{30}, \quad V_{40}, \tag{3.1.8}$$

*More complete expressions, both for the IR and UV expansions in Eq. 3.1.9, can be found in the Appendix of [1].

and the UV expansions are given by

$$
\begin{aligned}
e^{2g} &= c_+ e^{\frac{4}{3}\rho} - (4H_{11}\rho + Q_o + 2c_+ W_{20}^2) + \mathcal{O}(e^{-\frac{4}{3}\rho}),\\
e^{2h} &= \frac{c_+}{4} e^{\frac{4}{3}\rho} + \left(H_{11}\rho + \frac{Q_o}{4}\right) + \mathcal{O}(e^{-\frac{4}{3}\rho}),\\
e^{2k} &= \frac{2c_+}{3} e^{\frac{4}{3}\rho} + \frac{c_+ W_{20}^2}{3} + \mathcal{O}(e^{-\frac{4}{3}\rho}),\\
e^{\Phi-\Phi_\infty} &= 1 - \left(\frac{3N_c^2}{2c_+^2}\rho - e^{-4\Phi_\infty}\frac{\Phi_{30}}{4}\right) e^{-\frac{8}{3}\rho} + \mathcal{O}(e^{-4\rho}),\\
a &= W_{20} e^{-\frac{2}{3}\rho} + \left[\left(\frac{3H_{11}W_{20}}{c_+} + \frac{10W_{20}^3}{3}\right)\rho + 2e^{2\rho_\Lambda}\right] e^{-2\rho} + \mathcal{O}(e^{-\frac{10}{3}\rho}),\\
b &= \frac{9W_{20}}{4} e^{-\frac{2}{3}\rho} + \left[\frac{10W_{20}^3}{3}\rho^2 + \left(4e^{2\rho_\Lambda} - \frac{Q_o W_{20}}{c_+} - \frac{23W_{20}^3}{6}\right)\rho + V_{40}\right] e^{-2\rho} + \mathcal{O}(e^{-\frac{10}{3}\rho}).
\end{aligned}
\tag{3.1.9}
$$

The most obvious difference here, when compared to the Supersymmetric expansions in Eq. 2.2.15, is the fact that new terms are present at leading order in the background functions a and b in the UV (parametrised by W_{20}). We can recover the Supersymmetric case from these expansions by setting

$$
H_{11} = \frac{N_c}{2}, \quad W_{20} = 0, \quad \Phi_{30} = -\frac{3N_c}{4c_+^2} e^{4\Phi_\infty}(3N_c + 4Q_o), \quad V_{40} = \frac{2}{N_c} e^{2\rho_\Lambda}(N_c + Q_o). \tag{3.1.10}
$$

Note, that we must also fix the values of the integration constants $\rho_\Lambda = 0$ and $Q_o = -N_c$, to recover the exact expansions given in Eq. 2.2.15.

In summary, our solutions are described by the fourteen parameters, given by the five from the IR Eq. 3.1.3, and nine from the UV Eq. 3.1.8. However, if we consider only solutions which match both the IR and UV expansions these parameters are clearly not all independent. There can be at most five independent parameters, as the required solutions can be parametrised by the IR boundary conditions alone, although we generically expect even fewer. In Appendix. A.2 we discuss the equivalent IR expansions for non-Supersymmetric deformations of the walking background whose Supersymmetric solution has the IR expansion given in Eq. 2.2.12. This solution interpolates to the same general UV expansion presented in Eq. 3.1.9, and shares many similarities with the globally regular solutions we discuss here.

Our goal is to find a solution which smoothly interpolates between these IR and UV expansions. This will require that these two parametrisations lead to identical functions. We can

express this as a system of twelve equations, *

$$\begin{array}{ll} g(h_1 \dots w_2;\rho) = g(c_+ \dots V_{40};\rho), & \frac{d}{d\rho}g(h_1 \dots w_2;\rho) = \frac{d}{d\rho}g(c_+ \dots V_{40};\rho), \\ h(h_1 \dots w_2;\rho) = h(c_+ \dots V_{40};\rho), & \frac{d}{d\rho}h(h_1 \dots w_2;\rho) = \frac{d}{d\rho}h(c_+ \dots V_{40};\rho), \\ \vdots & \vdots \\ b(h_1 \dots w_2;\rho) = b(c_+ \dots V_{40};\rho), & \frac{d}{d\rho}b(h_1 \dots w_2;\rho) = \frac{d}{d\rho}b(c_+ \dots V_{40};\rho). \end{array} \tag{3.1.11}$$

This system can be further reduced using the constraint (see Appendix. A.1). We can for instance express the derivative of one of the functions in terms of the other functions and their derivatives. We are left with a system of eleven independent equations which we would expect to allow us to solve for eleven of our fourteen parameters. † Of the three remaining parameters, one corresponds to our ability to shift the dilaton, which has no other effect on the solution. The final two parameters we then associate with movement along the baryonic branch, and finally the breaking of Supersymmetry.

In much of the following it will be convenient to describe the solution space in terms of the parameters that appear in the IR expansions. Firstly, the smaller number of parameters makes finding suitable numerical solutions much simpler starting from the IR. Secondly, our IR ansatz Eq. 3.1.1 imposes a comparatively natural restriction on the solutions, while the UV ansatz Eq. 3.1.5 is more arbitrary, merely being a candidate for a generalisation of the Supersymmetric solution. We shall see that it does not apply in several special cases.

As with the Supersymmetric case, we choose h_1 to parametrise the position along the baryonic branch. We could then in principle choose any combination of the remaining IR parameters v_2, w_2 and k_2 to describe the remaining Supersymmetry-breaking degree of freedom. It turns out that a description in terms of v_2 is usually simplest, as it can be seen from Eq. 3.1.2, that its Supersymmetric value $v_2^s = -2/3$ is independent of h_1.

Finally, it has been checked that to these non-Supersymmetric backgrounds (which are dual to Theory A), we can apply the *rotation* procedure, and generate non-Supersymmetric solutions to the background with additional fluxes (dual to Theory B).

*We write the functions resulting from a given choice of the IR parameters $\{h_1, k_2, v_2, w_2\}$ in the form $g(h_1, k_2, v_2, w_2; \rho)$. Similarly the expressions of the form $g(c_+, c_-, Q_o, \rho_\Lambda, H_{11}, W_{20}, \Phi_{30}, V_{40}; \rho)$ refer to the functions resulting from a given choice of the UV parameters.

†Although in principle further redundancy in the system of equations Eq. 3.1.11 would allow for more independent parameters up to a maximum of five.

3.2 The non-Supersymmetric B_2

Here we will derive the form of the NS B_2 potential in the non-Supersymmetric case, as the result differs from that of the Supersymmetric case. We propose the following ansatz, using intuition gained from the Supersymmetric example

$$B_2 = b_1(\rho)e^{\rho 3} + b_2(\rho)e^{\theta\varphi} + b_3(\rho)e^{12} + b_4(\rho)e^{\theta 2} + b_5(\rho)e^{\varphi 1}. \tag{3.2.1}$$

By imposing that $dB_2 = H_3$, and further that the Page Charge vanishes $Q_{\text{Page, D3}} = 0$, we obtain (the computational details are discussed in more detail in Appendix. A.3)

$$\begin{aligned}
b_1 &= \frac{e^{2g-2k}}{4\hat{h}}\left[2b_3\Phi' - 3\hat{h}b_3\Phi' - 4\hat{h}b_3g' - 2\hat{h}b_3' + \kappa N_c e^{\frac{3\Phi}{2}-2h}\hat{h}^{\frac{1}{2}}\left(a^2 - 2ab + 1\right)\right] \\
b_2 &= \frac{e^{-2h}}{4\hat{h}^{1/2}}\left\{e^{2g}\hat{h}^{\frac{1}{2}}\left(1-a^2\right)b_3 - \frac{\kappa}{N_c}e^{\frac{3\Phi}{2}}\left[N_c^2(a-b)b' + 4e^{2(g+h)}\Phi'\right]\right\} \\
b_4 &= b_5 = -\frac{1}{2}e^{g-h}ab_3 - \frac{\kappa N_c e^{\frac{3\Phi}{2}-g-h}b'}{4\hat{h}^{1/2}},
\end{aligned} \tag{3.2.2}$$

where $b_3(\rho)$ is a function to be determined. The remaining freedom in the choice of $b_3(\rho)$ corresponds to a gauge transformation. A general B_2 can be expressed as

$$B_2 = (B_2)_{b_3=0} - \frac{1}{2}d\Big(e^{2g-k+\Phi/4}\hat{h}^{1/4}b_3\ e^3\Big). \tag{3.2.3}$$

In the next section, we calculate various observables of the strongly coupled non-Supersymmetric field theory B_2, but first it shall be prudent to define a (periodic) quantity that will appear in the analysis. Given the two-cycle defined by,

$$\Sigma_2 = [\theta = \tilde{\theta}, \varphi = 2\pi - \tilde{\varphi}, \psi = \psi_\Lambda], \tag{3.2.4}$$

we then define

$$b_\Lambda = \frac{1}{4\pi^2}\int_{\Sigma_2} B_2. \tag{3.2.5}$$

Using the explicit form of the B_2 potential in Eq. 3.2.1 and Eq. 3.2.2, we find that

$$b_\Lambda(\psi_\Lambda) = \frac{\kappa N_c}{4\pi}e^{2\Phi}b'(b + \cos\psi_\Lambda) - \frac{\kappa}{\pi N_c}e^{2\Phi+2h+2g}\Phi'. \tag{3.2.6}$$

These two quantities, as well as those appearing in the background of Eq. 2.1.14, will be important in the study of the non-perturbative field theory dynamics.

3.3 Field Theory Aspects and Observables

In this section, we will analyse various field theory aspects of a non-Supersymmetric version of the quiver theory, that of Theory B. We will use the non-Supersymmetric background one obtains when plugging our numerical solutions (see discussion in Section. 3.6.2) into the background of Eq. 2.1.14 dual to Theory A. We now move into the calculation of a number of observables that will help our understanding of the field theory interpretation of our new solution.

3.3.1 Interesting Asymptotic Behaviour

Let us begin by looking at some particular combinations of the background fields that are of interest. To do this, we reduce the system here to five-dimensions as in [20]. From the five-dimensional perspective, it was shown that some combinations of the background functions are invariant under the *rotation* procedure. As mentioned in Section. 2.3, these turn out to be, the dilaton Φ, and the combinations

$$M_1 = 4e^{2h-2g} + a^2 - 1, \qquad M_2 = e^{2h+2g-4k}. \tag{3.3.1}$$

In the case of the non-Supersymmetric solutions the associated UV expansions are given by

$$\begin{aligned} e^{\Phi-\Phi_\infty} &= 1 - \left(\frac{3N_c^2}{2c_+^2}\rho - e^{-4\Phi_\infty}\frac{\Phi_{30}}{4}\right)e^{-\frac{8}{3}\rho} + \mathcal{O}\left(e^{-4\rho}\right), \\ M_1 &= \frac{1}{c_+}\left(8H_{11}\rho + 3c_+W_{20}^2 + 2Q_o\right)e^{-4\rho/3} + \mathcal{O}\left(e^{-8\rho/3}\right), \\ M_2 &= \frac{9}{16} - \frac{27}{16}W_{20}^2 e^{-4\rho/3} + \mathcal{O}\left(e^{-8\rho/3}\right). \end{aligned} \tag{3.3.2}$$

Using the analysis presented in Section. 2.3 it can be seen, from the UV expansion above (using the definition $u = e^{2\rho/3}$), that the dilaton falls into the marginal operator category (and is associated with a certain combination of gauge couplings g_+^2 discussed below).

Applying the same analysis on the expansion of the function $b(\rho)$, presented here for convenience

$$b = \frac{9W_{20}}{4}e^{-\frac{2}{3}\rho} + \left[\frac{10W_{20}^3}{3}\rho^2 + \left(4e^{2\rho_\Lambda} - \frac{Q_oW_{20}}{c_+} - \frac{23W_{20}^3}{6}\right)\rho + V_{40}\right]e^{-2\rho} + \mathcal{O}\left(e^{-\frac{10}{3}\rho}\right), \tag{3.3.3}$$

indicates that the "Supersymmetry-breaking constant" W_{20} corresponds to the insertion of an operator of dimension-three into the Lagrangian. We associate this operator with the mass for

the gauginos and in an analogous way (consistent with the Supersymmetric case), the constant $e^{2\rho_\Lambda}$, which appears at next-to-leading order in M_1, is associated with the VEV for the gaugino as discussed in Section. 2.3.

It should be noted that this association is not exact once we have broken Supersymmetry. This is because the Supersymmetry-breaking parameter can also deform the gaugino VEV, as indicated by the contributions from W_{20} and V_{40} to M_1 in Eq. 3.3.2. Schematically we have

$$W_{20} \to m_\lambda \lambda\lambda, \quad e^{2\rho_\Lambda} \to \langle \mathrm{Tr}(\lambda\lambda) \rangle \sim \Lambda^3. \tag{3.3.4}$$

Following this logic, the expansion of the field $M_1 \sim u^{-2}$ is interpreted as the VEV for a dimension-two operator [60],

$$\mathcal{U} \sim \mathrm{Tr}(A^\dagger A - B^\dagger B). \tag{3.3.5}$$

This is the same operator which gains a VEV in the Supersymmetric case, and it is exactly that which allows us to explore the baryonic branch, as discussed around Eq. 2.1.7. Further, observe that the Supersymmetric breaking coefficient W_{20} contributes to this VEV, in the expansion in Eq. 3.3.2.

Finally, it is curious to note that, as Theory B has two gauge groups, we should expect two independent gaugino masses. Here, we are taking advantage of the fact that the solution is obtained by applying the *rotation* procedure on a background dual to Theory A, which has only one gauge group. It appears that we have only one integration constant which we are associating with gaugino mass, that of W_{20}. We may hope to find the extra freedom through terms like V_{21}, W_{21} which would appear in the functions $a \sim b \sim \rho e^{-2\rho/3}$ in the corresponding UV expansions. These could then be associated with this second mass parameter but they are forced to vanish in our particular solution, meaning this freedom is not realised.

3.3.2 Charges, Energy, Gauge Couplings and Beta Functions

Here we look at various quantities and how they are affected by the non-Supersymmetric deformation. Firstly, we define the Maxwell and Page Charges as

$$\begin{aligned} Q_{\text{Maxwell, D3}} &= \frac{1}{16\pi^4}\int_{\Sigma_5} F_5, \quad Q_{\text{Maxwell, D5}} = \frac{1}{4\pi^2}\int_{\Sigma_3} F_3, \\ Q_{\text{Page, D3}} &= \frac{1}{16\pi^4}\int_{\Sigma_5} F_5 - B_2 \wedge F_3, \end{aligned} \tag{3.3.6}$$

where we are using the manifolds $\Sigma_5 = [\theta, \varphi, \tilde{\theta}, \tilde{\varphi}, \psi]$, and $\Sigma_3 = [\tilde{\theta}, \tilde{\varphi}, \psi]$. As in the Supersymmetric case we have that

$$Q_{\text{Maxwell, D3}} = \frac{\kappa}{\pi} e^{2g+2h+2\Phi}\Phi', \qquad Q_{\text{Maxwell, D5}} = N_c. \tag{3.3.7}$$

Recall, we imposed that $Q_{\text{Page, D3}} = 0$ in determining the B_2 field in Eq. 3.2.1 (see Appendix. A.3). The reason behind this is that the vanishing of the D3-Page charge is a feature of the Supersymmetric non-singular solutions. * Using the UV expansions, the Maxwell charge for D3 branes is

$$\begin{aligned} Q_{\text{Maxwell, D3}} =& \frac{e^{\Phi_\infty}}{\pi}\rho - \frac{1}{24\pi}\left(9e^{\Phi_\infty} + 4c_+^2 e^{-3\Phi_\infty}\Phi_{30}\right) \\ &+ \frac{33e^{\Phi_\infty}W_{20}^2}{32\pi}e^{-4\rho/3} + \mathcal{O}\left(e^{-8\rho/3}\right). \end{aligned} \tag{3.3.8}$$

So, we see that W_{20}, the parameter we associate with the mass of the gaugino according to the discussion above, changes the large ρ value of the Maxwell charge (and correspondingly the c-function discussed below) in a subleading way, as one expected.

Taking the derived expression for the ADM Energy of the non-Supersymmetric backgrounds as derived in [1], and applying the map in Eq. 3.3.4, we obtain that

$$E_{\text{ADM}} \sim c_+^2 e^{2\Phi_\infty} e^{2\rho_\Lambda} W_{20} \sim m_\lambda \Lambda^3. \tag{3.3.9}$$

Thus the energy is proportional to the gaugino mass and the strong coupling scale, as expected. This result was first obtained in [71, 72].

Turning our attention to the gauge couplings and beta functions, we briefly review what happens in the Supersymmetric case. In the $SU(N_c + n) \times SU(n)$ Supersymmetric quiver, we have two couplings g_1, g_2. Close to the Klebanov-Witten conformal point (in the UV), the anomalous dimensions are $\gamma \sim -\frac{1}{2}$. This implies that the beta functions for the diagonal combinations

$$\beta_{\frac{8\pi^2}{g_-^2}} = \beta_{\frac{8\pi^2}{g_1^2}} - \beta_{\frac{8\pi^2}{g_2^2}} = 6N_c, \quad \beta_{\frac{8\pi^2}{g_+^2}} = \beta_{\frac{8\pi^2}{g_1^2}} + \beta_{\frac{8\pi^2}{g_2^2}} = 0. \tag{3.3.10}$$

*It would be interesting to see if one can obtain a regular non-Supersymmetric solution in the presence of sources indicated by a non-vanishing Page charge.

As in the Supersymmetric case, we will adopt the definitions *

$$\frac{4\pi^2}{g_+^2} = \pi e^{-\Phi}, \qquad \frac{4\pi^2}{g_-^2} = 2\pi e^{-\Phi}\left[1 - b_\Lambda(\pi)\right], \tag{3.3.11}$$

where $b_\Lambda(\psi_\Lambda)$ is defined in Eq. 3.2.5 and Eq. 3.2.6. We obtain

$$\frac{4\pi^2}{g_-^2} = 2e^{-\Phi}\left(\pi + \frac{\kappa}{N_c}e^{2g+2h+2\Phi}\Phi'\right) - \frac{\kappa N_c}{2}e^{\Phi}(b-1)b'. \tag{3.3.12}$$

Notice that this result is independent of the function $b_3(\rho)$. In the UV, these formulas can be trusted and the expansions are given by

$$\frac{4\pi^2}{g_+^2} = e^{-\Phi_\infty}\pi + \left(\frac{3e^{-\Phi_\infty}\pi}{2c_+^2}\rho - \frac{1}{4}e^{-5\Phi_\infty}\pi\Phi_{30}\right)e^{-8\rho/3} + \mathcal{O}(W_{20}^2 e^{-4\rho}) \tag{3.3.13}$$

and

$$\frac{4\pi^2}{g_-^2} = \left(2\rho - \frac{1}{3}c_+^2\Phi_{30}e^{-4\Phi_\infty} + 2\pi e^{-\Phi_\infty} - \frac{3}{4}\right) - \frac{3}{4}W_{20}e^{-2\rho/3} + \mathcal{O}(e^{-4\rho/3}). \tag{3.3.14}$$

Let us now compute the beta functions straight from the geometry. Using the energy/radius relation

$$u = e^{2\rho/3} = \frac{\mu}{\Lambda} \tag{3.3.15}$$

where μ is the energy scale at which we probe the process, and Λ the reference or strong coupling scale of the given gauge group. Notice that this choice is arbitrary, just reflecting the scheme dependence in choosing $\rho(\mu)$. To calculate the beta functions we perform

$$\beta_{\frac{8\pi^2}{g_+^2}} = \frac{d}{d\rho}\left(\frac{8\pi^2}{g_+^2}\right)\frac{d\rho}{d\log(\mu/\Lambda)} = \left(\frac{18e^{-\Phi_\infty}\pi}{c_+^2}\log\left(\frac{\Lambda}{\mu}\right) + \frac{9e^{-\Phi_\infty}\pi}{2c_+^2} + 2e^{-5\Phi_\infty}\pi\Phi_{30}\right)\left(\frac{\Lambda^4}{\mu^4}\right)$$
$$+ \mathcal{O}\left(W_{20}^2\log\left(\frac{\Lambda}{\mu}\right)\left(\frac{\Lambda^6}{\mu^6}\right)\right),$$
$$\beta_{\frac{8\pi^2}{g_-^2}} = \frac{d}{d\rho}\left(\frac{8\pi^2}{g_-^2}\right)\frac{d\rho}{d\log(\mu/\Lambda)} = 6N_c + W_{20}N_c\left(\frac{\Lambda}{\mu}\right) + \mathcal{O}\left(\frac{\Lambda^2}{\mu^2}\right). \tag{3.3.16}$$

With a naive use of the NSVZ expression for the Wilsonian beta functions, one may have interpreted this result for $\beta_{\frac{8\pi^2}{g_-^2}}$, as the Supersymmetric breaking parameter W_{20} only slightly changing the value of the anomalous dimensions $\gamma \sim -\frac{1}{2} + \mathcal{O}\left(W_{20}\frac{\Lambda}{\mu}\right)$, but this does not match the analogous calculation for $\beta_{\frac{8\pi^2}{g_+^2}}$, and thus this solution does not respect the NSVZ expression (as expected).

*These are strictly correct in the $\mathcal{N} = 2$ examples, and at the KW fixed point, thus we adopt the same definitions here to try to understand the non-Supersymmetric dynamics.

Finally, notice that while in the Supersymmetric case the beta functions receive corrections $\mathcal{O}\left(\frac{\Lambda^3}{\mu^3}\right)$, whereas here we have an example where the Supersymmetry breaking parameters produce lower order corrections $\mathcal{O}\left(\frac{\Lambda}{\mu}\right)$.

3.3.3 A non-Supersymmetric Seiberg-like Duality

Here we shall follow the method developed in [73] and compare the quantity $b_\Lambda(\psi)$ from Eq. 3.2.6 to the Supersymmetric case. The Seiberg duality is identified with a large gauge transformation such that $b_\Lambda \to b_\Lambda \pm 1$, and the charge of D3 branes changes by $\pm N_c$. If we consider the Page charge defined in Eq. 3.3.6, under a large gauge transformation to B_2, b_Λ will change by one unit, and this in turn corresponds to a change of N_c units in the Page charge (exactly as in [73]).

Now let us see how the Maxwell charge behaves under this Seiberg duality. Focusing on the UV of the background, where the cascade is known to work in the Supersymmetric case, and following the steps described in Appendix. A.4, we have

$$b_\Lambda = \frac{\hat{h}^{1/2}e^{\Phi/2}}{\pi}\left[b_2 e^{2h} - b_4(a+\cos\psi_\Lambda)e^{h+g}\right] = \frac{N_c}{\pi}\left[(f+\tilde{k}) + (\tilde{k}-f)\cos\psi_\Lambda\right], \tag{3.3.17}$$

with (using the explicit values for b_2, b_4)

$$\begin{aligned} f &= \frac{e^{\Phi/2}\hat{h}^{1/2}}{2N_c}\left[b_2 e^{2h} - b_4 e^{g+h}(a-1)\right] = \kappa\frac{e^{2\Phi}}{8}\left[b'(b-1) - \frac{4}{N_c^2}e^{2g+2h}\Phi'\right], \\ \tilde{k} &= \frac{e^{\Phi/2}\hat{h}^{1/2}}{2N_c}\left[b_2 e^{2h} - b_4 e^{g+h}(a+1)\right] = \kappa\frac{e^{2\Phi}}{8}\left[b'(b+1) - \frac{4}{N_c^2}e^{2g+2h}\Phi'\right], \\ &\to b_\Lambda = \frac{\kappa N_c e^{2\Phi}}{4\pi}b'(b+\cos\psi_\Lambda) - \frac{\kappa e^{2\Phi+2h+2g}}{\pi N_c}\Phi'. \end{aligned} \tag{3.3.18}$$

Notice that far in the UV, the Maxwell charge given by

$$Q_{\text{Maxwell},D3} = \frac{\kappa}{\pi}e^{2g+2h+2\Phi}\Phi' = \frac{\kappa N_c^2 e^{2\Phi}}{4\pi}b'(b+\cos\psi_\Lambda) - N_c b_\Lambda, \tag{3.3.19}$$

under a change in b_Λ, behaves as

$$b_\Lambda \sim b_\Lambda \pm 1 \to Q_{\text{Maxwell},D3} \sim Q_{\text{Maxwell},D3} \mp N_c. \tag{3.3.20}$$

There is a 'correction' of the form $b'(b+\cos\psi_\Lambda)$, but at large ρ this is suppressed. Note that in the Supersymmetric case, where $b' \sim e^{-2\rho}$, the suppression is greater than in our non-Supersymmetric solutions, where $b' \sim e^{-2\rho/3}$. Thus, the 'Seiberg duality', associated with a

large gauge transformation of index k, which changes the Maxwell charge by kN_c units, is better approximated in the Supersymmetric than in the non-Supersymmetric case. Nevertheless, in both cases, the transformation is correct to leading order.

So, as expected, in the far UV we could think of this decrease in the Maxwell charge, as a non-Supersymmetric version of Seiberg duality at work.

3.3.4 The Central Charge

Here we shall calculate the (holographic) central charge c of this non-Supersymmetric solution [74, 75]. In particular it is one of the anomaly coefficients, associated to the trace anomaly in four dimensions $\langle T^{\mu}_{\mu} \rangle \sim -aE_4 + cW^2_{\mu\nu\rho\sigma}$, where E_4 is the Euler Density and $W_{\mu\nu\rho\sigma}$ is the Weyl Tensor. Strictly it is only well defined at fixed points, but here we shall calculate it using holographic methods, allowing us to determine a 'candidate' central charge along the RG flow. It is conjectured to be monotonically decreasing towards the IR of the theory (see for instance [76]). This is in line with the idea that the central charge can be thought of as a measure of the number of degrees of freedom along such a flow, and thus as we integrate them out, its value decreases.

We shall see that in this case, it is indeed a monotonically decreasing function of ρ (from the UV to the IR), and reaches zero in the IR. * Instead of following the procedure presented in [74, 75], requiring a reduction to five dimensions, we instead shall follow an equivalent method [48]. This treatment indicates that the central charge (for $d = 3$) is given by $c \sim \frac{\beta^{3/2} H^{7/2}}{(H')^3}$ (see Eq. 5.1.2 and Eq. 5.1.3 for definitions of β and H), and thus is given in our case by

$$c \sim \frac{e^{2h+2g+2\Phi+4k\hat{h}^2}}{\left(2h' + 2g' + 2\Phi' + k' + \frac{\hat{h}'}{2\hat{h}}\right)^3} \tag{3.3.21}$$

In the IR, the expansion for the central charge is

$$\begin{aligned} c \sim\ & e^{2\phi_0 - 4\Phi_\infty} \left(e^{2\Phi_\infty} - e^{2\phi_0}\right)^2 h_1^4 \rho^5 \\ & + \frac{1}{9} e^{2\phi_0 - 4\Phi_\infty} \left(e^{2\Phi_\infty} - e^{2\phi_0}\right) h_1^2 \Big[e^{2\Phi_\infty} \left(-16 - 15h_1k_2 + 12h_1^2\right) \\ & + e^{2\phi_0} \left(28 + 15h_1k_2 - 12h_1^2 + 9v_2^2\right) \Big] \rho^7 + \mathcal{O}(\rho^9), \end{aligned} \tag{3.3.22}$$

*Due to the fact that in the far UV this theory does not actually reach a fixed point, we do not expect the central charge to attain a maximum value, but it will be zero in the IR due to the theory having a mass gap.

and in the UV,

$$c \sim e^{2\Phi_\infty}\rho^2 - \left(\frac{3}{4}e^{2\Phi_\infty} + \frac{1}{3}c_+^2 e^{-2\Phi_\infty}\Phi_{30}\right)\rho + \mathcal{O}\left(\frac{1}{\rho}\right). \tag{3.3.23}$$

It is easy to see that in the UV the Supersymmetry-breaking parameters are not present at the leading order. In the IR, the problem is slightly more subtle in that, although no Supersymmetry-breaking parameters appear in the leading term, there is still an effect. This is because, unlike the Supersymmetric case, fixing h_1 and ϕ_0 in the non-Supersymmetric case does not determine Φ_∞, and thus we can expect that under the deformation, it will change. Indeed, it turns out that if we compare Supersymmetric and non-Supersymmetric numerical solutions with the same h_1 and ϕ_0, we find that Φ_∞ changes (see Fig. 3.1).

3.3.5 Domain Walls

Here we shall compute the tension of a domain wall (already discussed in Section. 2.1), which in the Supersymmetric case separates adjacent vacua [60], as the effective tension of a fivebrane that sits at $\rho = \rho_\Lambda = 0$, and is extended along $\Sigma_6 = [t, x_1, x_2, \tilde{\theta}, \tilde{\varphi}, \psi]$. Before the *rotation* we obtain that the induced metric on such a fivebrane is (in string frame)

$$ds^2_{ind} = e^{\Phi}\left[dx^2_{1,2} + \frac{e^{2g}}{4}(d\tilde{\theta}^2 + \sin^2\tilde{\theta}d\tilde{\varphi}^2) + \frac{e^{2k}}{4}(d\psi + \cos\tilde{\theta}d\tilde{\varphi})^2\right] \tag{3.3.24}$$

The induced tension on the three-dimensional wall is

$$T_{eff} = 2\pi^2 T_{D5} e^{2\Phi+2g+k}\big|_{\rho=0} = \frac{\pi^2 T_{D5} e^{2\phi_0} h_1^{3/2}}{\sqrt{2}}, \tag{3.3.25}$$

which is unchanged from the Supersymmetric result.

After the *rotation* procedure, in the background of Eq. 2.1.13, placing a similar fivebrane, the induced metric is,

$$ds^2_{ind} = e^{\Phi}\Big[\frac{1}{\sqrt{\hat{h}}}dx^2_{1,2} + \sqrt{\hat{h}}\Big(\frac{e^{2g}}{4}(d\tilde{\theta}^2 + \sin^2\tilde{\theta}d\tilde{\varphi}^2) + \frac{e^{2k}}{4}(d\psi + \cos\tilde{\theta}d\tilde{\varphi})^2\Big)\Big]. \tag{3.3.26}$$

There is also an induced B_2 field,

$$B_2 = \frac{1}{4}\sqrt{\hat{h}}e^{2g+\Phi/2}b_3(\rho)\sin\tilde{\theta}d\tilde{\theta}\wedge d\tilde{\varphi}. \tag{3.3.27}$$

In order to have a gauge invariant Born-Infeld Action we add an F_2 field on the world-volume of the brane. Then the change due to a gauge transformation of the B_2 field can be cancelled

by a (non-gauge)-transformation on F_2, and thus implies that the full action will be

$$S = -T_{D5}(4\pi)^2 \frac{e^{2g+k+2\Phi}}{8} \int d^{2+1}x \tag{3.3.28}$$

which gives the same effective tension as in Eq. 3.3.25, and is again the same as in the Supersymmetric case. * Thus the effective tensions before and after the *rotation* procedure are the same.

3.4 Remarks on the Dual Field Theory

The comments in this section will be based on the ideas and analysis of [77], where the non-Supersymmetric deformations of $\mathcal{N} = 1$ SQCD are studied. † Here we are looking at a non-Supersymmetric deformation of the Klebanov-Strassler quiver field theory. In the Supersymmetric case, the Klebanov-Strassler field theory is understood as $\mathcal{N} = 1$ SQCD with a gauged flavor group, and a quartic superpotential (see for example [59]), and thus the results of [77] are important here. It should be noted, that these results require us to keep the Supersymmetry-breaking parameters much smaller than the relevant scale in the problem, namely Λ_{SQCD}, and thus we must be sure that W_{20} is small in size.

When this is true, much of the structure of Seiberg's SQCD [58] remains. Of particular interest is the fact that for $SU(N_c)$ SQCD with N_f flavors and where $N_f = N_c$, there exists a vacuum which spontaneously breaks the $U(1)$-baryonic symmetry. This vacuum persists through to the non-Supersymmetric analysis of [77]. Note that in the Supersymmetric case, the last step of the cascade is such that $N_f = N_c$. Thus we argue that the non-Supersymmetric backgrounds here describe a situation where the Supersymmetry-breaking occurs due to gaugino masses and other VEVs, and the baryonic symmetry is broken by the vacuum state.

To be more precise, in [77], the authors added a term to the SQCD Lagrangian

$$\begin{aligned} \mathcal{L} &= \mathcal{L}_{SQCD} + \Delta\mathcal{L}, \\ \Delta\mathcal{L} &\sim \int d^4\theta M_Q (Q^\dagger e^V Q + \tilde{Q}^\dagger e^{-V} \tilde{Q}) + \int d^2\theta M_g S, \end{aligned} \tag{3.4.1}$$

*In the Supersymmetric case we have (using Eq. A.3.1)

$$b_3 = -\kappa e^{3\Phi/2} \hat{h}^{-1/2} \cos\alpha, \tag{3.3.29}$$

which vanishes for $\rho = \rho_\Lambda = 0$.

†Similar ideas on (softly broken) non-Supersymmetric models can be found in [78, 79].

where S is the superfield $S = \mathrm{Tr}(W_\alpha W^\alpha)$, M_Q is a vector multiplet whose D-component equals the mass of the squarks ($-m_q^2$) and M_g is a chiral multiplet whose F-component is the mass of the gluino. It was then argued that, to leading order in the Supersymmetry-breaking parameters M_Q and M_g, one can write an effective Lagrangian in terms of mesons $\hat{\mathcal{M}}$, baryons $(\mathcal{B}, \tilde{\mathcal{B}})$ and S,

$$\Delta\mathcal{L} \sim \int d^4\theta B_M M_Q \mathrm{Tr}(\hat{\mathcal{M}}^\dagger\hat{\mathcal{M}}) + B_b M_Q(\mathcal{B}^\dagger\mathcal{B} + \tilde{\mathcal{B}}^\dagger\tilde{\mathcal{B}}) + \int d^2\theta M_g S + \ldots \tag{3.4.2}$$

One should then supplement the usual actions and superpotentials from the Supersymmetric case with the non-Supersymmetric terms discussed above. In the case of $N_f = N_c$ of interest, one should minimise the potential term coming from Eq. 3.4.2, as well as the potential coming from the Supersymmetric superpotential

$$W = W_{\text{tree}} + W_{\text{quant}} = \kappa\mathrm{Tr}(\hat{\mathcal{M}}^\dagger\hat{\mathcal{M}}) + \xi(\det\hat{\mathcal{M}} - \tilde{\mathcal{B}}\mathcal{B} - \Lambda^{2N_c}). \tag{3.4.3}$$

Thus, the vacua of the theory are those that minimise the potential coming from the tree-level superpotential, together with that of the Supersymmetry-breaking term, subject to the constraint W_{quant}. The result is that for the non-Supersymmetric case, one finds a vacuum state where where the mesons are at the origin of the moduli space ($\hat{\mathcal{M}} = 0$), and the baryons acquire a VEV.

Therefore, we argued that the solutions which break Supersymmetry, due to the presence of masses for the gauginos, have a very similar behaviour to the Klebanov-Strassler cascade. As we have seen, many aspects behave as they do in the Supersymmetric case at leading order. So, what is happening is that the Supersymmetry breaking terms, such as the gaugino masses indicated by W_{20}, are not important at high energy. They will enter into IR observables, but only as corrections to the Supersymmetric behaviour, and thus we take our breaking scale smaller than the strong coupling scale.

3.5 Some Remarks on (meta)-Stability

Here, we shall make some comments on the stability of our solutions in the presence of soft-breaking. To check for perturbative stability, we could fluctuate our background, and then look for the presence of tachyons. It may be that the precise fluctuations we study, are not those leading to the instability, or it could be that we find a tachyonic mode, and this ensures the instability of the solution. We will not perform this analysis here, but instead present some arguments in favour of the stability of these background solutions.

To begin with, we can draw close parallels between the Supersymmetric baryonic branch solutions, and the non-Supersymmetric deformations we present here. We are deforming the background by the presence of the coefficients w_2 and v_2 which break Supersymmetry. Taking these coefficients to be small is what allowed us in the last section to use the results of [77]. In that paper, it was shown (using field theory techniques) that the generated potential has a minimum, which we believe is the vacuum of the field theory dual to our background solutions (due to the analogous behaviour). This would then imply that tachyons are absent from the spectrum.

We could also suffer non-perturbative instabilities, associated with possible tunnelling between vacua with $\Lambda^3_{\text{new}} = -\Lambda^3$, and thus we make an argument in line with that of [70]. * In the non-Supersymmetric background at hand, the tension of the domain wall (separating the vacua of the original Supersymmetric theory) is not modified by the Supersymmetry-breaking parameters (see Section. 3.3.5). As discussed, so far we have solutions in which the strong coupling scale is hierarchically larger than the Supersymmetry-breaking scale, and in this way our solutions are 'close' to the Supersymmetric ones. Further, the authors of [70] estimate the action of a vacuum bubble introduced, for small values of m_λ (using the 'thin wall' approximation) to be given by $S_b \sim N_c \left(\frac{\Lambda}{m_\lambda}\right)^3$, where m_λ is the gaugino mass, and Λ is the strong coupling scale. † They conclude that the decay rate for tunnelling to other solutions is highly suppressed, at least for small values of m_Λ, and thus the solutions are free of such non-perturbative instabilities.

Finally, it would be best if we could make an argument along the lines of a 'fake supergravity' [80], but this would require the construction of a fake superpotential, and this seems an extremely challenging task.

3.6 Going Beyond Soft-Breaking

3.6.1 Deformation the CVMN Case

The CVMN solution [13, 18], obtained in the limit $h_1 \to 2N_c$, (see discussion around Eq. 2.2.5) can be described in terms of $SO(4)$ gauged seven-dimensional supergravity. The $SO(4)$ gauge group corresponds, in the full ten-dimensional description, to rotations of the three-sphere $(\tilde{\theta}, \tilde{\varphi}, \psi)$. If we then wrap the five branes on the two-sphere (θ, φ), we get a four-dimensional

*The authors make the following arguments for a particular non-Supersymmetric deformation of the original Klebanov-Strassler Theory (whose relation to the solutions presented here is discussed further in Section. 3.7.4). We can hope these ideas can be extended on to the Baryonic Branch, at least if we stay 'close' to their solutions.

†The shift in vacuum energy will be given by Eq. 3.3.9.

world-volume theory. As there is exists no covariantly constant spinor on S^2, a gauge field is introduced, and this preserves some of the supersymmetry through a neat cancellation of the spin connection of the S^2 in the variation of a fermion

$$\delta\Psi \sim D_\mu\epsilon = (\partial_\mu + \omega_\mu^{\nu\rho}\gamma^{\nu\rho} - A_\mu^{ij}\Gamma^{ij})\epsilon. \tag{3.6.1}$$

Such a cancellation can be achieved, whilst preserving $\mathcal{N} = 1$ Supersymmetry, through the introduction of an abelian gauge field $U(1) \subset SU(2)_L$, where $SO(4) \sim SU(2)_R \times SU(2)_L$. * From the ten-dimensional point of view, this corresponds to the 'twisting' given under the mixing of the S^2 coordinates θ and φ in Eq. 2.1.8,

$$E^3 \sim \tilde{\omega}_3 + \cos\theta d\varphi. \tag{3.6.2}$$

Although this solution turns out to be singular in the IR, it is possible to obtain the regular CVMN solution, by instead introducing a non-abelian $SU(2)$ gauge field. This can be seen through the additional mixing parametrised by the function $a(\rho)$ in Eq. 2.1.8 in the ten-dimensional description. If $a(\rho) = 1$, as occurs at the IR end-of-space in the Supersymmetric solution, the gauge field is pure gauge and there exists a gauge transformation removing the field, which can be written instead as a coordinate transformation removing the explicit mixing [83, 84].

It is possible to deform the CVMN solution, and this will prove useful for understanding the full space of deformations of the wrapped D5 system. In [30], the solution involving the full $SO(4) \sim SU(2)_L \times SU(2)_R$ gauge field, and solving the full equations of motion, rather than the BPS equations, was discussed. We shall not discuss this solution in its full generality, but shall discuss a simpler deformation, that of introducing a mass term to the single $SU(2)$ gauge group solution, and thus breaking supersymmetry. This appears to be the simplest supersymmetry-breaking deformation of the CVMN solution and corresponds to the globally regular extremal solutions obtained by Gubser, Tseytlin and Volkov (GTV) in [25].

These non-Supersymmetric solutions have the same restrictions on the background Eq. 2.1.8 as in the CVMN solution, that of

$$\frac{e^{2k}}{N_c} = \frac{e^{2g}}{N_c} = 1, \qquad a = b, \tag{3.6.3}$$

*It is possible to preserve $\mathcal{N} = 2$ Supersymmetry by instead choosing the $U(1)$ to be in a diagonal $SU(2)_D \subset SU(2)_R \times SU(2)_L$, as in [56, 81, 82].

for all values of the radial coordinate, but no longer have an exact form as in Eq. 2.2.5. Again, we rely on expansions for the the IR and UV, such that in the IR we have

$$\frac{e^{2h}}{N_c} = \rho^2 - \left(\frac{2}{9} + \frac{v_2^2}{2}\right)\rho^4 + \mathcal{O}(\rho^6), \qquad a = 1 + v_2\rho^2 + \mathcal{O}(\rho^4),$$
$$e^{4\Phi - 4\phi_0} = 1 + \left(\frac{4}{3} + v_2^2\right)\rho^2 + \mathcal{O}(\rho^4), \tag{3.6.4}$$

where the quantity v_2 is parametrising the Supersymmetry-breaking deformation. To recover the CVMN Supersymmetric solution, we take $v_2 = -\frac{2}{3}$. As was observed in [25], we must restrict to $-2 \leq v_2 \leq 0$, to find solutions which interpolate to a regular UV. For the expansions in the UV, we find a substantially different set of expansions for the background functions which (in the notation of [30]) are given by

$$\frac{e^{2h}}{N_c} = \rho + G_\infty + \mathcal{O}\left(\frac{1}{\rho}\right), \qquad a = M_a\rho^{-1/2} + \mathcal{O}(\rho^{-3/2}), \qquad \Phi = \rho + \mathcal{O}(\log\rho), \tag{3.6.5}$$

where the parameters G_∞ and M_a can be thought of as functions of v_2. The main difference to note, is the introduction in the expansions of e^{2h} and a, of terms which are decaying slower than exponentially. The interpretation of this presented in [27], is that here we are deforming Theory A by the addition of a gaugino mass, again through a soft Supersymmetry breaking mass deformation. * From the point of view of the above expansions in Eq. 3.6.5, the mass corresponds to the additional term in the background function $a(\rho)$, and is labelled by M_a. This leading order change in the expansion of $a(\rho)$ is reassuringly reminiscent of the leading order change in the more general UV expansions presented in Eq. 3.1.9.

When looking to understand the consequence of the Supersymmetry-breaking in this case, it is thus best to consider the change in behaviour of the background function $a(\rho)$. A generic non-Supersymmetric solution can be characterised by a scale ρ_s. Below the scale $\rho < \rho_s$ the qualitative behaviour is that of the Supersymmetric CVMN solution, but for $\rho > \rho_s$ we instead have the non-Supersymmetic UV behaviour dominating.

For a generic non-Supersymmetric solution we can define the deformation to a as

$$\Delta a = a - a_s. \tag{3.6.6}$$

Thus we can think of ρ_s as the scale at which the deformation Δa (which decays slowly in the

*The authors in [27] also discuss the fact that under the addition of a gaugino mass to the $\mathcal{N} = 1$ theory, the plane of vacua will be 'tilted' and thus instead of an N_c-fold degeneracy, we are left with a single unique vacuum.

UV) is of the same magnitude as a_s (which decays considerably faster). As a result, ρ_s moves towards the IR as we deform further away from the Supersymmetric solution. Note that this does not relate in an obvious way to the Supersymmetry-breaking scale. It would be more natural to associate the breaking scale with the scale above which Δa has decayed significantly, and which moves into the UV as we deform further away from the Supersymmetric solution.

For $v_2 \leq -\frac{2}{3}$, $a(\rho)$ has at least one zero. As v_2 moves toward the minimum value, it gains more oscillations (and thus more zeros), and in the limit $v_2 \to -\frac{2}{3}$ there are infinitely many zeros. In this limit, the UV changes again, such that the system approaches the "special Abelian solution" of [25] given by

$$\frac{e^{2h}}{N_c} \to \frac{1}{4}, \qquad \Phi \to \sqrt{2}\rho. \tag{3.6.7}$$

Finally, for $v_2 \geq 0$, $a(\rho)$ is always positive, and in the case $v_2 = 0$, $a(\rho) = 1$ for all values of the radial coordinate. As alluded to above, this means we have a gauge field that is pure gauge. Thus we may remove the mixing between the spheres by the appropriate change of coordinates, leaving the internal geometry as simply $S^2 \times S^3$, and is thus related to the solution presented in [85]. The UV behaviour of the other background functions h and Φ still have the form Eq. 3.6.5.

3.6.2 A Method for Finding Globally Regular Solutions

As discussed, for us to conclude that the IR expansion given in Eq. 3.1.4, and the UV expansion given in Eq. 3.1.9, describe the same system of solutions, we must find a numerical interpolation between them. To this end, we can make use of the simpler system of GTV solutions described in the last section. Just as the Supersymmetric CVMN solution is a limiting case of the Supersymmetric baryonic branch solutions (by taking the limit $h_1 \to 2N_c$), we can assume that the GTV solutions are the equivalent limit for the non-Supersymmetric defomations of the baryonic branch. Strictly, this is only a statement about the IR expansions, such that if one sets $w_2 = v_2$ and $k_2 = 0$ in Eq. 3.1.4, we recover the GTV IR expansions given in Eq. 3.6.4. The GTV UV expansion Eq. 3.6.5 on the other hand cannot be recovered from the general UV expansions Eq. 3.1.9. This is not surprising, as it is true that the Supersymmetric CVMN UV behaviour Eq. 2.2.7 cannot be obtained as a simple limit of the generic Supersymmetric UV Eq. 2.2.15.

As the GTV solutions have no redundant parameters in the IR, it is simple to generate numerical solutions. These can then be deformed by increasing h_1, and then adjusting w_2 and

v_2 to correct for the deviation from the UV behaviour. More precisely, for a given value of $v_2 = \Delta v_2 - 2/3$ it is trivial to obtain a numerical solution with $h_1 = 2N_c$, for which $w_2 = v_2$ and $k_2 = 0$. We then deform this by keeping Δv_2 fixed and setting $h_1 = 2N_c + \Delta h_1$. If we use a small perturbation Δh_1, we will require corrections of the form

$$w_2 = w_2^s(\Delta h_1) + \Delta v_2 + \delta w_2(\Delta h_1, \Delta v_2), \qquad k_2 = k_2^s(\Delta h_1) + \delta k_2(\Delta h_1, \Delta v_2), \tag{3.6.8}$$

where δw_2 and δk_2 are extremely small.

It turns out that indeed the UV of these new deformed solutions fits that of the general ansatz Eq. 3.1.9, and thus our assumption that the GTV solutions are the correct limit of our deformations, is justified. Thus we can use this method to allow us to understand the behaviour with generic values for both h_1 and v_2 in terms of the corresponding Supersymmetric baryonic branch and GTV solutions.

3.7 The Two-dimensional Solution Space

3.7.1 Understanding the Effects of h_1 and v_2

As discussed in Section. 3.1, there are two parameters which can be thought to describe the space of solutions, that of the position along the baryonic branch, and also that of the size of the Supersymmetry-breaking deformation. It is simpler to generate solutions by starting in the IR, and thus we choose h_1 and one of the three Supersymmetry-breaking parameters $\{w_2, v_2, k_2\}$. It turns out that the best choice is that of v_2 as it is independent of h_1 in the Supersymmetric case (there $v_2^s = -\frac{2}{3}$ for all h_1).

In Section. 2.3, we related the effect of varying h_1 to changes in the scale $\bar{\rho}$, corresponding to the change between the CVMN behaviour for P (linear) in the IR, and the generic exponential (Exp-like) P behaviour in the UV (corresponding to those Supersymmetric solutions that can be *rotated* to give solutions on the baryonic branch of Klebanov-Strassler). Further, in Section. 3.6.2 the scale ρ_s was introduced and associated with the transition between Supersymmetric CVMN behaviour in the IR, and the (non-Supersymmetric) GTV behaviour in the UV.

So for a generic non-Supersymmetic solution, corresponding to $h_1 > 2N_c$ and $v_2 \neq -\frac{2}{3}$, we find that these features survive, and both scales are present. Then the solutions depend on the ordering of the scales. If $\bar{\rho} < \rho_s$ the solutions have

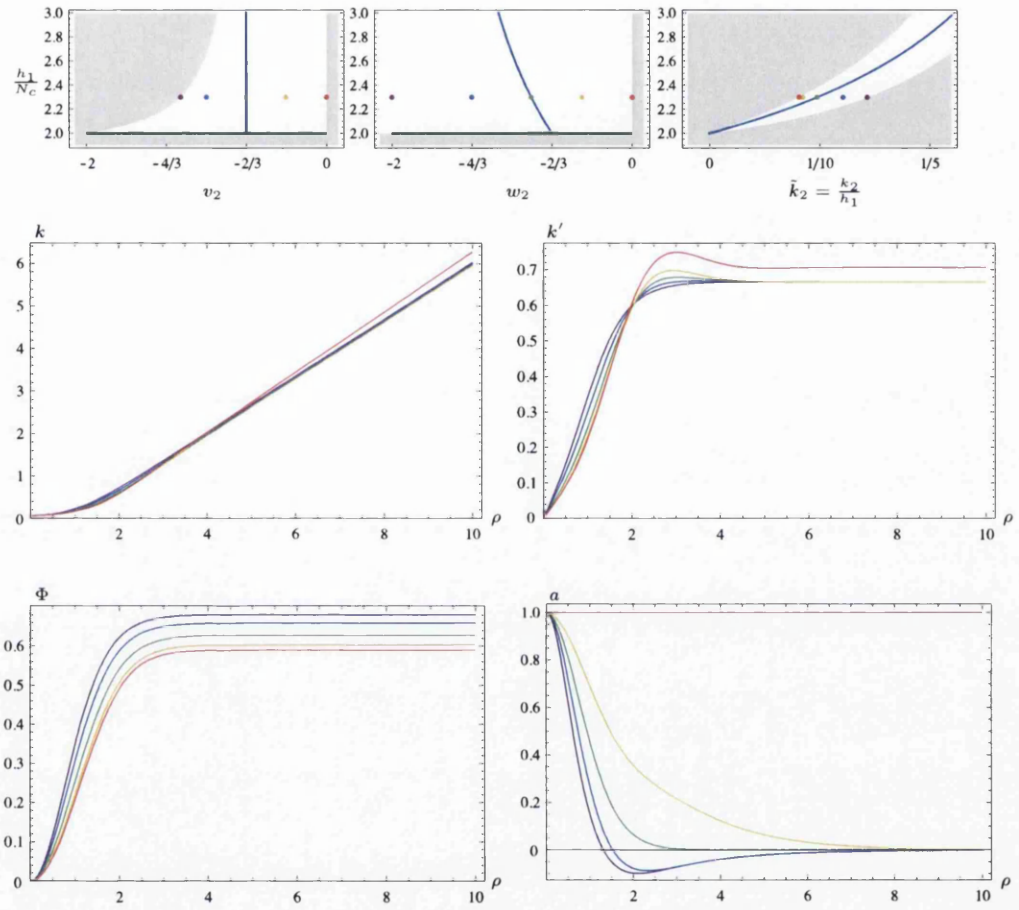

Figure 3.1: Plots of some of the background functions for different values of v_2, with $h_1 = \frac{23}{10}$, $N_c = 1$ and $\phi_0 = 0$. At the top of the page are the solution space plots, showing the values of v_2, w_2 and k_2 in each of the plots, which are colour-coded appropriately. The thick blue line represents the Supersymmetric solutions, the thick green line represents the GTV solutions, and the shaded grey areas are excluded from the space of solutions. Solutions with $w_2 < -2$ are discussed in Sec. 3.7.3. In the left-hand plot in the middle row, we plot k, showing that the Supersymmetry-breaking parameter v_2 has little effect on the behaviour unless one takes the limit $v_2 \to 0$ (depicted in red). In the right-hand plot in the middle row we plot k', and the transition between the two gradients ($k \sim \frac{2\rho}{3}$ and $k \sim \frac{\sqrt{2}\rho}{2}$) is shown clearly. We find that the effect of v_2 on the other background functions g, h is very similar to the change in k. In the left-hand plot in the bottom row, we plot the dilaton in the various cases, showing explicitly that the UV value Φ_∞ varies with v_2 (for constant h_1). Finally, in the right-hand plot in the bottom row, we plot the effect on a.

$$\begin{aligned}
\rho < \bar{\rho}: &\quad k \simeq g \sim \text{const}, \quad a \simeq b \sim e^{-2\rho} \quad \text{(SUSY, CVMN-like)} \\
\bar{\rho} < \rho < \rho_s: &\quad k \sim g \sim 2\rho/3, \quad a \sim b \sim e^{-2\rho} \quad \text{(SUSY, Exp-like)} \\
\rho > \rho_s: &\quad k \sim g \sim 2\rho/3, \quad a \sim b \sim e^{-2\rho/3} \quad \text{(non-SUSY, Exp-like)}
\end{aligned}$$

On the other hand, if $\rho_s < \bar{\rho}$ we have

$$\begin{aligned}
\rho < \rho_s: &\quad k \simeq g \sim \text{const}, \quad a \simeq b \sim e^{-2\rho} \quad \text{(SUSY, CVMN-like)} \\
\rho_s < \rho < \bar{\rho}: &\quad k \simeq g \sim \text{const}, \quad a \simeq b \sim \rho^{-1/2} \quad \text{(non-SUSY, GTV-like)} \\
\rho > \bar{\rho}: &\quad k \sim g \sim 2\rho/3, \quad a \sim b \sim e^{-2\rho/3} \quad \text{(non-SUSY, Exp-like)}
\end{aligned}$$

It appears that $\bar{\rho}$ is almost independent of v_2, and that ρ_s is almost independent of h_1, although this may break down for sufficiently large h_1 and v_2, depending on the precise definition used for the scales. In fact the presence of the two scales becomes less clear as they move into the IR for large h_1 and v_2. We show the behaviour of the background functions for some generic solutions in Fig. 3.1 where h_1 is large enough that $\bar{\rho}$ is close to the IR and is not visible.

3.7.2 Boundaries of the Solution Space

We noted earlier that the GTV solutions are restricted to $-2 < v_2 < 0$ for solutions with a regular UV. It is not obvious how to generalise these bounds for $h_1 > 2N_c$, but numerical observations suggest that $w_2(h_1, v_2)$ becomes independent of h_1 for $v_2 \to 0$, and that in particular there is a family of solutions with $a = b = 1$ and $g = k$ even for $h_1 > 2N_c$.

In our IR expansions in Eq. 3.1.4, this is equivalent to setting

$$w_2 = v_2 = 0, \qquad k_2 = \frac{h_1}{3} - \frac{4N_c^2}{3h_1} = \frac{5}{6}k_2^s, \tag{3.7.1}$$

and these agree with the numerical values obtained. It appears that if we take $v_2 > 0$, then $a(\rho) > 1$ for small ρ, and this leads to the background functions diverging for finite ρ, which seems to indicate that this is the correct generalisation of the boundary. An example of a solution on this boundary is given by the the solid red curves in Fig. 3.1.

Thus, if one sets $a = b = 1$ and $g = k$ in the equations of motion (the result is shown in Eq. A.1.10), we find that our ansatz for the UV expansions in Eq. 3.1.5, is no longer suitable. However, using the equivalent expansions in powers of $e^{\sqrt{2}\rho}$ does lead to a expansions of the form

$$\begin{aligned}
e^{2h} &= \frac{K_{00}}{2}e^{\sqrt{2}\rho} + \left(\frac{K_{00}K_{20} + N_c^2}{2K_{00}} + \frac{N_c^2}{2\sqrt{2}K_{00}}\rho\right)e^{-\sqrt{2}\rho} + \mathcal{O}\left(e^{-3\sqrt{2}\rho}\right) \\
e^{2k} &= K_{00}e^{\sqrt{2}\rho} + \left(K_{20} + \frac{N_c^2}{\sqrt{2}K_{00}}\rho\right)e^{-\sqrt{2}\rho} + \mathcal{O}\left(e^{-3\sqrt{2}\rho}\right) \\
e^{4\Phi - 4\Phi_\infty} &= 1 - \frac{1}{K_{00}^2}\left(4K_{00}K_{20} + N_c^2 + 2\sqrt{2}N_c^2\rho\right)e^{-2\sqrt{2}\rho} + \mathcal{O}\left(e^{-4\sqrt{2}\rho}\right)
\end{aligned} \tag{3.7.2}$$

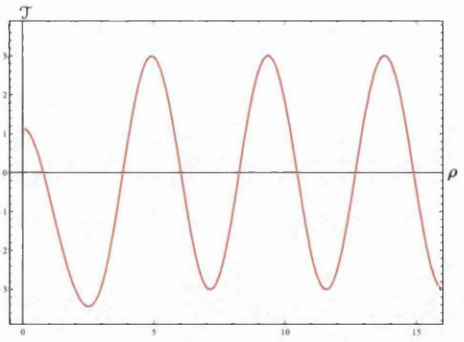

Figure 3.2: A plot of $\mathcal{T}$ for a $v_2 = 0$ boundary solution, showing the subleading oscillatory behaviour, as seen in Eq. 3.7.3. The corresponding solution is the solid red curves in Fig. 3.1.

Note that although the ansatz we used to get these expansions was just given by replacing $4\rho/3 \to \sqrt{2}\rho$ in Eq. 3.1.5, it is not possible to obtain these expansions from the generic UV in Eq. 3.1.9 simply by a rescaling, or change of coordinates. An example is given in the fact that for all these solutions we have $e^{2k} = e^{2g}$, whereas in the generic case $e^{2k} \sim 2e^{2g}/3$ for large ρ. Thus we do not attempt to match the parameters here to the usual set $\{c_+, c_-, \dots\}$. Instead, we denote the two free parameters by K_{00} and K_{20}, the leading parameter (roughly corresponding to c_+) being K_{00}. Note that, as we have set $v_2 = 0$, the two parameters K_{00} and K_{20} cannot be independent once we match to the IR. This also occurs when one wants to find globally regular solutions in the Supersymmetric case, in which the two UV parameters (c_+ and c_-) must be tuned, to match the one-parameter (h_1) IR solutions. If one then tries to use this form of UV expansion to find an interpolating solution, although the leading order behaviour is correct, there is a set of subleading terms that are missed by the general UV expansion ansatz. One must instead include the possibility of trigonometric functions, such that one finds expansions of the form

$$\begin{aligned} e^{2h} &= \frac{K_{00}}{2} e^{\sqrt{2}\rho} + \left(\frac{H_s}{\sqrt{2}} \sin\sqrt{2}\rho + H_c \cos\sqrt{2}\rho \right) + \mathcal{O}\left(e^{-\sqrt{2}\rho}\right) \\ e^{2k} &= K_{00} e^{\sqrt{2}\rho} - \frac{1}{5}\left(2(\sqrt{2}H_s + H_c)\sin\sqrt{2}\rho + (4H_c - \sqrt{2}H_s)\cos\sqrt{2}\rho \right) + \mathcal{O}\left(e^{-\sqrt{2}\rho}\right) \\ e^{4\Phi - 4\Phi_\infty} &= 1 - \frac{1}{K_{00}^2}\left(4K_{00}K_{20} + N_c^2 + 2\sqrt{2}N_c^2\rho \right) e^{-2\sqrt{2}\rho} + \mathcal{O}\left(e^{-3\sqrt{2}\rho}\right) \end{aligned} \tag{3.7.3}$$

where the trigonometric functions appear at the next order in Φ, and this appears to cover the behaviour for these boundary solutions. Again, we expect the new coefficients H_s and H_c to be determined in terms of one of the other coefficients, when we match to the IR. In Fig. 3.2 we

show the presence of this oscillatory behaviour by plotting the combination $\mathcal{T}(\rho) = e^{2k} - 2e^{2h}$, in which it is the oscillations which are the leading order behaviour.

In Section. 3.6.1 we noted that the 'twist' which mixes the S^2 and the S^3 could be removed by a change of coordinates when $a = b = 1$. In the solutions described above, we still have $g = k$, and thus the same coordinate transformation still works, leading to a simplified system, similar to the one discussed in [85]. With C_4 and F_5 unchanged from Eq. 2.1.14, we now find

$$\begin{aligned} ds_E^2 &= e^{\Phi/2}\left[\hat{h}^{-1/2}dx_{1,3}^2 + \hat{h}^{1/2}\left(e^{2k}d\rho^2 + e^{2h}d\Omega_2 + \frac{e^{2k}}{4}d\Omega_3\right)\right], \\ F_3 &= -\frac{N_c}{4}\tilde{\omega}_1 \wedge \tilde{\omega}_2 \wedge \tilde{\omega}_3, \\ H_3 &= 2N_c e^{2h-2k+2\Phi-\Phi_\infty}\sin\theta\; d\rho \wedge d\theta \wedge d\varphi. \end{aligned} \tag{3.7.4}$$

The boundary for $v_2 < -\frac{2}{3}$, corresponding to $v_2 = -2$ in the GTV solutions, seems to be much less accessible numerically, in part due to the presence of zeros in the functions a and b. Next we will discuss a possible way to learn more about this limit.

3.7.3 A $\mathbb{Z}_2$ Symmetry

The system described in Sec. 2.1, which contains all the solutions we consider, exhibits a $\mathbb{Z}_2$ symmetry $\mathscr{I}$ which exchanges the two S^2 of the conifold, and changes the signs of the three-forms F_3 and H_3 in Eq. 2.1.14. To see this symmetry, we will use the fact that all the solutions described here fall into the PT ansatz [15] which has a metric of the form

$$\begin{aligned} ds_E^2 &= e^{\Phi/2}(\hat{h}^{-1/2}dx_{1,3}^2 + \hat{h}^{1/2}ds_6^2), \\ ds_6^2 &= \frac{2}{3}e^{-8p+3q}(4d\rho^2 + g_5^2) + e^{2p+3q}\Big\{\cosh y\,\left[e^z(\omega_1^2+\omega_2^2) + e^{-z}(\tilde{\omega}_1^2+\tilde{\omega}_2^2)\right] \\ &\qquad - 2\sinh y\,(\omega_1\tilde{\omega}_1 + \omega_2\tilde{\omega}_2)\Big\}, \end{aligned} \tag{3.7.5}$$

where the angular forms ω and g_5 are given by

$$\omega_1 = d\theta, \qquad \omega_2 = -\sin\theta\, d\varphi, \qquad g_5 = \tilde{\omega}_3 + \cos\theta\, d\varphi. \tag{3.7.6}$$

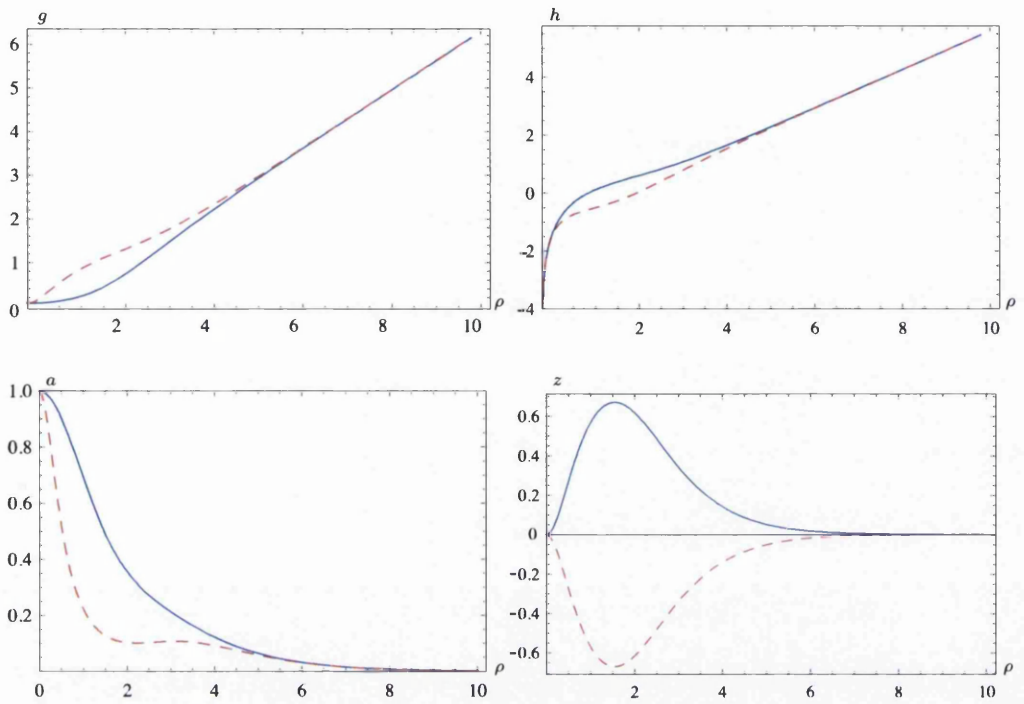

Figure 3.3: Plots comparing some of the background functions before and after the transformation in Eq. 3.7.8. The solid blue lines represent the original solution with $w_2 > -2$, and the red dashed line is the transformed solutions with $w_2 < -2$. This solution corresponds to that of the yellow point in Fig. 3.1. We plot the background functions g, h and a which are affected by the transformation, and also we plot z, which changes sign under the transformation.

It is possible to write down the explicit relationship between the background functions in our case and that of the PT ansatz. This takes the form

$$e^{10p} = \frac{4}{3}e^{g+h-2k}, \qquad e^{15q} = \frac{3}{8}e^{4g+4h+2k},$$
$$e^{y} = \frac{1}{2}e^{-h}\left(\sqrt{4e^{2h}+e^{2g}a^2} - ae^{g}\right), \qquad e^{z} = e^{-g}\sqrt{4e^{2h}+e^{2g}a^2}. \tag{3.7.7}$$

Under the exchange of $(\theta,\varphi) \leftrightarrow (\tilde{\theta},\tilde{\varphi})$, and the relabelling $z \leftrightarrow -z$, the metric and fields are unchanged (aside from a change of sign). In the Klebanov-Strassler solution, which we can obtain by taking the limit $h_1, c_+ \to \infty$ in the case of the Supersymmetric solutions, $z = 0$ and thus the transformation $\mathscr{I}$ reduces to a change of coordinates. One can think of this as the $N_f = 0$ version of the Seiberg Duality discussed in Section. 3.3.3 and [66–68].

In our generic globally regular solutions, it is no longer the case that $z = 0$, and thus we

now look at the effect of $\mathscr{I}$. It is possible to write down the effect of taking $z \to -z$ on the background functions as

$$e^{2g} \to e^{2g+2z}, \qquad e^{2h} \to e^{2h-2z}, \qquad a \to e^{-2z}a. \tag{3.7.8}$$

This transformation only has a subleading effect on g, h and a, as can be seen from the expansions

$$e^z = \begin{cases} 1 + (2+w_2)\rho^2 + \mathcal{O}(\rho^4) & \text{for } \rho \to 0 \\ 1 + \dfrac{1}{c_+}\left(4H_{11}\rho + Q_o + \dfrac{3}{2}c_+ W_{20}^2\right) e^{-4\rho/3} + \mathcal{O}(e^{-4\rho/3}) & \text{for } \rho \to \infty. \end{cases} \tag{3.7.9}$$

The transformed functions are still compatible with the form of the expansions in Eq. 3.1.1 and Eq. 3.1.5. More specifically, it can be seen that for $z \to -z$, we need to take $w_2 \to -4 - w_2$, which corresponds to a reflection in the line $w_2 = -2$. In Eq. 3.1.2, taking the limit $h_1 \to \infty$ means that $\hat{w}_2 \to -2$ and this is compatible with the fact that the Klebanov-Strassler solution has $z = 0$. Further, as the background functions k and b do not appear in Eq. 3.7.8, we can conclude that the other IR parameters are unchanged under the transformation $\mathscr{I}$.

Thus, for any solution specified by (h_1, v_2), we can obtain another solution, with a different value of w_2 and as the transformation $\mathscr{I}$ only acts on subleading terms in the expansions, we can be sure that the new solution will also be globally regular and fall within our ansatz. We compare two such solutions in Fig. 3.3. Although this means we have a new solution to the equations of motion describing the system, this solution does not correspond to a new background, and actually is just a non-trivial relabelling in the choice of basis we make.

By demanding that $z \to -z$ while the other functions remain unchanged, it is possible to write the effect on the UV parameters as

$$\begin{aligned} &\frac{c_-}{c_+^3} \to \frac{c_-}{c_+^3} - 32W_{20}\left(2\frac{Q_o}{c_+} + 3W_{20}^2\right)\left(2e^{2\rho_\Lambda} - \frac{Q_o}{c_+}W_{20} - \frac{3}{2}W_{20}^3\right), \\ &\frac{Q_o}{c_+} \to -\frac{Q_o}{c_+} - 3W_{20}^2, \qquad e^{2\rho_\Lambda} \to e^{2\rho_\Lambda} - \frac{Q_o}{c_+}W_{20} - \frac{3}{2}W_{20}^3, \qquad \frac{H_{11}}{c_+} \to -\frac{H_{11}}{c_+}, \end{aligned} \tag{3.7.10}$$

such that the values of $\{c_+, \Phi_\infty, W_{20}, V_{40}, \Phi_{30}\}$ are kept fixed.

For the family of solutions which lie on the line $w_2 = -2$, we find that the IR expansion for e^z given in Eq. 3.7.9 is such that all subleading terms vanish, leaving $z = 0$. From the numerical solutions, we can see that this appears to hold for all ρ. This would mean that as in the Klebanov-Strassler solution $\mathscr{I}$ is a symmetry of the geometry. This family of solutions is depicted as the yellow lines in Fig. 3.4, where it is known exactly in the (h_1, w_2)-plane, as here

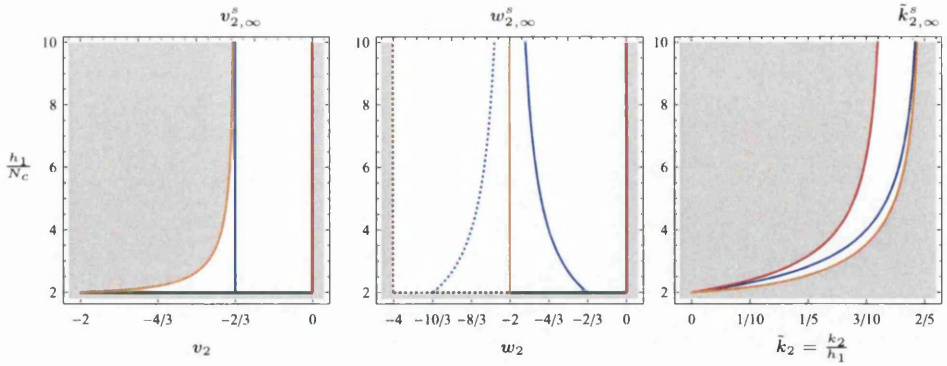

Figure 3.4: Plots of the full two-dimensional solution space for the IR parameters v_2, w_2 and $\tilde{k}_2$. The blue curves represent the Supersymmetric solutions and the green curves represent the GTV solutions. The red curves correspond to the case with $a = b = 1$ discussed in Section. 3.7.2, while the yellow curves correspond to the solutions which are invariant under $\mathscr{I}$ and thus have a $\mathbb{Z}_2$ symmetry of the geometry, discussed in Sec. 3.7.3. The dotted curves are the equivalent solutions with $w_2 \to -4 - w_2$. Assuming that the two boundaries are the correct generalisation to the requirement $-2 \leq v_2 \leq 0$ in the GTV solutions, the grey shaded areas show regions where no regular solutions exist.

$w_2 = -2$ for all h_1. For v_2 and k_2 it is has not been possible to determine the exact expressions for the corresponding line in the respective planes, but it can be shown numerically that

$$\begin{aligned} \Delta v_2(h_1) &= v_2(h_1) + 2/3 \sim -1/h_1^2, \\ \Delta k_2(h_1) &= k_2(h_1) - k_2^s(h_1) = \frac{16}{45h_1} - \epsilon(h_1), \end{aligned} \tag{3.7.11}$$

for large h_1, and the higher-order corrections to $\Delta k_2(h_1)$ are highly suppressed. Thus, the yellow curves in the corresponding (h_1, v_2)- and (h_1, k_2)-planes in Fig. 3.4 are fitted to expansions in powers of $\frac{1}{h_1}$ for a number of numerical solutions.

Further, as we seem to find that these solutions are indeed symmetric under $\mathscr{I}$ for all ρ, then we can look for equivalent relations between the UV parameters to $w_2 = -2$ in the IR. If we look at the form of Eq. 3.7.9 or Eq. 3.7.10, it appears that taking

$$W_{20}^2 = -\frac{2Q_o}{3c_+}, \qquad \frac{H_{11}}{c_+} = 0, \tag{3.7.12}$$

is the correct set of choices, leaving one degree of freedom, such that we can move along the line $w_2 = -2$. Notice that in the limit $c_+ \to \infty$ we would recover the correct Supersymmetric values corresponding to the Klebanov-Strassler solution.

This has implications for the GTV solutions from Section. 3.6.1 also. This suggests that if

we relax the condition $a = b$ (and thus $w_2 = v_2$) and we parametrise these solutions by w_2, that there is no obvious lower bound on w_2, but that $v_2(w_2)$ has a minimum at $w_2 = -2$. If we then interpret this minimum in $v_2(w_2)$ as the correct boundary, this would imply that $w_2 = -2$ is the correct generalisation of the GTV solutions for $h_1 > 2N_c$, and this is supported by the numerical analysis in that it appears we cannot find regular UV solutions for v_2 smaller than those which correspond to $w_2 = -2$. This should be taken as strong evidence of the boundary, but it could also be that there are discontinuities in the values of v_2 and k_2, across the line $w_2 = -2$.

3.7.4 The Limit $h_1, c_+ \to \infty$

As we have so far considered the non-Supersymmetric generalisation of the baryonic branch, an obvious next step is to consider the possible generalisation to the Klebanov-Strassler solution [12], which can be found in the limit $h_1 \sim c_+ \to \infty$ in the Supersymmetric case. We shall continue to use the notation introduced in Eq. 3.7.5. In this form, the Supersymmetric Klebanov-Strassler solution has a simple exact form with $z = 0$ and $\Phi = \text{const}$, and

$$e^{10p} = K(\rho)^3 \sinh 2\rho, \qquad e^{15q} = \frac{3^{5/4}}{2^{15/2}} K(\rho)^2 \sinh^4 2\rho, \qquad e^y = \tanh \rho, \tag{3.7.13}$$

where we have defined

$$K(\rho) \equiv \frac{(\sinh 4\rho - 4\rho)^{1/3}}{2^{1/3} \sinh 2\rho}. \tag{3.7.14}$$

The remaining function $b(\rho)$ is unchanged on the whole baryonic branch, and is given for instance in Eq. 2.2.9.

Thus we look to deform this solution, but to do so, we must first ask which characteristics of the Klebanov-Strassler Supersymmetric solution we would like to retain under the non-Supersymmetric deformation. We have already discussed in the last section, one such possibility, in that by demanding $z = 0$, we retain the $\mathbb{Z}_2$-symmetry of the geometry, associated with the family of solutions with $w_2 = -2$.

In [70], Dymarsky and Kuperstein (DK) looked at a different deformation. They used the fact that the Klebanov-Strassler background has several other simplifying features which are retained in the linear deformations studied in [61, 86], but are lost when one moves to the baryonic branch. These features are

1. A constant dilaton, $e^{\Phi} = g_s$

2. An imaginary self-dual three-form flux [*], $iG_3 = *_6 G_3$, where $G_3 \equiv F_3 + \frac{i}{g_s} H_3$

3. A RR four-form satisfying $C_4 = H^{-1}\text{Vol}_{(1,3)}$, where $ds^2 = H^{-1/2} dx^2_{(1,3)} + H^{1/2} ds^2_6$

4. A Ricci-flat six-dimensional unwarped metric

The outcome is that under these properties the fluxes decouple from the equations determining the metric. [†] By imposing these properties, a one-dimensional family of solutions remains, which breaks both Supersymmetry and the $\mathbb{Z}_2$-symmetry of the geometry. We thus look to see how these solutions appear in the two-dimensional solution space.

Let us try to identify the appropriate limit. From the generic IR expansions given in Eq. 3.1.4, it is possible to recover a constant dilaton by taking $h_1 \to \infty$, as happens in the Supersymmetric case. As mentioned, this means the first three conditions are satisfied, and the fourth can be seen to be satisfied upon the substitution of the IR expansion into the form of the six-dimensional Ricci scalar.

It will be illustrative to relate the three IR Supersymmetry-breaking parameters $\{w_2, v_2, k_2\}$ to the parameters $\{\zeta_1, \zeta_2, \zeta_3\}$, used in [70]. Initially, looking at the IR expansion for z and comparing with the equivalent expression in [70] we find that

$$w_2 = 4\zeta_1 - 2. \tag{3.7.15}$$

To gain the relation for k_2 we look at the expansion for e^y, and upon taking the limit $h_1 \to \infty$, we find that in the ρ^3 term there is not enough freedom when compared to [70]. This is fixed by taking $k_2 \to \infty$ while keeping fixed $\tilde{k}_2 \equiv k_2/h_1$. This then gives

$$e^y = \rho - \left(\frac{2}{3} + 4\zeta_1^2 - \frac{5}{6}\tilde{k}_2\right)\rho^3 + O(\rho^5), \tag{3.7.16}$$

which we can match to the result of [70] by setting

$$\tilde{k}_2 \equiv \frac{k_2}{h_1} = \frac{2}{65}(13 - 90\zeta_2). \tag{3.7.17}$$

Finally, we need to determine the relationship between v_2 and ζ_3. This can be achieved by comparing our expansion for b with that for $F = (1-b)/2$ in [70], from which we obtain

$$v_2 = -\frac{2}{3}(\zeta_3 + 1). \tag{3.7.18}$$

[*] Here $*_6$ is the six-dimensional Hodge dual

[†] Once 1. is implemented, 2. and 3. automatically follow in the solutions presented here.

In summary, in the limit $h_1 \to \infty$ we find the following relationships between our three SUSY-breaking IR parameters and those used in [70]:

$$w_2 = 4\zeta_1 - 2, \qquad \tilde{k}_2 \equiv \frac{k_2}{h_1} = \frac{2}{65}(13 - 90\zeta_2), \qquad v_2 = -\frac{2}{3}(\zeta_3 + 1). \tag{3.7.19}$$

Then, setting $\zeta_i = 0$, we recover the correct large h_1 values corresponding to the Supersymmetric solutions. We can further see that if one writes, for example $\Delta w_2(h_1) = w_2 - w_2^s(h_1)$, then

$$\zeta_1 = \frac{1}{4}\Delta w_2, \qquad \zeta_2 = -\frac{13}{36}\Delta\tilde{k}_2, \qquad \zeta_3 = -\frac{3}{2}\Delta v_2. \tag{3.7.20}$$

In the UV, it is more subtle, but it is clear from the numerical analysis that $c_+ \to \infty$ is still the correct limit, and we also know that we must take $\Phi_\infty \to \phi_0$ to gain a constant dilaton. Looking at the UV expansion for the six-dimensional Ricci Scalar, and the dilaton, we find that the limit $c_+ \to \infty$ is consistent with Ricci-flatness, and further taking the limit $\Phi_{30} \to 0$ leads to a constant dilaton.

Finally, we note that our numerical approach does not allow us to take the limit $h_1 \to \infty$ explicitly. That aside, it is possible to probe sufficiently large values of h_1, such that the solutions have many of the characteristics expected in the true limit.

3.7.5 Further Remarks on the Dual Field Theory

We shall finish by discussing a few more points about the dual field theories to the gravity backgrounds, in light of the discussions regarding moving beyond soft-breaking. Here we have not restricted ourselves to small deformations of the Supersymmetric backgrounds any longer.

Consider solutions with $h_1 > 2N_c$, the geometry is 'almost' asymptotically AdS_5. More precisely, for large ρ we can write the metric in the form

$$\begin{aligned} ds^2 &\sim \frac{u^2}{\hat{H}(u)^{1/2}} dx^2_{(1,3)} + \frac{\hat{H}(u)^{1/2}}{u^2} du^2 + ds_5^2, \\ \hat{H}(u) &\sim \text{const} + \log u + \mathcal{O}(u^{-2}), \end{aligned} \tag{3.7.21}$$

where we have defined a suitable radial coordinate $u = e^{2\rho/3}$ (which is increasing in ρ). For solutions with $v_2 = 0$ discussed in Section. 3.7.2, we instead require the definition $u = e^{\rho/\sqrt{2}}$. The term of order, $\log u$ in the correction to $\hat{H}(u)$, comes from the subleading behaviour of the dilaton (see for instance Eq. 3.1.9 and Eq. 3.7.2).

It appears that $W_{20} \to \infty$ (at least numerically) as we approach the boundary at $v_2 = w_2 = 0$. This suggests that we can interpret the solution at the boundary, with $a = b = 1$ for all ρ (see Section. 3.7.2) as corresponding to a field theory in which the gaugino has been given an infinite mass. We can say that we definitely no longer have soft-breaking here, and the theory is non-Supersymmetric all the way into the UV. Presumably, by sending the mass to infinity we are effectively removing the gaugino entirely, obtaining a completely non-Supersymmetric theory.

If we again look to the field combination M_1 in Eq. 3.3.2 (which can be thought of as corresponding to the VEV of a dimension-two operator $\mathcal{U}$, at least in the Supersymmetric case), notice that in the Supersymmetric case $W_{20} = 0$, the leading term of M_1 vanishes for $c_+ \to \infty$, and we recover the Supersymmetric Klebanov-Strassler background. This is also the limit in which the geometry is invariant under the $\mathbb{Z}_2$ symmetry $\mathscr{I}$ discussed in Section. 3.7.3. In fact, from the field theoretical point of view, the transformation $\mathscr{I}$ can be identified with swapping $A \leftrightarrow B$ [61].

As soon as we move away from the Supersymmetric solutions we can no longer make the identification Eq. 3.3.5. It is still instructive to consider the behaviour of the operator $\mathcal{U}$ associated with M_1. From Eq. 3.3.2, it is clear that we can expect $\mathcal{U}$ to be changed when we break Supersymmetry, while keeping c_+ fixed. Indeed, referring to the definition Eq. 3.3.1, we see that $M_1 = 0$ when $z = 0$. This applies at all ρ in all the solutions on the line $w_2 = -2$. It is interesting that the presence of the $\mathbb{Z}_2$ symmetry still corresponds to the vanishing of this quantity, even in the non-Supersymmetric case. This is perhaps indicative of the extent to which the structure of the Supersymmetric system survives in the generic non-Supersymmetric case.

As we increase v_2 (and W_{20}) from the Supersymmetric solutions, we find numerically that both terms at leading order in M_1 diverge. However, in the limit we obtain the solutions described in Section. 3.7.2, and the expansions Eq. 3.3.2 are no longer valid. Instead, for large ρ,

$$M_1 = 2 + \frac{4}{5\sqrt{2}K_{00}}\left((7H_s + \sqrt{2}H_c)\sin\sqrt{2}\rho + (7\sqrt{2}H_c - H_s)\cos\sqrt{2}\rho\right)e^{-\sqrt{2}\rho} + \mathcal{O}\left(e^{-2\sqrt{2}\rho}\right). \tag{3.7.22}$$

This is qualitatively different to the generic case. Firstly, we now have $M_1 \to 2$ in the UV, as opposed to $M_1 \to 0$. This indicates that these solutions do not recover the $\mathbb{Z}_2$ symmetry in the

UV. Secondly, the next-to-leading term now contains oscillatory functions, although these are still suppressed by u^{-2}.

There is some subtlety here in the fact that we have allowed our deformations of the Supersymmetric solutions to become large. It is then not clear that any deductions based on an analogy with the Supersymmetric solutions remain valid. In particular, we cannot not necessarily expect to find stable solutions for all values of W_{20}. However, the similarities between the Supersymmetric and non-Supersymmetric solutions are interesting. Note that we still find a continuous and smooth deformation of the Supersymmetric solutions between smaller and larger values of the non-Supersymmetric deformations in the IR. We only find a different UV expansion in the limiting cases (i.e. on the boundaries of our solution space).

Chapter 4

Probe-D7 Brane Embeddings

In this Chapter (mainly based on the work of [3, 4]), we study the idea of modelling Chiral-Symmetry breaking, via the introduction of a probe-D7 brane in the class of backgrounds defined in Section. 2.2. There are various scales that play a role in describing these Supersymmetric solutions (see Section. 2.3), and we shall explore how the probe behaves under changes in these scales.

We begin the Chapter by setting up a general formalism into which all the probes we study fall. We discuss properties of the functions describing the embedding of such probes into a background and further we derive a useful tool in analysing the perturbative stability of the probe solutions. This is given by the function $\mathcal{Z}$, and applying it in the various cases, will give us a greater insight into the stability of certain embeddings in this class of backgrounds, which have been studied in [39, 87–90]. These multi-scale setups were of particular interest to models of Technicolor and Electroweak-Symmetry breaking, see also the paper [91] for discussions.

We shall then discuss a resolution to a emergent problem in the context of the solutions with exponential growth in the UV of the function P defined in Eq. 2.2.14 (but is not resigned to these, as we shall show with a particularly simple example). This will lead us to introduce the idea of a 'bulk' phase transition [*], which can occur when we are required to introduce a UV cutoff, and then find that the probe dynamics are dominated by unphysical cutoff effects. This imposes unexpected bounds on the region of parameter space of the gravity theory as to where it is related to the dual field theory.

We then systematically explore the possibility that, the various gravity backgrounds described in Section. 2.2, produce a suitable model of Chiral-Symmetry breaking, keeping in

[*]This nomenclature is due to the similarity of this phenomenon with the idea of bulk phase transitions seen on the lattice (see for example [92]).

mind the perturbative stability of the probe, and the possibility of a bulk phase transition occurring.

Finally, a comment is in order: in this Chapter we are using the term "Chrial-Symmetry Breaking" to describe what is going on within the following setups, i.e. we have a $U(N_f)_L \times U(N_f)_R$-symmetry (due to the two sets of N_f branes in the UV being distinguishable and thus we have two sets of massless chiral fermions), and then this symmetry is spontaneously broken by a non-zero VEV in the IR (where the branes join in a U-shape and the two sets could now interact), resulting in a strongly-coupled model in which we are left with only a single $U(N_f)_D$. We will be using the same embedding as other models based on the conifold (such as [37, 38] where they argue the setup has Weyl spinors rather than Dirac spinors), and it is confirmed that the setup does indeed have a broken Chiral Symmetry, and the associated Goldstone boson (corresponding to a massless mode in the meson spectrum) has been identified. Thus here we rely on the close similarities between our models and those of [37, 38], and we shall use this term to describe what is going on in each of our setups, but of course to be sure this is actually the truth of the matter, we should attempt to identify the corresponding Goldstone boson in the spectrum. *

4.1 A General Formalism for Probes

4.1.1 Outline

Here we outline the form of some general results that will be applicable to the cases we study in this Chapter and the next. We shall keep the explicit dependence on the UV cutoff ρ_U as this will play an important role in what follows. Some of the considerations we shall make here can be also be found in [93–98].

The basic setup we shall investigate is as follows: consider a classical system describing an extended object (a string, a brane or some higher dimensional surface) which is to be treated as a probe (such that it does not have back-reaction on the geometry it is probing) and further assume that there are just two coordinates for which the probe embedding is determined dynamically. Here, one of these will be the radial coordinate on the space ρ, and the other we shall label x. We can parametrise the one-dimensional profile of the probe in the (x, ρ)-plane in terms of a single variable σ, such that $x = x(\sigma)$ and $\rho = \rho(\sigma)$. In what follows, the class of

*In these backgrounds in question, this is a challenging numerical task, and is one that we leave to future work.

actions we shall consider is of the form

$$S = \frac{T}{2\pi\alpha'} \int \mathrm{d}\sigma \sqrt{(x')^2 F^2 + (\rho')^2 G^2}, \tag{4.1.1}$$

where the prime represents the derivative with respect to σ, and T is a constant. The two functions, F and G, depend in general on the radial coordinate, but not explicitly on x, and are positive-definite and monotonically non-decreasing with ρ.

Taking this as the form of our action will be the strongest assumption made. Thus, for a system to be described by it, we shall potentially require that another embedding coordinate be fixed dynamically, or the Wess-Zumino term to vanish. In the cases that follow, both these conditions will be met (although not necessarily for the same reason in each case). Once we have an action that reduces to the form of the above, all of the following analysis applies, independent of the nature of the probe we are using and the background it is being used to explore.

The first configuration that we consider as a solution to the classical equations of motion coming from the above action, is given by $x' = 0$, and we shall call it *disconnected.* This configuration consists of two straight lines, between ρ_U and the IR end-of-space ρ_Λ. The energy of such a configuration is given by

$$E_0(\rho_U) = 2 \int_{\rho_\Lambda}^{\rho_U} d\rho\, G(\rho). \tag{4.1.2}$$

Another possible solution for the probe, is a configuration which forms a U-shape in the (ρ, x)-plane, starting at $\rho \to \infty$. We can then parametrise the embedding profile by the minimum value reached in the interior which we shall call ρ_0. To solve the equations, one can make use of the parametrisation invariance to set $\sigma = \rho$, and notice that there then must be two branches. We can define the following effective potential [97]

$$V_{\text{eff}}(\rho, \rho_0) \equiv \frac{F(\rho)}{G(\rho)} \left(\frac{F^2(\rho)}{F^2(\rho_0)} - 1 \right)^{1/2} \tag{4.1.3}$$

and we can write the probe's profile as

$$x(\rho, \rho_0) = \begin{cases} \frac{L}{2} - \int_{\rho_0}^{\rho} \mathrm{d}\omega \, \frac{1}{V_{\text{eff}}(\omega, \rho_0)}, & \left(x < \frac{L}{2}\right) \\ \frac{L}{2} + \int_{\rho_0}^{\rho} \mathrm{d}\omega \, \frac{1}{V_{\text{eff}}(\omega, \rho_0)}, & \left(x > \frac{L}{2}\right) \end{cases} \tag{4.1.4}$$

where angular separation L at the boundary between the two end-points of the probe in the x

direction is given by

$$L(\rho_0,\rho_U)=2\int_{\rho_0}^{\rho_U}\mathrm{d}\rho\,\frac{1}{V_{\rm eff}(\rho,\rho_0)}=2\int_{\rho_0}^{\rho_U}\mathrm{d}\rho\,\frac{G(\rho)}{F(\rho)}\frac{1}{\sqrt{\frac{F^2(\rho)}{F^2(\rho_0)}-1}}. \tag{4.1.5}$$

The total energy of the configuration is given by

$$E(\rho_0,\rho_U)=2\int_{\rho_0}^{\rho_U}\mathrm{d}\rho\,\frac{\mathrm{d}E}{\mathrm{d}\rho}=2\int_{\rho_0}^{\rho_U}\mathrm{d}\rho\,\frac{F(\rho)G(\rho)}{F(\rho_0)}\frac{1}{\sqrt{\frac{F^2(\rho)}{F^2(\rho_0)}-1}}, \tag{4.1.6}$$

which is obtained by replacing the classical solutions, with $\sigma=\rho$, into the action. In general there will be a UV divergence and thus we shall use a UV cutoff ρ_U, but bear in mind that physical results are expected to be independent of this. * We shall refer to configurations which are U-shaped as *connected* throughout.

In general $L(\rho_0)$ does not have to be a monotonic function (as will occur often in what follows), and as such we can have different solutions (parametrised by the value of ρ_0) which have the same separation L, but different values of E.

As we are interested in holography, information about the field theory is encoded in the boundary values of the relevant functions, which probe the bulk geometry, and these can be thought of as 'control parameters', which specify the boundary conditions for the appropriate bulk equations of motion. There are occasions, as mentioned above, where there are a number of different bulk configurations for the same value of the control parameter (with the same boundary conditions). In this case, we must evaluate the actions of the various classical configurations, for a given value of the control parameter, and keep only the one with the minimal action. The other solutions are often metastable, or unstable configurations. We shall, with a slight abuse of language, refer to the minimal action configurations as *stable*, and to any others (if they exist) as *unstable*.

We can ask about the perturbative stability of these classical solutions through the presence of tachyons, or lack thereof, in the spectrum of fluctuations. Note that being the minimal action solution does not mean that the spectrum of fluctuations is free of tachyons. Further, if we have a non-minimal action configuration, there is a possibility it could still be physically realised as a metastable state.

A quantity that will play an important role in our understanding of the perturbative stability

*The presence of a boundary in the space means we should add a boundary term to the action. We do not write it explicitly, but we use it implicitly to remove a divergence in the energy of the configurations.

of our configurations is given by

$$\mathcal{Z}(\rho) \equiv \partial_\rho \left(\frac{G(\rho)}{\partial_\rho F(\rho)} \right), \tag{4.1.7}$$

A derivation of this function and an explanation of its ability for diagnosing instabilities is presented in Appendix. B.1. We now define a set of necessary conditions on the above functions such that a U-shaped embedding exists.

- The function $F(\rho)$ must be positive definite and monotonically increasing for $\rho > \rho_\Lambda$. The reason for this is visible from the definitions Eq. 4.1.4 and Eq. 4.1.5. If $F(\rho)$ is not monotonically increasing then there will be values of ρ_0 such that $V_{\text{eff}}^2 < 0$. This can happen in the presence of singular behaviour in the background geometry. In this case, there are no classical embedding solutions for the probe that will reach the end-of-space, and instead the embeddings extend down to a minimum value ρ_{min}, such that $F(\rho)$ is monotonically increasing for $\rho > \rho_{\text{min}}$.

- The effective potential must be such that $\lim_{\rho \to +\infty} V_{\text{eff}} = +\infty$ which means the relevant boundary conditions will be satisfied. This condition is what allows us to make a comparison between the asymptotic separation and a field theoretic quantity. In other words one wants L to converge as $\rho_U \to \infty$.

- $\mathcal{Z} < 0$ is a sufficient condition in ensuring stability (meaning tachyonic fluctuations of the classical configuration are absent), and descends from the concavity conditions on the relevant thermodynamic potential. If $\mathcal{Z} > 0$ for every $\rho \geq 0$, then in the limit $\rho_U \to \infty$, all the U-shaped configurations are classically unstable.

The advantage of $\mathcal{Z}$ is that it is simple to compute, even in complicated backgrounds that are potentially only known semi-analytically, and if it becomes positive for some value of the radial coordinate, the embedding will be unstable in that region. Further, if $\mathcal{Z}$ is negative for all ρ then the probe is stable. It should be noted, that for more general embeddings, such as ones which have dynamics in a number of different directions, $\mathcal{Z}$ may fail to diagnose instabilities in these directions. For example, the functions F and G could depend on other internal angles, and the embedding could have instabilities along these other directions, as occurs in a number of examples studied in [94], and in these cases $\mathcal{Z}$ would fail to detect these problems.

There is a general result (see for instance [93, 97]),

$$\frac{\mathrm{d}E}{\mathrm{d}L} = F(\rho_0), \tag{4.1.8}$$

which is independent of whether we take the limit $\rho_U \to \infty$, or that E diverges in this limit and we are required to add a counterterm. This counterterm should be independent of ρ_0, and hence also independent of L. Thus we may consider $F(\rho_0)$ to be the effective tension of our probe.

Note two important things, firstly that if $\lim_{\rho_0 \to \rho_\Lambda} F(\rho_0) = 0$ then the connected configuration that reaches ρ_0 is indistinguishable from a disconnected configuration with the same value of L. We can thus compare the energies of the two different classes of solutions, and can regulate and renormalise them using the same methods. Secondly, the energy of the disconnected configuration E_0 is independent of the separation L, and this means there is a one-parameter family of disconnected configurations with the same value of E.

As the function F is positive-definite, $E(\rho_0)$ and $L(\rho_0)$ are either both increasing, or both decreasing functions. Further, as F is a monotonically increasing function, if we have two solutions which have the same L but different values of ρ_0, then it is the case that for the solution with larger ρ_0, must have a larger value of $F(\rho_0)$, and thus a larger gradient for $\mathrm{d}E/\mathrm{d}L$.

If we assume there are two different branches of connected configurations, for which we can vary ρ_0 in such a way that they approach a point (L_1, E_1) from the same side, in the (L, E)-plane, this means there exists a neighbourhood of this point where the two branches represent two different solutions for the same value of L. The solutions which have higher values of ρ_0, as argued, have a larger value of $\mathrm{d}E/\mathrm{d}L$, and hence will have lower E than solutions with smaller ρ_0, for $L < L_1$. This means, of the two branches, they will be a classical minimum. On the other hand, they will have a higher value of E for $L > L_1$, in which case the configurations with smaller ρ_0 are preferred. This will be of importance in what follows.

4.1.2 A Question of Limits

Let us now discuss a subtlety of the formalism we have set up. The parameter ρ_U is the point at which we introduce our UV cutoff, and as such we shall always choose it to be larger than any dynamical scale in the background we are studying. We should take the limit $\rho_U \to \infty$ to recover physical results. Looking at the forms of $E(\rho_0, \rho_U)$ in Eq. 4.1.6, and $L(\rho_0, \rho_U)$ in Eq. 4.1.5, we see that for large values of ρ_0 there are two possible orders in which we can take limits,

(i) first fix ρ_0, take the limit $\rho_U \to +\infty$, and then vary ρ_0

$$L_a \equiv \lim_{\rho_0 \to +\infty} \lim_{\rho_U \to +\infty} L(\rho_0, \rho_U)\,, \tag{4.1.9}$$

$$\bar{E}_a \equiv \lim_{\rho_0 \to +\infty} \lim_{\rho_U \to +\infty} \left(E(\rho_0, \rho_U) - E_0(\rho_U)\right)\,, \tag{4.1.10}$$

(ii) or, first fix the UV cutoff, study the system by varying ρ_0, and then finally take the limit $\rho_U \to \infty$

$$L_b \equiv \lim_{\rho_U \to +\infty} \lim_{\rho_0 \to +\rho_U} L(\rho_0, \rho_U) = 0\,, \tag{4.1.11}$$

$$\bar{E}_b \equiv \lim_{\rho_U \to +\infty} \lim_{\rho_0 \to +\rho_U} \left(E(\rho_0, \rho_U) - E_0(\rho_U)\right)\,. \tag{4.1.12}$$

where we have subtracted the disconnected configurations (defined in Eq. 4.1.2) to get $\bar{E}$, (in this scheme the disconnected configurations will always have vanishing energy). In many situations, these two limits commute, as often $L_a = L_b = 0$. A problem occurs when L_a is finite. There exists a number of examples where this is the case (see for instance the famous results of the D3-D7 system in [32]).

The convergence of the limits defining L_a means that if we take ρ_0 large enough, $\lim_{\rho_U \to \infty} L(\rho_0, \rho_U)$ is effectively independent of ρ_0. This is not true in the case of L_b. For ρ_0 large, L will initially tend to converge toward L_a, but when the configuration has ρ_0 close to ρ_U, then L begins to decrease such that the separation goes to zero in the limit. These short configurations exist for any value of the UV cutoff, but only probe a region of the geometry very close to the boundary. Thus these configurations are missed if we follow procedure (i) above.

It so happens that the short configurations are required to cure a pathology, namely that we would have a discontinuity in the energy as a function of the control parameter L, if we followed procedure (i). We shall see a number of examples of this in different contexts in what follows. These new short configurations are not always of interest, as they do not probe into the geometry described by F and G, and are thus not necessarily linked to the dual Field Theory. This aside, they become the minimal action solutions when $L < L_a$, inducing what we shall refer to as a bulk phase transition. For practical purposes, this indicates there is a lower bound on the L, below which the associated dynamics is dominated by cutoff effects.

Let us now see why procedure (ii) leads us to have a phase transition about L_a. Taking a large value of the UV cutoff ρ_U, we then vary ρ_0 in a region close to that corresponding to separations approaching L_a, it turns out there are two possibilities. Firstly, if $\mathrm{d}L/\mathrm{d}\rho_0 < 0$,

then nothing special happens, L_b will decrease and approach L_a, until ρ_0 becomes so close to ρ_U that the configuration becomes short, and L_b keeps decreasing monotonically. Secondly, if $\mathrm{d}L/\mathrm{d}\rho_0 > 0$ for some large ρ_0, by increasing ρ_0 the sign of this derivative will have to change, since ultimately L_b vanishes. This signals that there is a turning point in the (L_b, E_b)-plane, giving rise to two branches of solutions. As discussed earlier, in the neighbourhood close to the turning point, the derivative $\mathrm{d}E/\mathrm{d}L$ will be largest on the branch with larger ρ_0. This corresponds to the branch of the short configurations, which is favoured.

By looking at E_b it can be seen that the short solutions have a (divergent) negative $\bar{E}$ for $\rho_U \to +\infty$, and they are the minimal action configurations in the region they exist. However, this branch does not exist for $L > L_a$, but the disconnected solution exists for all L and has vanishing energy, which means that at L_a there must be a phase transition, with either the disconnected or a connected solution becoming the minimum of the energy in the physical region $L > L_a$.

To conclude, let us finally discuss why procedure (i) is sometimes problematic. This procedure leads to the same results as gained using procedure (ii) for all branches aside from the short configurations. They are suppressed when using procedure (i), and thus we may find unphysical discontinuities. This means that when computing physical observables (including the Gibbs Free Energy $\mathcal{G}$), we must first find the global minimum of the energy, only then afterwards apply subtractions, and then finally take the UV cutoff ρ_U to infinity. Following procedure (ii) ensures that $E(L)$ is always continuous, provides us with a natural bound $L > L_a$, and does not affect any phenomena occurring in the physical region above this lower bound.

4.2 Probe-D7 Brane Embeddings: The Setup

Making use of what we have discussed, we now look to embed a probe-D7 brane in the Type IIB background defined in Eq. 2.1.8, adopting the ansatz [37–39] such that the brane fills the four Minkowski directions and an internal three-manifold spanned by $\{\tilde{\theta}, \tilde{\varphi}, \psi\}$ and does not preserve any Supersymmetry. In Appendix. B.2, we discuss an alternative choice for the probe-D7 brane embedding, such that the brane fills the four Minkowski directions, but this time the internal three-manifold is spanned by $\{\theta, \varphi, \psi\}$. *

*To understand how these probes are modifying the dual field theory, we should look to the expansions of φ about the asymptotic separation $\bar{\varphi}$ in the UV, but as the backgrounds we probing have UV issues themselves (like the presence of a dimension-eight operator in the case of the wrapped D5 system), we are unlikely to find something meaningful. One thing we can learn from is the IR behaviour which should not be modified drastically by the *rotation*. The true goal would be to be able to place these probe-D7 branes in the full baryonic branch solutions, but due to the presence of non-trivial fluxes, the correct procedure is not obvious. An attempt in this

The transverse space is spanned by the remaining two-sphere whose coordinates are $0 < \theta \leq \pi$ and $0 < \varphi \leq 2\pi$. It was shown in [37] that it is consistent to assume the profile only depends on the embedding coordinate σ, and not the rest of the angles. Since in this background B_2 is trivial, the action for the probe-D7 reduces to the DBI part and we set the gauge field on the brane $\mathcal{F}_2 = 0$. We then have to solve the equations for the profile of $\rho(\sigma)$, $\varphi(\sigma)$ and $\theta(\sigma)$. Integrating the rest of the angular variables, the DBI action given by

$$S_{D7} \sim \int \mathrm{d}^8x\, e^{-\Phi} \sqrt{-\det \tilde{g}_8}, \tag{4.2.1}$$

becomes

$$S_{D7} \sim \int \mathrm{d}^4x\, \mathrm{d}\sigma \sqrt{e^{6\Phi+4g+4k}\rho'^2 + e^{6\Phi+4g+2k+2h}\left(\theta'^2 + \sin^2\theta\, \varphi'^2\right)}, \tag{4.2.2}$$

where the prime again denotes the derivative with respect to σ, and we have suppressed an overall constant. Due to the fact that the $SO(3)$ symmetry of the sphere remains unbroken, we see the problem is reduced essentially to finding geodesics on a sphere, and thus we can choose $\theta = \frac{\pi}{2}$ for convenience, as in [37, 39].

This means that after fixing the value of θ, our action falls into the class of Eq. 4.1.1, with x replaced with φ. * We shall denote the asymptotic angular separation $\bar{\varphi}$ which is equivalent to L in the general discussion.

We can thus use all the results we described in Section. 4.1, with the relevant functions taking the form

$$F^2 = e^{6\Phi+4g+2k+2h}, \qquad G^2 = e^{6\Phi+4g+4k}. \tag{4.2.3}$$

We can substitute for the background functions the equivalent form in terms of P and Q, giving

$$\begin{aligned} F^2 &= \frac{\sqrt{2}\, e^{6\phi_0} \sinh(2\rho)}{\sqrt{P'P^2 - P'Q^2}} \left(Q + P\sinh(4\rho) - Q\cosh(4\rho)\right), \\ G^2 &= 4\sqrt{2}\, P'^2 \left(Q\sinh(2\rho) - P\cosh(2\rho)\right)^2 \frac{e^{6\phi_0}\sinh(2\rho)}{\left(P'P^2 - P'Q^2\right)^{3/2}}. \end{aligned} \tag{4.2.4}$$

As discussed, an important quantity in what follows will be the value of the function F in the IR, which can be associated with the effective tension of the brane. Using the expansion given in Eq. 2.2.8, the globally regular solutions to P give

$$F_{IR} = \frac{2 \times 2^{3/4}\, e^{3\phi_0}}{h_1^{1/4}} \left(\rho + \frac{56\, N_c^2 - 60\, h_1\, N_c + 66\, h_1^2}{45 h_1^2}\, \rho^3\right) + \mathcal{O}\left(\rho^5\right), \tag{4.2.5}$$

direction was already made in [99].

*Here, there is a subtlety in that φ is a bounded coordinate, whereas x need not be.

where one can recover the CVMN solution by setting $h_1 = 2N_c$ as usual. For background with a walking IR (see Eq. 2.2.11), we find instead

$$F_{IR} = \frac{2 \times 2^{3/4}}{3^{1/4}} \frac{e^{3\phi_0}}{(c_0 \hat{k}_2)^{1/4}} \rho^{1/2} \left(1 + \frac{4}{3}\rho + \frac{3 c_0 \hat{k}_2 - 8 N_c}{6 c_0} \rho^3\right) + \mathcal{O}\left(\rho^{9/2}\right) . \tag{4.2.6}$$

In both cases it so happens that $F(0) = 0$, and thus the effective tension vanishes. This has repercussions on the types of embedding we may consider.

4.3 A Flavored Abelian Background

Here we will outline a related background to those defined in Chapter. 2. These are also solutions in Type IIB and are referred to as Abelian [68] (see discussion in Section. 3.6.1). This is because the background does not have the $SU(2)$-twisting associated with the non-Abelian solutions [18], meaning some of the background functions are not present (for instance $a(\rho) = 0$). They are the functions that are associated with the gaugino condensate, and the new solutions can be obtained by setting $\tau = 0$ in Eq. 2.2.1. The only further modification comes in the form of the dilaton, which now reads

$$e^{4\Phi} = \frac{1}{4} \frac{e^{4\phi_0} e^{4\rho}}{Y(P^2 - Q^2)}. \tag{4.3.1}$$

Now, we further modify the background by introducing flavor via N_f smeared D5 branes, using the procedure outlined in [67, 68, 100]. The background metric is the same as the ansatz in Eq. 2.1.8 and the modification is only to the functions Q, Y, and the Master Equation,

$$\begin{aligned} Y = \frac{N_f + P'}{8}, \qquad Q = \left(N_c - \frac{N_f}{2}\right)(2\rho - 1) + N_c - \frac{N_f}{2} + Q_o, \\ P'' + (P' + N_f)\left(\frac{P' + Q' + 2N_f}{P - Q} + \frac{P' - Q' + 2N_f}{P + Q} - 4\right) = 0. \end{aligned} \tag{4.3.2}$$

There is an exact solution, in the case of $N_f = 2N_c$,

$$P = \frac{9N_c}{4} + \hat{c}_+ e^{4\rho/3}, \qquad Q = \frac{3N_c}{4}, \tag{4.3.3}$$

where $\hat{c}_+ \geq 0$ is a constant [68]. * Further, an even simpler solution can be obtained if one sets $\hat{c}_+ = 0$, in which all the background functions become constant, except the dilaton (which is linear). With an abuse of language we shall term these solutions *scale invariant.*

*It should be noted that the IR end-of-space is now at $\rho \to -\infty$.

We now study this collection of solutions in Eq. 4.3.3 as an example. We do this as they will be simple enough to allow us perform some calculations analytically. Here the F and G take the form (with $N_c = 1$) ,

$$\begin{aligned} F^2 &= \frac{e^{6\rho}}{2}\sqrt{\frac{P-Q}{2(P+Q)(P'+N_f)}} \\ &= \frac{\sqrt{3}}{4}\frac{e^{6\rho}}{\sqrt{2\hat{c}_+ e^{4\rho/3}+6}}, \\ G^2 &= \frac{e^{6\rho}}{(P+Q)^2}\sqrt{\frac{(P^2-Q^2)(P'+N_f)}{2}} \\ &= \frac{e^{6\rho}}{\sqrt{6}}\frac{2\hat{c}_+ e^{4\rho/3}+3}{(\hat{c}_+ e^{4\rho/3}+3)^{3/2}}. \end{aligned} \tag{4.3.4}$$

Note that F and G are both monotonically increasing functions in ρ.

Setting $\hat{c}_+ = 0$ (corresponding to the *scale invariant* solutions), the above forms simplify to give

$$F^2 = \frac{e^{6\rho}}{4\sqrt{2}}, \qquad G^2 = \frac{e^{6\rho}}{3\sqrt{2}}, \tag{4.3.5}$$

and with this form of F and G we find

$$\begin{aligned} V_{\text{eff}}^2(\rho,\rho_0) &= \frac{3}{4}\left(e^{6(\rho-\rho_0)}-1\right), \\ \frac{\mathrm{d}E}{\mathrm{d}\rho} &= \frac{1}{2^{1/4}\sqrt{3}}\frac{e^{6\rho}}{\sqrt{e^{6\rho}-e^{6\rho_0}}}, \\ \mathcal{Z} &= 0. \end{aligned} \tag{4.3.6}$$

It is obvious that the relevant conditions on F and V_{eff} are satisfied in this case, but for $\mathcal{Z}$ it is more subtle, as this is the limiting case, i.e. it is vanishing for all ρ.

One can then perform the integrals for the asymptotic separation and the energy explicitly giving

$$\begin{aligned} \bar{\varphi}(\rho_0,\rho_U) &= \frac{4}{3\sqrt{3}}\arctan\sqrt{e^{6(\rho_U-\rho_0)}-1}, \\ E(\rho_0,\rho_U) &= \frac{2^{3/4}}{3\sqrt{3}}\sqrt{e^{6\rho_U}-e^{6\rho_0}}, \\ E_0(\rho_U) &= \frac{2^{3/4}}{3\sqrt{3}}e^{3\rho_U}. \end{aligned} \tag{4.3.7}$$

Using the procedure (i), we find notably strange behaviour, in that independent of ρ_0

$$\lim_{\rho_U \to \infty} \bar{\varphi}(\rho_0, \rho_U) = \frac{2\pi}{3\sqrt{3}} \equiv \bar{\varphi}_{\bar{a}},$$
$$\bar{E}(\rho_0, \rho_U) = E(\rho_0, \rho_U) - E_0(\rho_U) = -\frac{e^{3(\rho_0 - \rho_U)}}{2^{1/4} \times 3\sqrt{3}} + \cdots \to 0. \tag{4.3.8}$$

This means that all the connected configurations sit at one point in the $(\bar{\varphi}, \bar{E})$-plane. Adding in the disconnected configurations, which as $F(\rho) \to 0$ when we take $\rho_0 \to -\infty$, and thus for any value of $\bar{\varphi}$ there exists the disconnected configuration with the same value of $\bar{E}$ as the connected configurations.

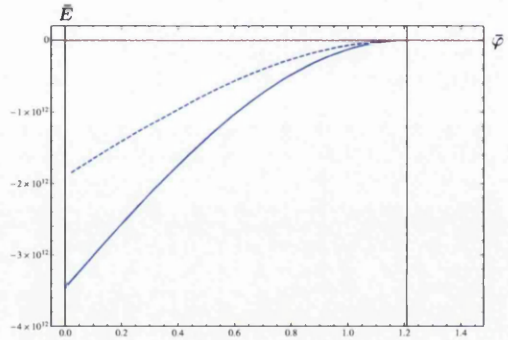

Figure 4.1: A plot of the function $\bar{E}(\bar{\varphi})$ in the scale invariant solutions of the Abelian flavored system. The disconnected configurations are shown in dashed red, alongside the connected configurations with fixed ρ_U, but varying ρ_0. The blue dashed line has $\rho_U = 9.8$, while the solid blue line has $\rho_U = 10$.

If instead we follow the procedure outlined in (ii), we obtain the new short configurations. The result is shown in Fig. 4.1. From this plot and also from the analytic calculation we can see a number of important things. The first is that, when they exist, the short configurations have a lower energy than the disconnected (and connected) configurations. Secondly, for larger values of ρ_U, the energy of the short configurations decreases. Also, at the point where the disconnected configurations and the short configurations meet (smoothly) in the $(\bar{\varphi}, \bar{E})$-plane at the point $(\bar{\varphi}_{\bar{a}}, \bar{E}_{\bar{a}})$ there is a second-order phase transition (as we shall show explicitly below). Finally, note that the short configurations have the correct concavity for stability (see discussion in Appendix. B.1 and Eq. 5.3.20).

As stated to earlier, the setup is simple enough so that we can solve for ρ_0 in terms of

$\bar{\varphi}(\rho_0, \rho_U)$, and then substitute this into $\bar{E}$ as follows

$$\begin{aligned}
\bar{E}(\bar{\varphi}, \rho_U) &= \frac{2^{3/4}}{3\sqrt{3}} e^{3\rho_U} \left(\sin\left(\frac{3\sqrt{3}}{4} \bar{\varphi} \right) - 1 \right), \\
\partial_{\bar{\varphi}} \bar{E}(\bar{\varphi}, \rho_U) &= \frac{1}{2^{5/4}} e^{3\rho_U} \cos\left(\frac{3\sqrt{3}}{4} \bar{\varphi} \right), \\
\partial^2_{\bar{\varphi}} \bar{E}(\bar{\varphi}, \rho_U) &= -\frac{3\sqrt{3}}{2^{1/4} \times 8} e^{3\rho_U} \sin\left(\frac{3\sqrt{3}}{4} \bar{\varphi} \right).
\end{aligned} \tag{4.3.9}$$

Thus as we take $\bar{\varphi} \to \bar{\varphi}_{\bar{a}}$, we have vanishing $\bar{E}$ and it also has a vanishing first derivative (with respect to $\bar{\varphi}$). It is only when we calculate its second derivative that we find a non-zero value and thus a discontinuity. This means we have a second-order phase transition.

We shall now consider the case in which $\hat{c}_+ \neq 0$. In the IR, the geometry reproduces the results we have just seen. In the UV, where $\hat{c}_+$ has a dominant effect, new behaviour appears, as can be seen in Fig. 4.2. If we calculate V_{eff} and $\mathcal{Z}$ in the solution defined by Eq. 4.3.3 (setting $\hat{c}_+ = 1$) we see that $V_{\text{eff}} \to \infty$ for $\rho \to \infty$, but $\mathcal{Z}$ is positive for all ρ. Thus the connected configurations are classically unstable for all ρ_0.

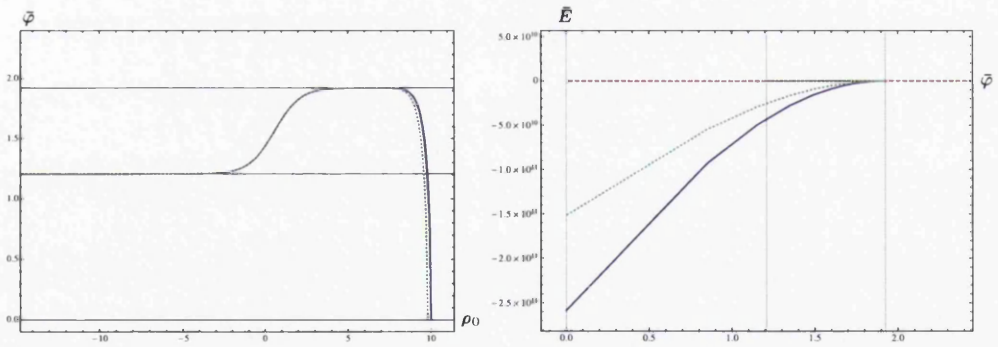

Figure 4.2: Plots of the functions $\bar{\varphi}(\rho_0)$ on the left, and $\bar{E}(\bar{\varphi})$ on the right, for Abelian flavored solution with $c_+ = N_c = 1$. The purple line represents the connected configurations with $\rho_U = 10$, the green are the connected configurations with $\rho_U = \frac{98}{10}$, and the red dashed line represents the disconnected configurations. The two grid lines represent the two asymptotic values of $\bar{\varphi} = \frac{2\pi}{3\sqrt{3}}$ and $\bar{\varphi} = \frac{\sqrt{6}\pi}{4}$.

So again, if we look at the connected configurations, and apply procedure (i), we find a branch which has $\bar{E} > 0$ for all values of ρ_0. This leads to two quite puzzling things, the first being that all of these solutions are unstable, and the second that they only exist over a restricted range i.e. $\frac{2\pi}{3\sqrt{3}} < \bar{\varphi} < \frac{\sqrt{6}\pi}{4}$. The presence of the lower bound is easily explained

through the fact that the IR of the geometry is very similar to that of the case with $\hat{c}_+ = 0$. In the UV, we find the new bound is due to the presence of the exponentially growing term. If we approximate the geometry by setting $Q = N_f = 0$ and $P = e^{4\rho/3}$, we find that

$$\bar{\varphi}(\rho_0, \rho_U) = \sqrt{\frac{3}{2}} \arctan \sqrt{e^{\frac{16}{3}(\rho_U - \rho_0)} - 1}\,, \tag{4.3.10}$$

which for large values of ρ_U converges to the upper bound $\frac{\sqrt{6}\pi}{4}$.

So instead, using procedure (ii), we find a new branch of short configurations which exist for $\bar{\varphi} < \frac{\sqrt{6}\pi}{4}$ which are energetically preferred when they exist. This can be seen in Fig. 4.2, and further noted again that the short configurations are more dominant for larger values of the UV cutoff ρ_U.

In this case, the transition is first-order, and also the connected solutions have energy differing from the disconnected configurations, unlike the *scale invariant* case. The connected configurations always have energy greater than both the short and the disconnected configurations. In this case, we conclude that this phase transition is associated with a bound on the values of $\bar{\varphi}$. Further, the disconnected configuration is always preferred for $\bar{\varphi} > \frac{\sqrt{6}}{4}$, and thus this setup cannot be used to describe Chiral-symmetry breaking.

4.4 Probe-D7 brane Embeddings in the Wrapped D5 System

4.4.1 Solutions with Linear P

Let us now focus on the solutions where P is linear in the UV. As already discussed, these are a one-parameter class of solutions to Eq. 2.2.2, parametrised by ρ_*, at which scale the behaviour of P changes from approximately constant (for small ρ), to approximately linear (for large ρ). This can be seen in the left plot of Fig. 4.3, where the three curves correspond to the CVMN background Eq. 2.2.5, and two other walking solutions with $\rho_* \simeq 3$ and $\rho_* \simeq 6$. In the right-hand plot of Fig. 4.3, we have plotted M_1, the function associated with the baryonic VEV Eq. 3.3.1. This is suppressed in the region below ρ_* (with respect to the CVMN case), because the $\mathbb{Z}_2$ symmetry between the two S^2 of $T^{1,1}$ is partially restored, due to the presence of a VEV for a dimension-six operator.

The stability analysis introduced in Section. 4.1.1 tells us that in the case of the CVMN background, as $\mathcal{Z} \leq 0$ for all ρ (as can be seen in the right-hand plot of Fig. 4.4), the embedding

we are considering is stable, in the sense that we do not expect tachyonic excitations to exist. In this case, for every possible $\bar{\varphi}$ there is a unique value of ρ_0 such that the U-shaped embedding of the probe-D7 brane exists (and satisfies the correct boundary conditions).

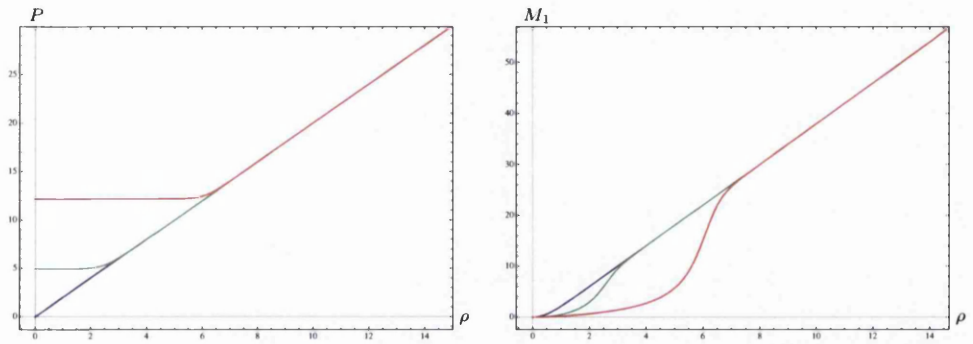

Figure 4.3: Plots of the functions $P(\rho)$ on the left, and $M_1(\rho)$ on the right, for three examples of backgrounds with linear P at large ρ. The purple line represents the special CVMN solution, the green is a related walking solution with $\rho_* \simeq 3$ and the red line is a related walking solution with $\rho_* \simeq 6$.

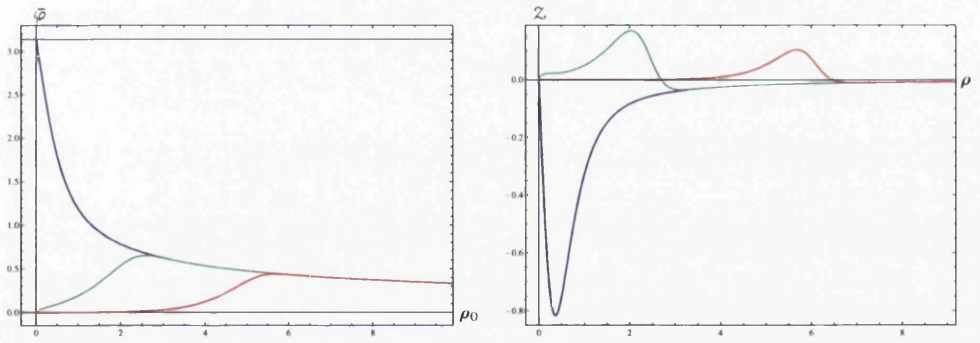

Figure 4.4: Plots of the functions $\bar{\varphi}(\rho_0)$ on the left, and $\mathcal{Z}(\rho)$ on the right, for three examples of backgrounds with linear P at large ρ. The purple line represents the special CVMN solution, the green is a related walking solution with $\rho_* \simeq 3$ and the red line is a related walking solution with $\rho_* \simeq 6$.

Turning our attention to the walking solutions, we see that in this case there is a region (for $\rho \lesssim \rho_*$) in which $\mathcal{Z}$ is positive and thus we would expect the embeddings which probe this region to be perturbatively unstable. This is corroborated by the fact that in the left-hand plot of Fig. 4.4, we see there are different values of ρ_0 with the same $\bar{\varphi}$, and thus we expect to find

the lower energy one is classically preferred. Further, any finite choice of the scale ρ_* leads to a maximum value for $\bar{\varphi}_m < \pi$, above which the connected configurations do not exist.

It is illustrative to look at how the shape of the embedding changes in the (ρ, ϕ)-plane. This is shown for a range of values of ρ_0 in Fig. 4.5. The CVMN case is is shown in the left-hand plot and is such that embeddings which only probe the UV of the space have smaller values for $\bar{\varphi}$ than those which probe down to the IR of the space, with the antipodal configuration reaching down the the end-of-space (with $\bar{\varphi} = \pi$). This is similar to the behaviour seen in the Sakai-Sugimoto case [33]. However, there is a difference, in that the transverse S^2 is of finite size at the IR end-of-space, so the antipodal configuration has an arc which sits along the equator of the sphere at $\rho = 0$. This will be important in the following discussion. The main point to take away is that all of the embeddings within the CVMN background appear stable and smooth.

When the scale ρ_* is introduced, the behaviour of the embeddings changes. Examples of various embeddings in such a background (with $\rho_* \simeq 3$) are shown in the right-hand panel of Fig. 4.5. For embeddings in which the turning point is much larger than the scale ρ_* there is little difference in the behaviour to that of the CVMN case just discussed. It is only when the embeddings probe deeper into the space than ρ_* that we see a significant change. As the probing depth ρ_0 increases further, the separation $\bar{\varphi}$ decreases. A similar property occurred in the study of Wilson Loops in the same backgrounds in [97]. Unlike the Wilson Loop, in the limit $\rho_0 \to 0$, the embedding profile degenerates into a cusp, effectively becoming two straight lines lying on top of each other in the (ρ, ϕ)-plane. The UV angular separation also vanishes in this limit.

Since the effective tension $F(\rho_0)$ is vanishing at the end-of-space Eq. 4.2.5, it is prudent for us to compare the energy of the connected with the disconnected configurations. Our connected configurations deform continuously as they move to smaller ρ_0 effectively becoming two independent branes in the limit. Thus we compare to the energy of the disconnected branes E_0 defined in Eq. 4.1.2. The vanishing of the effective tension at the IR end-of-space is a signal that (at least part of) the compact space which the branes are wrapping effectively collapses. *We stress that this comparison is only allowed due to the fact that the energy of a single U-shaped configuration degenerates into a special case of two disconnected branes allowing us to fix an additive overall constant that would remain undetermined otherwise.* *

*See the critical discussions in [96] in which the exchange of bulk supergravity modes between disconnected objects are considered, the famous result of [95] showing that in particular cases non-perturbative effects are captured by special cases of connected configurations of extended objects, and an example of these special

As the energy of the disconnected configuration is independent of the separation $\bar{\varphi}$ the two separate branches do not see each other. Thus we can interpret the disconnected configurations as chiral-symmetry preserving, whereas the connected configurations are Chiral-symmetry breaking. We must consider all the possible configurations, and find the minimal energy configuration, as this is the one that will be realised in practice. This is by analogy with the thermodynamic curve for $\mathcal{G}(p)$ (see discussion in Appendix. B.1).

Looking at the right-hand plot of Fig.4.6, we can see that there is another interesting value for $\bar{\varphi}$, which is the point at which the disconnected configuration crosses the connected one. We shall call this point $\bar{\varphi}_c$ from now on. Thus, for $0 \leq \bar{\varphi} < \bar{\varphi}_c$ there are three possible choices for the classical solution. The minimal solution is the branch which is similar to the CVMN behaviour and thus has a large value of $\rho_0 > \rho_*$. The other connected configuration, which has a value for the turning point $\rho_0 < \rho_*$ is a maximum of $\bar{E}$, which explains its tachyonic nature. The disconnected configurations sit at an $\bar{E}$ in between these two connected configurations.

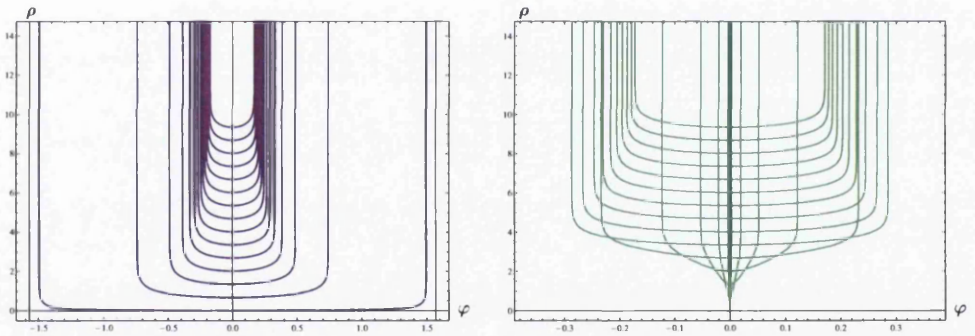

Figure 4.5: Plots of the U-shaped embeddings in two examples of the backgrounds from Fig. 4.3 in the (φ, ρ)-plane, for various values of ρ_0. The purple lines represent the special CVMN solution and the green lines are a related walking solution with $\rho_* \simeq 3$.

Moving to the region $\bar{\varphi}_c < \bar{\varphi} < \bar{\varphi}_m$, the disconnected solution becomes the minimal solution, and the two branches of the connected configuration have larger energy. Thus we have a first-order phase transition occurring at $\bar{\varphi}_c$. For values of $\bar{\varphi} < \bar{\varphi}_c$ we have a system which prefers a Chiral-symmetry breaking phase, whereas for $\bar{\varphi} > \bar{\varphi}_c$ we have a Chiral-symmetry restored phase preferred. Finally, as already discussed, above $\bar{\varphi}_m$, only the disconnected solution exists. The discontinuity in the derivative of $\bar{E}(\bar{\varphi})$ (when looking at only the minimal energy configurations) is analogous to the first-order gas/liquid phase transition of the Van der Waals gas, seen in $\mathcal{G}(p)$.

configurations is presented in [98] in the background sometimes referred to as QCD_3.

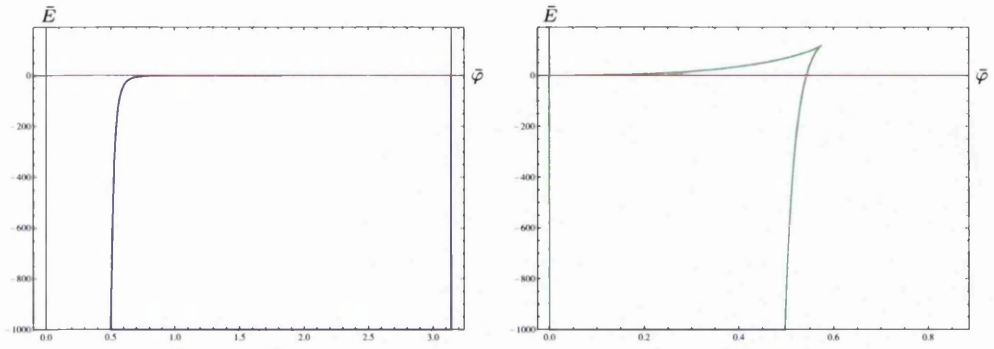

Figure 4.6: Plots of the functions $\bar{E}(\bar{\varphi})$ on the left in the CVMN background, and $\bar{E}(\bar{\varphi})$ on the right in the walking background with $\rho_* \simeq 3$. The red dotted line in both plots represents the disconnected configurations. The plots are zoomed in such that one can see $\bar{\varphi}_c$ and $\bar{\varphi}_m$ in the right-hand plot more clearly.

Before concluding this section it should be noted how this relates to the geometric properties of the backgrounds at hand. In the CVMN case, the manifold wrapped by the probe-D7 branes (spanning $\tilde{\theta}$, $\bar{\varphi}$ and ψ) is a round sphere [20], and this carries through to any background which has a region for which P behaves linearly. Regions which are not linear, lead to a squashing of the S^3 and it seems from what we have seen so far, that this squashing is associated with instabilities in the U-shaped configurations. It should also be noted that in the CVMN background, the quantity M_1 (in Eq. 3.3.1) grows without bound. This corresponds to the largest breaking of the $\mathbb{Z}_2$ symmetry between the two S^2. As mentioned earlier, the walking region corresponds to a region in which this symmetry is being recovered, and this is the region where instabilities arise.

We conclude that, backgrounds with UV asymptotics like that of the CVMN background, there exist stable configurations for all values of $\bar{\varphi} \leq \pi$. There is a first-order phase transition in any backgrounds in which the scale ρ_* is present, and it occurs at the value $\bar{\varphi}_c$ which decreases for larger values of ρ_*. This phenomenon can be thought of as the formation of a symmetry-breaking condensate or the presence of an explicit symmetry-breaking deformation. This condensate then only forms in the presence of a large enough source for the symmetry breaking (such that $\bar{\varphi} < \bar{\varphi}_c$) in the walking backgrounds, whereas it is always present for the CVMN backgrounds.

4.4.2 Solutions with Exponential P

Here we shall discuss the globally regular solutions (such that $P \to 0$ in the IR and thus $c_0 = 0$ as in Eq. 2.2.8), which again form a one-parameter family, with the scale this time being set by $\bar{\rho}$, which is the scale at which the behaviour of P changes from linear for $\rho < \bar{\rho}$, to exponential for $\rho < \bar{\rho}$. The UV parameter c_+ (see Eq. 2.2.14) controls the scale $\bar{\rho}$, and as discussed this is the scale below which the associated dimension-two (baryonic) VEV is important. An example of a background in this class is presented in Fig. 4.7, with $\bar{\rho} \simeq 3$ (which is obtained using $h_1 = 2.0044$). Here the relevant conditions for F and V_{eff} are satisfied, but the function $\mathcal{Z}$ is positive for $\rho > \bar{\rho}$, so we expect the connected configurations to be unstable in this region.

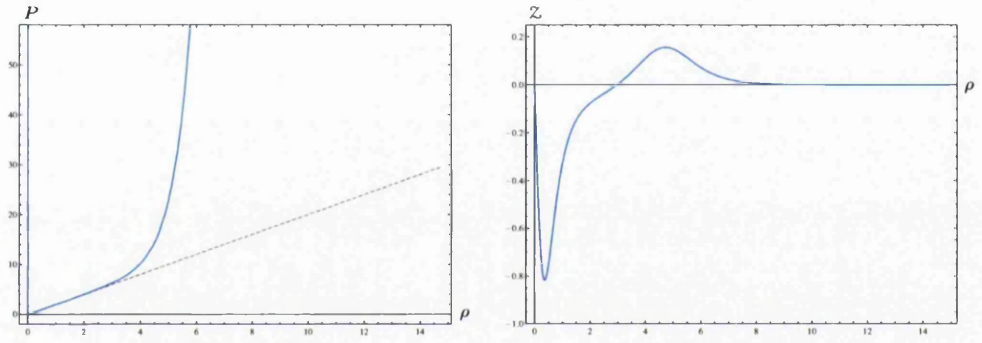

Figure 4.7: Plots of the functions $P(\rho)$ on the left, and $\mathcal{Z}(\rho)$ on the right, for a solution with $\bar{\rho} \simeq 3$. The grey dashed line represents the special CVMN solution for comparison.

In the IR, we find that the behaviour is the same as that of the CVMN case, such that at $\rho_0 \to 0$, we find again $\bar{\varphi} \to \pi$. Further, as can be seen in Fig. 4.8, in this limit $\bar{E} \to 0$. Again, at the IR end-of-space, we find that the effective tension $F(0) = 0$, meaning that the connected configurations approach the disconnected configurations from below (in the $(\bar{\varphi}, \bar{E})$-plane). As such they are the stable configurations, for small $\rho_0 < \bar{\rho}$, with the correct concavity.

In each of the three plots in Fig. 4.8, showing the $(\bar{\varphi}, \bar{E})$-plane (the top-left and the bottom row), we can see the four branches present, and the details of their behaviour. As discussed, the branch meeting the antipodal configuration $\bar{\varphi} \to \pi$, which exists for $\bar{\varphi} > \bar{\varphi}_1$, the minimum value which depends on $\bar{\rho}$, can be best seen in the bottom-right plot of Fig. 4.8 (from the plot $\bar{\varphi}_1 \simeq 0.75$). If one looks at the plot in the bottom-left, one can see the presence of an unstable second branch, with the wrong concavity, and corresponding to connected configurations which have $\rho_0 > \bar{\rho}$. The configurations on this branch have a larger value of $\bar{E}$ than those of the

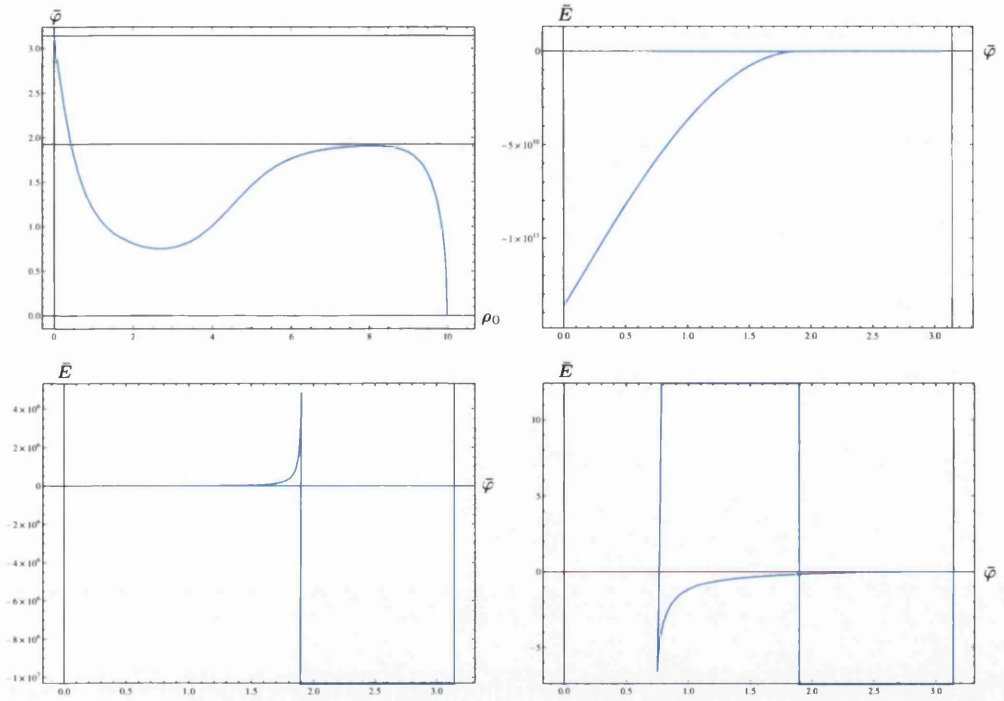

Figure 4.8: Plots of the functions $\bar{\varphi}(\rho_0)$, and $\bar{E}(\bar{\varphi})$, for a solution with $\bar{\rho} \simeq 3$. The solid blue lines have $\rho_U = 10$, the red dashed line is the disconnected configuration, and each of the three $\bar{E}(\bar{\varphi})$-plots are zoomed in to show a different branch more clearly.

CVMN-like IR branch, and are restricted to only take values $\bar{\varphi}_1 < \bar{\varphi} < \bar{\varphi}_a = \frac{\sqrt{6}\pi}{4}$. There is also a third set of solutions given by the disconnected configurations.

We now turn our attention to the fourth branch of configurations. If only the three discussed so far had existed (which is what occurs when one follows procedure (i)) then we would be faced with the following problem. If we want to interpret the minimal solutions in $\bar{E}$ as the free energy $\mathcal{G}$, then we would be left with a discontinuity in $\mathcal{G}$ as a function of the separation $\bar{\varphi}$. Thus in this case we would end with some results which do not make any sense. Instead, using procedure (ii), we have the fourth branch of configurations which are close to the UV-cutoff. These configurations can be seen in the top-left plot of Fig. 4.8, and correspond to the branch which joins the UV separation $\bar{\varphi}_a$ to zero, on the right-hand side of the plot. This is the fourth branch which is visible in the top-right plot of the same figure, and corresponds to the minimal configuration for $\bar{E}$ over the region that they exist i.e. $\bar{\varphi} < \bar{\varphi}_a$. Further note that they have the correct concavity for stability, and have a very large gradient in the $(\bar{\varphi}, \bar{E})$-plane, which

actually diverges in the limit $\rho_U \to \infty$.

It is important to note that, for any choice of the scale $\bar{\rho}$, the minimum point of the connected configurations $\bar{\varphi}_1$ in the $(\bar{\varphi}, \bar{E})$-plane is always smaller than the UV asymptotic value $\bar{\varphi}_a$. This is very important as it tells us that $\bar{E}$ is always continuous. The value of $\bar{\varphi}_1$ is dictated by the value of $\bar{\rho}$ (or equivalently h_1). In the small h_1/large $\bar{\rho}$ limit, the value of $\bar{\varphi}_1 \to 0$ and thus we recover the CVMN case. In the opposite limit (for large h_1/small $\bar{\rho}$) we find $\bar{\varphi}_1 \to \bar{\varphi}_a$. In the second case, the limit corresponds to a suppression of the dimension-two VEV, and we recover (after *rotation*) the Klebanov-Strassler background [20, 62]. It can be checked numerically that $\bar{\varphi}_1 < \bar{\varphi}_a$ for very large values of $h_1 \simeq 10^5$, because any configurations with $\rho_0 > \bar{\rho}$ will still have $\frac{\mathrm{d}\bar{E}}{\mathrm{d}\bar{\varphi}} > 0$, and for this to occur we must have $\bar{\varphi}_1 < \bar{\varphi}_a$.

At the value $\bar{\varphi}_a$, we thus conclude that a first-order bulk phase transition takes place. For values of $\bar{\varphi}$ larger than $\bar{\varphi}_a$, we have long connected configurations with $\rho_0 < \bar{\rho}$, which are the minimal solutions. Below $\bar{\varphi}_a$, we must appeal to the short configurations, and these do not probe the bulk of the geometry. This leads us to describe this type of transition as a physical bound on $\bar{\varphi}$ and that for values of $\bar{\varphi} < \bar{\varphi}_a$ it is not possible to interpret the results in terms of the dual field theory.

4.4.3 Walking Solutions with Exponential P

Here, we shall look at the backgrounds originally considered in [87], for which the probe-D7 brane embeddings have been shown to be classically unstable [88]. These are solutions such that P at no point resembles the CVMN solution, and thus we will see a combination of the behaviour studied in the previous two sections playing an important role.

An example of a solution in this class is shown in Fig. 4.9, with P in the left-hand plot, which is approximately constant for $\rho < \rho_*$, and exponential for $\rho > \rho_*$. In the right-hand plot, we plot the function $\mathcal{Z}$, and it is positive definite in this case, which we associate with a classical instability. This is in line with the discovery of a tachyon in the computation of the fluctuations of these particular embeddings [88].

From the left-hand plot in Fig. 4.10 it can be seen that the value of $\bar{\varphi}$ is a monotonically decreasing function of ρ_0, for $\rho_0 < 8$. This is ultimately the reason for the instability found. Further, from the right-hand plot, it can be seen that the disconnected configurations have a lower value of $\bar{E}$ than the connected configurations for all choices of $\bar{\varphi}$. We find that, for $\bar{\varphi} < \bar{\varphi}_a$, the third branch (associated with the solutions which are close to the UV-cutoff), is energetically favoured. From a geometrical point of view, backgrounds of this form approximately recover the

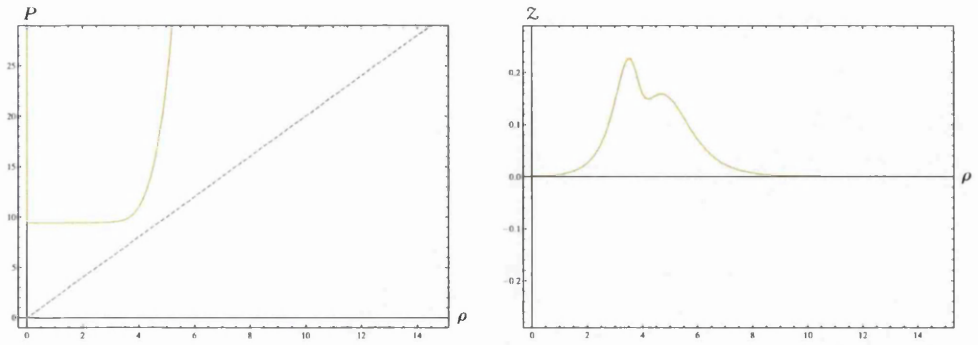

Figure 4.9: Plots of the functions $P(\rho)$ on the left, and $\mathcal{Z}(\rho)$ on the right, for a solution with $\rho_* \simeq 3$ and exponential asymptotics. The grey dashed line represents the special CVMN solution for comparison.

$\mathbb{Z}_2$-symmetry between the two S^2 in the internal geometry, and considering what we discussed when P had linear UV asymptotics it is likely that this is the source of the instability.

In conclusion, we have a first-order bulk phase transition at $\bar{\varphi}_c = \bar{\varphi}_a$ between the disconnected configurations and the short configurations. If we again interpret these short configurations as a physical bound, we can conclude that in this background one cannot realise Chiral-symmetry breaking, since only the Chiral-symmetry restoring disconnected configurations are physical.

We now consider backgrounds in which we have a non-vanishing P in the IR, behave exponentially as $P \simeq e^{4\rho/3}$ in the far UV , and also an intermediate region where P is approximately linear (as in the CVMN case). In the left-hand plot of Fig. 4.11 we show an example of P for a background in this class. There are now two physical scales which we can manipulate, the scale ρ_* below which P is approximately constant and $\bar{\rho}$ above which P is exponentially growing. There is a third fixed scale set by the IR end-of-space chosen to be at $\rho_\Lambda = 0$. In the range $\rho_* < \rho < \bar{\rho}$ is the region in which P looks like the CVMN solution. In the right-hand plot of Fig. 4.11, we can see that $\mathcal{Z}$ has two places where it changes sign. One of these is in the far UV and is associated with the change of sign we saw upon the introduction of the exponential UV behaviour of P, and the other is in the IR and associated with the introduction of the constant behaviour in P. In the intermediate region $\rho_* < \rho < \bar{\rho}$, we see that $\mathcal{Z}$ approximately follows the CVMN solution ($\mathcal{Z} < 0$). We can associate the zeros of $\mathcal{Z}$ with the two scales, i.e. $\rho_* \simeq 0.2$ and $\bar{\rho} \simeq 3$.

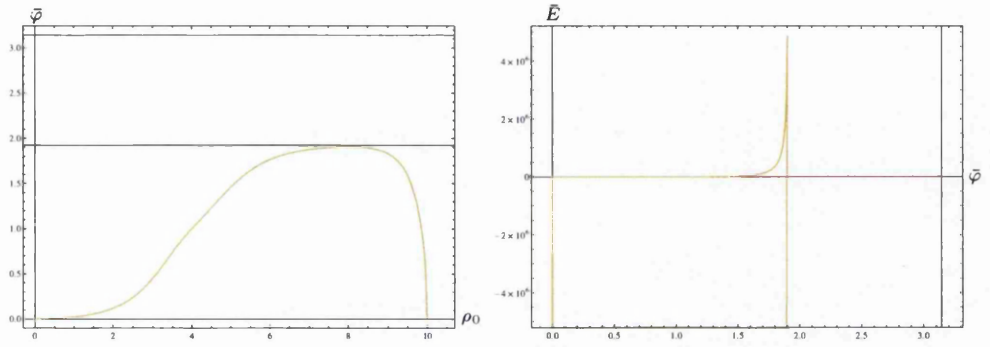

Figure 4.10: Plots of the functions $\bar{\varphi}(\rho_0)$, and $\bar{E}(\bar{\varphi})$, for a solution with $\rho_* \simeq 3$ and exponential asymptotics. The solid yellow lines have $\rho_U = 10$ and the red dashed line is the disconnected configuration.

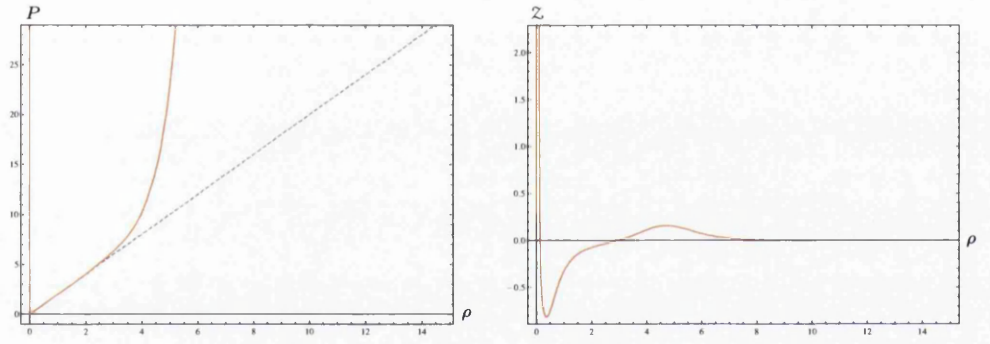

Figure 4.11: Plots of the functions $P(\rho)$ on the left, and $\mathcal{Z}(\rho)$ on the right, for a solution with $\rho_* \simeq 0.2$ and $\bar{\rho} \simeq 3$. The grey dashed line represents the special CVMN solution for comparison.

In Fig. 4.12 we show the resulting plots for this background. These have been made with UV-cutoff $\rho_U = 10$. One should notice that the results are similar to the respective results previously seen, for $\rho_0 > \rho_*$ the background is of the form of those with CVMN and exponential behaviour for P discussed in Section. 4.4.3, and thus the resulting probe-D7 brane embeddings are the same. For $\rho_0 < \rho_*$, we find the same classical instability associated with this scale (it has the wrong concavity in the $(\bar{\varphi}, \bar{E})$-plane), and thus we find the introduction of a fifth branch to the four seen in Section. 4.4.3.

We now have a more complex structure of phase transitions than before. The configurations close to the UV-cutoff are the minimal solutions for $\bar{\varphi} < \bar{\varphi}_a$, and increasing $\bar{\varphi}$ we find a first-order bulk phase transition, such that between $\bar{\varphi}_a < \bar{\varphi} < \bar{\varphi}_c$ the connected configurations replace

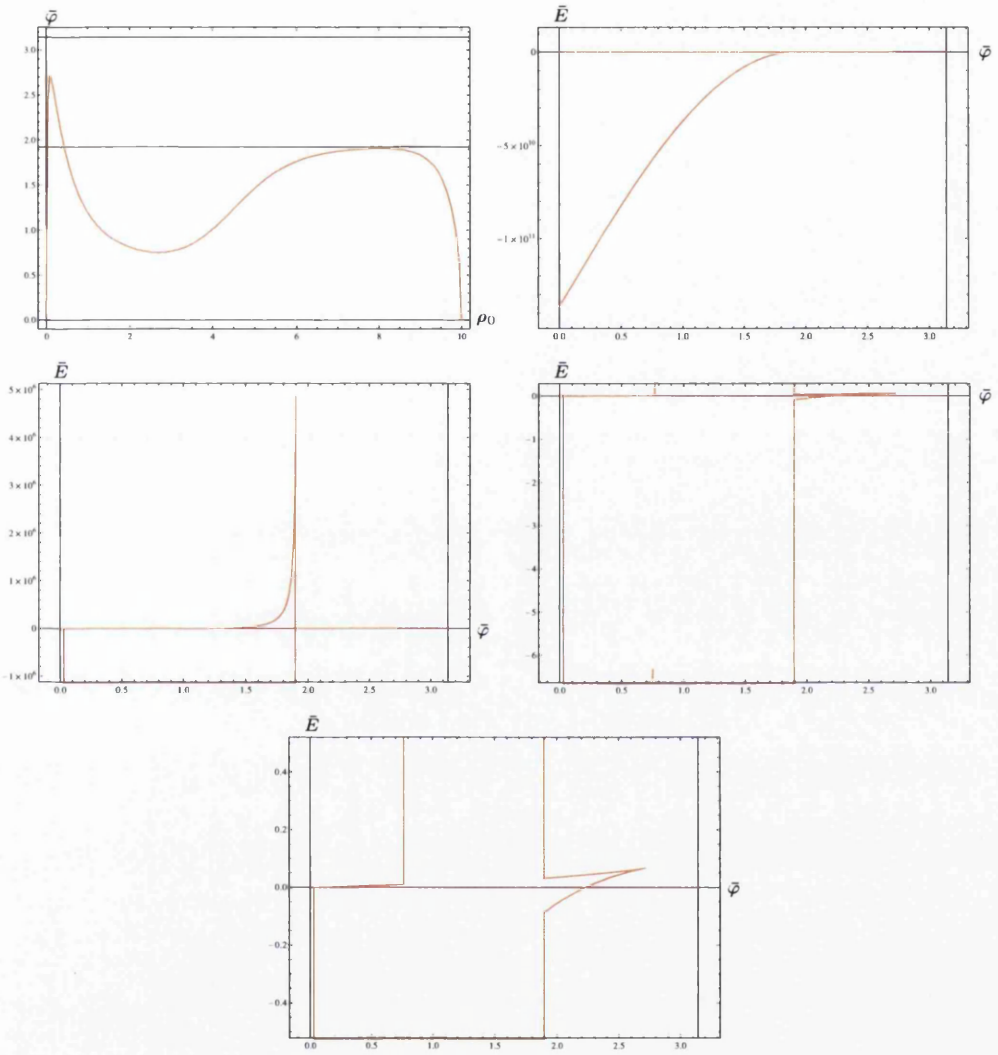

Figure 4.12: Plots of the functions $\bar{\varphi}(\rho_0)$, and $\bar{E}(\bar{\varphi})$, for a solution with $\rho_* \simeq 0.2$ and $\bar{\rho} \simeq 3$. The solid orange lines have $\rho_U = 10$, the red dashed line is the disconnected configuration, and each of the four $\bar{E}(\bar{\varphi})$-plots are zoomed to show a different branch more clearly.

them as the minimal solutions. As we have seen before upon the introduction of the scale ρ_*, this branch of connected configurations no longer reaches all the way to the antipodal configuration at $\bar{\varphi} \to \pi$, but attains a maximum, and the new fifth unstable branch of configurations is introduced. This branch has $\bar{\varphi} \to 0$ as $\rho_0 \to 0$. Thus for values of $\bar{\varphi} > \bar{\varphi}_c$ we again find that the disconnected configurations are the minimal solutions. Thus we have a physically interesting first-order phase transition between the connected and disconnected configurations at the point $\bar{\varphi}_c$.

For us to have this phase transition, we must keep the value of ρ_* small, irrespective of the size of $\bar{\rho}$. We approximate (by inspection of the top left-hand plot in Fig. 4.12) that if $\rho_* \gtrsim 0.5$ then all the connected configurations have $\bar{\varphi} < \bar{\varphi}_a$, and so are never the preferred configurations, as this is the regime where the short configurations dominate. If $\rho_* > 0.5$ the embeddings look like those of the first half of this section, such that the disconnected configuration is the minimal solution for $\bar{\varphi} > \bar{\varphi}_a$.

4.5 A Compendium of Possible Solutions

We now give an overview of all the possible solutions for the backgrounds discussed in the previous sections. The full collection is presented in Fig. 4.13 and Fig. 4.14.

These correspond to the five possible supersymmetric solutions, which we have discussed, to the wrapped D5 system (which are not badly singular). The probe-D7 branes behave differently in each case and we discuss this here in the same order they take in Fig. 4.13 and Fig. 4.14.

- In the CVMN case, there exist both disconnected and connected configurations for all values of $\bar{\varphi}$. The connected configurations (representing a broken Chiral-symmetry phase) are always preferred to the disconnected, are classically stable in the sense that they have the correct concavity in the $(\bar{\varphi}, \bar{E})$-plane, and have $\mathcal{Z} < 0$ for all ρ.

- Upon the introduction of the scale ρ_*, a new branch appears in the $(\bar{\varphi}, \bar{E})$-plane, which is associated with the IR, but beyond this scale we have the same UV behaviour as the CVMN case. This new branch is always a maximum of $\bar{E}$, is classically unstable (such that it introduces a region with $\mathcal{Z} > 0$), and is characterised by an endpoint with $\rho_0 < \rho_*$. The connected solutions for $\rho_0 > \rho_*$ have the same behaviour as the CVMN case, but have a maximum at $\bar{\varphi}_1 < \pi$, such that they exist only in the range $0 \leq \bar{\varphi} \leq \bar{\varphi}_1$. There is a first-order phase transition with a critical value $\bar{\varphi}_c$ which depends on ρ_*. For $\bar{\varphi} > \bar{\varphi}_c$, the

disconnected configurations are preferred, and Chiral-symmetry is restored. For $\bar{\varphi} < \bar{\varphi}_c$ the connected configurations are preferred, and thus we have a model for chiral-symmetry breaking.

- Alternatively, one can look at backgrounds with a different UV, such that the scale is set by $\bar{\rho}$, below which in the IR, P grows approximately like the CVMN solution (linearly), but above in the UV P grows exponentially. Here there are four branches to the solution. The disconnected configurations are never the minimal solutions of $\bar{E}$. The connected configurations again have two parts as in the previous bullet point. The first is a stable branch, which minimises $\bar{E}$ for $\bar{\varphi} > \bar{\varphi}_a = \frac{\sqrt{6}\pi}{4}$, and the second is an unstable branch that is never preferred. These branches only exist for $\bar{\varphi} > \bar{\varphi}_1$, with $\bar{\varphi}_1 < \bar{\varphi}_a$, and $\bar{\varphi}_1$ is a function of $\bar{\rho}$ (and now a minimum). The short configurations, for $\bar{\varphi} < \bar{\varphi}_a$, are the dynamically preferred solutions. We say that at $\bar{\varphi}_a$ there is a bulk phase transition. Thus the broken Chiral-symmetry (associated with the connected solutions) is the physical one connected to the field theory.

- We have P such that, the walking scale ρ_* dictates the IR behaviour, but P grows exponentially for $\rho > \rho_*$ in the UV. In this case there are only three branches of configurations. The connected configurations exist for $\bar{\varphi} < \bar{\varphi}_a$, and are classically unstable so never preferred. The short configurations, which exist for $\bar{\varphi} < \bar{\varphi}_a$, are the dominant solutions in this region and are classically stable. Further, they have negative (divergent) $\bar{E}$, and at $\bar{\varphi}_a$ there is a first-order (bulk) phase transition, such that for larger values of $\bar{\varphi} > \bar{\varphi}_a$ the disconnected configurations are preferred. The disconnected solutions are in the Chiral-symmetry restored phase, and below $\bar{\varphi}_a$ the system is not related to the field theory.

- Finally, we can have backgrounds which have the two scales separated, such that P is like the CVMN solution (linear) for some intermediate region $\rho_* < \rho < \bar{\rho}$. For $\rho < \rho_*$, P is approximately constant, and for $\rho > \bar{\rho}$, P is exponentially growing. These solutions are the most complicated and have five branches in the $(\bar{\varphi}, \bar{E})$-plane. Below $\bar{\varphi}_a$ the gravity is not related to the field theory as there is a bulk phase transition at $\bar{\varphi}_a$. If we keep ρ_* small (i.e. $\rho_* \lesssim \frac{1}{2}$) , then there is another first-order phase transition at $\bar{\varphi}_c > \bar{\varphi}_a$. For $\bar{\varphi} < \bar{\varphi}_c$, the connected configurations are preferred and thus we are in a chiral-symmetry broken phase. For $\bar{\varphi}_c < \bar{\varphi} < \pi$, the disconnected solutions are preferred and thus we are in a chiral-symmetry restored phase. If we increase the scale ρ_*, we find the point $\bar{\varphi}_c$ moves to smaller values of $\bar{\varphi}$ until it is masked by the fixed bulk transition at $\bar{\varphi}_a$ and

thus we lose our physical phase transition as in the last bullet point. In this scenario, for any $\bar{\varphi} < \bar{\varphi}_a$, the Chiral-symmetry is restored (as the disconnected solution is preferred). In the $(\bar{\varphi}, \bar{E})$-plane there are two turning points of the connected configurations at $\bar{\varphi}_1$ and $\bar{\varphi}_2$, which connect the different branches. They both appear in regions which are energetically disfavoured.

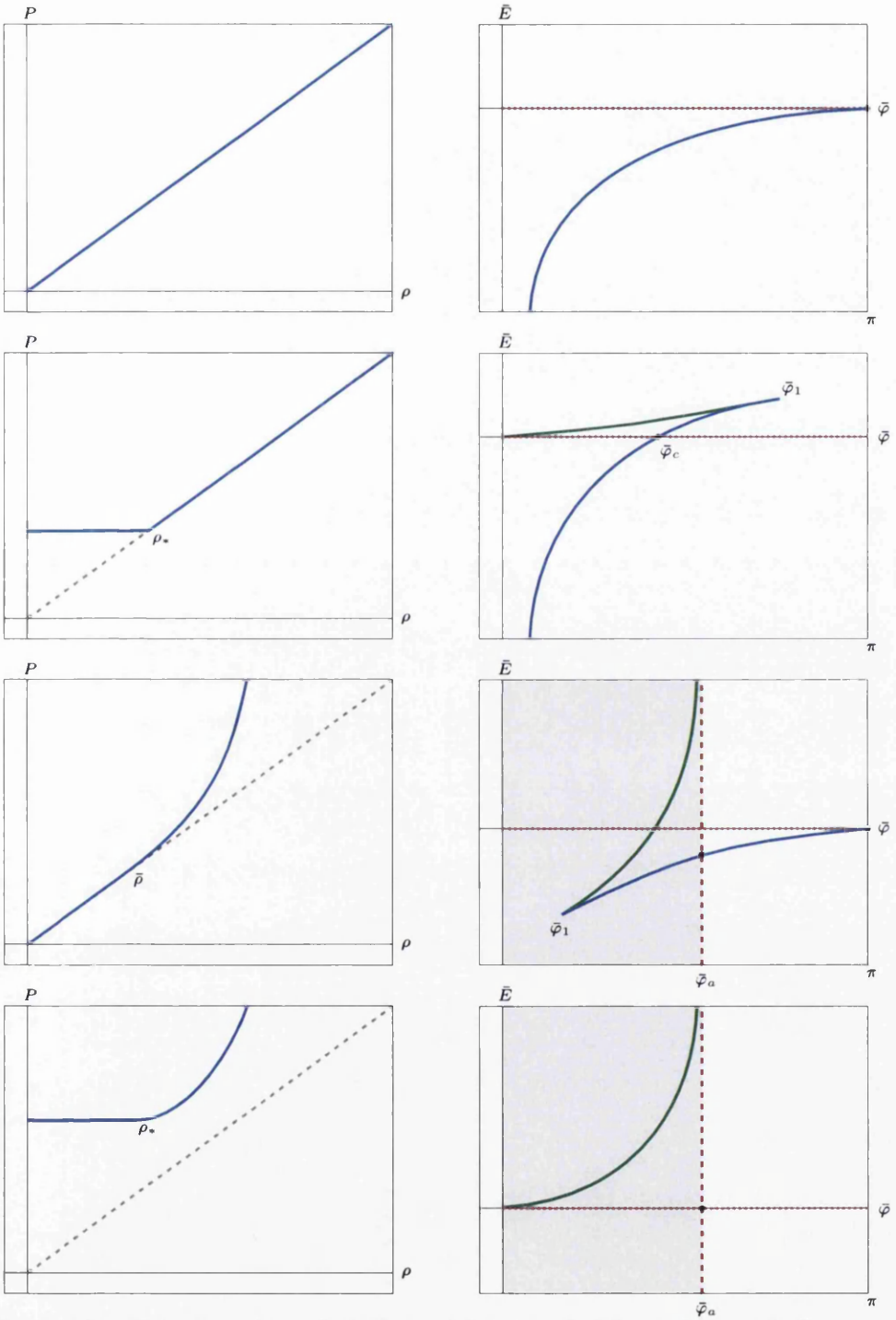

Figure 4.13: Plots of generic solutions of probe-D7 brane embeddings for all cases in the wrapped D5 system discussed. On the left-hand side we have plots of P as a function of ρ, while on the right-hand side we have $\bar{E}$ as a function of $\bar{\varphi}$ in the corresponding backgrounds. The connected configurations are given in solid blue (stable) and green (unstable), the disconnected configurations given by dotted red, and the short configurations in dashed red lines. The physically realised configurations are those with the lowest $\bar{E}$ for a particular value of $\bar{\varphi}$. We argue that the grey shaded region, to the left of the short configurations, is disconnected from the continuum limit, such that these results do not have an obvious interpretation in terms of the dual field theory.

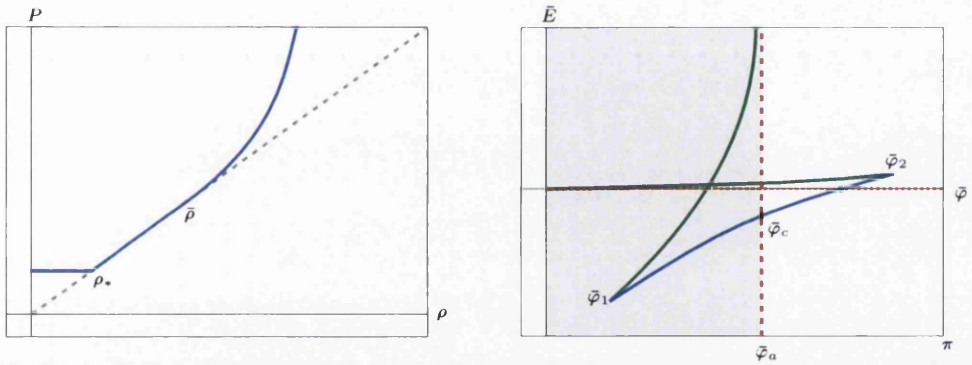

Figure 4.14: A continuation of the plots of of generic solutions of probe-D7 brane embeddings for all cases in the wrapped D5 system discussed. These have the same colouring as in Fig. 4.13.

Chapter 5

Holographic Entanglement Entropy and Confinement

In this Chapter (mainly based on the work in [5]), we shall study the calculation of (holographic) Entanglement Entropy in models which admit confinement, and explore the idea that in the case where the entangling region is described by an infinite strip, there is always a first-order phase transition in the Entanglement Entropy of such models, as proposed in [48]. We shall discuss similarities and differences, between this calculation and that of the Rectangular Wilson Loop [101] (from a holographic perspective), using some of the general formalism proposed in Section. 4.1. Also, we will derive a set of sufficient conditions on the functions forming the background, for the Entanglement Entropy to admit such a phase transition, and then check these conditions in various cases.

Further to this, we shall be interested in the idea that the Entanglement Entropy as a diagnostic tool for confinement, has implications on the UV behaviour, as well as the IR behaviour, of the background in question. We shall argue what kind of connection we expect between confinement and the UV behaviour of the dual Quantum Field Theory. This will require us to discuss the calculation of Entanglement Entropy in Quantum Field Theories which have some non-locality, and we shall use a number of examples (involving D5 and D6 branes) to show that, in spite of the IR geometry of the background being a suitable dual to a confining Quantum Field Theory, the phase transition in the Entanglement Entropy is missing. We associate this with a UV non-locality in the Quantum Field Theory, and then propose that through the introduction of a UV cutoff (in line with the discussion in Section. 4.1.2) and the corresponding new configurations that emerge, we recover the phase transition. We then finish

by studying the Entanglement Entropy in Theory A and Theory B defined in Chapter. 2 (and some related backgrounds including sources), to see how the *rotation* procedure (as a suitable UV-completion) recovers locality in these models.

This all suggests that the Entanglement Entropy is not only a useful quantity to diagnose confinement, but further it can be used to study the question of UV locality in a Quantum Field Theory.

First, we shall present the definition of Entanglement Entropy following the discussions of [43]. A quantum mechanical system with multiple degrees of freedom, at zero temperature, is described by the pure ground state $|\Psi\rangle$ (assuming no degeneracies). The total system has a von Neumann Entropy equal to zero ($S_{\rm t} = -{\rm Tr}[\rho_{\rm t} \log \rho_{\rm t}]$), where the density matrix is given in terms of the pure state as $\rho_{\rm t} = |\Psi\rangle\langle\Psi|$. If we separate the system into two subsystems labelled A and B, then we can write the total Hilbert space $\mathcal{H}$ as a direct product of two subspaces $\mathcal{H} = \mathcal{H}_A \otimes \mathcal{H}_B$. From this we can define the reduced density matrix ρ_A associated to subsystem A as $\rho_A = {\rm Tr}_B \rho_{\rm t}$ (where the trace is over $\mathcal{H}_B$), which is what an observer will see, if they only have access to subsystem A. The von Neumann Entropy of the reduced density matrix ρ_A is thus given by

$$S_A = -{\rm Tr}[\rho_A \log \rho_A]. \tag{5.0.1}$$

and this is what is taken as the definition of the Entanglement Entropy of the subsystem A. As we are at zero temperature, the Entanglement Entropy associated to subsystem B is such that it is equal to S_A, assuming B is the complement of A. For finite temperature, this equality is no longer true.

To extend the definition of Entanglement Entropy to Quantum Field Theories, it should be considered that a Quantum Field Theory can be thought of as an infinite number of copies of a quantum mechanical system, such that the associated Hilbert space is given by all the possible field configurations as a fixed time. Thus it is true that on a given time slice, the submanifold A is defined uniquely by its boundary ∂A. Due to this dependence on the submanifold A, in the context of Quantum Field Theories, the Entanglement Entropy is sometimes known as *Geometric Entropy.*

A holographic description for calculating the Entanglement Entropy was first proposed in [46]. In the context of a $d+1$ dimensional Conformal Field Theory, dual to an AdS_{d+2} background, the holographic Entanglement Entropy is then given by minimising the d dimensional area γ_A in the dual background, whose boundary coincides with the boundary of the entangling

region, i.e. $\partial\gamma_A = \partial A$. In this setup, it was then conjectured that the entanglement entropy S_A in the $d+1$ dimensional Conformal Field Theory can be computed using the formula

$$S_A = \frac{\text{Area}(\gamma_A)}{4G_N^{(d+2)}}. \tag{5.0.2}$$

Here $G_N^{(d+2)}$ is the $(d+2)$-dimensional Newton constant of the AdS gravity theory. This quantity is generally divergent, and the leading order divergence is $\sim a^{-(d-1)}$ and is proportional to the boundary ∂A, where a is a UV cutoff introduced in the theory, and this term is what is commonly known as an *Area-Law divergence*. The original conjecture has been extended to be able to study theories which exhibit confinement [48], and this will be the subject of what follows.

Finally, we briefly discuss some ideas which motivated the proposal of the presence of a phase transition in the Entanglement Entropy of a confining theory. It was argued [48] that the phase transition present in the Entanglement Entropy in Confining Theories is reminiscent of the finite temperature deconfinement phase transition [102] in a large-N_c theory of glueballs (or in a string theory). In such a theory, the density of states grows exponentially fast. Thus, for a mass m, the number of states $N(m)$ is be given by

$$N(m) \sim m^{2b} e^{+\beta_H m}, \tag{5.0.3}$$

where β_H is the inverse Hagedorn Temperature (which sets an energy scale), and b is a number, and the thermal partition function will be roughly given by

$$Z \sim \int \mathcal{D}m\, N(m) e^{-\beta m} = \int \mathcal{D}m\, m^{2b} e^{+\beta_H m - \beta m}. \tag{5.0.4}$$

We see for temperatures higher than β_H this partition function grows rapidly, while for temperatures lower than β_H it goes to zero.

This led the authors of [48] to write the Entanglement Entropy as

$$S_A \sim \int \mathcal{D}m\, m^{2b} e^{+\beta_H m - 2mL_A}, \tag{5.0.5}$$

where they used that, for non-interacting scalar degrees of freedom (our large-N_c glueballs for instance), the Entanglement Entropy behaves as e^{-2mL_A}, where L_A is the separation of the entangled regions. In a "truly" confining Quantum Field Theory (such as Yang-Mills) we should see a similar phase transition in the Entanglement Entropy. The phase transition is

phenomenologically similar to the deconfinement phase transition discussed above. It is thus expected that for a given critical value for $L_A = L_c$, below this the Entanglement Entropy grows rapidly, but above it is constant.

5.1 Entanglement Entropy in Confining Backgrounds: A Review

To begin, let us review a number of known results that were discussed in [48]. The authors discussed a generalisation to the original Ryu-Takayanagi conjecture (see discussion around Eq. 5.0.2) for the Entanglement Entropy, which covered non-conformal theories, such as those dual to large N_c confining gauge theories. The correct generalisation [47] is given by (in String Frame)

$$S_A = \frac{1}{4G_N^{(10)}} \int_{\Sigma_8} \mathrm{d}^8\sigma\, e^{-2\Phi}\sqrt{g_8}, \tag{5.1.1}$$

where $G_N^{(10)}$ is the 10-dimensional Newton constant and g_8 is the induced metric on Σ_8. From this, we can then calculate the Entanglement Entropy, by minimising the given action in Eq. 5.1.1 with respect to all surfaces which approach the boundary of the entangling surface. In what follows we shall only consider, as the entangling surface, a strip of length L_A. In the cases studied in [48], it was found that there were two such local minima of the action. The first a *connected* surface, a U-shaped configuration whose length depends on L_A, and the second a *disconnected* surface, consisting of two lines separated by a distance L_A. *

We will work with backgrounds that in general have a metric that can be written (in the String Frame) in the following form

$$ds^2 = \alpha(\rho)\left[dx^2_{(1,d)} + \beta(\rho)\, d\rho^2\right] + g_{ij}\, dy^i dy^j, \tag{5.1.2}$$

where x^μ parametrises an $\mathbb{R}^{d+1}$, and ρ is the holographic coordinate that runs between $\rho_\Lambda \leq \rho < \infty$. The $8-d$ internal coordinates are denoted by y^i (with $i = d+2, \ldots, 9$). The background can be further imbued with a non-trivial dilaton Φ. The background may also have RR or NS fluxes present, but these will not play a role in our analysis. An important quantity in the computation of the Entanglement Entropy is the volume of the internal space (which is described by the y coordinates) and is given by $V_{int} = \int dy\sqrt{\det[g_{ij}]}$. Constructed from this,

*Here L_A plays the role of L in the general discussion in Section. 4.1.1.

we can define another quantity that will be of great importance in what follows

$$H(\rho) = e^{-4\Phi} V_{int}^2 \alpha^d. \tag{5.1.3}$$

It is worth mentioning at this point some properties of the functions $\beta(\rho)$ and $H(\rho)$ as they will be central to our calculations of the Entanglement Entropy. $H(\rho)$ includes a factor of the volume of the internal manifold, and part of this typically shrinks to zero size at $\rho = \rho_\Lambda$, as one would expect in line with the vanishing of the central charge at zero energies. Also, $H(\rho)$ is in general a monotonically increasing function of ρ in confining backgrounds. $\beta(\rho)$ on the other hand, (sometimes called a red-shift factor) can become constant or diverge at $\rho = \rho_\Lambda$, and is typically a monotonically decreasing function of ρ.

By defining the minimal value that the *connected* surface probes along the ρ direction into the bulk by ρ_0, the Entanglement Entropy is given by

$$S_c(\rho_0) = \frac{V_{d-1}}{2G_N^{(10)}} \int_{\rho_0}^{\infty} d\rho \sqrt{\frac{\beta(\rho) H(\rho)}{1 - \frac{H(\rho_0)}{H(\rho)}}}. \tag{5.1.4}$$

One can further define the Entanglement Entropy of the *disconnected* solution

$$S_d = \frac{V_{d-1}}{2G_N^{(10)}} \int_{\rho_\Lambda}^{\infty} d\rho \sqrt{\beta(\rho) H(\rho)}, \tag{5.1.5}$$

which, it should be noted, is independent of ρ_0 (and L_A). We can define the length of the strip for the *connected* solution as a function of ρ_0 as

$$L_A(\rho_0) = 2 \int_{\rho_0}^{\infty} d\rho \sqrt{\frac{\beta(\rho)}{\frac{H(\rho)}{H(\rho_0)} - 1}}. \tag{5.1.6}$$

Noting that in general the Entanglement Entropy is UV divergent, we will always calculate the difference between the *connected* $S_c(\rho_0)$ and *disconnected* S_d contributions

$$\frac{4G_N^{(10)}}{V_{d-1}} S_A(\rho_0) \equiv \frac{2G_N^{(10)}}{V_{d-1}} \left(S_c(\rho_0) - S_d\right) = 2 \int_{\rho_0}^{\infty} d\rho \sqrt{\frac{\beta(\rho) H(\rho)}{1 - \frac{H(\rho_0)}{H(\rho)}}} - 2 \int_{\rho_\Lambda}^{\infty} d\rho \sqrt{\beta(\rho) H(\rho)}, \tag{5.1.7}$$

which is generally finite. It is easily seen that these definitions fall into the general formalism for probes that we discussed in Section. 4.1. The relationship between the functions is given by

$$F(\rho) = \sqrt{H(\rho)}, \qquad G(\rho) = \sqrt{H(\rho)\beta(\rho)}. \tag{5.1.8}$$

For a given value of L_A (or ρ_0), S_c can either be positive or negative. When negative, it is the minimal solution, whereas when positive, the disconnected solution is the minimal solution. Between these two regions, we find a first order phase transition, characteristic of confining theories as described by Fig. 5.1.

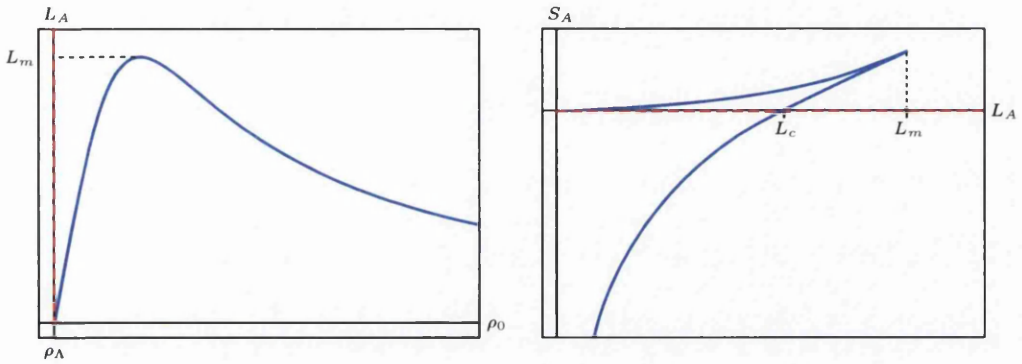

Figure 5.1: The generic phase diagram for the Entanglement Entropy of a strip in confining theories. On the left, the length of the connected solution as a function of the minimal radial position in the bulk $L_A(\rho_0)$, which is a non-monotonic function in confining theories. On the right, the Entanglement Entropy of the strip as a function of its length $S_A(L_A)$. The solid blue line represents the connected solution while the dashed red line is the disconnected solution. At the point $L_A = L_c$ there is a first order phase transition between the two types of solution.

The connected solution only exists over a finite range $0 \leq L_A \leq L_m$ and within this range there are two possible values for the connected solution for every value of ρ_0, corresponding to the two branches, depicted in Fig. 5.1. As a result of this double-valued behaviour, there is a first order phase transition at the point $L_A = L_c$, between the connected and disconnected solutions. Thus, in alignment with [48], the signal for confinement is the non-monotonicity of $L_A(\rho_0)$. We shall show later in a number of examples, that every peak in $L_A(\rho_0)$ corresponds to a possible phase transition in the Entanglement Entropy $S_A(L_A)$.

5.2 Wilson Loops in Confining Backgrounds: A Review

Here we will review some known results concerning rectangular Wilson Loops in confining backgrounds. Many of the results below were found in [101]. Defining the function $g(\rho) \equiv \alpha(\rho)\sqrt{\beta(\rho)}$, one can then write the regularised energy of the Wilson Loop as

$$E_W(\rho_0) = 2\int_{\rho_0}^{\infty} \mathrm{d}\rho \, \frac{g(\rho)}{\alpha(\rho)} \sqrt{\frac{\alpha(\rho)^2}{1 - \frac{\alpha(\rho_0)^2}{\alpha(\rho)^2}}} - 2\int_{\rho_\Lambda}^{\infty} \mathrm{d}\rho \, g(\rho). \tag{5.2.1}$$

From the point of view of the Wilson Loop calculation, the first term is the bare energy, while the second term, which is subtracted to regularise the divergence, is the energy of two straight strings (stretched between the IR end-of-space $\rho = \rho_\Lambda$ and the boundary). There is also the length of the Wilson Loop given by

$$L_W(\rho_0) = 2\int_{\rho_0}^{\infty} \mathrm{d}\rho \frac{g(\rho)}{\alpha(\rho)} \sqrt{\frac{1}{\frac{\alpha(\rho)^2}{\alpha(\rho_0)^2} - 1}}. \tag{5.2.2}$$

Thus for a background to admit linear confinement, one of the following conditions on the functions must be satisfied [101]

$$\begin{aligned} &1. \quad \alpha(\rho) \text{ has a minimum} \\ &2. \quad g(\rho) \text{ diverges} \end{aligned} \tag{5.2.3}$$

If one of these conditions is satisfied at a particular value of $\rho = \rho_T$, then the corresponding effective tension is given by $\alpha(\rho_T) \neq 0$. Thus, the energy at long distances will behave as

$$E_W(L_W) = \alpha(\rho_T) L_W + 0\left(\frac{1}{L_W}\right) \tag{5.2.4}$$

if one of the above two conditions is satisfied. Again, these definitions fall into the general formalism for probes that we discussed in Section. 4.1. The relationship between the functions is given by

$$F(\rho) = \alpha(\rho), \qquad G(\rho) = g(\rho) = \alpha(\rho)\sqrt{\beta(\rho)}. \tag{5.2.5}$$

Further it was shown that in confining backgrounds, $L_W(\rho_0)$ is a monotonically decreasing function. This then corresponds to the fact that $E_W(L_W)$ is a monotonically increasing function i.e. that it always increases with the length of the rectangular Wilson Loop. We finish by noting that in general, in the confining backgrounds we will study, the Wilson Loop has $\rho_T = \rho_\Lambda$.

5.3 Comparison of Entanglement Entropy and Wilson Loops in Confining Backgrounds

In the last two sections, we have reviewed some long-known results for both the Entanglement Entropy and the Wilson Loop, in confining backgrounds. On the surface, these two observables have quite different behaviours, as we have discussed, in that generically the Entanglement Entropy shows a phase transition, whereas the Wilson Loop is monotonic. Curiously though,

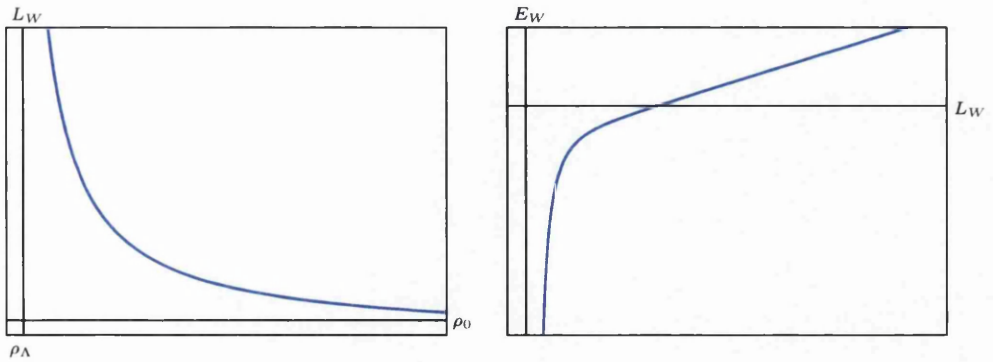

Figure 5.2: The generic phase diagram for the rectangular Wilson Loop in confining theories. On the left, the length of the Wilson Loop as a function of the minimal radial position in the bulk $L_W(\rho_0)$, which is a monotonically decreasing function in confining theories. On the right, the regularised Energy of the Wilson Loop as a function of its length $E_W(L_W)$. Linear confinement corresponds to the fact that the Energy is linear in the Length at long distances.

as they are both probes of confinement, this hints at a deeper relation between them. Further, the functional form of both calculations, from a holographic point of view, is very similar and both fall into the general formalism of Section. 4.1.

We can write the length of the Entangling strip (in Eq. 5.1.6) and the length of the rectangular Wilson Loop (in Eq.5.2.2) as

$$\left.\begin{matrix} L_A(\rho_0) \\ L_W(\rho_0) \end{matrix}\right\} = \mathfrak{L}(F) = 2\int_{\rho_0}^{\infty} \mathrm{d}\rho \sqrt{\frac{\beta(\rho)}{\frac{F(\rho)^2}{F(\rho_0)^2} - 1}} \tag{5.3.1}$$

where the corresponding function $F(\rho)$ is given in by

$$F_A(\rho) = \sqrt{H(\rho)}, \tag{5.3.2}$$

$$F_W(\rho) = \alpha(\rho). \tag{5.3.3}$$

We can write the Entanglement Entropy of the strip (in Eq. 5.1.7) and the Energy of the rectangular Wilson Loop (in Eq. 5.2.1) in a similar form

$$\left.\begin{matrix} \frac{4G_N^{(10)}}{V_{d-1}} S_A(\rho_0) \\ E_W(\rho_0) \end{matrix}\right\} = \mathfrak{S}(F) = 2\int_{\rho_0}^{\infty} \mathrm{d}\rho\, F(\rho) \sqrt{\frac{\beta(\rho)}{1 - \frac{F(\rho_0)^2}{F(\rho)^2}}} - 2\int_{\rho_\Lambda}^{\infty} \mathrm{d}\rho\, F(\rho)\sqrt{\beta(\rho)} \tag{5.3.4}$$

We can manipulate Eq. 5.3.4 into the following form

$$\mathfrak{S}(F) \equiv F(\rho_0)\mathfrak{L}(F(\rho_0)) - 2\mathfrak{K}(F(\rho_0)), \tag{5.3.5}$$

$$\mathfrak{K}(F) \equiv \int_{\rho_\Lambda}^{\infty} d\rho F(\rho)\sqrt{\beta(\rho)} - \int_{\rho_0}^{\infty} d\rho\sqrt{\beta(\rho)\,(F(\rho)^2 - F(\rho_0)^2)}. \tag{5.3.6}$$

This rearrangement of Eq. 5.3.5, makes it easy to see that the long distance behaviour of E_W is linear (in the case of the Wilson Loop) and that $F(\rho_0)$ is a monotonically increasing function in both cases. Further, as both the Entanglement Entropy and the Wilson Loop calculations are based on minimisation problems, the fact that both observables can be written in the same functional form, is not entirely surprising.

The remaining question is where the difference between them lies. The claim is that, in a confining Quantum Field Theory, the behaviour of $F(\rho_0)$ close to the IR end-of-space ρ_Λ is dictating this difference in behaviour. The Wilson Loop in confining backgrounds, in the IR, is related to the confining string tension, and thus $F(\rho_\Lambda) = \alpha(\rho_\Lambda) \neq 0$. This is not the case for the Entanglement Entropy, as we have discussed, in that $F(\rho_\Lambda) = \sqrt{H(\rho_\Lambda)} = 0$, in accordance with the shrinking of the internal volume, and its agreement with the vanishing of the central charge at zero energies, characteristic of confining field theories. Hence this appears to be the qualitative difference between the two observables.

Let us now turn our attention to a specific example, that of Dp branes wrapped on a circle, which are backgrounds dual to confining field theories in p space-time dimensions. These are generalisations of that written by Witten, as a dual to a Yang-Mills-like 4-dimensional Quantum Field Theory [21, 86, 103, 104] (with $\alpha' = g_s = 1$),

$$ds^2 = \left(\frac{\rho}{R}\right)^{\frac{7-p}{2}}\left[dx^2_{(1,p-1)} + \left(\frac{R}{\rho}\right)^{7-p}\frac{d\rho^2}{f(\rho)}\right] + \left(\frac{\rho}{R}\right)^{\frac{7-p}{2}} f(\rho)\,d\varphi_c^2 + \left(\frac{\rho}{R}\right)^{\frac{p-3}{2}} R^2\,d\Omega^2_{(8-p)},$$

$$f(\rho) = 1 - \left(\frac{\rho_\Lambda}{\rho}\right)^{7-p}, \quad e^{-2\Phi} = \left(\frac{\rho}{R}\right)^{\frac{(7-p)(3-p)}{2}}, \quad \alpha(\rho) = \left(\frac{\rho}{R}\right)^{\frac{7-p}{2}}, \quad g(\rho) = \frac{1}{\sqrt{f(\rho)}}, \tag{5.3.7}$$

which means that we have

$$F_A^2 = (S_{7-p} \times 2\pi R_c)^2\, R^{7-p}\rho^{9-p} f(\rho), \qquad F_W^2 = \left(\frac{\rho}{R}\right)^{7-p}. \tag{5.3.8}$$

Here, R_c is the radius associated with the compact cycle (see for example [105]), and is given by

$$R_c = \frac{2}{7-p}\left(\frac{R}{\rho_\Lambda}\right)^{\frac{7-p}{2}}\rho_\Lambda \tag{5.3.9}$$

and $S_{n-1} = \frac{2\pi^{\frac{n}{2}}}{\Gamma\left(\frac{n}{2}\right)}$ is the surface area of an n-sphere.

From eq. 5.3.8, it is easy to see that the behaviour near the IR end of space differs dramatically between the two quantities. In the case of the Wilson Loop, $F_W(\rho_\Lambda) \sim \rho_\Lambda^{(7-p)/2} \neq 0$, whereas in the case of the Entanglement Entropy $F_A(\rho_\Lambda) = 0$ (this is caused by the presence of the function $f(\rho)$ in $F_A(\rho)$, and its notable absence in $F_W(\rho)$). It is exactly this difference that leads us to the monotonic behaviour of the Wilson Loop, with the linear growth in $E_W(L_W)$ at large separations. This is not reproduced in the case of the Entanglement Entropy, in which we see a first order phase transition (in $S_A(L_A)$), due to the vanishing of F_A at the IR end-of-space.

5.3.1 Sufficient Conditions for a Phase Transition

We have already seen the relevant conditions a background must satisfy, in order for the Wilson Loop to show the corresponding confining behaviour in Eq. 5.2.3, which were originally derived in [103]. We have further noted that the behaviour differs from that of the Entanglement Entropy (at least in the IR), but it is informative to consider that they are still both probes of confinement, and thus ask what conditions exist on a background such that we have a phase transition in the Entanglement Entropy.

Following the logic of [103], we will look to derive sufficient conditions on the background, such that the Entanglement Entropy shows a phase transition. What we mean by this is that we will look for conditions on backgrounds that lead to the function $L_A(\rho_0)$ decreasing for asymptotically large values of ρ_0 and increasing in ρ_0 close to ρ_Λ. These asymptotic properties will lead to (at least one) maximum $L_A(\rho_0)$, and thus it will be double-valued, as required for a phase transition.

Initially, we look at conditions on the UV of the background, such that $L_A(\rho_0)$ is a decreasing function for large ρ. Close to the boundary, we can expand as (with $j, k > 0$)

$$H(\rho) = h_j \rho^j + \mathcal{O}(\rho^{j-1}), \qquad \beta(\rho) = \beta_k \rho^{-k} + \mathcal{O}(\rho^{-k+1}), \tag{5.3.10}$$

such that we find

$$\begin{aligned} L_A(\rho_0) &= 2\sqrt{\beta_k} \int_{\rho_0}^{\infty} d\rho\, \rho^{-\frac{k}{2}} \frac{1}{\sqrt{\left(\frac{\rho}{\rho_0}\right)^j - 1}} \\ &= 2\sqrt{\beta_k}\, \rho_0^{1-\frac{k}{2}} \int_1^{\infty} dr \frac{r^{-\frac{k}{2}}}{\sqrt{r^j - 1}} = 2\sqrt{\beta_k} \frac{\sqrt{\pi}}{j} \frac{\Gamma\left(\frac{1}{2} - \frac{2-k}{2j}\right)}{\Gamma\left(1 - \frac{2-k}{2j}\right)} \rho_0^{1-\frac{k}{2}}. \end{aligned} \tag{5.3.11}$$

To get this result, we have used the change of variables $r \equiv \left(\frac{\rho}{\rho_0}\right)$, and we read off that the condition for $L_A(\rho_0)$ to be monotonically decreasing near the boundary is that

$$k > 2. \tag{5.3.12}$$

This means that we require $\beta(\rho)$ to approach zero faster than $\frac{1}{\rho^2}$ in the UV. For $k \leq 2$, we would expect $L_A(\rho_0)$ to diverge (for $k < 2$), or saturate to a constant value (for $k = 2$).

We can perform the equivalent calculation for the IR of the background, such that $L_A(\rho_0)$ is an increasing function for small ρ. Assuming the following expansions for $H(\rho)$ and $\beta(\rho)$ (with $m, n > 0$),

$$H(\rho) = h_m(\rho - \rho_\Lambda)^m + \mathcal{O}(\rho - \rho_\Lambda)^{m+1}, \qquad \beta(\rho) = \beta_n(\rho - \rho_\Lambda)^{-n} + \mathcal{O}(\rho - \rho_\Lambda)^{-n+1}, \tag{5.3.13}$$

and we can approximate the integrand in $L_A(\rho_0)$ using this (as the major contribution to the integral comes from the divergence of the integrand close to the IR end-of-space)

$$\begin{aligned} L_A(\rho_0) &= 2\sqrt{\beta_n}\int_{\rho_0}^{\infty} d\rho\ (\rho - \rho_\Lambda)^{-\frac{n}{2}} \frac{1}{\sqrt{\left(\frac{\rho-\rho_\Lambda}{\rho_0-\rho_\Lambda}\right)^m - 1}} \\ &= 2\sqrt{\beta_n}\ (\rho_0 - \rho_\Lambda)^{1-\frac{n}{2}} \int_1^{\infty} dr\ \frac{r^{-\frac{n}{2}}}{\sqrt{r^m - 1}} \\ &= 2\sqrt{\beta_n}\frac{\sqrt{\pi}}{m}\frac{\Gamma\left(\frac{1}{2} - \frac{2-n}{2m}\right)}{\Gamma\left(1 - \frac{2-n}{2m}\right)}\ (\rho_0 - \rho_\Lambda)^{1-\frac{n}{2}}. \end{aligned} \tag{5.3.14}$$

This time we used the change of variables $r \equiv \left(\frac{\rho-\rho_\Lambda}{\rho_0-\rho_\Lambda}\right)$, and can read off that the condition for $L_A(\rho_0)$ to be monotonically increasing is

$$n < 2. \tag{5.3.15}$$

Thus, close to ρ_Λ, $\beta(\rho)$ should not diverge faster than $\frac{1}{(\rho-\rho_\Lambda)^2}$.

Between these two limits, we will find a maximum (labelled by L_m in Fig. 5.1), giving the required double-valued behaviour we require for a phase transition in $S_A(L_A)$. Before we look at some examples to show agreement with the above results, it is interesting to note that these conditions are only on $\beta(\rho)$, and not $H(\rho)$. Further, we expect there are backgrounds that would fall outside of our ansatz for the expansions proposed above, and we shall see an example of this in the next section.

5.3.2 Examples of Criteria for a Phase Transition

It will now be instructive to see how the above criteria work in models, that either exhibit confinement, or do not. We shall look at the famous example of $AdS_5 \times S^5$, the Hard- and Soft-wall models, as well as Dp branes wrapped on a circle (for $3 \geq p \geq 6$) defined in Eq. 5.3.7, and finally the Klebanov-Strassler model.

First we start with the canonical example of $AdS_5 \times S^5$, and the Entanglement Entropy of $\mathcal{N} = 4$ Super-Yang-Mills, as a demonstration of a non-confining model, and show that it does not admit a phase transition. The relevant metric in this case takes the form

$$ds^2_{AdS_5} = \left(\frac{\rho^2}{R^2}\right) dx^2_{(1,3)} + \left(\frac{R^2}{\rho^2}\right) d\rho^2 + R^2 d\Omega^2_5 \tag{5.3.16}$$

where $(\rho_\Lambda = 0) \leq \rho < \infty$, and the dilaton is constant. This leads to the following for the functions

$$\beta(\rho) = \left(\frac{R}{\rho}\right)^4, \qquad H(\rho) = \left(\frac{8\pi^2}{3}\right)^2 R^4 \rho^6. \tag{5.3.17}$$

Thus we can read off that $k = n = 4$. In this case the condition on n is violated and thus we do not find a phase transition, as expected in a conformal theory. The length of the strip $L_A(\rho_0)$, and also the Entanglement Entropy $S_A(L_A)$, are plotted in Fig. 5.3.

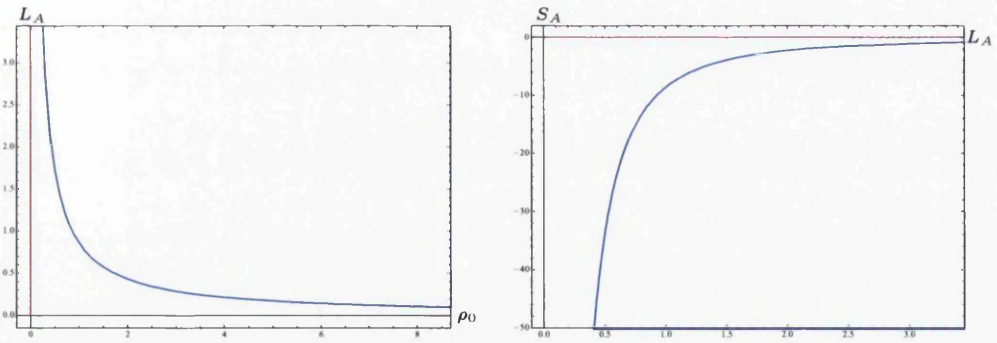

Figure 5.3: Plots of the functions $L_A(\rho_0)$ on the left, and $S_A(L_A)$ on the right, in the case of $AdS_5 \times S^5$. The solid blue line represents the connected solution while the dashed red line is the disconnected solution.

In this case, it is possible to perform the integrals explicitly, such that we find

$$L_A(\rho_0) = \frac{\Gamma\left(\frac{2}{3}\right)\Gamma\left(\frac{5}{6}\right)}{\sqrt{\pi}} \frac{R^2}{\rho_0} \tag{5.3.18}$$

and

$$S_A(\rho_0) = -\frac{4\pi^2 R^4}{3}\frac{\Gamma\left(\frac{2}{3}\right)\Gamma\left(\frac{5}{6}\right)}{\sqrt{\pi}}\rho_0^2. \tag{5.3.19}$$

From the above, it can be seen that $L_A(\rho_0)$ goes to zero for large ρ_0, and diverges for small ρ_0. Further, $S_A(L_A)$ will always be negative (and monotonically increasing), and thus the connected solution is always preferred to the disconnected. This of course means that there is no phase transition between the two. It is instructive to note that the concavity of $S_A(L_A)$ is such that

$$\frac{d^2 S_A}{dL_A^2} < 0, \tag{5.3.20}$$

throughout the space, and thus one would call this *stable* according to the appropriately derived conditions (see for example [93, 106] and the discussions in Chapter. 4 and Appendix. B.1).

We move our attention to the Hard- and Soft-wall models. The Hard-wall model was proposed in [107] to describe the low-energy properties of QCD from a holographic approach. This was achieved introducing a hard cutoff of the radial coordinate, of the AdS setup, at a value $\rho = \rho_\Lambda$. Thus the metric takes the same form as Eq. 5.3.16, and the relevant functions are those in Eq. 5.3.17. We plot the resulting functions $L_A(\rho_0)$ and $S_A(L_A)$ in Fig. 5.4.

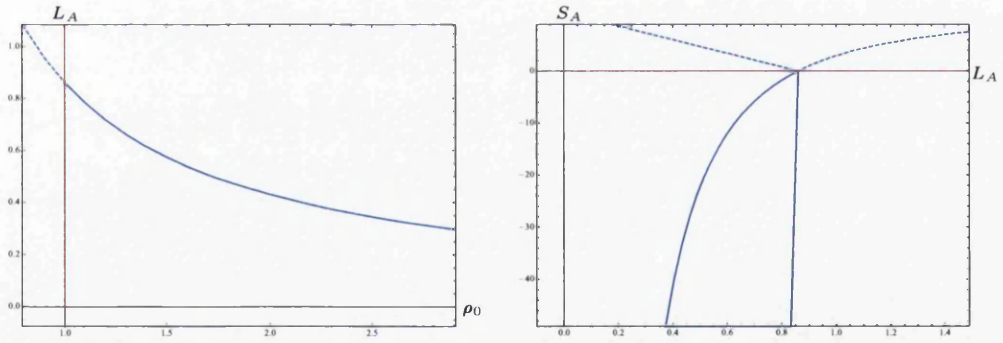

Figure 5.4: Plots of the functions $L_A(\rho_0)$ on the left, and $S_A(L_A)$ on the right, in the Hard-wall model. The location of the Hard-wall was set to $\rho_\Lambda = 1$ in the figures. The solid blue line represents the connected solution, while the dashed red line is the disconnected solution and the dashed blue line represents the continuation of the AdS solution beyond the Hard-wall.

As an improvement to the Hard-wall model, in [108], a modification was suggested. The new model still cuts the AdS space, but now the cut is made in a smooth manner. This smoothing is achieved by retaining the form of the metric in Eq. 5.3.16, but introducing a non-trivial dilaton

of the form

$$e^{\Phi(\rho)} = e^{\left(\frac{1}{\rho}\right)^2} \tag{5.3.21}$$

which leads to a modification of the form

$$\beta(\rho) = \left(\frac{R}{\rho}\right)^4, \qquad H(\rho) = \left(\frac{8\pi^2}{3}\right) R^4 \rho^6 e^{-\left(\frac{2}{\rho}\right)^2}. \tag{5.3.22}$$

The difference is shown in the new form of $H(\rho)$, such that is goes to zero exponentially fast, as we move toward the IR end-of-space, which is now fixed at $\rho_\Lambda = 0$. We plot the resulting functions $L_A(\rho_0)$ and $S_A(L_A)$ in Fig. 5.5.

As the Hard-wall model is just a cut AdS-space, and the Soft-wall model does not admit an expansion of the form Eq. 5.3.13 for $H(\rho)$ in the IR due to the presence of the exponential, it is not possible to check the derived conditions for confinement.

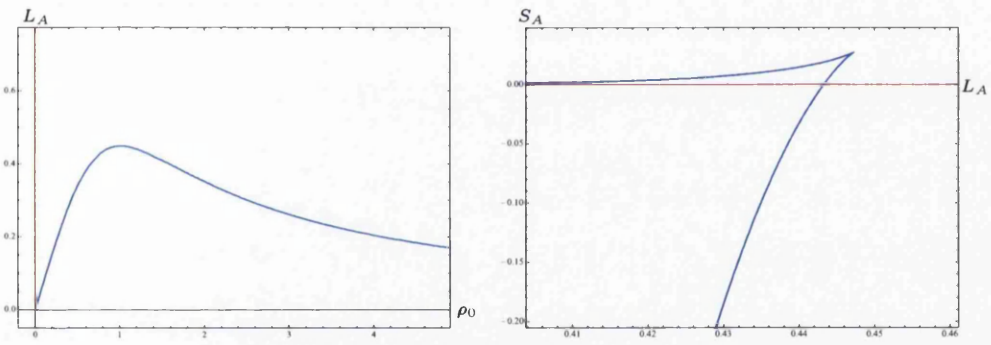

Figure 5.5: Plots of the functions $L_A(\rho_0)$ on the left, and $S_A(L_A)$ on the right, in the Soft-Wall model. The solid blue line represents the connected solution while the dashed red line is the disconnected solution.

Next we turn our attention to the backgrounds initially discussed in Eq. 5.3.7, those of Dp branes wrapped on a circle. In this case, one finds when expanding close to the IR end-of-space $\rho = \rho_\Lambda$,

$$\beta(\rho) = \left(\frac{R}{\rho_\Lambda}\right)^{7-p} \left(\frac{\rho_\Lambda}{7-p}\right) \frac{1}{(\rho - \rho_\Lambda)} + \ldots \tag{5.3.23}$$

where the "..." represent the sub-leading (finite) terms.

From this it is easy to see that $n = 1$, thus for any value of p the condition Eq. 5.3.15 is satisfied and in the IR the function $L_A(\rho_0)$ will always approach zero. In the UV, $\beta(\rho_0) \sim \rho_0^{p-7}$, meaning $k = 7-p$. As this is not independent of p, we find a change in behaviour as we move to

higher dimensional branes. For $p \leq 4$, the condition Eq. 5.3.12 is satisfied and we find a phase transition in the Entanglement Entropy (see the top two rows in Fig. 5.6), whereas for $p = 5$, we see that $L_A(\rho_0)$ takes a finite value near the boundary (see the third row in Fig. 5.6) and for $p = 6$ we see that $L_A(\rho_0)$ grows without bound (see the bottom row in Fig. 5.6). Further, there is a change in the concavity of the UV branch, when $p \geq 5$ the condition Eq. 5.3.20 is violated.

We will finally look at another case discussed in [48], which is the Entanglement Entropy in the background dual to the Klebanov-Strassler. The Entanglement Entropy exhibits a phase transition similar to that of the D3 and D4 branes wrapped on a circle, as expected for a confining theory. We will try to see how this background follows the conditions for exhibiting a phase transition.

The supergravity solution of the deformed conifold is of the following form [12, 109]

$$\begin{aligned} ds^2_{KS} &= \hat{h}^{-\frac{1}{2}}(\tau)\, dx^2_{(1,3)} + \hat{h}^{\frac{1}{2}}(\tau)\, d\tilde{s}^2_6, \\ d\tilde{s}^2_6 &= \frac{1}{2}\epsilon^{\frac{4}{3}} K(\tau)\Bigg(\frac{1}{3K^3(\tau)}\left[d\tau^2 + \left(g^5\right)^2\right] + \sinh^2\left(\frac{\tau}{2}\right)\left[\left(g^1\right)^2 + \left(g^2\right)^2\right] \\ &\qquad + \cosh^2\left(\frac{\tau}{2}\right)\left[\left(g^3\right)^2 + \left(g^4\right)^2\right]\Bigg), \end{aligned} \tag{5.3.24}$$

where $\tilde{s}^2_6$ is the metric of the deformed conifold, ϵ is the scale and

$$\begin{aligned} \hat{h}(\tau) &= 2^{\frac{2}{3}}(g_s\alpha')^2 M^2 \epsilon^{-\frac{8}{3}} \int_\tau^\infty dz \left[\frac{z\coth(z) - 1}{\sinh^2(z)}\right](\sinh(2z) - 2z)^{\frac{1}{3}}, \\ K(\tau) &= \frac{(\sinh(2\tau) - 2\tau)^{\frac{1}{3}}}{2^{\frac{1}{3}}\sinh(\tau)}. \end{aligned} \tag{5.3.25}$$

The radial coordinate is τ and it runs between $0 \leq \tau < \infty$. From this we have,

$$\begin{aligned} \alpha(\tau) &= \hat{h}^{-\frac{1}{2}}(\tau), \qquad \beta(\tau) = \frac{\hat{h}(\tau)\epsilon^{\frac{4}{3}}}{6K^2(\tau)}, \\ V_{int} &= \frac{8\pi^6}{3}\epsilon^{\frac{20}{3}}\hat{h}^{\frac{5}{2}}(\tau)K^2(\tau)\sinh^4(\tau), \\ H(\tau) &= e^{-4\phi}V^2_{int}\alpha^3 = \frac{8\pi^6}{3}\epsilon^{\frac{20}{3}}\hat{h}(\tau)K^2(\tau)\sinh^4(\tau). \end{aligned} \tag{5.3.26}$$

In this case, for small values of the radial coordinate τ, the function $\beta(\tau)$ approaches a finite value, meaning we have $n = 0$ and agreement with the condition in Eq. 5.3.15. For large values of the radial coordinate τ, we find that the leading order in the background functions $\hat{h}(\tau)$ and

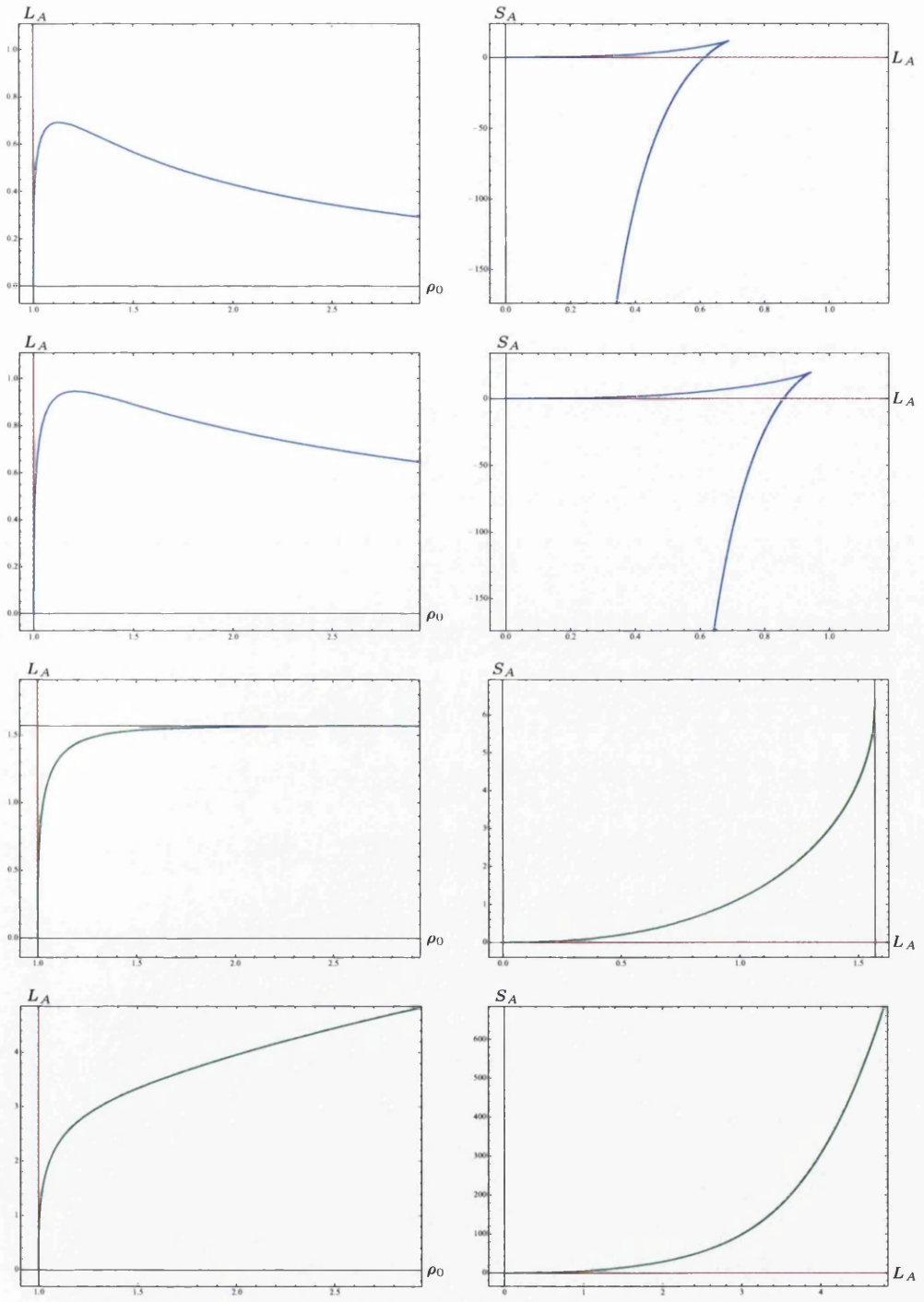

Figure 5.6: Plots of the functions $L_A(\rho_0)$ on the left, and $S_A(L_A)$ on the right, in the near extremal Dp brane backgrounds for $p = 3, 4, 5, 6$, moving down the page. The solid blue line represents the connected solution while the dashed red line is the disconnected solution. The location of the horizon was set to $\rho_\Lambda = 1$ in the plots. The D3 and D4 branes show a phase transition while in the D5 and D6 branes there is no phase transition.

$K(\tau)$, takes the form *

$$\hat{h}(\tau) \to 3 \times 2^{\frac{1}{3}} (g_s \alpha')^2 M^2 \epsilon^{-\frac{8}{3}} \left(\tau - \frac{1}{4}\right) e^{-\frac{4\tau}{3}}, \qquad K(\tau) \to 2^{\frac{1}{3}} e^{-\frac{\tau}{3}}, \tag{5.3.27}$$

such that the relevant functions used in calculating the Entanglement Entropy behave as

$$\beta(\tau) \to \frac{1}{2^{\frac{4}{3}}} \epsilon^{-\frac{4}{3}} (g_s \alpha')^2 M^2 \left(\tau - \frac{1}{4}\right) e^{-\frac{2\tau}{3}}, \quad H(\tau) \to \pi^6 \epsilon^4 (g_s \alpha')^2 M^2 \left(\tau - \frac{1}{4}\right) e^{2\tau}. \tag{5.3.28}$$

Thus, in this region, the functions do not admit the power expansion we assumed. We note due to the exponentially fast decay of $\beta(\tau)$ toward the UV, that this is a sufficiently strong decay and thus in agreement with $k > 2$, and from direct computation [48] $L_A(\rho_0)$ does go to zero, and the Entanglement Entropy does admit a phase transition

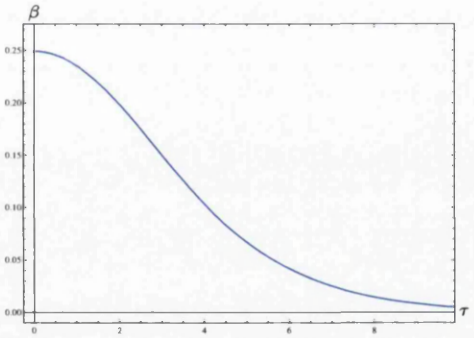

Figure 5.7: A plot of the function $\beta(\tau)$ in the Klebanov-Strassler background. $\beta(\tau)$ saturates to a finite value at the origin $\tau = 0$ and therefore meets the condition for a phase transition.

5.4 Confinement and Phase Transitions: A Discussion

Let us now look at how the conditions for confinement we have derived coincide in the two cases at hand, the phase transition in the Entanglement Entropy (i.e. those presented in Eq. 5.3.15 and Eq. 5.3.12), and the conditions on the Wilson Loop (i.e. those discussed in Eq. 5.2.3). From a physical perspective, both the observables are probes of confinement, thus we expect agreement between the two cases. Although we will not prove the last statement, we will give indication of its success in some examples, and discuss how in other cases a puzzle arises. We will then look to resolve this contention.

*Here we have written the equivalent functions to those presented in Eq. 3.7.13, but with the replacement $\tau = 2\rho$, consistent with the notation of [48].

The conditions on the Wilson Loop in Eq. 5.2.3, are really only a statement about the IR, and such should be compared to the conditions on the Entanglement Entropy in the IR. The condition Eq. 5.3.12 required $\beta(\rho)$ should not diverge faster than $\frac{1}{(\rho-\rho_\Lambda)^2}$ such that a phase transition will be observed in the Entanglement Entropy. As $\alpha(\rho_\Lambda)$ sets the string tension in the case of the Wilson Loop, and must be finite under the conditions for linear confinement, it will not play a part in IR divergences. Thus we associate the divergence of $\beta(\rho)$ with the divergence of $g(\rho)$, i.e. the second condition in Eq. 5.2.3.

If we take the case of Dp branes wrapped on a circle (see Eq. 5.3.7) as an example, we see that in the IR

$$g^2(\rho) = \left(\frac{\rho_\Lambda}{7-p}\right)\frac{1}{\rho-\rho_\Lambda} + \dots \tag{5.4.1}$$

where the "..." correspond to finite corrections. This agrees with the condition Eq.5.3.15 on $\beta(\rho)$ for all the relevant values of p.

Although unaware of a particular example, a stronger divergence of $g(\rho)$ could lead to a violation of Eq. 5.3.15. * In the case of the Wilson Loop, when $\alpha(\rho)$ has a minimum at $\rho = \rho_\Lambda$ (i.e. the first condition in Eq. 5.2.3), it seems the equivalent condition for the Entanglement Entropy would be $\beta(\rho)$ is constant in the IR. When this occurs, it appears that the relation $\beta \sim \frac{1}{\alpha^2}$, such that the maximum of $\beta(\rho)$ corresponds to the minimum of $\alpha(\rho)$, at $\rho = \rho_\Lambda$. An example of this can be seen in Fig. 5.7.

So, if we now focus on the UV, we see there is a puzzle. As far as the Wilson Loop is concerned, the only condition we demand is linearity at long distances, and this as we have discussed is a condition on the IR. In contrast, we have a condition in the UV for a phase transition in the Entanglement Entropy Eq. 5.3.12, as well as one in the IR. As we have seen, in the case of Dp branes wrapped on a circle with $p > 4$, this UV condition is not satisfied. This leads us to the following question: Is it true that there are cases which show linear confinement in the Wilson Loop, but do not show a phase transition in the Entanglement Entropy?

With the aid of Volume-Law behaviour for the Entanglement Entropy, ideas surrounding non-locality in Quantum Field Theories, UV-cutoffs and UV-completion (approaching a near conformal point), we shall attempt to answer this question. Further, we shall then look at a variety of models based on wrapped branes, and see how one can further understand models of confinement through studies of the corresponding Entanglement Entropy.

*An example may be a background with not one, but two shrinking circles, such that the tip of the cigar in both, is situated at the same radial position.

5.5 Area-Laws, Volume-Laws, UV-Cutoffs and Confinement

We shall bring together what we have seen in the last section, to lead us toward an answer to the question posed. Initially, we shall analyse the case of $AdS_5 \times S^5$ and compare to duals of confinement, move on to NS5/D5 branes, looking at the role non-locality plays in the dual field theory, and finally look again at the analogue of Witten's confining model, but instead D5 branes wrapping a circle.

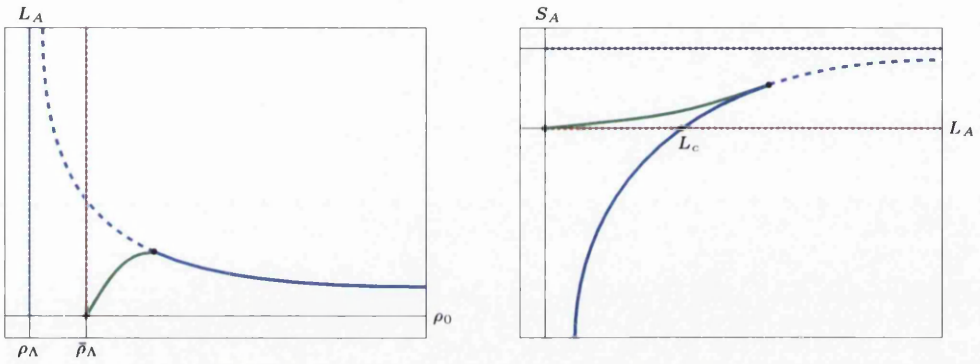

Figure 5.8: Plots of the generic change in behaviour of $L_A(\rho_0)$ and $S_A(L_A)$ when we have a theory with confinement. The navy blue lines (solid and dashed) in both plots represent the behaviour of the connected part of conformal solutions, like that of $AdS_5 \times S^5$ (i.e. $L_A(\rho_0) \sim \rho_0^{-1}$), the green line is the *unstable* branch introduced by confinement (as in the Soft-wall model). The dotted navy blue (at ρ_Λ) and red (at $\bar{\rho}_\Lambda$) lines represent the disconnected solution in the respective cases. In the confining case there is a phase transition at the point L_c.

Returning to the calculation of the Entanglement Entropy in the well understood $AdS_5 \times S^5$ background, which we shall use as a basis of comparison in what follows, the connected solution is always preferred and is thus the minimal solution throughout the space. The disconnected solution always has a higher value for the Entanglement Entropy (see Fig. 5.3). For a local field theory, the Entanglement Entropy follows what is sometimes termed a "Heisenberg-like" relation, such that $L_A(\rho_0) \sim \frac{1}{\rho_0}$, for some region of the minimal solution. The leading order divergence is the expected Area-Law. In the case at hand, this is easily seen from the fact that the connected solution asymptotes the connected solution from below for large ρ_0. This type of behaviour is characterised by the navy blue lines (both solid and dashed) in Fig. 5.8.

Another point to notice from Fig. 5.8 is that the introduction of confinement can be thought of as an effect on the IR region of the corresponding $AdS_5 \times S^5$ behaviour for the Entanglement

Entropy. As discussed, this effect can be modelled by a Soft-Wall background, and this leads to us replacing the usual $L_A(\rho_0) \sim \frac{1}{\rho_0}$ IR behaviour, with an unstable branch (see the green lines in Fig. 5.8). * The effect is such that the disconnected branch now comes into play, being moved down (in the $S_A(L_A)$ plot) and meeting at $L_A = L_c$ the stable connected branch. These solutions still follow the standard Area-Law behaviour for the leading order divergence. The presence of the unstable branch will occur for all theories we study that exhibit confinement.

Moving our attention to the NS5/D5 branes, as discussed in [50], we find that the connected branch has $L_A(\rho_0) = \frac{\pi R}{2}$, where $R = \alpha' g_s N_c$. This means we have an infinite number of connected solutions, parametrised by ρ_0, which have the same separation $L_A = L_c$. For $L_A > L_c$, we have the standard case in that the disconnected solution is preferred and the minimal surfaces fall all the way though the space. For $L < L_c$, it was proposed in [50] (using the approximation of a capped cylinder similar to the one we shall discuss shortly), these are solutions that must live near the UV, or near the UV-cutoff when one is imposed. In these solutions, the main contribution to the Entanglement Entropy comes from the cap of the cylinder, and thus we find that the leading divergence is no longer an Area-Law, but instead of a Volume-Law and this is associated with non-locality in the dual Quantum Field Theory.

This leads us back to our discussion of the D5 branes wrapped on a circle, which is a model of a confining $4+1$-dimensional Quantum Field Theory. In our new language, the connected solution here is similar throughout the space to the unstable IR branch of the Soft-wall model mentioned above. The difference lies in the lack of a stable branch, as we move toward the UV, such that we would only keep the green branch in Fig. 5.8. Thus our example of D5 branes wrapped on a circle have the IR features of a confining model (reminiscent of the Soft-Wall model), but the UV behaviour of a non-local Quantum Field Theory (akin to that of the NS5/D5 branes). So even though the Wilson Loop shows the behaviour associated with confinement, for the Entanglement Entropy we have the disconnected branch preferred throughout, instead of the unstable connected branch (which always has higher Entanglement Entropy) and thus no phase transition. We will look to clarify the details of this example further.

*We use this description as this branch does not obey the criteria in Eq. 5.3.20.

5.5.1 A Useful Quantity

As an aside, we will introduce a combination of the background functions, which is closely related to $\mathcal{Z}$ defined in Eq. 4.1.7, by the following

$$\mathcal{Z} = \frac{1}{\pi}\partial_\rho\left(\mathcal{Y}(\rho)\right). \tag{5.5.1}$$

This function in terms of β and H takes the form

$$\mathcal{Y}(\rho) = 2\pi\frac{H(\rho)\sqrt{\beta(\rho)}}{H'(\rho)}, \tag{5.5.2}$$

This function approximates the integral for $L_A(\rho_0)$ defined in Eq. 5.1.6, and is very useful in a number of cases where the background is only known semi-analytically, as in many of those we shall discuss in Section. 5.6.

5.5.2 Study of D5 branes on S^1 System

By considering the simplest confining field theory in $4+1$-dimensions, constructed by wrapping N_c D5 branes on a circle, imposing periodic boundary conditions for the bosons and anti-periodic boundary conditions for the fermions, we will try to emphasise that the UV behaviour of the field theory dictates whether (or not), we will find a phase transition in the Entanglement Entropy. This example is in analogy with that of Witten in [21] generated by double Wick rotating a black-brane solution.

Choosing $p = 5$ in Eq. 5.3.7, we have in the string frame, a metric of the form

$$\frac{ds^2}{\alpha'} = \left(\frac{u}{R}\right)\left[dx^2_{(1,4)} + f(u)\,d\varphi_c^2\right] + \left(\frac{R}{u}\right)\frac{du^2}{f(u)} + R\,u\,d\Omega_3^2, \qquad R = \sqrt{g_s\alpha' N_c}, \tag{5.5.3}$$

where $f(u)$ and the background dilaton read

$$f(u) = 1 - \left(\frac{\Lambda}{u}\right)^2, \qquad e^{\Phi} = g_s\alpha'\left(\frac{u}{R}\right). \tag{5.5.4}$$

One can change to the radial variable $\rho = \alpha' u$ such that the background and relevant functions

for our calculations are,

$$
\begin{aligned}
ds^2 &= \left(\frac{\rho}{R}\right)\left[dx^2_{(1,4)} + \alpha' f(\rho)\, d\varphi_c^2\right] + \left(\frac{R}{\rho}\right)\frac{d\rho^2}{f(\rho)} + R\rho\, d\Omega_3^2, \qquad R = \sqrt{g_s\alpha' N_c}, \\
f(\rho) &= 1 - \left(\frac{R_\Lambda}{\rho}\right)^2, \qquad e^{\Phi} = g_s\left(\frac{\rho}{R}\right), \qquad R_\Lambda = \alpha'\Lambda, \\
\alpha(\rho) &= \left(\frac{\rho}{R}\right), \qquad \beta(\rho) = \left(\frac{R^2}{\rho^2}\right)\frac{1}{f(\rho)}, \qquad V_{int} = (4\pi)^2\,\ell_\varphi\, R\sqrt{f(\rho)}\,\rho^2, \\
H(\rho) &= \frac{(4\pi)^4}{g_s^4}\, R^2\,\ell_\varphi^2\, f(\rho)\,\rho^4, \qquad \ell_\varphi = \sqrt{\alpha'}\oint d\varphi.
\end{aligned}
\tag{5.5.5}
$$

Using the approximation presented in eq. 5.5.2, one can compute that $L_A(\rho_0)$ asymptotes a constant value from below

$$
L_A(\rho_0 \to \infty) \sim \mathcal{Y}(\rho \to \infty) = \lim_{\rho\to\infty} \pi R \frac{\sqrt{\rho^2(\rho^2 - R_\Lambda^2)}}{(2\rho^2 - R_\Lambda^2)} = \frac{\pi}{2}\sqrt{g_s\alpha' N_c}. \tag{5.5.6}
$$

This means that $L_A(\rho_0)$ does not have any double-valued behaviour for the connected solution and thus the Entanglement Entropy does not exhibit a phase transition (see the third row of Fig. 5.6). Further, the concavity of the connected branch is such that it is unstable throughout the space, and indeed the disconnected solution is the minimal Entanglement Entropy solution for all L_A.

We now venture to ask: are there other solutions with a smaller value for the Entanglement Entropy for some range of values for L_A, that we should also consider?

In [50, 51], it was discussed how non-locality can affect the Entanglement Entropy, and argued that one should add a UV cutoff, such that one can consider solutions that live 'close' to it (solutions represented by B in Fig. 5.9). In the presence of these new solutions, we can have a new minimum for the Entanglement Entropy, but these solutions no longer follow the standard Area-Law divergence, and instead posses an extensive 'Volume-Law' divergence. This observation has also been made in other cases [52–54], and we shall work to understand how these solutions are relevant to our question. Note the similarities to the discussion in Section. 4.1.2 involving the introduction of a UV cutoff.

The possibility of these new solutions, leads us to find that there is also a likelihood of a phase transition between the two divergence behaviours, and thus we can reconcile our puzzle of some models of confinement and lack of the expected phase transition. We shall find in what follows that the Volume-Law behaviour is always associated with the non-local UV behaviour of our models.

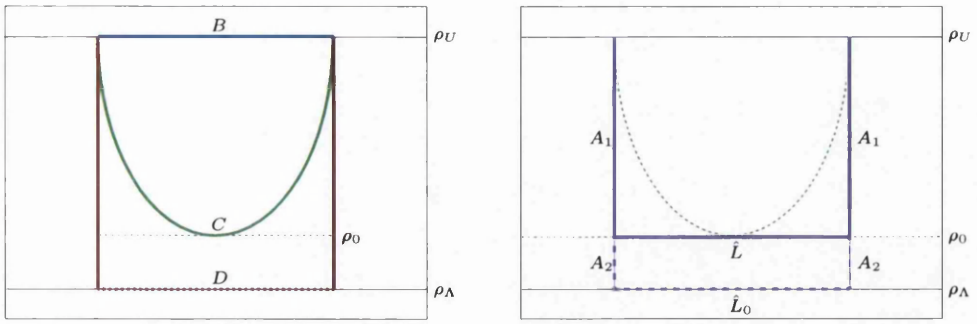

Figure 5.9: Plots of the types of solutions we shall be considering in the left plot and details of the approximation in the right plot. In both, ρ_U represents the UV boundary and ρ_Λ is the IR end-of-space. In the left plot, the red lines (including the dashed line at ρ_Λ) represent the disconnected solution (D), the green line represents a generic connected solution (C) which probes down to a depth ρ_0 and finally in blue are the solutions which live close to the boundary (B) and behave under the Volume Law for the Entanglement Entropy. In the right plot, we outline the various sections of the approximation. The solid purple lines map out the approximation to the connected dashed green solution, which we split into three parts: two vertical contributions labelled as A_1 and a horizontal contribution labelled $\hat{L}$. The surface mapped out by the dashed purple lines, which is useful when we regularise our approximation, consists again of three parts: the two vertical contributions labelled A_2 and the horizontal contribution labelled $\hat{L}_0$.

Let us return to the D5 branes wrapped on a circle to see how our new solutions play a role. As we already know, the introduction of a confinement scale can be associated with the introduction of an unstable branch in the Entanglement Entropy. This now joins our disconnected solutions (with a mutual point at one end of the green unstable branch labelled X in Fig. 5.10) to our new near UV solutions (with a mutual point at the other end of the green unstable branch labelled Y in Fig. 5.10).

Finally, it is important to note that with the introduction of the short configurations, and the possibility of a phase transition between these extensive solutions and the disconnected solution at the point L_c, we can argue this as a sign of non-locality [52–54]. Further, we can propose that this may be a sign that one may want to try and UV complete these theories in a non-trivial way, if they are to be correct duals to fully local Quantum Field Theories.

5.5.3 The Short Configurations

Here we shall further motivate the existence of the short configurations as a completion for some Entanglement Entropy diagrams. It will be instructive to use an approximation similar to the one used in [50].

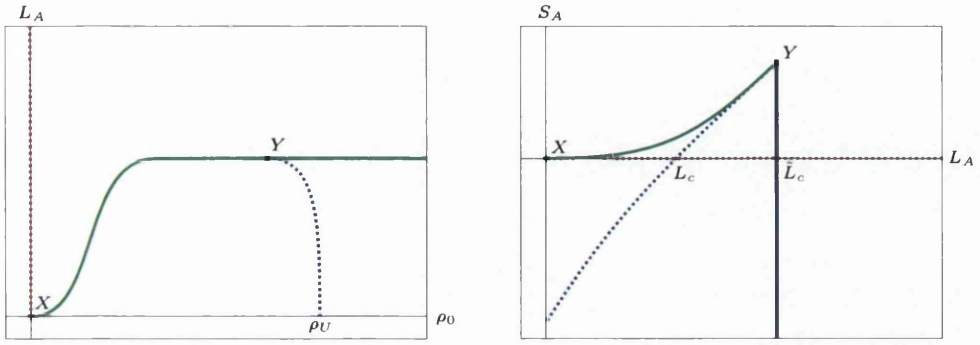

Figure 5.10: Plots of the different types of behaviour in a background like that of the D5 branes wrapped on an S^1. The dashed red line represents the disconnected solution, the green that of the confinement branch, and these join at the point X. With finite UV cutoff ρ_U, we would find something similar to the dashed navy blue branch in both plots for solutions near the cutoff scale. If we increase the UV cutoff (equivalent to moving the point Y to larger values of ρ_0), we find that the gradient of the UV branch increases (and also the value of $L_c < \tilde{L}_c$), such that in the limit that we remove the cutoff completely, it becomes the vertical solid navy blue line and we have a degeneracy of extensive solutions with different values of S_A, but the same value of $L_A = \tilde{L}_c$.

We choose our approximating surface to be a rectangle (which is traced out by the solid purple lines in the right-hand plot of Fig. 5.9), consisting of a horizontal piece $\hat{L}$ sitting at constant ρ_0, and such that it has sides (labelled A_1) which follow the same path as the disconnected surface between ρ_0 and ρ_U (where ρ_U is the point at which we shall cut the space in the UV, and can be removed by taking the limit $\rho_U \to \infty$). To be more precise, we can start by rewriting the Entanglement Entropy of the disconnected solution S_d, by splitting it into a similar construction to that of the approximation,

$$S_d = 2(A_1 + A_2) + \hat{L}_0, \tag{5.5.7}$$

where A_1 is the contribution between ρ_U and ρ_0, while A_2 is the contribution between ρ_0 and the IR end-of-space ρ_Λ. The extra term $\hat{L}_0$ comes from the horizontal piece sitting at the IR end-of-space, but this will be zero in the cases we shall be considering. As alluded to above, we can write the approximating surface as

$$S_a = 2A_1 + \hat{L}. \tag{5.5.8}$$

These approximating solutions are not solutions to the equations of motion and thus are not actual smooth extremal surfaces of the background. But, as A_1 and A_2 are constant for a

particular value of ρ_0, whereas $\hat{L}$ is proportional to L_A, in the limit $L_A \to 0$ we will also find $\hat{L} \to 0$. This leads us to conclude: *there will always exist a small enough value of* L_A *such that* $\hat{L} < 2A_2$, *meaning* $S_a < S_d$. Thus for small enough values of L_A there will exist lower Entanglement Entropy solutions than the disconnected solution.

We will now construct the form of the approximation in terms of the relevant functions to computing the Entanglement Entropy. Starting with $\hat{L}$, we have

$$\hat{L} = \int \prod_{i=1}^{8-d} \prod_{j=1}^{d-1} dy^i \, dx^j \sqrt{g_{ind}} \int du \sqrt{g_{\mu\nu} \dot{X}^\mu \dot{X}^\nu} \tag{5.5.9}$$

describing a volume filling surface in all directions, aside from x_1 and the radial direction ρ. Using the standard parametrisation, with $u = \{-\frac{L_A}{2}, \frac{L_A}{2}\}$, we find

$$\hat{L} \sim V_{int} \, \alpha^{\frac{d}{2}} \, e^{-2\Phi}\Big|_{\rho=\rho_0} L_A = \sqrt{H(\rho_0)} \, L_A. \tag{5.5.10}$$

One can define the distance A_1 by

$$A_1 = \int_{\rho_0}^{\rho_U} d\rho \sqrt{\beta(\rho) H(\rho)} \tag{5.5.11}$$

which is divergent in the limit $\rho_U \to \infty$. Choosing the same regularisation we performed in the case of S_A, we remove the value of the disconnected solution S_d (see Eq. 5.1.5). Thus the approximation is given by

$$S_a(L_A) = \left(\frac{2}{\pi}\right) \sqrt{H(\rho_0)} \, L_A - 2 \int_{\rho_\Lambda}^{\rho_0} d\rho \sqrt{\beta(\rho) H(\rho)} \tag{5.5.12}$$

where an extra multiplicative factor has been added by hand to improve the approximation.

We will now look at how the approximation works in the cases studied in the previous section. Due to our removal of the disconnected solutions from the approximation, in all the following it will again sit on the L_A-axis of the $S_a(L_A)$ plots. Further, the collection of lines given by the approximation, maps out the path of the connected solution in each case very well. Each of the lines which are given by the approximation will cut the L_A-axis whenever $S_a(L_A) = 0$ and this quantity is defined by

$$M_a(\rho_0) = \frac{\int_{\rho_\Lambda}^{\rho_0} d\rho \sqrt{\beta(\rho) H(\rho)}}{\sqrt{H(\rho_0)}} \pi. \tag{5.5.13}$$

In the $AdS_5 \times S^5$ case, depicted in the top left-hand plot of Fig. 5.11, we find that M_a is a

monotonically decreasing function of ρ_0, such that the solutions which are toward the UV of the background sit nearly flat against the S_a-axis, and the solutions toward the IR approach the disconnected solution from below.

In the Soft-Wall case, depicted in the top right-hand plot of Fig. 5.11, we see that the UV solutions again look similar to those of the $AdS_5 \times S^5$ case, as expected. They differ as we move toward the IR, where the lines, instead of having increasing M_a, actually attain a maximum intercept of the L_A-axis (around the point L_c). They then have decreasing intercept approaching the disconnected solution this time from above. The phase transition is mapped out as expected in this case.

Moving to the backgrounds that exhibit non-locality, we initially study the case of the D5 branes (as studied in [50]) and depicted in the bottom left-hand plot of Fig. 5.11. In this case all the lines of the approximation have the same intercept at $L_A = \frac{\pi R}{2}$ (where we have set $R = 1$ in the plot). The gradient of the lines increases as we move toward the UV (for larger values of ρ_0). In the infinite cutoff limit we would expect to find a vertical line passing through $L_A = \frac{\pi R}{2}$, as anticipated.

Finally, we move to the case of D5 branes wrapped on a circle, which is depicted in the bottom right-hand plot of Fig. 5.11. Moving from the IR (with small values of ρ_0) toward the UV, we find an increasing intercept, which approaches the same value as that of the D5 branes above, that of $L_A = \frac{\pi R}{2}$ (with the choice $R = 1$ in the plot). The difference between the two D5 brane cases is that although both exhibit a phase transition between the Area-Law and the Volume-Law behaviour, in the D5 case, the connected solutions all sit at the point of the phase transition $L_A = L_c$, whereas in the case of the wrapped D5 branes, the connected solutions make up the unstable branch.

The introduction of these short configurations living near the cutoff surface play an integral part in the recovery of the phase transition, in the presence of non-locality in the associated Quantum Field Theory, in models of confinement, introducing a stable connected branch to the Entanglement Entropy diagrams, just as happened in the probe-D7 branes in Chapter. 4.

In the following sections we shall see other models which require this cutoff effect, but will show that in some of these cases, a similar resolution can be introduced through a non-trivial UV-completion of the Quantum Field Theory. This then gives a well-behaved phase transition in the Entanglement Entropy, which avoids Volume-Law behaviour for the leading divergence.

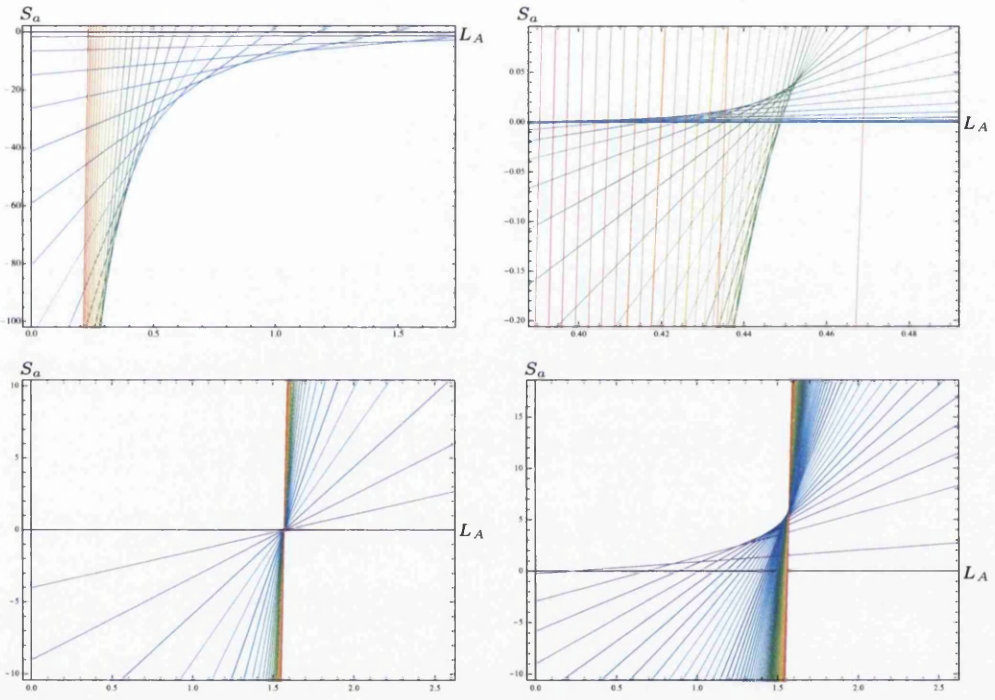

Figure 5.11: Plots of a number of the approximating surfaces $S_a(L_A)$ in different models. The colour scheme is such that purple lines are surfaces with ρ_0 approaching ρ_Λ, and the red solutions which have ρ_0 approaching ρ_U. The top left-hand plot is that of $AdS_5 \times S^5$, the top right-hand is the Soft-Wall model, the bottom left-hand is D5 branes, and the bottom right-hand is D5 branes wrapped on a circle.

5.6 The Absence of Phase Transitions in (Some) Confining Models

One may argue that the model we discussed, i.e. that of the D5 wrapped on a circle, is not a good choice of model for that of a confining theory. As, in principle, $4+1$ dimensional field theories would have weakly coupled IR behaviour, and strongly coupled UV behaviour, it could be that what we observe is just an echo of this, in contradiction to us assuming the model as confining. Then, it would be expected that when looking at duals to $3+1$ dimensional field theories (or $2+1$ dimensional as in Appendix. C.1), that the phase transition should be recovered.

To this end, we shall now analyse the case of a dual Quantum Field Theory obtained by wrapping N_c D5 branes on a two-cycle of the resolved conifold, that we presented as Theory A in Chapter. 2. We find that the UV behaviour is not so different from the one of the D5 branes analysed in Sec. 5.5. Again, one may think that this is because the theory at high energy, has a higher dimensional dual Quantum Field Theory (which can be seen through the fact that there is an infinite set of 'Kaluza-Klein' modes coming from the compactification of the branes). This is correct, but the point is subtle. It has been shown [56] that in the perturbative regime, the field theory is equivalent to four-dimensional $\mathcal{N}=1^*$ Yang-Mills, expanded about a particular point on its Higgs branch, which is a well-defined four-dimensional Quantum Field Theory. Further, we would find the same 'Kaluza-Klein' modes in the case of wrapping a stack of D4 branes on a circle (discussed in Eq. 5.3.7), and it was seen that there is a phase transition associated with the model confining. We shall now calculate the Entanglement Entropy for this model.

The functions required to calculate the Entanglement Entropy in the background Eq. 2.1.10 (in the string-frame) are,

$$\alpha = e^{\Phi}, \quad \beta = \alpha' g_s e^{2k}, \quad V_{int}^2 = (2\pi)^6 (\alpha' g_s)^5 e^{4h+4g+5\Phi+2k},$$
$$H = (2\pi)^6 (\alpha' g_s)^5 e^{4\Phi+4g+4h+2k}. \tag{5.6.1}$$

Initially, we will look at the case of the CVMN model, which is known analytically and presented in Eq. 2.2.5. This is characterised in terms of the function $\hat{P}(\rho) = 2N_c\rho$ from the perspective of solutions to the 'Master Equation'. In this case, the behaviour of the dilaton is $e^{4\Phi} \sim \frac{e^{4\rho}}{\rho}$ which is reminiscent of the dilaton behaviour in Eq. 5.5.5 (when one makes the change of variable as $\rho \sim \log r$), and thus both are examples of backgrounds with a linear dilaton.

If we now calculate the Entanglement Entropy $S_A(L_A)$ in the CVMN case, then it can be seen (as in Fig. 5.12) that the minimal solution is given by the disconnected solution and the connected solution maps out an unstable branch for all L_A. Further, the connected branch only exists $0 < L_A < \frac{\pi}{2}\sqrt{g_s\alpha' N_c}$ such that $S_c(L_A \to 0) = 0$ and $S_c(L_A \to \frac{\pi}{2}\sqrt{g_s\alpha' N_c}) = \infty$. Using

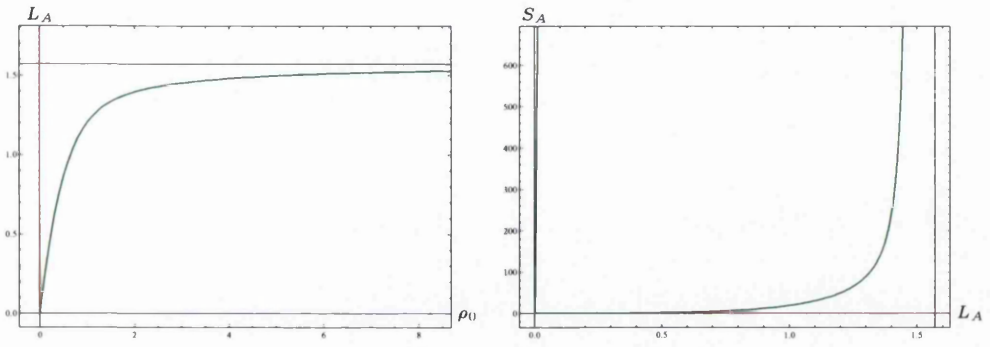

Figure 5.12: Plots of the functions $L_A(\rho_0)$ on the left, and $S_A(L_A)$ on the right, in the CVMN system of D5 branes wrapped on a two-cycle. The solid blue line represents the connected solution while the dashed red line is the disconnected solution.

the approximation in Eq. 5.5.2, we find that

$$\begin{aligned} L_A(\rho) \sim \mathcal{Y}(\rho) &= \sqrt{\alpha' g_s}\pi \frac{e^k}{2\Phi' + 2h' + 2g' + k'} \\ &= \frac{\pi\sqrt{\alpha' g_s}P'}{\sqrt{2}} \frac{(P^2 - Q^2)}{\left(2P^2\coth(2\rho) + PP' - QQ' - 2Q^2\coth(2\rho)\right)}. \end{aligned} \tag{5.6.2}$$

such that using the CVMN exact solution gives for the approximated asymptotics of the function $L_A(\rho_0)$,

$$L_A(\rho_0 \to 0) \sim \frac{\pi\sqrt{\alpha' g_s N_c}}{2}\rho_0, \qquad L_A(\rho_0 \to \infty) \sim \frac{\pi\sqrt{\alpha' g_s N_c}}{2}(1 - \frac{1}{4\rho_0}). \tag{5.6.3}$$

It is interesting to note that the Heisenberg-like relation $L_A \sim \frac{1}{\rho_0}$ is violated here. Further, we see that the entropy scales as

$$\frac{G_{10}S_c}{V_2} \sim (\alpha' g_s)^3 N_c^{\frac{3}{2}}.$$

So, as in the example of D5 branes wrapped on a circle, we see that the connected configuration is unstable, such that it doesn't satisfy the correct concavity condition in Eq. 5.3.20. Again, we do not have a phase transition and thus we look to the short configurations and the effect of a

UV cutoff. *

In Fig. 5.13, we show the effect of adding in the short configurations upon the introduction of a UV cutoff. They are (as we have also seen in the context of the probe-D7 branes in the last Chapter), the *correct* configurations to consider, allowing us to remove the issue we face with the instability of the connected branch of configurations. Thus, the phase transition in $S_A(L_A)$ is recovered, and one would expect from a confining model [48].

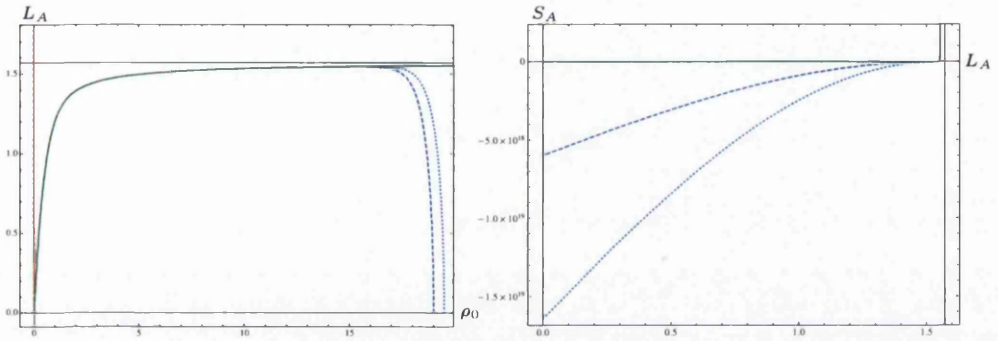

Figure 5.13: Plots of the functions $L_A(\rho_0)$ on the left, and $S_A(L_A)$ on the right, in the system of D5 branes wrapped on a two-cycle, but this time with a UV cutoff in place. The green line is the solution without UV cutoff, the dashed blue line is with the UV cutoff at $\rho_U = 19$, the dotted blue is with the cutoff at $\rho_U = 19.5$, and finally the dashed red line represents the disconnected solution. Notice that increasing the value of ρ_U leads to an increase in the gradient in the visible branch in the $S_A(L_A)$ plot in the right-hand plot.

5.6.1 Further Comments on Non-Locality

If we now turn our attention to the solutions with exponential asymptotics for $P(\rho)$ defined in Eq. 2.2.14, which describe another family of solutions associated with Theory A (but the field theory has different operators driving the dynamics), we shall try to further understand the ideas surrounding this non-locality.

In contrast to the CVMN solution, as mentioned before, we only know this second solution semi-analytically. The corresponding expansions are given in Eq. 2.2.8, and Eq. 2.2.14. As discussed, the IR expansion is similar to that of the CVMN solution, but in the UV the behaviour of $P(\rho)$ is exponential rather than linear. We have also seen how this is associated with a dimension-eight irrelevant operator driving the dynamics. One can think of this as a similar

*These "finite size" effects reflected in the non-zero asymptotic value of L_A at infinity have also been observed in the Wilson Loop when calculated in the CVMN background [66, 110–112].

situation to retaining a constant factor in the warp factor of the D3 brane solution, such that the warp factor then reads $\hat{h} = 1 + \frac{L^4}{r^4}$, and this extra factor makes the background dual to $\mathcal{N} = 4$ Super Yang-Mills in the presence of a dimension-eight operator. Then to UV complete the Quantum Field Theory, we are required to reintroduce the whole tower of string modes.

The non-locality in the new background will turn out to be more severe than in the case of the CVMN solution. Calculating the Entanglement Entropy in this case (where the irrelevant operator is inserted with a small coefficient $h_1 = 2N_c + \epsilon$), we find the results depicted in Fig. 5.14. It can be seen from the left-hand plot, that $L_A(\rho_0)$ increases without bound, and again there is only the disconnected configurations as the minimal solutions. This behaviour is such that we depart further from the Heisenberg-like scaling we expect for local field theories.

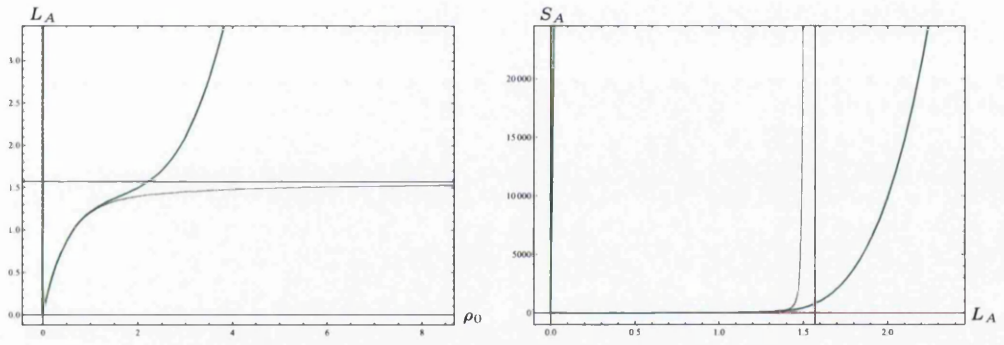

Figure 5.14: Plots of the functions $L_A(\rho_0)$ on the left, and $S_A(L_A)$ on the right, in the system of D5s on a two-cycle, but this time with exponential behaviour in P ($h_1 = \frac{203}{100}N_c$). The solid blue line represents the connected solution while the dashed red line is the disconnected solution. The grey line is the linear P solution ($h_1 = 2N_c$) for comparison.

So even when we have a dual background which exhibits a confining Wilson Loop [*], the system fails to show a phase transition in the Entanglement Entropy and thus we must again appeal to the short configurations to recover our phase transition. This is due to the UV properties of the field theory. In Appendix. C.1 we discuss another system which have similar high energy behaviour in the field theory.

In the next section, we shall see that if one uses the *rotation* procedure described in Chapter. 2, such that we UV complete the field theory of this setup in terms of an inverse Higgs Mechanism, we fully recover the phase transition with the correct Heisenberg-like scaling.

[*] In the case of $P(\rho)$ growing exponentially for large ρ, the Wilson Loop calculation cannot strictly be performed due to the violation of the boundary conditions for the strings at infinity [97].

5.6.2 The Baryonic Branch of Klebanov-Strassler

We have seen that in the case of the field Theory A (dual to a stack of N_c D5 branes compactified on a two-cycle of the resolved conifold), the non-local UV properties require the introduction of a UV cutoff (and the associated short configurations) to recover a phase transition in the Entanglement Entropy (even if the Wilson Loop displays the correct Area-Law). Here we look at a different way of recovering the phase transition with local UV behaviour, by using the *rotation*, which connects this system to that of the baryonic branch of Klebanov-Strassler described by Theory B.

As we discussed, the specific choice of the constant κ associated with the *rotation*, is associated with choosing the warp factor such that it goes to zero and switches off the dimension-eight irrelevant operator, whilst preserving the IR behaviour of the background. The new background generated (with the presence of extra fluxes) is written in Eq. 2.1.14.

Now, the quantities required for the calculation of the Entanglement Entropy are given by

$$\begin{aligned} \alpha = e^{\Phi}\hat{h}^{-1/2}, \quad \beta =& g_s\alpha' e^{2k}\hat{h}, \quad V_{int}^2 = (2\pi)^6(\alpha' g_s)^5 e^{4h+4g+5\Phi+2k}\hat{h}^{5/2}, \\ H =& (2\pi)^6(\alpha' g_s)^5 e^{4\Phi+4g+4h+2k}\hat{h}. \end{aligned} \tag{5.6.4}$$

The obvious difference between Eq. 5.6.1 and these new quantities is the presence of the factor $\hat{h}$, defined in Eq. 2.1.15. At large ρ this warp factor behaves as,

$$\hat{h} \sim \frac{3N_c^2}{8c_+^2}(8\rho - 1)e^{-8\rho/3} + \dots \tag{5.6.5}$$

and it is this that brings back the decaying behaviour and thus the phase transition in the Entanglement Entropy. Using the approximation of L_A given in Eq. 5.5.2

$$L_A(\rho) \sim \mathcal{Y}(\rho) = 2\pi\sqrt{\alpha' g_s}\frac{e^k\sqrt{\hat{h}}}{(4\Phi' + 4g' + 4h' + 2k') + \frac{\hat{h}'}{\hat{h}}}, \tag{5.6.6}$$

with IR and UV behaviour given by

$$L_A(\rho_0 \to 0) \sim \rho_0, \qquad L_A(\rho_0 \to \infty) \sim e^{-2\rho_0/3}. \tag{5.6.7}$$

As anticipated, the IR behaviour is basically unchanged from the CVMN case, as the warp factor is approximately one for small ρ. The UV behaviour on the other hand is different, and now dominated by the behaviour of the warp factor at large ρ. Notice also, that in a convenient

radial variable $r = e^{2\rho/3}$, we have

$$L_A(r_0 \to \infty) \sim \frac{1}{r_0}, \tag{5.6.8}$$

which is a signal of locality according to [50]. Thus we see that the UV-completion by *rotating* onto the baryonic branch field theory (Theory B) has recovered locality. What does this mean for the phase transition in the Entanglement Entropy? The results for the calculation of the Entanglement Entropy in association with the baryonic branch of the Klebanov-Strassler field theory can be seen in Fig. 5.15.

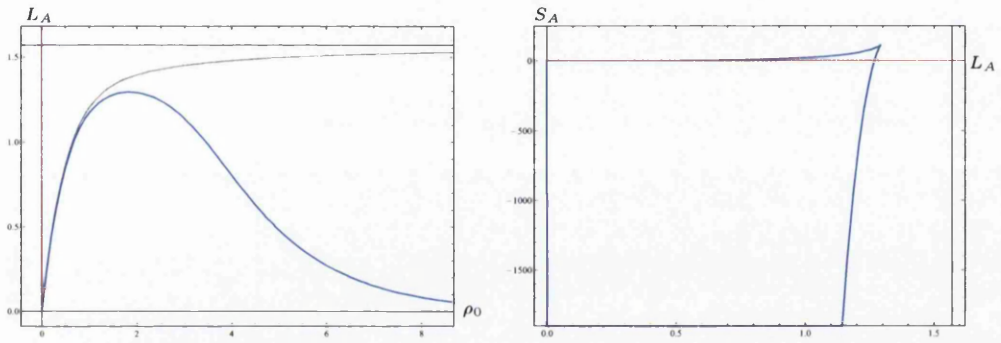

Figure 5.15: Plots of the functions $L_A(\rho_0)$ on the left, and $S_A(L_A)$ on the right, for a typical solution on the baryonic branch of Klebanov-Strassler ($h_1 = \frac{203}{100}N_c$). The solid blue line represents the connected solution while the dashed red line is the disconnected solution. The grey line is the linear P solution ($h_1 = 2N_c$) for comparison.

Thus we have solved the problem of recovering the phase transition in the Entanglement Entropy for these models of confinement.

To conclude this section we shall briefly look at the effect of introducing the dimension-six VEV associated with the walking solutions defined in Eq. 2.2.11. In [20], the authors showed that changing the scale ρ_* associated with this VEV introduced a first-order phase transition in the calculation of the rectangular Wilson Loop. It is interesting to see how the equivalent effect translates to the Entanglement Entropy. In the presence of this VEV, it appears that the Entanglement Entropy is suppressed in the IR of the theory, below the associated scale ρ_*. This effect can be seen in Fig. 5.16, and it appears that increasing the size of the VEV is directly linked to increasing the severity of the first-order phase transition in the Entanglement Entropy. This is supported by the fact that in [20] they also calculated the central charge in the same walking solutions, and that in the presence of the VEV they argued that in field theory

terms a large number of degrees of freedom freeze below the scale ρ_*, and the central charge is suppressed.

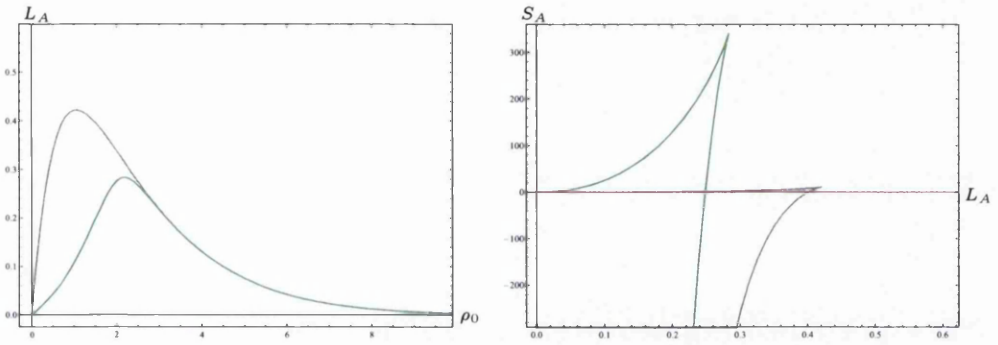

Figure 5.16: Plots of the functions $L_A(\rho_0)$ on the left, and $S_A(L_A)$ on the right, for a typical walking solution on the baryonic branch of Klebanov-Strassler (with $\rho_* \simeq 2$). The solid green line represents the connected solution for the walking case, while the dashed red line is the disconnected solution and the grey line is the equivalent solution on the baryonic branch with no walking present.

Now we look at a number of calculations which will lead to an improved understanding of the Klebanov-Strassler system (in agreement with the ideas presented in [60]). We will move our field theory to a mesonic branch. Initially, we shall do this in such a way, as was argued in [62], that towards high energies the evolution of the Quantum Field Theory is described in terms of Seiberg dualities, but more importantly successive 'Higgsing', which changes the matter content quickly. This growth of the matter content is equivalent to the addition of another irrelevant operator (of dimension-six in this case, different from the dimension-eight one we have discussed above). This was discussed in detail in [62, 113].

As a consequence of the insertion of this new high-dimensional irrelevant operator, with the added non-localities to the Quantum Field Theory (originally discussed in [113]), we will lose the phase transition. We will then explain how to restore the phase transition, through a precise way of switching off this new irrelevant operator.

5.6.3 The Addition of Sources

Here we shall look at the effect on the Entanglement Entropy if we move our Theory B (that of the Klebanov-Strassler Quantum Field Theory on the baryonic branch) to a mesonic branch. From the point of view of the quiver theory, we do this by de-tuning the ranks of the two gauge groups, which in baryonic branch is given by $SU(N_c + n) \times SU(n)$. If we add matter in the

form of D5 branes with induced D3 brane charge in the dual background we can change the gauge group to $SU(N_c + n + n_f + \frac{N_f}{2}) \times SU(n + n_f)$. The N_f D5 branes and n_f D3 branes are added as sources such that the background is a solution to the equations of motion of Type IIB Supergravity, but also there is a Born-Infeld Wess-Zumino action for the sources. The associated solutions were discussed in detail in [62, 113]. A characteristic of these backgrounds is that the sources must be added with a 'profile' $\mathcal{S}$ (describing how the sources are smeared), which vanishes toward the IR end-of-space to avoid curvature singularities (see discussions in [69, 112, 113]). Such a profile that preserves the same amount of Supersymmetry as the background and avoids singularities is given by [112]

$$\mathcal{S}(\rho) = N_f \tanh(2\rho)^4. \tag{5.6.9}$$

Further, this profile can be translated to become 'active' at a finite value of $\hat{\rho}$

$$\mathcal{S}(\rho) = N_f \, \Theta(\rho - \hat{\rho}) \tanh(2\rho - 2\hat{\rho})^4 \tag{5.6.10}$$

which still preserves the same amount of Supersymmetries and avoids singular behaviour.

There exists a change of basis for the background functions similar to the one we described in Chapter. 2, such that it can be reduced to solving a modified version of the 'Master Equation' for a single function $P(\rho)$. This will contain all the effects of the extra (N_f, n_f) D5 and D3 brane sources. Further, an equivalent *rotation* technique was derived, which takes solutions onto the mesonic branch of the Klebanov-Strassler Field Theory. We shall present the form of the modified 'Master Equation' below but a clear summary of the details of the setup can be found in [113].

The modified 'Master Equation' is of the form [113]

$$P'' + N_f \mathcal{S}' + (P' + N_f \mathcal{S}) \left(\frac{P' + Q' + 2N_f \mathcal{S}}{P - Q} + \frac{P' - Q' + 2N_f \mathcal{S}}{P + Q} - 4 \coth(2\rho) \right) = 0, \tag{5.6.11}$$

where we have chosen the IR end-of-space to be at $\rho_\Lambda = 0$. The modified form of Q is given by

$$Q = \coth(2\rho) \left(\int_0^\rho dx \, \frac{2N_c - N_f \mathcal{S}(x)}{\coth(2x)^2} \right), \tag{5.6.12}$$

where an integration constant has been set to avoid singularities in the IR. These can be seen to reduce to Eq. 2.2.2 when $N_f = \mathcal{S} = 0$.

A solution encoding the effect of the sources was found in [62, 113]. The large radius asymptotics of the warp factor $\hat{h}$ (as in Eq. 2.1.15) using the radial coordinate $u = e^{2\rho/3}$, is

given by

$$\lim_{u\to\infty} \hat{h} \sim \frac{N_f u^2 + 3N_c^2 \log u}{u^4}, \tag{5.6.13}$$

which deviates from the cascading behaviour of the Klebanov-Strassler Quantum Field Theory in Eq. 5.6.5 by (what appears to be) the addition of a dimension-six irrelevant operator. As discussed in [113], from a field theory perspective, the number of additional D3 brane sources given by n_f grows very fast as

$$n_f \sim \mathcal{S}(\rho)(\sinh(4\rho) - 4\rho)^{1/3} \sim e^{4\rho/3}, \tag{5.6.14}$$

and this rapid growth of the gauge group ranks as we move to higher energies (a 'Higgsing' occurs every time a sourced D3 brane is crossed) means that the Quantum Field Theory loses the four-dimensional character of the Klebanov-Strassler Quantum Field Theory.

In the calculation of the Wilson Loop in these backgrounds, for the solutions discussed, the result is that of an Area-Law behaviour indicative of confinement [111]. From what we have seen earlier, we should expect that even though the Wilson Loop shows the correct behaviour, for the Entanglement Entropy we shall not have a phase transition due to the presence of this dimension-six irrelevant operator. *

If we now move to calculate the Entanglement Entropy in this case one finds this is true. If we look at the IR behaviour $L_A(\rho_0 \to 0) \sim \rho_0$ it is unchanged, whereas in the UV we find

$$L_A(\rho_0 \to \infty) = \mathcal{Y}(\rho \to \infty) \sim \frac{3\pi\sqrt{\alpha' g_s N_f}}{8}. \tag{5.6.15}$$

The results can be seen in Fig. 5.17, such that unless we appeal to the short configurations, we do not have a phase transition.

One may conclude from this that although the field theory maybe be in a mesonic branch with good IR properties, we need to remove the fast growth of source degrees of freedom as we move to higher energies, by 'localising' the sources. This should allow us to recover the high energy four-dimensional behaviour seen in the case of the baryonic branch of Klebanov-Strassler (by UV-completing the system via the *rotation* procedure).

5.6.4 Sources with a Decaying Profile

As we have just discussed, the phase transition in the Entanglement Entropy being removed (without introducing the short configurations), as well as the form of the warp factor given

*Note that the Wilson Loop does experience finite-size effects similar to those seen in the CVMN case.

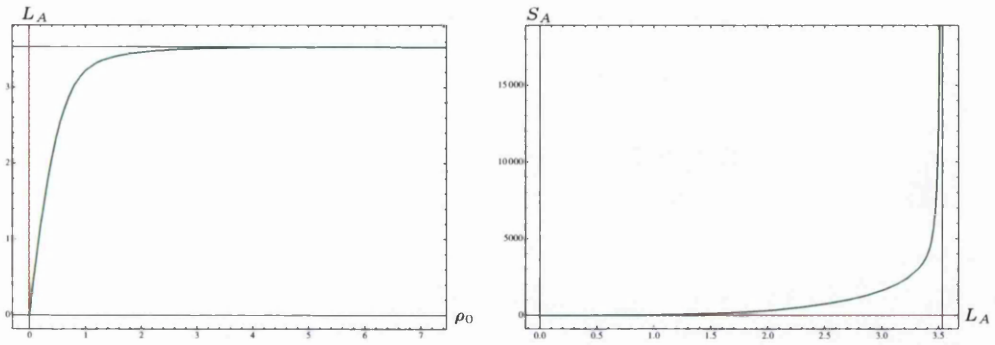

Figure 5.17: Plots of the functions $L_A(\rho_0)$ on the left, and $S_A(L_A)$ on the right, for a typical solution with $\mathcal{S} \to N_f$ in the UV ($N_c = 4$ and $N_f = 9$). The solid blue line represents the connected solution while the dashed red line is the disconnected solution. Note that we have chosen a value of h_1 such that we have hardly any linear behaviour in P.

in Eq. 5.6.13, indicates that the dual Quantum Field Theory is not behaving as a nice four-dimensional field theory, in the sense that 'locality' is being lost. As described, this appears to be due to the rapid growth of degrees of freedom [113], due to the addition of sources.

In backgrounds where we have a profile given by $\mathcal{S} \sim \tanh(2\rho)^4$, this is reflected in the fact that as we flow to the UV, we have a superposition of two behaviours. The first is the Seiberg dualities as seen through the presence of the logarithmic term in Eq. 5.6.13, and a 'Higgsing', shown by the term which is quadratic in the radial variable u. Similar interplay between these two effects have been before in [114, 115]. As a consequence, the solution with the source profile $\mathcal{S} \sim \tanh(2\rho)^4$ at high energies, is dominated by the 'Higgsing', and thus the UV of the field theory has behaviour differing from that of a four-dimensional Quantum Field Theory. This is reflected in the Entanglement Entropy, and the lack of a well behaved phase transition, unlike that achieved in Section. 5.6.2.

We now look to see if it is possible to force this mesonic branch solution of the Klebanov-Strassler Field Theory, to behave like four-dimensional Quantum Field Theory in the UV. To this end, we slow down the growth of the degrees of freedom by proposing (as in [113]) a *phenomenologically* supported profile for the sources. This profile is not derived from first principles, unlike a profile which is kappa symmetric, but nevertheless it will be of interest. The profile in question does have the following properties,

1. The background still satisfies BPS equations, suggesting the preservation of Supersymmetry.

2. The energy density of the sources T_{00} is positive definite for profiles that decay at most as fast as the one we will propose.

3. The central charge of the dual Quantum Field Theory when calculated with this profile is a monotonically increasing function.

and takes the form

$$\mathcal{S}(\rho) = N_f \tanh(2\rho)^4 e^{-4\rho/3}. \tag{5.6.16}$$

With a profile of this form it is possible to find a background solution in which it can be thought that the sources are 'localised', and the dual Quantum Field Theory is in a mesonic branch. The explicit background solution and a more detailed explanation can be found in [113].

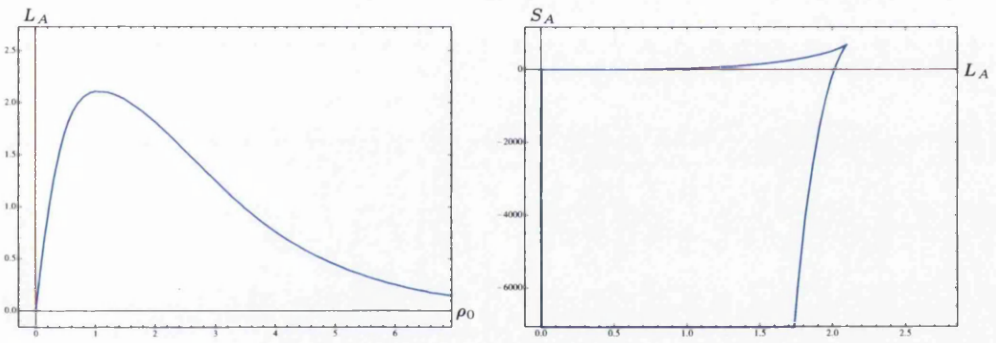

Figure 5.18: Plots of the functions $L_A(\rho_0)$ on the left, and $S_A(L_A)$ on the right, for a typical solution with $\mathcal{S} \to 0$ in the UV ($N_c = 4$ and $N_f = 9$). The solid blue line represents the connected solution while the dashed red line is the disconnected solution. Note that we have chosen a value of h_1 such that we have hardly any linear behaviour in P.

The warp factor in these new solutions is modified such that it now reads

$$\hat{h}(\rho \to \infty) \sim \frac{3}{8c^2}\Big[N_c^2(8\rho - 1) + 2cN_f - 4N_c N_f \mathcal{S}_\infty\Big] e^{-8\rho/3} + \dots$$
$$\mathcal{S}_\infty = \int_0^\infty d\rho\, \mathcal{S} \tanh(2\rho)^2.$$

If we compare this with Eq. 5.6.13, the decay of the warp factor is the same, and the cascade of Seiberg dualities is present through the term $N_c^2\rho$ (which takes this form in the radial coordinate ρ). Further, the constant term is the effect of the sources, which still contribute even though they are heavily suppressed as we move into the UV. If we look at this in terms of the radial

coordinate $u = e^{2\rho/3}$, we see that the sources contribute to the warp factor as $\hat{h} \sim \frac{N_f}{u^4}$, which is as expected for a localised stack of $N_f \sim n_f$ D3 branes.

If we then calculate the Entanglement Entropy in this setup, we find that the phase transition is recovered, as can be seen in Fig. 5.18. In this case we still find that $L_A(\rho \to \infty) \sim \frac{1}{\rho_0}$, in agreement with the locality criteria of [50]. An interesting observation is that we can again translate the point $\hat{\rho}$ at which the sources become active by using a profile of the form

$$\mathcal{S}(\rho) = N_f\, \Theta(\rho - \rho_*) \tanh(2\rho - 2\rho_*)^4 e^{-4\rho/3} \tag{5.6.17}$$

and this introduces another scale into the system. Then it turns out that it is possible to gain a double-phase transition in the Entanglement Entropy (for a more detailed discussion of the role of the various scales, see [5]), as shown in Fig. 5.19, and calculated in the mesonic branch of the Klebanov-Strassler field theory, in the presence of a localised distribution of matter, represented by a D3-D5 bound state.

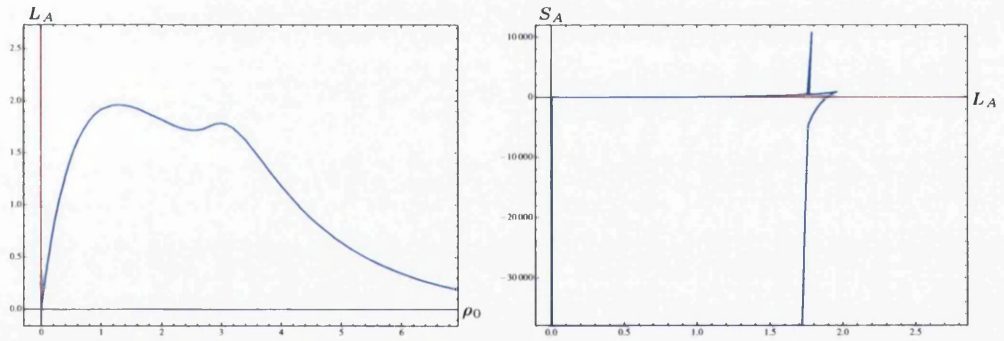

Figure 5.19: Plots of the functions $L_A(\rho_0)$ on the left, and $S_A(L_A)$ on the right, for a typical solution with $\mathcal{S} \to 0$ in the UV but $\hat{\rho} = \frac{25}{10}$ ($N_c = 4$ and $N_f = 9$). The solid blue line represents the connected solution while the dashed red line is the disconnected solution. Note that we have chosen a value of h_1 such that we have hardly any linear behaviour in P.

Finally, we close by emphasising that our findings are in line with that of [48] in that a phase transition in the Entanglement Entropy is a signal of a confining Quantum Field Theory. What we have seen is that we should be careful about the UV behaviour of the field theory, for instance if non-local effects play a role, we should look to cutoff effects or a UV completion, to recover the associated phase transition. Further, we can think of our findings for the Entanglement Entropy as a good diagnostic tool in deciding if a Quantum Field Theory is showing, or is

not showing, the correct high energy behaviour expected from a four-dimensional (or lower) Quantum Field Theory, free of non-localities.

Chapter 6

Conclusions

Here we summarise the findings of this thesis, and present a number of potentially interesting avenues of investigation.

In Chapter. 3 of this thesis we used IR and UV expansions, and the numerical interpolation between them, to study the globally regular backgrounds dual to particular non-Supersymmetric field theories. The field theories were those defined in Chapter. 2, Theory A and Theory B. We calculated a number of observables at low and high energies, which supported the field theory interpretation as soft-breaking via the introduction of masses for the gauginos. This is such that much of the structure of the Supersymmetric case remains and the non-Supersymmetric deformation only gives corrections to this.

We progressed to studying the full two-dimensional solution space, which generalises the Supersymmetric baryonic branch solutions, in more detail. This prompted us to find generalisations to its limiting cases (that of the CVMN background and the Klebanov-Strassler background). In the corresponding limit of the Supersymmetric CVMN case we obtained, as the correct non-Supersymmetric generalisation, the solutions presented in [25] (GTV). In the limit corresponding to the Supersymmetric Klebanov-Strassler solution, we found the solutions of [70] (DK). The behaviour of the generic solutions lying away from these boundaries was understood to be a combination of the effects seen in the Supersymmetric baryonic branch solutions, and those of GTV.

In addition to these two limiting cases, we found two additional one-parameter families of solutions. The first is the boundary on which the solution space has $v_2 = w_2 = 0$ where it appears that Supersymmetry is no longer softly broken, and we find the geometry changes to an intrinsically non-Supersymmetric case (a cone over $S^2 \times S^3$ related to the solution presented in

[85]). Further, the UV expansion now has new trigonometric terms appearing at a subleading order. A second family is in the case where $w_2 = -2$, where the geometry possesses a $\mathbb{Z}_2$ symmetry like that of the Supersymmetric Klebanov-Strassler solution. Curiously, in all the solutions in this family, the function M_1, which we associated in the Supersymmetric case with the baryonic VEV, is zero throughout the space. We discussed the fact that for every solution with $w_2 > -2$, there is a corresponding solution with $w_2 < -2$, and they are related via a $\mathbb{Z}_2$ transformation. These two solutions, although appearing different, actually describe the same physical system, which seems to correspond to the freedom to interchange the baryons A and B.

It would be possible to learn more about how much of the Supersymmetric system is preserved if we were to calculate the mass spectrum and compare this with the results from the Supersymmetric baryonic branch case. Although in the case of soft-breaking we discussed some idea to support the stability of these non-Supersymmetric deformations, this discussion does not necessarily extend beyond soft-breaking. Thus it would be of interest to see if these solutions in the full two-dimensional solution space are actually stable.

It would also be of interest to look at other models which may lead to a similar solution space under non-Supersymmetric deformations. A suitable candidate is the setup describing D5 branes wrapped on a three-cycle (described in Appendix. C.1). One would expect a similar set of boundaries to emerge, with the possibility of finding a completely non-Supersymmetric case analogous to that of Section. 3.7.2. Here the dual field theory would be $2+1$-dimensional. Further, due to the simplicity of the boundary solutions which exhibit the oscillatory behaviour in the background functions, we may try applying the ideas of Non-Abelian T-duality to these solutions (see for instance [116]), which may turn up interesting new features in the dual field theory.

In Chapter. 4 of this thesis, we studied the behaviour of probe-D7 branes in a collection of backgrounds. We began by introducing a general formalism for dealing with probes that have an action of the form Eq. 4.1.1. Using this form, we proposed an effective diagonostic tool $\mathcal{Z}$ for perturbative stability, arguing that $\mathcal{Z} \leq 0$ is a sufficient condition for perturbative stability. On the other hand, if $\mathcal{Z} > 0$ for any range of the radial coordinate, then these backgrounds present instabilities. This was discussed through a thermodynamic anology in Appendix. B.1.

Further to this, we discussed the fact that in particular cases (relevant to the backgrounds with P exponentially growing in the UV), there can be a problem if one does not first introduce a UV cutoff in the calculation, find the minimal solutions with the cutoff fixed, and only

thereafter remove the cutoff. In this case there are configuratons, which exist close to the cutoff surface, that are the minimal action configurations in some cases where the separation of the usual connected configurations is non-zero for large values of ρ_0. Thus we examined the idea of a bulk phase transition, which in effect puts a bound on the allowed range of the control parameter, showing that below this point the gravity calculation is no longer connected to the dual field theory. Notably, a new feature emerged in the context of the flavored Abelian background, namely the bulk phase transition is second-order. It would be interesting to try to understand whether this arises in other instances (in all other cases we discussed, the bulk phase transition was of first-order).

We then systematically discussed the various Supersymmetric solutions presented in Section. 2.2 and found that one can effectively model Chiral-symmetry breaking in the walking model with CVMN UV asymptotics for P. This setup, in the presence of the walking scale ρ_*, has a first-order phase transition between the connected and disconnected configurations at a point $\bar{\varphi}_c$ which depends on ρ_*. Also, Chiral-symmetry breaking can be modelled in a background with a small value for ρ_* and exponential behaviour for P in the UV. Here there is also a bulk phase transition, this time with $\bar{\varphi}_a = \frac{\sqrt{6}\pi}{4}$, limiting the range over which $\bar{\varphi}$ is related to the dual field theory. Further, the smallness of ρ_* means it is likely that the walking region (associated with the 'slow running' of the gauge coupling defined in Eq. 2.2.13) in these backgrounds is negligible.

We also discovered the origin of the instability found in [88], by using $\mathcal{Z}$. In this case $\mathcal{Z} > 0$ for all values of the radial coordinate, so that all connected configurations are unstable and the (Chiral-symmetry preserving) disconnected configurations are preferred for all allowed values of $\bar{\varphi} > \bar{\varphi}_a$. At $\bar{\varphi}_a$ there is a bulk phase transition, but this only limits the allowed values of $\bar{\varphi}$.

It would be of particular interest to find non-Supersymmetric probe-D7 brane embeddings on the baryonic branch of Klebanov-Strassler, but due to the presence of the background B_2, these type of embeddings would likely fall outside of our formalism setup in Section. 4.1.1. Also, it would be interesting to investigate the behaviour of these probe-D7 branes, in a recent set of backgrounds related to Klebanov-Strassler [117] in the presence of a dimension-six VEV, reminiscent of the one in the walking solutions. Further, it would be interesting to complete the picture of the alternative embedding discussed in Appendix. B.2.

Finally, in Chapter. 5 of this thesis we discussed the behaviour of Entanglement Entropy in models of confinement. We began by considering the analogy between the holographic calculations of the Wilson Loop and the Entanglement Entropy. Since both are minimisation

problems, they display many of the same features. This aside, the two observables behave differently in the case of confining theories, where the Wilson Loop has a linear IR dependence between the energy and separation of the quark-antiquark pair, whereas in the Entanglement Entropy we find a first-order phase transition. Next we calculated a set of conditions under which the Entanglement Entropy shows such a phase transition, and tested these in a number of examples.

We then showed that in some models based on higher Dp branes ($p > 4$) there was an absence of a phase transition in the Entanglement Entropy. This led us to the idea of non-locality in a Quantum Field Theory, Volume-Law behaviour for the Entanglement Entropy and the realisation that we are required to introduce a UV cutoff to recover some short configurations (which has crossover with the ideas of Section. 4.1.2) which complete the Entanglement Entropy diagrams.

This resolution may seem somewhat hard to stomach, but we point out that it recovers what one would expect if a UV completion for the field theory was given. This point was made clearer by using the solutions described in Chapter. 2, and showing that under the *rotation* procedure one is no longer required to introduce the short configurations to gain a well behaved phase transition in the Entanglement Entropy. This recovery of a first-order phase transition was shown, in the case of both the baryonic branch and the mesonic branch (through backgrounds in the presence of sources with a decaying profile). This gave a pleasing picture, linking confining, non-local Quantum Field Theories, and their local UV-completed counterparts. Thus we can understand the Entanglement Entropy as a measure of both locality and confinement.

We also considered the case of the walking solutions on the baryonic branch, which have been shown to give a first-order phase transition in the calculation of the Wilson Loop. Interestingly, the presence of the dimension-six VEV (associated with the walking scale ρ_*), led to an increase in the severity of the phase transition associated with the Entanglement Entropy. It would be useful to find a more complete picture of the relationship between phase transitions in the two observables.

It would be interesting to see if there are a set of rules that can be derived using the form of the Entanglement Entropy, that could then be used to give ideas about how to reverse-engineer backgrounds that have both confinement, and UV locality. This could potentially be used in conjunction with invariance of the Entanglement Entropy under different dualities (it is already understood to be invariant under S-duality and non-Abelian T-duality [116, 118]) to discover new supergravity solutions.

Appendix A

Appendix A

A.1 Equations of Motion

In this appendix we write the full equations of motion, associated with the setup Eq. 2.1.8. We start with the effective Lagrangian and the constraint, and then write the equations of motion and have set $N_c = 1$ for simplicity.

The effective Lagrangian is $L = T - U$, with

$$T = -\frac{1}{128}e^{2\Phi}\Big\{e^{4g}\left(a'\right)^2 + \left(b'\right)^2 - 8e^{2(g+h)}\Big[2g'\left(2h' + k' + 2\Phi'\right) + \left(g'\right)^2 + 2h'\left(k' + 2\Phi'\right) + \left(h'\right)^2 + 2\Phi'\left(k' + \Phi'\right)\Big]\Big\}, \tag{A.1.1}$$

$$\begin{aligned} U = \frac{1}{256}e^{-2(g+h-\Phi)}\Big\{ & a^4e^{4g}\left(1 + e^{4k}\right) - 4a^3be^{4g} + 2a^2e^{2g}\Big(2b^2e^{2g} + e^{2g} \\ & + 4e^{2h} - 8e^{2(g+h+k)} + 4e^{4g+2h} - e^{2g+4k} + 4e^{2h+4k}\Big) \\ & - 4abe^{2g}\left(e^{2g} + 4e^{2h}\right) + 8b^2e^{2(g+h)} + e^{4g} + 16e^{4h} \\ & - 16e^{2(2g+h+k)} - 64e^{2(g+2h+k)} + e^{4(g+k)} + 16e^{4(h+k)}\Big\}. \end{aligned} \tag{A.1.2}$$

The constraint is given by

$$\begin{aligned} 0 &= T + U \\ &= e^{-2(g+h-\Phi)}\Big[-2\left(a'\right)^2e^{6g+2h} + a^4e^{4g}\left(e^{4k} + 1\right) - 4a^3be^{4g} \\ &\quad + 2a^2e^{2g}\Big(2b^2e^{2g} - 8e^{2(g+h+k)} + 4e^{4g+2h} - e^{2g+4k} + e^{2g} \\ &\quad + 4e^{2h+4k} + 4e^{2h}\Big) - 4abe^{2g}\left(e^{2g} + 4e^{2h}\right) - 2\left(b'\right)^2e^{2(g+h)} \\ &\quad + 64e^{4(g+h)}g'h' + 32e^{4(g+h)}g'k' + 64e^{4(g+h)}g'\Phi' + 16e^{4(g+h)}\left(g'\right)^2 \end{aligned}$$

$$+ 8b^2c^{2(g+h)} + 32c^{4(g+h)}h'k' + 64e^{4(g+h)}h'\Phi' + 16c^{4(g+h)}\left(h'\right)^2$$
$$+ 32e^{4(g+h)}k'\Phi' - 16e^{2(2g+h+k)} - 64e^{2(g+2h+k)} + 32e^{4(g+h)}\left(\Phi'\right)^2$$
$$+ e^{4(g+k)} + e^{4g} + 16e^{4(h+k)} + 16e^{4h}\Big]. \tag{A.1.3}$$

The equations of motion are given by

$$g'' = \frac{1}{8}e^{-4g-2h}\Big[e^{6g}\left(a'\right)^2 - 4a^2e^{2g+4k} - 4a^2e^{2g} + 4a^2e^{6g} + 8abe^{2g}$$
$$- e^{2g}\left(b'\right)^2 - 4b^2e^{2g} - 16e^{4g+2h}g'h' - 16e^{4g+2h}g'\Phi'$$
$$- 16e^{4g+2h}\left(g'\right)^2 + 32e^{2g+2h+2k} - 16e^{2h+4k} - 16e^{2h}\Big], \tag{A.1.4}$$

$$h'' = -\frac{1}{8}e^{-2g-4h}\Big[\left(a'\right)^2e^{4g+2h} + a^4e^{2g+4k} + a^4e^{2g} - 4a^3be^{2g} + 4a^2b^2e^{2g}$$
$$- 8a^2e^{2g+2h+2k} + 4a^2e^{4g+2h} - 2a^2e^{2g+4k} + 2a^2e^{2g}$$
$$+ 4a^2e^{2h+4k} + 4a^2e^{2h} - 4abe^{2g} - 8abe^{2h} + e^{2h}\left(b'\right)^2$$
$$+ 4b^2e^{2h} + 16e^{2g+4h}g'h' + 16e^{2g+4h}h'\Phi' + 16e^{2g+4h}\left(h'\right)^2$$
$$- 8e^{2g+2h+2k} + e^{2g+4k} + e^{2g}\Big], \tag{A.1.5}$$

$$k'' = \frac{1}{8}e^{-4g-4h}\Big[a^4e^{4g+4k} - a^4e^{4g} + 4a^3be^{4g} - 4a^2b^2e^{4g} + 8a^2e^{2g+2h+4k}$$
$$- 8a^2e^{2g+2h} - 8a^2e^{6g+2h} - 2a^2e^{4g+4k} - 2a^2e^{4g} + 16abe^{2g+2h}$$
$$+ 4abe^{4g} - 8b^2e^{2g+2h} - 16e^{4g+4h}g'k' - 16e^{4g+4h}h'k'$$
$$- 16e^{4g+4h}k'\Phi' + e^{4g+4k} - e^{4g} + 16e^{4h+4k} - 16e^{4h}\Big], \tag{A.1.6}$$

$$\Phi'' = \frac{1}{8}e^{-4g-4h}\Big[a^4e^{4g} - 4a^3be^{4g} + 4a^2b^2e^{4g} + 8a^2e^{2g+2h} - 16abe^{2g+2h}$$
$$+ 2a^2e^{4g} - 4abe^{4g} + 2\left(b'\right)^2e^{2g+2h} + 8b^2e^{2g+2h} - 16e^{4g+4h}g'\Phi'$$
$$- 16e^{4g+4h}h'\Phi' - 16e^{4g+4h}\left(\Phi'\right)^2 + e^{4g} + 16e^{4h}\Big], \tag{A.1.7}$$

$$a'' = e^{-4g-2h}\Big[-4a'e^{4g+2h}g' - 2a'e^{4g+2h}\Phi' + a^3e^{2g+4k} + a^3e^{2g} - 3a^2be^{2g}$$
$$+ 2ab^2e^{2g} - 8ae^{2g+2h+2k} + 4ae^{4g+2h} - ae^{2g+4k} + ae^{2g}$$
$$+ 4ae^{2h+4k} + 4ae^{2h} - be^{2g} - 4be^{2h}\Big], \tag{A.1.8}$$

$$b'' = -e^{-2h}\left[a^3e^{2g} - 2a^2be^{2g} + ae^{2g} + 4ae^{2h} + 2e^{2h}b'\Phi' - 4be^{2h}\right]. \tag{A.1.9}$$

The boundary case discussed in Section. 3.7.2, associated with setting $v_2 = 0$, is far simpler. After setting $a = b = 1$ and $g = k$, the equations of motion for the remaining three background

functions $\{k, h, \Phi\}$ are

$$\begin{aligned} k'' &= 2 - 2e^{-4k} - 2h'k' - 2(k')^2 - 2k'\Phi', \\ h'' &= e^{2k-2h} - 2h'k' - 2(h')^2 - 2h'\Phi', \\ \Phi'' &= 2e^{-4k} - 2h'\Phi' - 2(\Phi')^2 - 2k'\Phi', \end{aligned} \tag{A.1.10}$$

and the constraint is reduced to

$$0 = (h')^2 + 3(k')^2 + 2(\Phi')^2 + +6h'k' + 4h'\Phi' + 6k'\Phi' + e^{-4k} - e^{2k-2h} - 3. \tag{A.1.11}$$

A.2 Non-Supersymmetric Walking Solutions

Here we present the equivalent set of IR expansions to Eq. 3.1.4, for the non-Supersymmetric generalisation of the walking solutions defined in Eq. 2.2.12. In the IR we choose an ansatz for the expansions of the form (here we have set the IR to be at $\rho_\Lambda = 0$ as usual)

$$\begin{aligned} e^{2g} &= \sum_{n=-1}^{\infty} [g_n]\rho^n, & e^{2h} &= \sum_{n=1}^{\infty} [h_n]\rho^n, & e^{2k} &= \sum_{n=2}^{\infty} [k_n]\rho^n, \\ e^{4\Phi} &= \sum_{n=0}^{\infty} [\phi_n]\rho^n, & a &= \sum_{n=0}^{\infty} [w_n]\rho^n, & b &= \sum_{n=0}^{\infty} [v_n]\rho^n. \end{aligned} \tag{A.2.1}$$

Substituting these expansions into the equations of motion, we find nine independent parameters, which we take to be $[g_{-1}]$, $[h_2]$, $[k_2]$, $[k_3]$, $[\phi_0]$, $[\phi_1]$, $[w_0]$, $[w_3]$ and $[v_2]$. We relabel $[g_{-1}] = \frac{1}{2}c_0$, $[k_2] = \frac{3}{2}c_0\hat{k}_2$ and $[\phi_0] = e^{4\phi_0}$, so that we can recover the Supersymmetric case Eq. 2.2.12 by making the choices

$$[h_2] = [k_3] = [\phi_1] = 0, \quad [w_0] = 1, \quad [w_3] = \frac{8N_c}{3c_0}, \quad [v_2] = -\frac{2}{3}. \tag{A.2.2}$$

From now on we will drop the [ ] on the coefficients. After this relabelling, the nine independent free parameters are

$$c_0, \quad \hat{k}_2, \quad \phi_0, \quad \phi_1, \quad h_2, \quad k_3, \quad v_2, \quad w_0, \quad w_3. \tag{A.2.3}$$

We can restrict our expansions further, by demanding an IR satisfying one of the conditions for a background with a 'good' type of singularity as discussed in [20]. Looking at the expansions for three curvature invariants, the Ricci scalar $\mathcal{R}$, the Ricci tensor squared $\mathcal{R}_{\mu\nu}\mathcal{R}^{\mu\nu}$ and the

A. APPENDIX A

Riemann tensor squared $\mathcal{R}_{\mu\nu\tau\sigma}\mathcal{R}^{\mu\nu\tau\sigma}$ (or Kretschmann scalar), we see that they behave as

$$\mathcal{R} \sim \frac{\frac{1}{4}w_0^4c_0^2\phi_1^2 + 4\left(-1+w_0^2\right)^2 e^{8\phi_0}}{12c_0^3\hat{k}_2 w_0^4 (e^{4\phi_0})^{17/8}}\frac{1}{\rho^2} + \mathcal{O}\left(\frac{1}{\rho}\right), \tag{A.2.4}$$

$$\mathcal{R}_{\mu\nu}\mathcal{R}^{\mu\nu} \sim \frac{\frac{1}{16}c_0^4w_0^8\phi_1^4 - c_0^2\left(w_0^2-1\right)^2 w_0^4 e^{8\phi_0}\phi_1^2 + 72\left(w_0^2-1\right)^4 e^{16\phi_0}}{144c_0^6\hat{k}_2^2 w_0^8\left(e^{4\phi_0}\right)^{17/4}}\frac{1}{\rho^4} + \mathcal{O}\left(\frac{1}{\rho^3}\right),$$

$$\mathcal{R}_{\mu\nu\tau\sigma}\mathcal{R}^{\mu\nu\tau\sigma} \sim \frac{320}{9c_0^2\hat{k}_2^2(e^{4\phi_0})^{1/4}}\frac{1}{\rho^8} - \frac{16\left(15w_0^2c_0\hat{k}_2\phi_1 + 16e^{4\phi_0}\left(4w_0^2k_3 + 3h_2\hat{k}_2\right)\right)}{27\left(w_0^2c_0^3\hat{k}_2^3\left(e^{4\phi_0}\right)^{5/4}\right)}\frac{1}{\rho^7} + \mathcal{O}\left(\frac{1}{\rho^6}\right).$$

From these quantities it seems that setting $w_0 = 1$ and $\phi_1 = 0$ will remove the leading term in both the Ricci scalar and Ricci tensor squared in the IR. Making these choices leaves them both finite, but leaves the Kretschmann scalar unchanged, at least to leading order. With these two choices, we now write down the IR expansions,*

$$e^{2g} = \frac{c_0}{2}\frac{1}{\rho} + c_0\left(\frac{2}{3} - \frac{h_2(h_2\hat{k}_2+2k_3)}{18c_0^2 9\hat{k}_2}\right)\rho + \frac{c_0}{18}\left(9\hat{k}_2 - 9w_3 + \frac{6h_2^3 + \frac{4h_2^2k_3}{\hat{k}_2}}{c_0^3} - \frac{24h_2}{c_0}\right)\rho^2 + \mathcal{O}(\rho^3),$$

$$e^{2h} = \frac{c_0}{2}\rho + h_2\rho^2 + \frac{\left(-12c_0^2\hat{k}_2 + 3h_2^2\hat{k}_2 + 2h_2k_3\right)}{18c_0\hat{k}_2}\rho^3 + \frac{1}{2}c_0\left(w_3+\hat{k}_2\right)\rho^4 + \mathcal{O}(\rho^5),$$

$$e^{2k} = \frac{3}{2}c_0\hat{k}_2\rho^2 + k_3\rho^3 + \frac{\left(6c_0^2\hat{k}_2^2 + 3h_2^2\hat{k}_2 - h_2\hat{k}_2k_3 + k_3^2\right)}{18c_0\hat{k}_2}\rho^4 + \mathcal{O}(\rho^5),$$

$$e^{4\Phi-4\phi_0} = 1 + \frac{2\left(4+3v_2^2\right)}{3c_0^2}\rho^4 - \frac{4h_2\left(4+27v_2^2\right)}{15c_0^3}\rho^5 + \mathcal{O}(\rho^6),$$

$$a = 1 - 2\rho^2 + w_3\rho^3 + \frac{2}{9}\left(15 - \frac{2h_2\left(3h_2\hat{k}_2+2k_3\right)}{c_0^2\hat{k}_2}\right)\rho^4 + \mathcal{O}(\rho^5),$$

$$b = 1 + v_2\rho^2 - \frac{v_2h_2}{c_0}\rho^3 + \frac{6\left(2+v_2\right)c_0^2\hat{k}_2 + 4v_2h_2\left(12h_2\hat{k}_2 - k_3\right)}{45c_0^2\hat{k}_2}\rho^4 + \mathcal{O}(\rho^5). \tag{A.2.5}$$

Thus we have seven independent parameters governing our IR expansions

$$c_0, \quad \hat{k}_2, \quad \phi_0, \quad k_3, \quad v_2, \quad w_3, \quad h_2. \tag{A.2.6}$$

It is possible to use these IR expansions to find a smooth numerical interpolation to the generalised UV expansions in Eq. 3.1.9, which contain enough freedom to match to these solutions which, unlike those discussed in Chapter. 3, are not globally regular. These solutions are thus the correct non-Supersymmetric deformation of the Supersymmetric walking solutions.

*$N_c = 1$ in the following to be concise

A.3 Detailed Calculation of the Non-Supersymmetric B_2

Here we discuss in more detail the calculation of the B_2 field in the non-Supersymmetric setup. In the Supersymmetric case, we have

$$B_2 = \kappa \frac{e^{\frac{3}{2}\Phi}}{\hat{h}^{1/2}} \left[e^{\rho 3} - \cos\alpha (e^{\theta\varphi} + e^{12}) - \sin\alpha (e^{\theta 2} + e^{\varphi 1}) \right], \tag{A.3.1}$$

with

$$\cos\alpha = \frac{\cosh(2\rho) - a}{\sinh(2\rho)}, \qquad \sin\alpha = -\frac{2e^{h-g}}{\sinh(2\rho)}. \tag{A.3.2}$$

This is not valid in the general non-Supersymmetric case as although we obtain the same H_3 as in the Supersymmetric case in Eq. 2.1.14, the relationship to Eq. A.3.1 requires the BPS equations, as does the consistency of the definitions Eq. A.3.2.

Instead, we must determine B_2 by requiring that $dB_2 = H_3$. Assuming that B_2 has the same general structure as Eq. A.3.1

$$B_2 = b_1(\rho) e^{\rho 3} + b_2(\rho) e^{\theta\varphi} + b_3(\rho) e^{12} + b_4(\rho) e^{\theta 2} + b_5(\rho) e^{\varphi 1}, \tag{A.3.3}$$

which results in

$$\begin{aligned}
dB_2 = & \frac{e^{-h-k-\frac{\Phi}{4}} \left(a b_3 e^g + 2 b_4 e^h\right)}{\hat{h}^{1/4}} e^{1\theta 3} + \frac{e^{-h-k-\frac{\Phi}{4}} \left(a b_3 e^g + 2 b_5 e^h\right)}{\hat{h}^{1/4}} e^{\varphi 23} \\
& - \frac{\left(b_4 - b_5\right) e^{-h-\frac{\Phi}{4}} \cot\theta}{\hat{h}^{1/4}} e^{\theta\varphi 1} \\
& + \frac{e^{-2g-k-\frac{\Phi}{4}}}{2\hat{h}^{5/4}} \left(e^{2g} \left\{ \hat{h} \left[b_3 \left(4g' + \Phi'\right) + 2 b_3' \right] + b_3 \hat{h}' \right\} + 4 b_1 \hat{h} e^{2k} \right) e^{\rho 12} \\
& + \frac{e^{-h-k-\frac{\Phi}{4}}}{2\hat{h}^{5/4}} \Big(b_3 e^g \hat{h} a' - 2 a b_1 e^{-g} \hat{h} e^{2k} \\
& \qquad + e^h \left\{ \hat{h} \left[b_4 \left(2g' + 2h' + \Phi'\right) + 2 b_4' \right] + b_4 \hat{h}' \right\} \Big) e^{\rho\theta 2} \\
& + \frac{e^{-h-k-\frac{\Phi}{4}}}{2\hat{h}^{5/4}} \Big(b_3 e^g \hat{h} a' - 2 a b_1 e^{-g} \hat{h} e^{2k} \\
& \qquad + e^h \left\{ \hat{h} \left[b_5 \left(2g' + 2h' + \Phi'\right) + 2 b_5' \right] + b_5 \hat{h}' \right\} \Big) e^{\rho\varphi 1} \\
& + \frac{e^{-h-k-\frac{\Phi}{4}}}{2\hat{h}^{5/4}} \Big(-(b_4 + b_5) e^g \hat{h} a' - \left(a^2 - 1\right) b_1 \hat{h} e^{2k-h} \\
& \qquad + e^h \left\{ \hat{h} \left[b_2 \left(4h' + \Phi'\right) + 2 b_2' \right] + b_2 \hat{h}' \right\} \Big) e^{\rho\theta\varphi}.
\end{aligned} \tag{A.3.4}$$

If we compare this with Eq. 2.1.14, it can be seen that the $e^{\theta\varphi 1}$ component of H_3 vanishes, and this leads us to find that $b_4 = b_5$ as in the Supersymmetric case. The $e^{\rho\theta 2}$ and $e^{\rho\varphi 1}$ components of Eq. A.3.4 are then identical, as are the $e^{1\theta 3}$ and $e^{\varphi 23}$ components. This leaves us with four remaining independent equations.

Equating the $(e^{1\theta 3} + e^{\varphi 23})$ components results in

$$b_4 = -\frac{1}{2}e^{g-h}ab_3 - \frac{\kappa N_c e^{\frac{3\Phi}{2}-g-h}b'}{4\hat{h}^{1/2}}, \tag{A.3.5}$$

and the $e^{\rho 12}$ component gives

$$\begin{aligned} b_1 = \frac{e^{2g-2k}}{4\hat{h}}\Big[&2b_3\Phi' - 3\hat{h}b_3\Phi' - 4\hat{h}b_3g' - 2\hat{h}b_3' \\ &+ \kappa N_c e^{\frac{3\Phi}{2}-2h}\hat{h}^{\frac{1}{2}}\left(a^2 - 2ab + 1\right)\Big]. \end{aligned} \tag{A.3.6}$$

This leaves only b_2 and b_3 undetermined. Substituting these results back into Eq. A.3.4, we find that the $(e^{\rho\theta 2} + e^{\rho\varphi 1})$ component of $H_3 = dB_2$ reduces to the equation of motion Eq. A.1.9 for b. The remaining equation is that associated with the $e^{\rho\theta\varphi}$ component. It is a first-order differential equation in terms of the functions b_2 and b_3 given by

$$\begin{aligned} 0 = {} & 8\hat{h}e^{2g+4h}b_2' + 2\left(a^2-1\right)\hat{h}e^{4g+2h}b_3' + e^{2(g+h)}\hat{h}'\left[\left(a^2-1\right)e^{2g}b_3 + 4e^{2h}b_2\right] \\ & + \hat{h}e^{2(g+h)}\left[4ae^{2g}a'b_3 + (a^2-1)e^{2g}\left(4g'+\Phi'\right)b_3 + 4b_2e^{2h}\left(4h'+\Phi'\right)\right] \\ & - \kappa N_c\sqrt{\hat{h}}e^{3\Phi/2}\Big[-2a'b'e^{2(g+h)} + (a^4-1)e^{4g} \\ & \qquad - 2(a^2-1)abe^{4g} + 2abe^{4g} - 16e^{4h}\Big]. \end{aligned} \tag{A.3.7}$$

which can be solved for b_2 to give

$$\begin{aligned} b_2 = \frac{e^{-2h-\Phi/2}}{\sqrt{\hat{h}}}\int^{\rho} d\rho'\Bigg(&\frac{e^{-2g-2h+\frac{\Phi}{2}}}{8\sqrt{\hat{h}}}\Big\{-\left(a^2-1\right)e^{4g+2h}\hat{h}'b_3 \\ & - \hat{h}e^{4g+2h}\Big[4aa' + a^2\left(4g'+\Phi'\right) - 4g' - \Phi'\Big]b_3 \\ & + \kappa N_c\sqrt{\hat{h}}e^{3\Phi/2}\left[(a^4-1)e^{4g} - 2(a^2-1)abe^{4g} - 2a'b'e^{2(g+h)} - 16e^{4h}\right]\Big\} \\ & - \frac{1}{4}\left(a^2-1\right)\sqrt{\hat{h}}e^{2g+\frac{\Phi}{2}}b_3'\Bigg), \end{aligned} \tag{A.3.8}$$

which is not particularly useful. Instead, if we use the fact that we want $Q_{\text{Page, D3}} = 0$ (see Eq. 3.3.6), we are required to impose that the $e^{\theta\varphi 123}$ component of $F_5 - B_2 \wedge F_3$ vanishes. This

results in an equation which is algebraic in b_2 and b_3, and results in

$$b_2 = \frac{e^{-2h}}{4\hat{h}^{1/2}} \left\{ e^{2g}\hat{h}^{\frac{1}{2}} \left(1-a^2\right) b_3 - \frac{\kappa}{N_c} e^{\frac{3\Phi}{2}} \left[N_c^2 (a-b) b' + 4e^{2(g+h)}\Phi' \right] \right\}. \tag{A.3.9}$$

Together with the results of b_1, b_4 and b_5 derived above, this completes Eq. 3.2.2. We then check that the above form of b_2 is compatible with the requirement $dB_2 = H_3$. Substituting into Eq. A.3.7, we find that b_3 cancels, and we are left with

$$\begin{aligned} 0 = 4e^{4(g+h)} &\left\{ 2\hat{h} \left[2g'\Phi' + 2h'\Phi' + \Phi'' + 2\left(\Phi'\right)^2 \right] - 2g'\hat{h}' - 2h'\hat{h}' - \hat{h}'' \right\} \\ &+ N_c^2 \Big[a^4 e^{4g} - 2a^3 b e^{4g} + 2(a-b)b'' e^{2(g+h)} + 4(a-b)b' e^{2(g+h)}\Phi' \\ &+ 2abe^{4g} - 2\left(b'\right)^2 e^{2(g+h)} - e^{4g} - 16e^{4h} \Big]. \end{aligned} \tag{A.3.10}$$

This is solved by the equations of motion for Φ in Eq. A.1.7, and the one for b in Eq. A.1.9.

To further understand the effect of the undetermined function b_3, we look at the difference $\Delta B_2 = B_2 - (B_2)_{b_3=0}$, which is of the form

$$\begin{aligned} \Delta B_2 = F_1(\rho) \sin\theta \; d\theta \wedge d\varphi + F_2(\rho) \sin\tilde{\theta} \; d\tilde{\theta} \wedge d\tilde{\varphi} + F_3(\rho) \cos\theta \; d\rho \wedge d\varphi \\ + F_4(\rho) \cos\tilde{\theta} \; d\rho \wedge d\tilde{\varphi} + F_5(\rho) \; d\rho \wedge d\psi, \end{aligned} \tag{A.3.11}$$

where the F_i depend on g, Φ, $\hat{h}$, b_3 and their derivatives. If we set this equal to

$$d\left[\beta_1(\rho) \cos\theta \; d\varphi + \beta_2(\rho) \cos\tilde{\theta} \; d\tilde{\varphi} + \beta_3(\rho) \; d\psi \right] \tag{A.3.12}$$

we can solve for the β_i, giving

$$\begin{aligned} \Delta B_2 &= -\frac{1}{4} d\left[e^{2g+\Phi/2} \sqrt{\hat{h}} b_3 (\cos\theta \; d\varphi + \cos\tilde{\theta} \; d\tilde{\varphi} + d\psi) \right] \\ &= -\frac{1}{2} d\Big(e^{2g-k+\Phi/4} \hat{h}^{1/4} b_3 \; e^3 \Big). \end{aligned} \tag{A.3.13}$$

A.4 A Seiberg-like Duality

In Section. 3.3.3, we discussed how Seiberg duality acts on our non-Supersymmetric solutions. Here we present two cases which will be helpful to compare to, both the Klebanov-Strassler and the baryonic branch case.

A.4.1 The Klebanov-Strassler Case

We follow the treatment presented in [73], in the case where we have no flavors ($N_f = 0$), then the NS B_2 potential is given by,

$$B_2 = \frac{N_c}{2}[f g_1 \wedge g_2 + \tilde{k} g_3 \wedge g_4] \tag{A.4.1}$$

where the definition of $g_1, ..., g_4$ can be found in [73]. When we then restrict this to the cycle

$$\Sigma_2 = [\theta = \tilde{\theta}, \varphi = 2\pi - \tilde{\varphi}, \psi = \psi_\Lambda], \tag{A.4.2}$$

we obtain that

$$B_2\Big|_{\Sigma_2} = \frac{N_c}{2}[(f + \tilde{k}) + (\tilde{k} - f)\cos\psi_\Lambda] \sin\theta d\theta \wedge d\varphi. \tag{A.4.3}$$

From this one finds

$$b_\Lambda = \frac{1}{4\pi^2}\int_{\Sigma_2} B_2 = \frac{N_c}{\pi}\left[f \sin^2\left(\frac{\psi_\Lambda}{2}\right) + k\cos^2\left(\frac{\psi_\Lambda}{2}\right)\right] \tag{A.4.4}$$

On the other hand (as computed in [73]), the Maxwell charge of the D3 branes is given by

$$Q_{\text{Maxwell},D3} = \frac{N_c^2}{\pi}\left[f - (f - \tilde{k})F\right]. \tag{A.4.5}$$

Under the change

$$f \to f - \frac{\pi}{N_c}, \qquad \tilde{k} \to \tilde{k} - \frac{\pi}{N_c} \tag{A.4.6}$$

the D3 branes Maxwell charge changes by

$$Q_{\text{Maxwell},D3} \to Q_{\text{Maxwell},D3} - N_c, \qquad b_\Lambda \to b_\Lambda - 1. \tag{A.4.7}$$

these transformations, are equivalent to changing the NS B_2 potential by a large gauge transformation

$$B_2 \to B_2 + \frac{\pi}{2}[g_1 \wedge g_2 + g_3 \wedge g_4] \tag{A.4.8}$$

which when evaluated on the cycle Σ_2, produces the changes in Eq. A.4.7. Next, we discuss the Supersymmetric baryonic branch case.

A.4.2 The Baryonic Branch Case

In this case the NS B_2 potential is given by Eq. A.3.1, and evaluating it on Σ_2, we get

$$\begin{aligned} b_\Lambda =& \frac{\kappa e^{2\Phi}}{\pi}\left[\left(\tilde{k}+f\right)+\left(\tilde{k}-f\right)\cos\psi_\Lambda\right], \\ \tilde{k}+f =& \frac{\kappa e^{2\Phi}}{N_c}\left[\left(\frac{e^{2g}}{4}(a^2+1)-e^{2h}\right)\cos\alpha + a\, e^{h+g}\sin\alpha\right], \\ \tilde{k}-f =& \frac{\kappa e^{2\Phi}}{N_c}\left[\frac{e^{2g}}{2}a\,\cos\alpha + e^{h+g}\sin\alpha\right], \end{aligned} \tag{A.4.9}$$

Using the explicit expressions given in Eq. A.3.2, we have

$$\tilde{k} = -\frac{\kappa e^{2\Phi}}{4N_c}Q\coth(\rho), \quad f = -\frac{\kappa e^{2\Phi}}{4N_c}Q\tanh(\rho) \tag{A.4.10}$$

Then the Maxwell charge for D3 branes can be written as

$$Q_{\text{Maxwell},D3} = \frac{\kappa}{\pi}e^{2g+2h+2\Phi}\Phi' \tag{A.4.11}$$

and by using the BPS equation for Φ', we find

$$Q_{\text{Maxwell},D3} = \frac{N_c^2}{\pi}\Big[2f+(\tilde{k}-f)F\Big], \tag{A.4.12}$$

where $F=(1-b)$. So, once again, we obtain that under a large gauge transformation,

$$b_\Lambda \to b_\Lambda - 1, \qquad Q_{\text{Maxwell},D3} \to Q_{\text{Maxwell},D3} - N_c. \tag{A.4.13}$$

A. APPENDIX A

Appendix B

Appendix B

B.1 Discussion of $\mathcal{Z}$

Here we shall discuss the function $\mathcal{Z}$ defined in Eq. 4.1.7, and how it relates to perturbative instabilities. Some of the arguments presented here can be found in [93, 97]. Starting from the expression for L given in Eq. 4.1.5, we assume that locally $L(\rho_0)$ is invertible, and then rewrite it as

$$L = 2\int_{\rho_0}^{\rho_U} \mathrm{d}\rho\, \frac{G(\rho)}{F(\rho)}\, \mathcal{K}\left[\frac{F(\rho)}{F(\rho_0)}\right] \tag{B.1.1}$$

where the functional $\mathcal{K}$ is defined as

$$\mathcal{K}[y] \equiv \frac{1}{\sqrt{y^2-1}}\,. \tag{B.1.2}$$

As we know that $\rho > \rho_0$ and the function F is a monotonically increasing function, meaning $\mathcal{K}$ is real and positive definite. Performing an integration by parts (where the boundary terms must be retained), it is possible to rewrite the derivative of the separation L with respect to ρ_0 as

$$\frac{\mathrm{d}L}{\mathrm{d}\rho_0} = 2\lim_{\rho_U\to\infty} \frac{\partial_\rho F(\rho_0)}{F(\rho_0)} \left\{ -\frac{G(\rho_U)}{\partial_\rho F(\rho_U)}\, \mathcal{K}\left[\frac{F(\rho_U)}{F(\rho_0)}\right] + \int_{\rho_0}^{\rho_U} \mathrm{d}\rho\, \mathcal{K}\left[\frac{F(\rho)}{F(\rho_0)}\right] \partial_\rho\left(\frac{G(\rho)}{\partial_\rho F(\rho)}\right) \right\}. \tag{B.1.3}$$

Under an appropriate change of variables $\rho \to \log F$, it can be seen that the convergence at the upper limit of Eq. 4.1.5, together with the divergence of F, that the quantity $(V_{\mathrm{eff}}\partial_\rho \log F)^{-1} \to 0$ as $\rho \to \infty$. Under this condition (which is relevant for all cases we study) the first term in

Eq. B.1.3 vanishes (see also the arguments in [94]). Thus we obtain

$$\frac{\mathrm{d}L}{\mathrm{d}\rho_0} = 2 \lim_{\rho_U \to \infty} \frac{\partial_\rho F(\rho_0)}{F(\rho_0)} \int_{\rho_0}^{\rho_U} \mathrm{d}\rho \, \mathcal{K} \left[\frac{F(\rho)}{F(\rho_0)} \right] \mathcal{Z}(\rho) \, . \tag{B.1.4}$$

By definition $F > 0$, and we have already said that it is monotonically increasing, meaning $\partial_\rho F > 0$. As discussed, $\mathcal{K} > 0$ and thus we conclude that the sign of $\mathrm{d}L/\mathrm{d}\rho_0$ is dictated by $\mathcal{Z}$. In particular, in order for $\mathrm{d}L/\mathrm{d}\rho_0 \leq 0$, a sufficient condition is $\mathcal{Z} \leq 0$. On the other hand, if $\mathcal{Z}$ is positive over a certain range, $\mathrm{d}L/\mathrm{d}\rho_0$ can vanish or become positive for some values of ρ_0. There are a number of ways to argue that this indicates the presence of an instability.

Through a similar exercise for E the exact relation

$$\frac{\mathrm{d}E}{\mathrm{d}\rho_0} = F(\rho_0) \frac{\mathrm{d}L}{\mathrm{d}\rho_0} \, , \tag{B.1.5}$$

can be found. To understand better the stability conditions of the system, it will be instructive to turn to a thermodynamic analogy. It is possible to identify the function E with the Gibbs Free Energy $\mathcal{G}(p,T)$, where the variable p is the pressure (we work at constant temperature T) which corresponds to the separation L in Section. 4.1. Thus it is possible to recognise Eq. B.1.5 as simply the statement

$$\frac{\mathrm{d}\mathcal{G}}{\mathrm{d}p} = V \equiv F(\rho_0) \geq 0 \tag{B.1.6}$$

which is positive definite as expected. Further, we know that the system will be in the configuration with minimal free energy as a function of the volume V at fixed p. This means we must single out the solution that minimises $E(\rho_0)$. Additionally, there are also well known concavity conditions which $\mathcal{G}$ must satisfy

$$\frac{\mathrm{d}V}{\mathrm{d}p} \leq 0 \qquad \Longleftrightarrow \qquad \frac{\mathrm{d}^2\mathcal{G}}{\mathrm{d}p^2} \leq 0 \tag{B.1.7}$$

that, using the dictionary back to our setup, can be translated to be $\mathrm{d}L/\mathrm{d}\rho_0 \leq 0$, which is verified for $\mathcal{Z} \leq 0$. The conditions in Eq. B.1.6 and Eq. B.1.7 together are the requirements for local stability. These coincide with the concavity conditions discussed in [94] for the quark-antiquark potential, dual to a string probe which falls into the class of Eq. 4.1.1, and discussed a little in Section. 5.2.

In summary, we have presented strong evidence that $\mathcal{Z} \leq 0$ is a necessary and sufficient condition for stability of probe embeddings described by an action of the form Eq. 4.1.1.

B.2 A Related Probe-D7 Brane Embedding

In Chapter. 4 we studied an embedding for a probe-D7 brane which chooses a particular set of coordinates to be those that are transverse. These are the coordinates that parametrise the manifest S^2 in the metric described by the angles $\{\theta, \varphi\}$. In the past, making this choice of coordinates to be transverse was of little significance, as the two S^2 within the backgrounds had the same behaviour throughout the space. In the backgrounds we study here this is not the case, as with the introduction of a non-trivial (baryonic) dimension-two VEV, and the symmetry between the two S^2 is broken. With this in mind we explore how an embedding which chooses the other S^2 (with angles $\{\tilde{\theta}, \tilde{\varphi}\}$) as its transverse directions behaves.

Following the same steps as with the original embedding we find that the corresponding functions $\tilde{F}$ and $\tilde{G}$ are given by

$$\begin{aligned}\tilde{F}^2 &= F^2 \times (M_1 + 1) = e^{4g+2k+2h+6\Phi}\,(M_1 + 1)\,, \\ \tilde{G}^2 &= G^2 \times (M_1 + 1)^2 = e^{4g+4k+6\Phi}\,(M_1 + 1)^2\,. \end{aligned} \tag{B.2.1}$$

We can replace the expressions for the background functions, and write $\tilde{F}$ and $\tilde{G}$ in terms of the functions P and Q:

$$\begin{aligned}\tilde{F}^2 &= F^2 \times \left(\frac{2Q}{P\coth(2\rho) - Q} + 1\right), \\ \tilde{G}^2 &= G^2 \times \left(\frac{2Q}{P\coth(2\rho) - Q} + 1\right)^2. \end{aligned} \tag{B.2.2}$$

We see that these quantities are the same as the ones defined in Eq. 4.2.3 up to the additional piece proportional to M_1 (defined in Eq. 3.3.2). This means that we expect for large h_1 that the behaviour of the embeddings should be the same (as $M_1 \to 0$, as $h_1 \to \infty$), and (after the *rotation*) we recover the Klebanov-Strassler background. We shall use the same notation as in Section. 4.2, in that we shall call the angular separation $\bar{\varphi}$, and the energy will be given by $\bar{E}$.

We shall only give a summary of the behaviour of the probes in the case where the dimension-two VEV takes its largest value, i.e. that of the CVMN background and the related walking solutions. We shall not present the results of the actual numerical analysis but shall instead discuss the effects in a summary similar to that seen in Section. 4.5. Plots of the generic behaviour of the alternative probe-D7 brane in these backgrounds can be seen in Fig. B.1 in the same order as the bullet points below.

B. APPENDIX B

- In the CVMN case there are now four branches in this solution. The disconnected configurations are never the minimal solutions of $\bar{E}$. The connected configurations have two parts, the first of which is a stable branch that is preferred for $(\bar{\varphi}_b = \frac{2\pi}{3}) < \bar{\varphi} \leq \pi$, and the second is an unstable branch that is never preferred. The branches only exist for $\bar{\varphi} > \bar{\varphi}_1$, with $\bar{\varphi}_1 < \bar{\varphi}_b$. Note in this case, there is no parameter in this solution which will change the value of $\bar{\varphi}_1$. The short configurations, for $\bar{\varphi} < \bar{\varphi}_b$ are the dynamically preferred and we thus say there is a bulk phase transition at $\bar{\varphi}_b$. Thus the broken Chiral-symmetry phase (associated with the connected configurations) is the physical one connected to the field theory.

- Introducing the scale $\rho_* \lesssim \frac{1}{2}$, we find that this introduces a new branch in the $(\bar{\varphi}, \bar{E})$-plane, which is associated to the IR, but beyond this scale we retain the UV behaviour of the CVMN case. In this case there are then five branches. The new branch associated with the new scale ρ_* is unstable and is never preferred. The short configurations are still the preferred branch for $\bar{\varphi} < \bar{\varphi}_b$. The connected configurations with $\rho_0 > \rho_*$ have the same behaviour as in the CVMN case, but now have a maximum $\bar{\varphi}_2 < \pi$, such that they are preferred only in the range $\bar{\varphi}_b < \bar{\varphi} < \bar{\varphi}_c$. At $\bar{\varphi}_c$ there is a first-order phase transition and the value of $\bar{\varphi}_c$ depends on ρ_*. For $\bar{\varphi} > \bar{\varphi}_c$ there is the Chiral-symmetry restored phase as here the disconnected configurations are preferred. At $\bar{\varphi}_b$ we again have a bulk phase transition involving the connected configurations. Thus for $\bar{\varphi} > \bar{\varphi}_b$ we have a model of Chiral-symmetry breaking.

- If the scale $\rho_* \gtrsim \frac{1}{2}$, we find that there are only three branches of configurations, with the connected configurations existing for $\bar{\varphi} < \bar{\varphi}_b$ which are classically unstable, so are never preferred. The short configurations exist for $\bar{\varphi} < \bar{\varphi}_b$ and are the dominant (classically stable) solutions in this region. Again at $\bar{\varphi}_b$ there is a bulk phase transition such that for $\bar{\varphi} > \bar{\varphi}_b$ the disconnected configurations are preferred. Thus we do not have a model of Chiral-symmetry breaking as the disconnected configurations are in the Chirally-restored phase, and below $\bar{\varphi}_b$ the system is not related to the field theory.

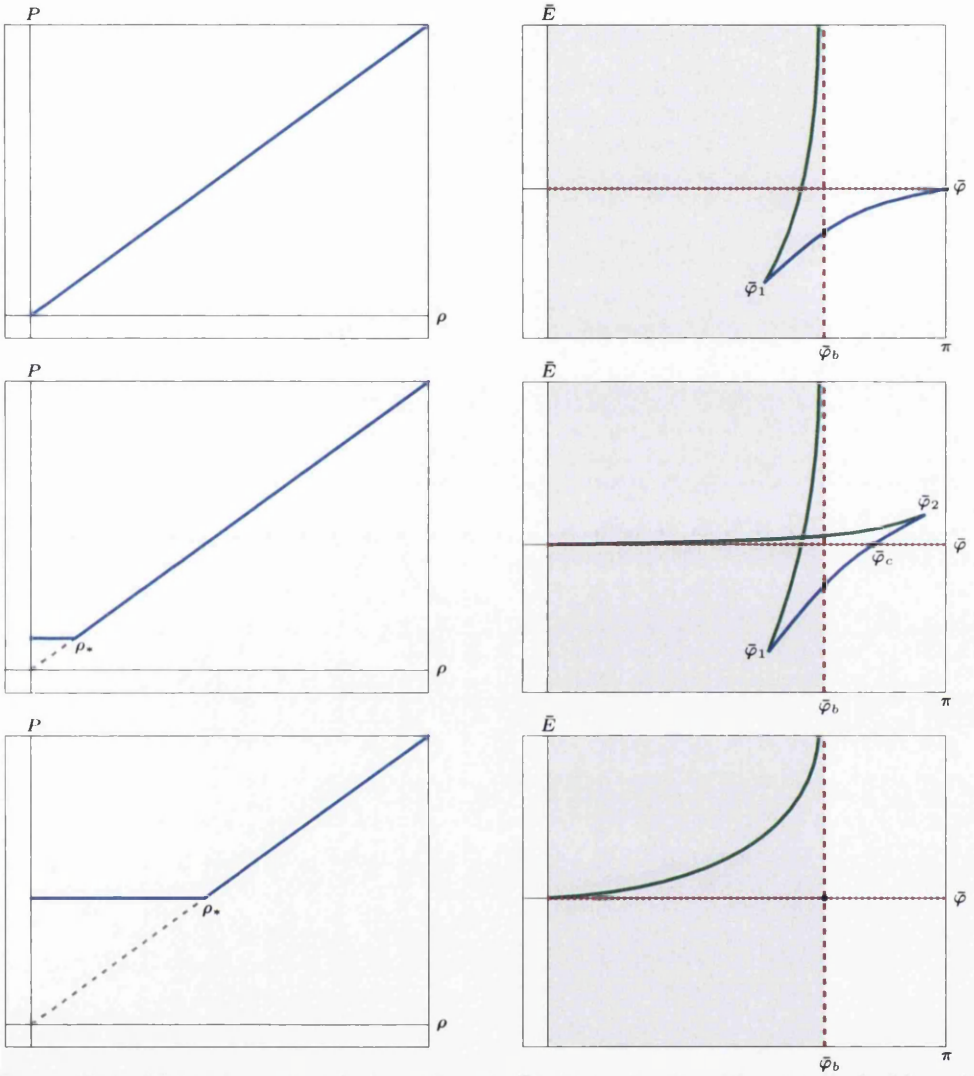

Figure B.1: Plots of generic solutions of probe-D7 brane for the alternative embeddings for all cases in the wrapped D5 system discussed. On the left-hand side we have plots of P as a function of ρ, while on the right-hand side we have $\bar{E}$ as a function of $\bar{\varphi}$ in the corresponding backgrounds. The connected configurations are given in solid blue (stable) and green (unstable), the disconnected configurations given in dotted red, and the short configurations in dashed red lines. The physically realised configurations are those with the lowest $\bar{E}$ for a particular value of $\bar{\varphi}$. We argue that the grey shaded region, to the left of the short configurations, is disconnected from the continuum limit, such that these results do not have an obvious interpretation in terms of the dual field theory.

B. APPENDIX B

Appendix C

Appendix C

C.1 D5 Branes Wrapped on a Three-Cycle

Here we look at the backgrounds presented in [119], and generalised in [120, 121], which are dual to a $2+1$ dimensional $\mathcal{N}=1$ Chern-Simons Theory. We start by defining the following ansatz, such that there are two sets of $SU(2)$ left-invariant one-forms, σ^i and $\tilde{w}^i$ $(i=1,2,3)$, which obey

$$d\sigma^i = -\frac{1}{2}\epsilon_{ijk}\sigma^j \wedge \sigma^k, \qquad d\tilde{w}^i = -\frac{1}{2}\epsilon_{ijk}\tilde{w}^j \wedge \tilde{w}^k. \tag{C.1.1}$$

Each parametrises a three-sphere, and can be represented by three angles, (θ, φ, ψ),

$$\sigma_1 = \cos\psi d\theta + \sin\psi\sin\theta d\varphi, \quad \sigma_2 = -\sin\psi d\theta + \cos\psi\sin\theta d\varphi, \quad \sigma_3 = d\psi + \cos\theta d\varphi \tag{C.1.2}$$

and similarly, three angles $(\tilde{\theta}, \tilde{\phi}, \tilde{\psi})$ for $\tilde{w}$, which take a similar explicit form. * Our spheres will also be fibered with a one-form A^i. The A^i take the form

$$A^i = \frac{1}{2}(1+w)\,\sigma^i \tag{C.1.3}$$

where w is a function of the radial coordinate. We can then write down our Type IIB metric ansatz (in Einstein Frame), in terms of the following vielbeins,

$$\begin{aligned} &E^{x^j} = e^{\frac{\Phi}{4}}dx^j, \quad E^{\rho} = e^{\frac{\Phi}{4}+g}d\rho, \quad E^{\theta} = \frac{e^{\frac{\Phi}{4}+h}}{2}\sigma^1, \quad E^{\varphi} = \frac{e^{\frac{\Phi}{4}+h}}{2}\sigma^2, \quad E^{\psi} = \frac{e^{\frac{\Phi}{4}+h}}{2}\sigma^3, \\ &E^1 = \frac{e^{\frac{\Phi}{4}+g}}{2}(\tilde{w}^1 - A^1), \quad E^2 = \frac{e^{\frac{\Phi}{4}+g}}{2}(\tilde{w}^2 - A^2), \quad E^3 = \frac{e^{\frac{\Phi}{4}+g}}{2}(\tilde{w}^3 - A^3) \end{aligned} \tag{C.1.4}$$

*The range of the angles here is $0 \le \theta, \tilde{\theta} < \pi$, $0 \le \varphi, \tilde{\varphi} < 2\pi$ and $0 \le \psi, \tilde{\psi} < 4\pi$.

where x^j represents the Minkowski metric in $2+1$ dimensions, ρ is the radial coordinate, and $\{f, g, h\}$ are only functions of ρ. This means we can write the metric compactly as

$$ds_E^2 = \sum_i (E^i)^2 \tag{C.1.5}$$

The theory also contain a non-trivial dilaton Φ. There is also a RR three-form F_3 but we shall not require its expression here.

There is a solution generating procedure [122] (similar to the *rotation* discussed in the case of D5 branes wrapped on a two-cycle in Section. 2.1) which takes us from this solution to one of Type IIA (with extra fluxes). Here we write the relevant parts, we can write our metric in the String Frame using $ds_s^2 = e^{\Phi/2} ds^2$, then use an S-duality. The S-duality takes

$$ds_s^2 \to e^{-\Phi} ds_s^2 = ds_{str}^2, \qquad F_3 \to H_3, \qquad \Phi \to -\Phi, \tag{C.1.6}$$

leaving us in the common Type II NS-sector. Then after applying the dualities we generate the following Type IIA solution

$$d\hat{s}_{str}^2 = \hat{h}^{-1/2} dx_i^2 + \hat{h}^{1/2} ds_7^2, \qquad e^{2\hat{\Phi}} = \hat{h}^{1/2} e^{-2\Phi}, \qquad \hat{h} = \frac{1}{\cosh^2 \beta} \left(1 - \tanh^2 \beta \, e^{2(\Phi - \Phi_\infty)}\right), \tag{C.1.7}$$

where hatted quantities denote the new *rotated* solution and the unhatted are the original Type IIB functions. Again, we shall not require the explicit forms of F_4 and H_3 for what follows. We can recover the original string frame metric by taking $\hat{h} \to 1$.

We again read off the relevant quantities to calculate the Entanglement Entropy as

$$V_{\text{int}} = 4\pi^4 \times \hat{h}^{3/2} e^{3g+3h}, \qquad H(\rho) = e^{-4\hat{\Phi}} V_{\text{int}}^2 \alpha^2, \qquad \alpha(\rho) = \hat{h}^{-1/2}, \qquad \beta(\rho) = \hat{h} e^{2g} \tag{C.1.8}$$

and making the appropriate substitutions we find that

$$\sqrt{H(\rho)} = 2\pi^2 \times \hat{h}^{1/2} e^{3g+3h+2\Phi}, \qquad \sqrt{\beta} = \hat{h}^{1/2} e^g. \tag{C.1.9}$$

We can now discuss the behaviour of the Entanglement Entropy in each case. For the Maldacena-Nastase (MNa) case, we find the same as in the CVMN case (with linear $P = 2N_c\rho$), such that the separation L_A grows with ρ_0, and finds a maximum at $L_A(\rho_0 \to \infty) \sim \frac{\pi}{2}$. The solution before *rotation* initially follows the MNa behaviour in the IR, but then blows up, whereas the *rotated* result (which again follows the MNa result up to around the same scale as the solution

before *rotation*), goes to zero for larger ρ_0. This is presented in Figure C.1.

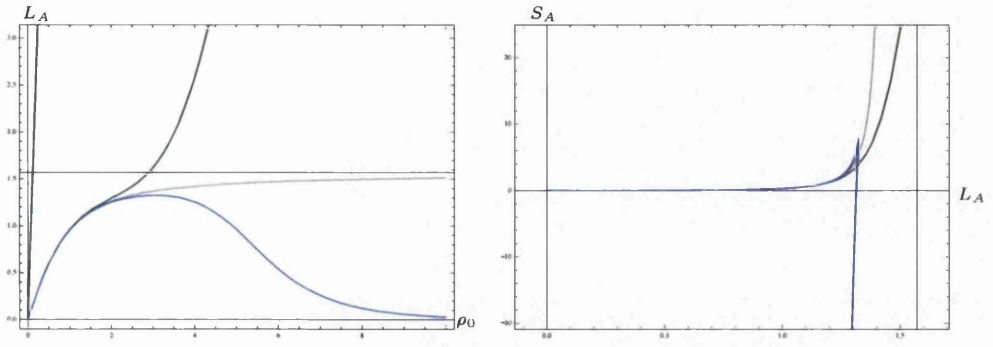

Figure C.1: Plots of the functions $L_A(\rho_0)$ on the left, and $S_A(L_A)$ on the right, for solutions associated with the Maldacena-Nastase Background and its generalisation. The MNa background is in grey ($g_0 = 1$), the solution before *rotation* in green, and *rotated* in blue (both have $g_0 = 1 + 10^{-2}$).

This means that for the Entanglement Entropy, in both the MNa and solution before *rotation*, the disconnected branch is always the lower than the connected branch and thus we again require the short configurations and cutoff effects. This is not true in the *rotated* case, where we find a behaviour like that of a first-order phase transition (thanks to the presence of the warp factor $\hat{h}$), akin to what happened with the D5 branes wrapped on a two-cycle, after moving the system onto the baryonic branch solution.

References

[1] S. Bennett, E. Caceres, C. Nunez, D. Schofield, and S. Young, "The Non-SUSY Baryonic Branch: Soft Supersymmetry Breaking of N=1 Gauge Theories," *JHEP* **1205** (2012) 031, arXiv:1111.1727 [hep-th]. ii, 19, 21, 27

[2] S. Bennett and D. Schofield, "The Structure of the Non-SUSY Baryonic Branch of Klebanov-Strassler," *JHEP* **1206** (2012) 176, arXiv:1204.2799 [hep-th]. 20

[3] A. F. Faedo, M. Piai, and D. Schofield, "On the stability of multiscale models of dynamical symmetry breaking from holography," *Nucl.Phys.* **B880** (2014) 504–527, arXiv:1312.2793 [hep-th]. 51

[4] A. F. Faedo, M. Piai, and D. Schofield, "Gauge/gravity dualities and bulk phase transitions," *Phys.Rev.* **D89** (2014) 106001, arXiv:1402.4141 [hep-th]. 51

[5] U. Kol, C. Nunez, D. Schofield, J. Sonnenschein, and M. Warschawski, "Confinement, Phase Transitions and non-Locality in the Entanglement Entropy," *JHEP* **1406** (2014) 005, arXiv:1403.2721 [hep-th]. ii, 81, 119

[6] J. M. Maldacena, "The Large N limit of superconformal field theories and supergravity," *Adv.Theor.Math.Phys.* **2** (1998) 231–252, arXiv:hep-th/9711200 [hep-th]. 1

[7] S. Gubser, I. R. Klebanov, and A. M. Polyakov, "Gauge theory correlators from noncritical string theory," *Phys.Lett.* **B428** (1998) 105–114, arXiv:hep-th/9802109 [hep-th].

[8] E. Witten, "Anti-de Sitter space and holography," *Adv.Theor.Math.Phys.* **2** (1998) 253–291, arXiv:hep-th/9802150 [hep-th]. 1

[9] P. Candelas and X. C. de la Ossa, "Comments on Conifolds," *Nucl.Phys.* **B342** (1990) 246–268. 1

[10] I. R. Klebanov and E. Witten, "Superconformal field theory on three-branes at a Calabi-Yau singularity," *Nucl.Phys.* **B536** (1998) 199–218, arXiv:hep-th/9807080 [hep-th]. 1, 6

[11] I. R. Klebanov and A. A. Tseytlin, "Gravity duals of supersymmetric SU(N) x SU(N+M) gauge theories," *Nucl.Phys.* **B578** (2000) 123–138, arXiv:hep-th/0002159 [hep-th].

[12] I. R. Klebanov and M. J. Strassler, "Supergravity and a confining gauge theory: Duality cascades and chi SB resolution of naked singularities," *JHEP* **0008** (2000) 052, arXiv:hep-th/0007191 [hep-th]. 1, 6, 7, 16, 46, 95

[13] J. M. Maldacena and C. Nunez, "Towards the large N limit of pure N=1 superYang-Mills," *Phys.Rev.Lett.* **86** (2001) 588–591, arXiv:hep-th/0008001 [hep-th]. 1, 5, 12, 34

[14] A. Butti, M. Grana, R. Minasian, M. Petrini, and A. Zaffaroni, "The Baryonic branch of Klebanov-Strassler solution: A supersymmetric family of SU(3) structure backgrounds," *JHEP* **0503** (2005) 069, arXiv:hep-th/0412187 [hep-th]. 1, 2, 7, 17

[15] G. Papadopoulos and A. A. Tseytlin, "Complex geometry of conifolds and five-brane wrapped on two sphere," *Class.Quant.Grav.* **18** (2001) 1333–1354, arXiv:hep-th/0012034 [hep-th]. 1, 42

[16] D. Cassani and A. F. Faedo, "A Supersymmetric consistent truncation for conifold solutions," *Nucl.Phys.* **B843** (2011) 455–484, arXiv:1008.0883 [hep-th]. 1

[17] I. Bena, G. Giecold, M. Grana, N. Halmagyi, and F. Orsi, "Supersymmetric Consistent Truncations of IIB on $T^{1,1}$," *JHEP* **1104** (2011) 021, arXiv:1008.0983 [hep-th]. 1

[18] A. H. Chamseddine and M. S. Volkov, "Non-Abelian BPS monopoles in N=4 gauged supergravity," *Phys.Rev.Lett.* **79** (1997) 3343–3346, arXiv:hep-th/9707176 [hep-th]. 1, 12, 34, 60

[19] J. Maldacena and D. Martelli, "The Unwarped, resolved, deformed conifold: Fivebranes and the baryonic branch of the Klebanov-Strassler theory," *JHEP* **1001** (2010) 104, arXiv:0906.0591 [hep-th]. 2, 5, 8, 9, 16

[20] D. Elander, J. Gaillard, C. Nunez, and M. Piai, "Towards multi-scale dynamics on the baryonic branch of Klebanov-Strassler," *JHEP* **1107** (2011) 056, arXiv:1104.3963 [hep-th]. 2, 5, 8, 11, 15, 17, 25, 68, 71, 113, 127

[21] E. Witten, "Anti-de Sitter space, thermal phase transition, and confinement in gauge theories," *Adv.Theor.Math.Phys.* **2** (1998) 505–532, arXiv:hep-th/9803131 [hep-th]. 2, 3, 89, 101

[22] A. Buchel, "Finite temperature resolution of the Klebanov-Tseytlin singularity," *Nucl.Phys.* **B600** (2001) 219–234, arXiv:hep-th/0011146 [hep-th]. 2

[23] A. Buchel, C. Herzog, I. R. Klebanov, L. A. Pando Zayas, and A. A. Tseytlin, "Nonextremal gravity duals for fractional D-3 branes on the conifold," *JHEP* **0104** (2001) 033, arXiv:hep-th/0102105 [hep-th].

[24] S. Gubser, C. Herzog, I. R. Klebanov, and A. A. Tseytlin, "Restoration of chiral symmetry: A Supergravity perspective," *JHEP* **0105** (2001) 028, arXiv:hep-th/0102172 [hep-th].

[25] S. S. Gubser, A. A. Tseytlin, and M. S. Volkov, "Non-Abelian 4-d black holes, wrapped five-branes, and their dual descriptions," *JHEP* **0109** (2001) 017, arXiv:hep-th/0108205 [hep-th]. 2, 20, 35, 36, 37, 121

[26] O. Aharony, E. Schreiber, and J. Sonnenschein, "Stable nonsupersymmetric supergravity solutions from deformations of the Maldacena-Nunez background," *JHEP* **0204** (2002) 011, arXiv:hep-th/0201224 [hep-th]. 2

[27] N. J. Evans, M. Petrini, and A. Zaffaroni, "The Gravity dual of softly broken N=1 superYang-Mills," *JHEP* **0206** (2002) 004, arXiv:hep-th/0203203 [hep-th]. 6, 36

[28] V. Borokhov and S. S. Gubser, "Nonsupersymmetric deformations of the dual of a confining gauge theory," *JHEP* **0305** (2003) 034, arXiv:hep-th/0206098 [hep-th].

[29] J. Babington, D. E. Crooks, and N. J. Evans, "A Nonsupersymmetric deformation of the AdS / CFT correspondence," *JHEP* **0302** (2003) 024, arXiv:hep-th/0207076 [hep-th].

[30] R. Apreda, "Non-supersymmetric regular solutions from wrapped and fractional branes," arXiv:hep-th/0301118 [hep-th]. 35, 36

[31] J. Babington, D. E. Crooks, and N. J. Evans, "A Stable supergravity dual of nonsupersymmetric glue," *Phys.Rev.* **D67** (2003) 066007, arXiv:hep-th/0210068 [hep-th]. 2

[32] A. Karch and E. Katz, "Adding flavor to AdS / CFT," *JHEP* **0206** (2002) 043, arXiv:hep-th/0205236 [hep-th]. 3, 57

[33] T. Sakai and S. Sugimoto, "Low energy hadron physics in holographic QCD," *Prog.Theor.Phys.* **113** (2005) 843–882, arXiv:hep-th/0412141 [hep-th]. 3, 66

[34] C. D. Carone, J. Erlich, and M. Sher, "Holographic Electroweak Symmetry Breaking from D-branes," *Phys.Rev.* **D76** (2007) 015015, arXiv:0704.3084 [hep-th]. 3

[35] T. Hirayama and K. Yoshioka, "Holographic Construction of Technicolor Theory," *JHEP* **0710** (2007) 002, arXiv:0705.3533 [hep-ph].

[36] O. Mintakevich and J. Sonnenschein, "Holographic technicolor models and their S-parameter," *JHEP* **0907** (2009) 032, arXiv:0905.3284 [hep-th]. 3

[37] S. Kuperstein and J. Sonnenschein, "A New Holographic Model of Chiral Symmetry Breaking," *JHEP* **0809** (2008) 012, arXiv:0807.2897 [hep-th]. 3, 52, 58, 59

[38] A. Dymarsky, S. Kuperstein, and J. Sonnenschein, "Chiral Symmetry Breaking with non-SUSY D7-branes in ISD backgrounds," *JHEP* **0908** (2009) 005, arXiv:0904.0988 [hep-th]. 3, 52

[39] L. Anguelova, "Electroweak Symmetry Breaking from Gauge/Gravity Duality," *Nucl.Phys.* **B843** (2011) 429–454, arXiv:1006.3570 [hep-th]. 3, 51, 58, 59

[40] C. Nunez, I. Papadimitriou, and M. Piai, "Walking Dynamics from String Duals," *Int.J.Mod.Phys.* **A25** (2010) 2837–2865, arXiv:0812.3655 [hep-th]. 3, 13, 14

[41] J. Eisert, M. Cramer, and M. Plenio, "Area laws for the entanglement entropy - a review," *Rev.Mod.Phys.* **82** (2010) 277–306, arXiv:0808.3773 [quant-ph]. 4

[42] M. Headrick, "General properties of holographic entanglement entropy," *JHEP* **1403** (2014) 085, arXiv:1312.6717 [hep-th].

[43] T. Nishioka, S. Ryu, and T. Takayanagi, "Holographic Entanglement Entropy: An Overview," *J.Phys.* **A42** (2009) 504008, arXiv:0905.0932 [hep-th]. 82

[44] H. Casini and M. Huerta, "Entanglement entropy in free quantum field theory," *J.Phys.* **A42** (2009) 504007, arXiv:0905.2562 [hep-th].

[45] P. Calabrese and J. Cardy, "Entanglement entropy and conformal field theory," *J.Phys.* **A42** (2009) 504005, arXiv:0905.4013 [cond-mat.stat-mech]. 4

[46] S. Ryu and T. Takayanagi, "Holographic derivation of entanglement entropy from AdS/CFT," *Phys.Rev.Lett.* **96** (2006) 181602, arXiv:hep-th/0603001 [hep-th]. 4, 82

[47] S. Ryu and T. Takayanagi, "Aspects of Holographic Entanglement Entropy," *JHEP* **0608** (2006) 045, arXiv:hep-th/0605073 [hep-th]. 4, 84

[48] I. R. Klebanov, D. Kutasov, and A. Murugan, "Entanglement as a probe of confinement," *Nucl.Phys.* **B796** (2008) 274–293, arXiv:0709.2140 [hep-th]. 4, 30, 81, 83, 84, 86, 95, 97, 110, 119

[49] J. M. Maldacena, "Wilson loops in large N field theories," *Phys.Rev.Lett.* **80** (1998) 4859–4862, arXiv:hep-th/9803002 [hep-th]. 4

[50] J. L. Barbon and C. A. Fuertes, "Holographic entanglement entropy probes (non)locality," *JHEP* **0804** (2008) 096, arXiv:0803.1928 [hep-th]. 4, 100, 102, 103, 106, 113, 119

[51] J. L. Barbon and C. A. Fuertes, "A Note on the extensivity of the holographic entanglement entropy," *JHEP* **0805** (2008) 053, arXiv:0801.2153 [hep-th]. 102

[52] W. Fischler, A. Kundu, and S. Kundu, "Holographic Entanglement in a Noncommutative Gauge Theory," *JHEP* **1401** (2014) 137, arXiv:1307.2932 [hep-th]. 102, 103

[53] J. L. Karczmarek and C. Rabideau, "Holographic entanglement entropy in nonlocal theories," *JHEP* **1310** (2013) 078, arXiv:1307.3517 [hep-th].

[54] N. Shiba and T. Takayanagi, "Volume Law for the Entanglement Entropy in Non-local QFTs," *JHEP* **1402** (2014) 033, arXiv:1311.1643 [hep-th]. 4, 102, 103

[55] R. Andrews and N. Dorey, "Spherical deconstruction," *Phys.Lett.* **B631** (2005) 74–82, arXiv:hep-th/0505107 [hep-th]. 5, 8

[56] R. Andrews and N. Dorey, "Deconstruction of the Maldacena-Nunez compactification," *Nucl.Phys.* **B751** (2006) 304–341, arXiv:hep-th/0601098 [hep-th]. 5, 8, 35, 108

[57] F. C. Fernandez, "D-branes in Supersymmetric Backgrounds," arXiv:0804.4878 [hep-th]. 6

[58] N. Seiberg, "Electric - magnetic duality in supersymmetric nonAbelian gauge theories," *Nucl.Phys.* **B435** (1995) 129–146, arXiv:hep-th/9411149 [hep-th]. 7, 32

[59] M. J. Strassler, "The Duality cascade," arXiv:hep-th/0505153 [hep-th]. 7, 32

[60] A. Dymarsky, I. R. Klebanov, and N. Seiberg, "On the moduli space of the cascading SU(M+p) x SU(p) gauge theory," *JHEP* **0601** (2006) 155, arXiv:hep-th/0511254 [hep-th]. 7, 8, 26, 31, 114

[61] S. S. Gubser, C. P. Herzog, and I. R. Klebanov, "Symmetry breaking and axionic strings in the warped deformed conifold," *JHEP* **0409** (2004) 036, arXiv:hep-th/0405282 [hep-th]. 8, 46, 49

[62] J. Gaillard, D. Martelli, C. Nunez, and I. Papadimitriou, "The warped, resolved, deformed conifold gets flavoured," *Nucl.Phys.* **B843** (2011) 1–45, arXiv:1004.4638 [hep-th]. 8, 13, 71, 114, 115

[63] R. Minasian, M. Petrini, and A. Zaffaroni, "New families of interpolating type IIB backgrounds," *JHEP* **1004** (2010) 080, arXiv:0907.5147 [hep-th].

[64] N. Halmagyi, "Missing Mirrors: Type IIA Supergravity on the Resolved Conifold," arXiv:1003.2121 [hep-th].

[65] E. Caceres, C. Nunez, and L. A. Pando-Zayas, "Heating up the Baryonic Branch with U-duality: A Unified picture of conifold black holes," *JHEP* **1103** (2011) 054, arXiv:1101.4123 [hep-th]. 8, 10, 11

[66] R. Casero, C. Nunez, and A. Paredes, "Towards the string dual of N=1 SQCD-like theories," *Phys.Rev.* **D73** (2006) 086005, arXiv:hep-th/0602027 [hep-th]. 11, 13, 43, 110

[67] R. Casero, C. Nunez, and A. Paredes, "Elaborations on the String Dual to N=1 SQCD," *Phys.Rev.* **D77** (2008) 046003, arXiv:0709.3421 [hep-th]. 11, 60

[68] C. Hoyos-Badajoz, C. Nunez, and I. Papadimitriou, "Comments on the String dual to N=1 SQCD," *Phys.Rev.* **D78** (2008) 086005, arXiv:0807.3039 [hep-th]. 43, 60

[69] C. Nunez, A. Paredes, and A. V. Ramallo, "Unquenched Flavor in the Gauge/Gravity Correspondence," *Adv.High Energy Phys.* **2010** (2010) 196714, arXiv:1002.1088 [hep-th]. 11, 115

[70] A. Dymarsky and S. Kuperstein, "Non-supersymmetric Conifold," *JHEP* **1208** (2012) 033, arXiv:1111.1731 [hep-th]. 20, 34, 46, 47, 48, 121

[71] S. Kuperstein and J. Sonnenschein, "Analytic nonsupersymmetric background dual of a confining gauge theory and the corresponding plane wave theory of hadrons," *JHEP* **0402** (2004) 015, arXiv:hep-th/0309011 [hep-th]. 27

[72] M. Schvellinger, "Glueballs, symmetry breaking and axionic strings in non-supersymmetric deformations of the Klebanov-Strassler background," *JHEP* **0409** (2004) 057, arXiv:hep-th/0407152 [hep-th]. 27

[73] F. Benini, F. Canoura, S. Cremonesi, C. Nunez, and A. V. Ramallo, "Backreacting flavors in the Klebanov-Strassler background," *JHEP* **0709** (2007) 109, arXiv:0706.1238 [hep-th]. 29, 132

[74] D. Freedman, S. Gubser, K. Pilch, and N. Warner, "Renormalization group flows from holography supersymmetry and a c theorem," *Adv.Theor.Math.Phys.* **3** (1999) 363–417, arXiv:hep-th/9904017 [hep-th]. 30

[75] L. Girardello, M. Petrini, M. Porrati, and A. Zaffaroni, "Novel local CFT and exact results on perturbations of N=4 superYang Mills from AdS dynamics," *JHEP* **9812** (1998) 022, arXiv:hep-th/9810126 [hep-th]. 30

[76] J. L. Cardy, "Is There a c Theorem in Four-Dimensions?," *Phys.Lett.* **B215** (1988) 749–752. 30

[77] O. Aharony, J. Sonnenschein, M. E. Peskin, and S. Yankielowicz, "Exotic nonsupersymmetric gauge dynamics from supersymmetric QCD," *Phys.Rev.* **D52** (1995) 6157–6174, arXiv:hep-th/9507013 [hep-th]. 32, 34

[78] N. J. Evans, S. D. Hsu, and M. Schwetz, "Exact results in softly broken supersymmetric models," *Phys.Lett.* **B355** (1995) 475–480, arXiv:hep-th/9503186 [hep-th]. 32

[79] N. J. Evans, S. D. Hsu, M. Schwetz, and S. B. Selipsky, "Exact results and soft breaking masses in supersymmetric gauge theory," *Nucl.Phys.* **B456** (1995) 205–218, arXiv:hep-th/9508002 [hep-th]. 32

[80] D. Freedman, C. Nunez, M. Schnabl, and K. Skenderis, "Fake supergravity and domain wall stability," *Phys.Rev.* **D69** (2004) 104027, arXiv:hep-th/0312055 [hep-th]. 34

[81] F. Bigazzi, A. Cotrone, and A. Zaffaroni, "N=2 gauge theories from wrapped five-branes," *Phys.Lett.* **B519** (2001) 269–276, arXiv:hep-th/0106160 [hep-th]. 35

[82] J. P. Gauntlett, N. Kim, D. Martelli, and D. Waldram, "Five-branes wrapped on SLAG three cycles and related geometry," *JHEP* **0111** (2001) 018, arXiv:hep-th/0110034 [hep-th]. 35

[83] E. G. Gimon, L. A. Pando Zayas, J. Sonnenschein, and M. J. Strassler, "A Soluble string theory of hadrons," *JHEP* **0305** (2003) 039, arXiv:hep-th/0212061 [hep-th]. 35

[84] U. Gursoy and C. Nunez, "Dipole deformations of N=1 SYM and supergravity backgrounds with U(1) x U(1) global symmetry," *Nucl.Phys.* **B725** (2005) 45–92, arXiv:hep-th/0505100 [hep-th]. 35

[85] L. A. Pando Zayas and A. A. Tseytlin, "3-branes on resolved conifold," *JHEP* **0011** (2000) 028, arXiv:hep-th/0010088 [hep-th]. 37, 42, 122

[86] S. S. Gubser, C. P. Herzog, and I. R. Klebanov, "Variations on the warped deformed conifold," *Comptes Rendus Physique* **5** (2004) 1031–1038, arXiv:hep-th/0409186 [hep-th]. 46, 89

[87] L. Anguelova, P. Suranyi, and L. Wijewardhana, "Holographic Walking Technicolor from D-branes," *Nucl.Phys.* **B852** (2011) 39–60, arXiv:1105.4185 [hep-th]. 51, 71

[88] T. Clark, S. Love, and T. ter Veldhuis, "Holographic Walking Technicolor and Stability of Techni-Branes," *Nucl.Phys.* **B872** (2013) 1–20, arXiv:1208.0817 [hep-th]. 71, 123

[89] L. Anguelova, P. Suranyi, and L. C. R. Wijewardhana, "On the stability of $D7 - \overline{D7}$ probes in near-conformal backgrounds," *Nucl.Phys.* **B881** (2014) 309–326, arXiv:1306.1981 [hep-th].

[90] L. Anguelova, P. Suranyi, and L. Wijewardhana, "Stability of D-brane embeddings in nontrivial backgrounds," *JHEP* **1401** (2014) 143, arXiv:1309.6678 [hep-th]. 51

[91] M. Piai, "Lectures on walking technicolor, holography and gauge/gravity dualities," *Adv.High Energy Phys.* **2010** (2010) 464302, arXiv:1004.0176 [hep-ph]. 51

[92] B. Lucini, A. Patella, A. Rago, and E. Rinaldi, "Infrared conformality and bulk critical points: SU(2) with heavy adjoint quarks," *JHEP* **1311** (2013) 106, arXiv:1309.1614 [hep-lat]. 51

[93] A. Brandhuber and K. Sfetsos, "Wilson loops from multicenter and rotating branes, mass gaps and phase structure in gauge theories," *Adv.Theor.Math.Phys.* **3** (1999) 851–887, arXiv:hep-th/9906201 [hep-th]. 52, 55, 93, 135

[94] S. D. Avramis, K. Sfetsos, and K. Siampos, "Stability of strings dual to flux tubes between static quarks in N = 4 SYM," *Nucl.Phys.* **B769** (2007) 44–78, arXiv:hep-th/0612139 [hep-th]. 55, 136

[95] D. J. Gross and H. Ooguri, "Aspects of large N gauge theory dynamics as seen by string theory," *Phys.Rev.* **D58** (1998) 106002, arXiv:hep-th/9805129 [hep-th]. 66

[96] D. Bak, A. Karch, and L. G. Yaffe, "Debye screening in strongly coupled N=4 supersymmetric Yang-Mills plasma," *JHEP* **0708** (2007) 049, arXiv:0705.0994 [hep-th]. 66

[97] C. Nunez, M. Piai, and A. Rago, "Wilson Loops in string duals of Walking and Flavored Systems," *Phys.Rev.* **D81** (2010) 086001, arXiv:0909.0748 [hep-th]. 53, 55, 66, 111, 135

[98] A. Armoni, M. Piai, and A. Teimouri, "Correlators of Circular Wilson Loops from Holography," *Phys.Rev.* **D88** no. 6, (2013) 066008, arXiv:1307.7773 [hep-th]. 52, 67

[99] A. Dymarsky, "Flavor brane on the baryonic branch of moduli space," *JHEP* **1003** (2010) 067, arXiv:0909.3083 [hep-th]. 59

[100] R. Casero and A. Paredes, "A Note on the String Dual of N=1 SQCD-like Theories," *Fortsch.Phys.* **55** (2007) 678–685, arXiv:hep-th/0701059 [hep-th]. 60

[101] Y. Kinar, E. Schreiber, and J. Sonnenschein, "Q anti-Q potential from strings in curved space-time: Classical results," *Nucl.Phys.* **B566** (2000) 103–125, arXiv:hep-th/9811192 [hep-th]. 81, 86, 87

[102] O. Aharony, J. Marsano, S. Minwalla, K. Papadodimas, and M. Van Raamsdonk, "The Hagedorn - deconfinement phase transition in weakly coupled large N gauge theories," *Adv.Theor.Math.Phys.* **8** (2004) 603–696, arXiv:hep-th/0310285 [hep-th]. 83

[103] N. Itzhaki, J. M. Maldacena, J. Sonnenschein, and S. Yankielowicz, "Supergravity and the large N limit of theories with sixteen supercharges," *Phys.Rev.* **D58** (1998) 046004, arXiv:hep-th/9802042 [hep-th]. 89, 90

[104] O. Aharony, "The NonAdS / nonCFT correspondence, or three different paths to QCD," arXiv:hep-th/0212193 [hep-th]. 89

[105] U. Kol and J. Sonnenschein, "Can holography reproduce the QCD Wilson line?," *JHEP* **1105** (2011) 111, arXiv:1012.5974 [hep-th]. 89

[106] C. Bachas, "Convexity of the Quarkonium Potential," *Phys.Rev.* **D33** (1986) 2723. 93

[107] J. Erlich, E. Katz, D. T. Son, and M. A. Stephanov, "QCD and a holographic model of hadrons," *Phys.Rev.Lett.* **95** (2005) 261602, arXiv:hep-ph/0501128 [hep-ph]. 93

[108] A. Karch, E. Katz, D. T. Son, and M. A. Stephanov, "Linear confinement and AdS/QCD," *Phys.Rev.* **D74** (2006) 015005, arXiv:hep-ph/0602229 [hep-ph]. 93

[109] A. Loewy and J. Sonnenschein, "On the holographic duals of N=1 gauge dynamics," *JHEP* **0108** (2001) 007, arXiv:hep-th/0103163 [hep-th]. 95

[110] S. Bennett, "Wilson loops in warped resolved deformed conifolds," *Annals Phys.* **326** (2011) 2934–2956, arXiv:1102.5731 [hep-th]. 110

[111] M. Warschawski, "Wilson Loops of Klebanov-Strassler like Wrapped Brane Models," arXiv:1212.3472 [hep-th]. 116

[112] E. Conde, J. Gaillard, and A. V. Ramallo, "On the holographic dual of $N = 1$ SQCD with massive flavors," *JHEP* **1110** (2011) 023, arXiv:1107.3803 [hep-th]. 110, 115

[113] E. Conde, J. Gaillard, C. Nunez, M. Piai, and A. V. Ramallo, "A Tale of Two Cascades: Higgsing and Seiberg-Duality Cascades from type IIB String Theory," *JHEP* **1202** (2012) 145, arXiv:1112.3350 [hep-th]. 114, 115, 116, 117, 118

[114] O. Aharony, "A Note on the holographic interpretation of string theory backgrounds with varying flux," *JHEP* **0103** (2001) 012, arXiv:hep-th/0101013 [hep-th]. 117

[115] T. J. Hollowood and S. P. Kumar, "An N=1 duality cascade from a deformation of N=4 SUSY Yang-Mills theory," *JHEP* **0412** (2004) 034, arXiv:hep-th/0407029 [hep-th]. 117

[116] G. Itsios, C. Nunez, K. Sfetsos, and D. C. Thompson, "Non-Abelian T-duality and the AdS/CFT correspondence:new N=1 backgrounds," *Nucl.Phys.* **B873** (2013) 1–64, arXiv:1301.6755 [hep-th]. 122, 124

[117] D. Elander, "A light scalar from deformations of Klebanov-Strassler," arXiv:1401.3412 [hep-th]. 123

[118] Y. Lozano, E. O. Colgain, and D. Rodriguez-Gomez, "Hints of 5d Fixed Point Theories from Non-Abelian T-duality," arXiv:1311.4842 [hep-th]. 124

[119] J. M. Maldacena and H. S. Nastase, "The Supergravity dual of a theory with dynamical supersymmetry breaking," *JHEP* **0109** (2001) 024, arXiv:hep-th/0105049 [hep-th]. 141

[120] F. Canoura, P. Merlatti, and A. V. Ramallo, "The Supergravity dual of 3d supersymmetric gauge theories with unquenched flavors," *JHEP* **0805** (2008) 011, arXiv:0803.1475 [hep-th]. 141

[121] N. T. Macpherson, "SuGra on G_2 Structure Backgrounds that Asymptote to AdS_4 and Holographic Duals of Confining $2+1d$ Gauge Theories with $N=1$ SUSY," *JHEP* **1304** (2013) 076, arXiv:1301.5178 [hep-th]. 141

[122] J. Gaillard and D. Martelli, "Fivebranes and resolved deformed G_2 manifolds," *JHEP* **1105** (2011) 109, arXiv:1008.0640 [hep-th]. 142